

M.Sc. Stephen Peter Brookes

**Thermo-mechanical fatigue behaviour of  
the near- $\gamma$ -titanium aluminide alloy TNB-V5  
under uniaxial and multiaxial loading**

Die vorliegende Arbeit entstand an der BAM Bundesanstalt für Materialforschung und -prüfung.

Impressum

**Thermo-mechanical fatigue behavior of the  
near- $\gamma$ -titanium aluminide alloy TNB-V5  
under uniaxial and multiaxial loading**

2009

Herausgeber:

BAM Bundesanstalt für Materialforschung und -prüfung  
Unter den Eichen 87

12205 Berlin

Telefon: +49 30 8104-0

Telefax: +49 30 8112029

E-Mail: [info@bam.de](mailto:info@bam.de)

Internet: [www.bam.de](http://www.bam.de)

Copyright © 2009 by

BAM Bundesanstalt für Materialforschung und -prüfung

Layout: BAM-Arbeitsgruppe Z.64

ISSN 1613-4249

ISBN 978-3-9812910-5-6

# **Thermo-mechanical fatigue behaviour of the near- $\gamma$ -titanium aluminide alloy TNB-V5 under uniaxial and multiaxial loading**

vorgelegt von

Stephen Peter Brookes B.Eng., M.Sc.  
aus Hitchin, Hertfordshire,  
England

von der Fakultät für Maschinenbau  
der Ruhr-Universität Bochum  
zur Erlangung des akademischen Grades

Doktor der Ingenieurwissenschaften  
- Dr.-Ing. -

genehmigte Dissertation

Promotionsausschuss:

Vorsitzender:	Prof. Dr. rer. nat. Klaus Hackl
1. Bericht:	Priv.-Doz. Dr.-Ing. Birgit Skrotzki
2. Bericht:	Prof. Dr.-Ing. Gunther Eggeler

Tag der mündlicher Prüfung: 16. Juli 2009

Bochum 2009



To

*Oliver,  
Rhea,  
Hannah,  
Sophia  
and Nicholas*

*"Not everything that counts can be counted,  
and not everything that can be counted counts".*

Albert Einstein.



## Zusammenfassung

Mit wachsendem Umweltbewusstsein und der allgemeinen Notwendigkeit, die Verwendung von fossilen Brennstoffen zu minimieren, steigt auch in der Industrie der Druck zur verstärkten Anwendung von effizienteren Gasturbinenriebwerken. Die intermetallische Gamma-Titanaluminide ( $\gamma$ -TiAl) Legierung ist ein Material, welches die Effizienz von Gasturbinen steigern kann. Bei diesem Werkstoff handelt es sich um eine relativ neue Entwicklung, der sich durch geringe Dichte und hohe Festigkeit bei hoher Temperatur auszeichnet und damit das Potenzial hat, die heute verwendeten Ni-Basis-Superlegierungen zu ersetzen. Bauteile in Fluggasturbinen sind üblicherweise variierenden, mehr-achsigen Spannungszuständen sowie nicht isothermen Zuständen unterworfen. Turbinenschaufeln sind z. B. vornehmlich drei-achsiger thermo-mechanischer Ermüdung (TMF) ausgesetzt. Dies erfordert eine sorgfältige Charakterisierung des zyklischen Verformungs- und Ermüdungsverhaltens unter komplexen thermischen und mechanischen Belastungen von  $\gamma$ -TiAl.

Die vorliegende Arbeit untersucht die Wirkungen, die diese multi-axialen Beanspruchungen, auf eine  $\gamma$ -TiAl, (Ti -45 Al -5 N.B. -0,2 B -0,2 C) Legierung unter thermo-mechanischer Ermüdung haben. Das ein-achsige, torsions- und axial-torsionale thermo-mechanische Ermüdungsverhalten dieser  $\gamma$ -TiAl Legierung ist bei 400 – 800°C mit Dehnungsamplituden von 0,15% zu 0,7% geprüft worden. Die Tests wurden an beiden thermo-mechanischen Phasen, in-phase (IP) und out-of-phase (OP), durchgeführt und ausgewählte Tests enthielten außerdem eine Haltezeit von 180 Sekunde.

Die Lebensdauer hängt stark von der Dehnungsamplitude ab. Ein-achsige Versuche unter IP Bedingungen zeigten bei gleicher mechanischer Dehnung eine längere Lebensdauer als Versuche unter OP-Bedingungen. Unter rein torsionaler Belastung zeigten die Proben bei der gleichen Vergleichsspannungsamplitude eine längere Lebensdauer als in axialen OP-Versuchen. Bei nicht-proportionaler axial-torsionaler und thermo-mechanischer OP Versuchsführung ist die Lebensdauer bei gleicher mechanischer Vergleichsdehnungsamplitude geringer als bei ein-achsiger OP-Belastung.

Die Wirkungen von TMF auf die Mikrostruktur wurden auch untersucht. Für alle Arten von Tests ist interkristalliner Bruch überwiegend. Ausfallschäden am Material sind stark von Umweltbedingungen beeinflusst.

Diese Studie vergleicht Ergebnisse von TMF von TiAl mit vorherigen TMF Untersuchungen von Ni-Basislegierungen, IN 738 und Nimonic 90. IN 738 zeigt ein ähnliches thermomechanisches Verhalten wie  $\gamma$ -TiAl, indem es bei ein-achsiger IP Belastung die längste Lebensdauer hat. Nimonic 90 zeigt ein entgegengesetztes Verhalten im Vergleich zu IN 738 und  $\gamma$ -TiAl.

Ein Lebensdauermodell, das für diese near- $\gamma$ -TiAl Legierung entwickelt wurde, beschreibt erfolgreich alle Dehnungs-Temperatur-Pfade, d. h. das thermo-mechanische Ermüdungsverhalten im Bereich der Testtemperaturen bei Verwendung eines einzelnen Belastungsparameters. Der Belastungsparameter basiert auf der plastischen Arbeit pro Zyklus und ist abhängig nicht nur von der von der Mises-Spannung sondern von der mittlern Zugspannung und von der maximalen Hauptspannung. Dieser Belastungsparameter reagiert dann auf verschiedene Dehnungs-Temperatur-Pfade unterschiedlich. Das Modell beschreibt das Lebensdauerverhalten einschließlich der ein-achsigen IP und OP, der proportional-axial-torsionalen und nicht-proportional axial-torsionalen Beanspruchungspfade, und den Einfluss der Haltezeit.

## Abstract

With increasing environmental awareness and the general need to economise on the use of fossil fuels, there is growing pressure for industry to produce lighter, more efficient, gas turbine engines. One such material that will help to achieve these improvements is the intermetallic gamma titanium aluminide ( $\gamma$ -TiAl) alloy. At only half the density of current nickel-based superalloys its weight saving capability is highly desirable, however, its mechanical properties have not yet been fully explored especially, when it is to be considered for structural components in aeronautical gas turbine engines. Critical components in these engines typically experience large variations in temperatures and multiaxial states of stress under non-isothermal conditions. These stress states are known as tri-axial thermo-mechanical fatigue (TMF).

The work presented here investigates the effects these multi-axial stresses, have on a  $\gamma$ -TiAl, (Ti-45Al-5Nb-0.2B-0.2C) alloy under TMF conditions. The uniaxial, torsional and axial-torsional TMF behaviour of this  $\gamma$ -TiAl alloy have been examined at 400 – 800°C with strain amplitudes ranging from 0.15% to 0.7%. The tests were conducted at both thermo-mechanical in-phase (IP) and out-of-phase (OP). Selected tests additionally contained a 180 seconds hold period.

Fatigue lifetimes are strongly influenced by the strain amplitude, a small increase in amplitude reduces the lifetime considerably. The uniaxial IP tests showed significantly longer fatigue lifetimes than of all the tests performed. Torsional loading although have shorter fatigue lifetimes than the uniaxial IP loading they have longer fatigue lifetimes than the uniaxial OP loading. The non-proportional axial-torsional 90 degree OP test is most damaging which resulted in a shorter lifetime than the uniaxial OP test with the same Mises equivalent mechanical strain amplitude. A hold period at maximum temperatures reduced the lifetime for all tests regardless of the temperature-strain history. The effects of TMF on the microstructure were also investigated. For all types of tests intergranular fracture is predominant. Failure is strongly influenced by environmental conditions.

This study compares TMF results of TiAl with previous TMF investigations on the nickel-based alloys IN 738 and Nimonic 90. IN 738 shows similar TMF behaviour to  $\gamma$ -TiAl in that uniaxial IP loading has the longest fatigue lifetimes. Nimonic 90 shows the opposite behaviour to both of these alloys.

A lifetime model developed for this near- $\gamma$ -TiAl alloy, successfully describes all temperature-strain TMF loading conditions over the test temperature range, with the use of a single loading parameter. The loading parameter is based on the plastic work per cycle, and is not only dependant on the mean tensile stress but also on the maximum principal stress. The loading parameter responds to various strain-temperature-paths differently. It describes the lifetime relation between uniaxial IP and OP loading, axial and torsional loading and the hold period effect.



# Contents

<b>Zusammenfassung</b>	<b>i</b>
<b>Abstract</b>	<b>ii</b>
<b>Contents</b>	<b>iii</b>
<b>Symbols and abbreviations</b>	<b>v</b>
<b>1. Introduction</b>	<b>1</b>
1.1. Titanium aluminides	1
1.1.1. Applications	10
1.2. Fatigue of metals	13
1.2.1. Uniaxial and multi-axial fatigue tests	19
1.2.2. Isothermal and non-isothermal fatigue	20
1.2.3. Fatigue of TiAl	21
1.3. Objectives	24
<b>2. Experimental method</b>	<b>27</b>
2.1. Material	27
2.2. Specimen preparation	27
2.3. Evaluation of elastic and shear moduli	29
2.4. Mechanical testing	30
2.5. Microscopy	34
<b>3. Results</b>	<b>36</b>
3.1. The as-received material	36
3.2. Material composition	38
3.3. Elastic and shear moduli	39
3.4. Thermo-mechanical fatigue behaviour	40
3.4.1. Uniaxial TMF tests	40
3.4.2. Torsional TMF tests	50
3.4.3. Axial-torsional TMF tests	55
3.4.4. Summary of thermo-mechanical fatigue behaviour	69
3.5. Fractography	71

<b>4. Discussion</b>	<b>86</b>
4.1. Evaluation of mechanical tests	86
4.1.1. Lifetime behaviour of TiAl	86
4.1.2. Fractography and microstructure observations	91
4.2. An comparison of TiAl with the Ni-based IN738 and Nimonic 90 alloys	95
4.3. Lifetime modelling	98
4.3.1. Description of the lifetime Model	98
4.3.2. Modelling approaches	100
4.3.3. The maximum principal stress model	101
4.3.4. The maximum principal stress sensitivity model	102
4.4. A generalised lifetime model	103
<b>5. Summary</b>	<b>105</b>
<b>6. References</b>	<b>107</b>
<b>Appendix 1: Test matrix data</b>	<b>116</b>
<b>Appendix 2: Table of figures</b>	<b>117</b>
<b>Appendix 3: Table of tables</b>	<b>127</b>
<b>Author's publications</b>	<b>128</b>
<b>Author's curriculum vitae</b>	<b>129</b>
<b>Acknowledgements</b>	<b>130</b>

## Symbols and Abbreviations

Symbol	Units	Explanation
$\alpha_2$		Alpha 2 phase, hexagonal DO <sub>19</sub> structure in Ti <sub>3</sub> Al
$\beta$		Beta phase, bcc structure in Ti
$\beta$		Material parameter
$\gamma$		Gamma phase, fct structure in TiAl
$\gamma$	[%]	Shear strain
$\dot{\gamma}$	[s <sup>-1</sup> ]	Shear strain rate
$\gamma_{\max}$	[%]	Maximum shear strain
$\gamma_{\min}$	[%]	Minimum shear strain
$\Delta\varepsilon$	[%]	Total strain range
$\Delta\varepsilon_e$	[%]	Elastic strain range
$\Delta\varepsilon_p$	[%]	Plastic strain range
$\Delta\gamma_p$	[%]	Plastic shear strain range
$\Delta\varepsilon/2$	[%]	Total strain amplitude
$\Delta\varepsilon_e/2$	[%]	Elastic strain amplitude
$\Delta\varepsilon_p/2$	[%]	Plastic strain amplitude
$\Delta\sigma$	[MPa]	Stress range
$\Delta\tau$	[MPa]	Shear stress range
$\dot{\varepsilon}$	[s <sup>-1</sup> ]	Strain rate
$\dot{\varepsilon}_m$	[s <sup>-1</sup> ]	Mechanical strain rate
$\dot{\varepsilon}_{eq}$	[s <sup>-1</sup> ]	Equivalent strain rate
$\varepsilon'_f$		Fatigue ductility co-efficient
$\varepsilon_{el}$	[%]	Elastic strain
$\varepsilon_{eq}$	[%]	Equivalent strain
$\varepsilon_{eq,a}$	[%]	Equivalent strain amplitude
$\varepsilon_{eq,p}$	[%]	Equivalent plastic strain amplitude
$\varepsilon_m$	[%]	Mechanical strain
$\varepsilon_{\max}$	[%]	Maximum axial strain
$\varepsilon_{\min}$	[%]	Minimum axial strain
$\varepsilon_{pl}$	[%]	Plastic strain
$\varepsilon_{th}$	[%]	Thermal strain
$\varepsilon_{tot}$	[%]	Total mechanical strain
$\rho$	[g/cm <sup>3</sup> ]	Density
$\sigma$	[MPa]	Stress
$ \sigma $	[MPa]	Stress magnitude
$\sigma_a$	[MPa]	Variable stress amplitude
$\sigma_{eq}$	[MPa]	Mises Equivalent stress
$\sigma'_f$	[MPa]	Fatigue strength co-efficient
$\sigma_m$	[MPa]	Mean stress
$\bar{\sigma}_m$	[MPa]	Mean tensile stress
$\sigma_{\max}$	[MPa]	Maximum stress
$\sigma_{\min}$	[MPa]	Minimum stress
$\sigma_{P, \max}$	[MPa]	Maximum principal stress
$\tau$	[MPa]	Shear stress

## Symbols and abbreviations

$\tau_{\max}$	[MPa]	Maximum shear stress
$\tau_{\min}$	[MPa]	Minimum shear stress
$\nu$		Poisson's Ratio
$\pi$		Pi
$\varphi_{\varepsilon-\gamma}$	[°]	Phase shift axial strain – shear strain
$\varphi_{T-\varepsilon}$	[°]	Phase shift temperature – strain
$\varphi_{T-\gamma}$	[°]	Phase shift temperature – shear strain
$\chi$		Stress function
$a$	[nm]	Lattice parameter
$A$	[-]	Amplitude ratio
$c$	[nm]	Lattice parameter
$d_i$	[mm]	Inner diameter
$d_o$	[mm]	Outer diameter
$E$	[GPa]	Modulus of elasticity or Young's modulus
$G$	[GPa]	Shear modulus
$K_{IC}$	[MPa m <sup>1/2</sup> ]	Fracture toughness
$L_o$	[mm]	Gauge length
$N$	[-]	Number of fatigue cycles
$N_f$	[-]	Fatigue life
$R$	[-]	Stress or strain ratio
$R_a$	[μm]	Roughness value
$R_m$	[MPa]	Tensile strength
$R_{p 0.2}$	[MPa]	Proof strength
$t$	[s]	Time
$T$	[°C]	Temperature
$T_m$	[°C]	Melting point
$T_{\max}$	[°C]	Maximum temperature
$T_{\min}$	[°C]	Minimum temperature
$T_e$	[°C]	Eutectoid temperature
$\dot{T}$	[K <sup>-1</sup> ]	Temperature rate
$V_f$	[%]	Volume fraction

<b>Abbreviation</b>	<b>Explanation</b>
Al	Chemical element – Aluminium
Al <sub>2</sub> O <sub>3</sub>	Aluminium oxide – Alumina
AR	As-received
at%	Atom percent
B	Chemical element – Boron
b	Burgers vector
BDTT	Brittle to ductile transition temperature
BSE	Backscattered electrons
C	Chemical element – Carbon
CCD	Counter clock-wise direction
CD	Clock-wise direction
Cr	Chemical element – Chromium
CSS	Cyclic stress-strain
Cu	Chemical element – Copper
EBS	Electron backscatter diffraction
EDM	Electrode discharge machining
EDS	Electron dispersive spectroscopy
EPMA	Electron probe micro analyzer
Fe	Chemical element – Iron
FeAl	Iron aluminide – intermetallic compound
HCF	High-cycle fatigue, $N > 10^4$
Hf	Chemical element – Hafnium
HPC	High pressure compressor
HT	High temperature
HV	Vickers hardness
H <sub>2</sub> O	Water
IN 738	Ni-based superalloy
IP	In-phase
LCF	Low cycle fatigue, $N < 10^4$
LPT	Low pressure turbine
M	Torsional moment
Mn	Chemical element – Magnesium
Mo	Chemical element – Molybdenum
N	Chemical element – Nitrogen
Nb	Chemical element – Niobium
Ni	Chemical element – Nickel
NiAl	Nickel aluminide – intermetallic compound
Nimonic 90	Ni-based superalloy
O	Chemical element – Oxygen
OP	Out-of-phase
PM	Powder metallurgy
RT	Room (ambient) temperature
SE	Secondary electrons
SEM	Scanning electron microscopy or microscope
SFE	Stacking fault energy
Si	Chemical element – Silicon
SiC	Silicon carbide
TEM	Transmission electron microscopy or microscope
Ta	Chemical element – Tantalum

## Symbols and abbreviations

Ti	Chemical element – Titanium
TiAl	Titanium aluminide – intermetallic compound
TiAl <sub>3</sub>	Titanium aluminide – intermetallic compound
Ti <sub>3</sub> Al	Titanium aluminide – intermetallic compound
TMF	Thermo-mechanical fatigue
TNB-V5	3 <sup>rd</sup> generation $\gamma$ -TiAl based alloys with a Nb content of (5-10 at%.)
Tors.	Torsion
V	Chemical element – Vanadium
vol%	Volume percent
W	Chemical element – Tungsten
WDX	Wave length dispersive x-ray micro-analysis
WEDM	Wire cut electrical discharge machining
wt%	Weight percent
XD45	3rd generation TiAl with 45%Al and a duplex microstructure
Zn	Chemical element – Zinc
Zr	Chemical element – Zirconium

## 1. Introduction

Performance and efficiency of gas turbine engines have been a long standing consideration. The development of the gas turbine blade, from the simple wrought nickel based alloys of the 1940's, to the highly refined, monocrystalline (single crystal) superalloy currently in service, has been a steady ongoing process of innovation and design [1]. However, the goal to achieve general reduction in engine weight and higher operating temperatures, which in turn lead to a more efficient fuel burn and less environmental damage, has pushed the boundaries of the superalloys up to their limits, in fact close to their melting temperature [2]. This has ultimately led to the consideration of lighter weight materials especially for less critical components of the engine. In the late 1970's intermetallic alloys began to be seriously contemplated for use as high temperature engineering alloys as their properties became more defined and potential applications explored [3].

As an intrinsic part of metallurgy, intermetallics were used by man, 4,500 years ago. However, because of their brittleness they were not employed as structural materials, instead they were utilized as hardeners in alloys with low melting temperatures, for decorative applications, such as mirrors, and - taking advantage of their wear resistance - as durable surfaces especially with cutting implements. It was not until the 1950's, that intermetallics were successfully exploited to strengthen second phases in superalloys. Through this, their potential as structural materials in their own right, became the interest for further research [4].

Intermetallics are compounds of metals whose crystal structures are different from those of the constituent metals. The term intermetallic also includes intermetallic phases and ordered alloys [4]. The metallic and covalent/ionic bonding is very strong in intermetallics, but the symmetry of deformation behaviour is low, which gives rise to their embrittlement at low temperatures. Generally, they have a wide range of crystal structures; body centred cubic (b.c.c. – B2, D0<sub>3</sub>, L2<sub>1</sub> and C11<sub>b</sub>); face centred cubic (f.c.c. – L1<sub>2</sub>, L1<sub>0</sub>, D0<sub>22</sub> and D0<sub>23</sub>) and hexagonal close packed (h.c.p.– D0<sub>19</sub> and C40). The properties of intermetallics can be described as a compromise between a ceramic and metal [4, 5].

Dimiduk [6] compared the mechanical properties of three intermetallic alloys, the L1<sub>2</sub> structured nickel aluminides (NiAl), the B2 structured iron aluminides (FeAl) and the L1<sub>0</sub> structured gamma titanium aluminides ( $\gamma$ -TiAl) with other engineering alloys. His conclusion was that of the three intermetallics mentioned above the most promising was that of  $\gamma$ -TiAl. In summary, he considered that they offer strengths greater than, or similar to, many Al and Ni alloys and their low density where minimum weight structures are important.

### 1.1. Titanium aluminides

With more environmental awareness, fuel economisation and subsequently reduced fuel costs, titanium aluminide offers many attractive properties to improve future transportation and energy technologies. At less than half the weight of any nickel based alloy and with excellent high temperature properties, their potential for aerospace applications is considerable. Figure 1.1 clearly shows the advantages TiAl alloys have over Ti alloys and superalloys at high temperatures where the specific strength is concerned with the gap gradually being closed on single crystal superalloys. Although the positive aspects are extremely good, TiAl also have negative properties, which to some extent, have held up their industrial implementation.

# 1. Introduction

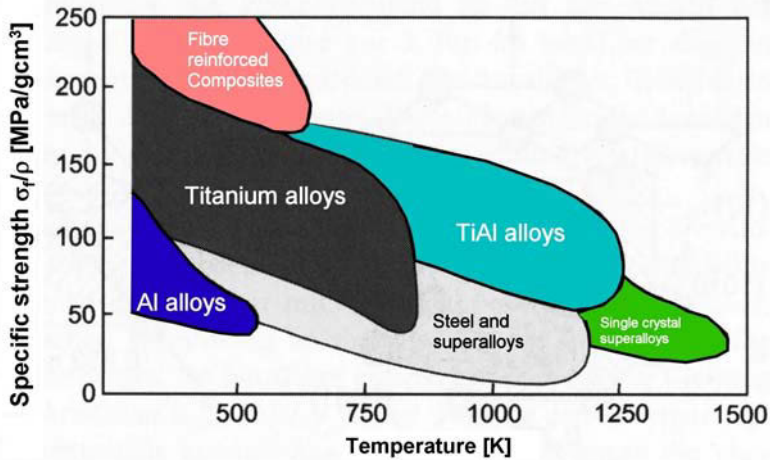


**Figure 1.1:** Specific strength  $\sigma_f / \rho$ , plotted against temperature for structural materials,  $\sigma_f$  is the yield strength for metals and tensile strength for composites. The high specific strength of TiAl alloys compared to conventional Ti alloys, heat treated steels and superalloys at higher temperatures are very attractive [7, 8].

Within the TiAl system there are effectively three ordered titanium aluminide intermetallic compounds which have the best high temperature properties,  $Ti_3Al$  ( $\alpha_2$ ), TiAl ( $\gamma$ ) and  $TiAl_3$  (see Figure 1.2 and Table 1.1).

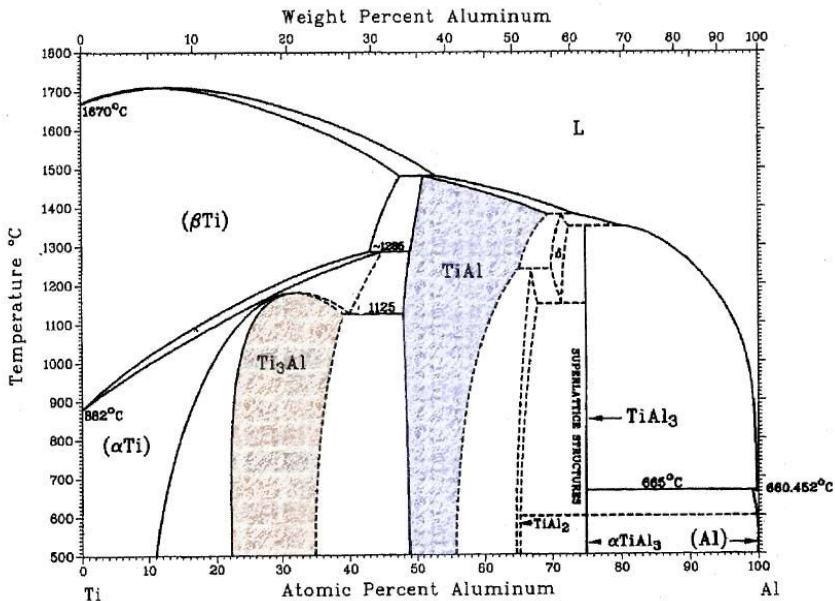


**Figure 1.2:** The titanium-aluminium binary equilibrium phase diagram [9]. The compounds  $Ti_3Al$  ( $\alpha_2$ ), and TiAl ( $\gamma$ ) are highlighted and the compounds  $TiAl_2$  and  $TiAl_3$  are indicated by arrows as they are very narrow phases.



The most favourable of these are;  $\text{TiAl}_3$  and  $\gamma\text{-TiAl}$ , because they have better oxidation resistance and very good strength to weight ratio at higher temperatures. In the ordered superlattice<sup>\*</sup>, the strong bonding of the two different atoms restricts dislocation movement and atomic diffusion at higher temperatures which promotes creep properties.

**Table 1.1:** Physical properties of the TiAl compounds [10]

Compound	Crystal structure	Lattice parameter (nm)	Melting point (°C)	Density (g/cm <sup>3</sup> )	Elastic modulus (GPa)
$\text{TiAl}_3$	$\text{DO}_{22}$ ordered tetragonal	$a = 0.3840$ $c = 0.8596$	1340	3.4	200
$\text{TiAl}$ ( $\gamma$ )	$\text{L1}_0$ ordered f.c. tetragonal	$a = 0.4005$ $c = 0.4070$	1460	3.9	175
$\text{Ti}_3\text{Al}$ ( $\alpha_2$ )	$\text{DO}_{19}$ ordered hexagonal	$a = 0.5782$ $c = 0.4629$	1600	4.3	145

The  $\text{TiAl}_3$  compound has a  $\text{DO}_{22}$  ordered tetragonal crystal structure and has the best oxidation resistance, lowest density and specific stiffness of all the TiAl compounds (see Figure 1.3a).

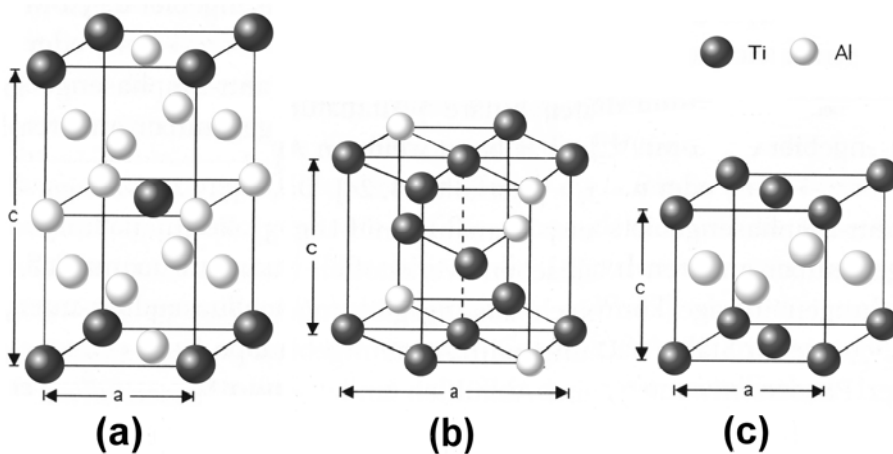


**Figure 1.3:** Crystal structures of the TiAl compounds (a)  $\text{TiAl}_3$  ordered tetragonal  $\text{DO}_{22}$  structure (for lattice parameters see Table 1.1), (b)  $\alpha_2\text{-Ti}_3\text{Al}$  ordered hexagonal  $\text{DO}_{19}$  structure and (c)  $\gamma\text{-TiAl}$  ordered (alternative layers of Ti and Al) face-centred tetragonal (fct)  $\text{L1}_0$ [11, 12].

The main disadvantage of this compound is that it is very brittle. Attempts have been made to improve ductility by the addition of ternary transition metals in particular Cu, Mn, Zn, Fe, Cr, however, despite an improvement, they are still brittle and tend to suffer from cleavage fracture.

The compound  $\text{Ti}_3\text{Al}$  ( $\alpha_2$ ) has been extensively studied (see Figure 1.3b). Compared to conventional titanium alloys its main attraction has been due to its outstanding strength to weight ratios, but the creep strength is low. Within the composition range 22-39% aluminium (see Figure 1.2),  $\alpha_2\text{-Ti}_3\text{Al}$  undergoes an order/disorder transition to form a  $\text{DO}_{19}$

<sup>\*</sup> The ordered arrangement of periodically alternating layers of different atoms.

## 1. Introduction

ordered hexagonal structure. Alloyed with niobium, the low temperature ductility is improved by increasing the number of active slip systems. This is achieved by substitution of niobium (Nb) atoms for titanium atoms in the crystal lattice. Alloys have been developed which contain 17 at% Nb [10].

Of these three compounds, general attention is now concentrated on  $\gamma$ -TiAl (see Figure 1.3c). Alpha and super-alpha compositions (TiAl<sub>3</sub> based) are no longer of significant interest, because  $\gamma$ -TiAl has shown to have superior mechanical and physical properties [12, 13].

Compared to other titanium based alloys (see Table 1.2),  $\gamma$ -TiAl has superior values of elastic moduli ( $E = 171$  GPa at 26°C - 134 GPa at 1000°C [14]) this is why it has become the focus of attention within the TiAl compounds. Other positive properties are: high temperature strength, high oxidation resistance up to 750°C, lower sensitivity to hydrogen embrittlement, low thermal expansion coefficient, a high thermal conductivity, good creep resistance and they are burn resistant. However, they have some properties which could limit their applications. They have low fracture toughness and high fatigue crack growth rates which lead to poor damage tolerance (see Table 1.2) [13, 15].

**Table 1.2:** Properties of Ni based, Ti-based and  $\gamma$ -TiAl alloys [4, 5, 12, 13, 15-22]

Property	Ni-based	Ti-based	$\gamma$ -TiAl
Young's modulus (E) (GPa) RT	195 - 220	95 - 115	170
Young's modulus (E) (GPa) 800°C	150 - 160	60 - 70	150
Shear modulus (G) (GPa) RT	76 - 80	40 - 48	62
Shear modulus (G) (GPa) 800°C	60	23 - 30	52
Proof strength ( $R_{p0.2}$ ) (MPa) RT	800 - 1200	345 - 1000	350 - 600
Tensile strength ( $R_m$ ) (MPa) RT	1250 - 1450	480 - 1200	450 - 800
Density ( $\rho$ ) (g/cm <sup>3</sup> )	7.9 - 8.5	4.5 - 4.6	3.7 - 4
Thermal expansion ( $\mu\text{m}/(\text{m}\cdot\text{K})$ ) RT	11.2 - 14.6	7.2 - 9.5	8.6
Ductility (%) RT	3 - 5	10 - 25	1 - 3
Ductility (%) HT	10 - 20	12 - 50	10 - 90
Creep limit (°C)	800 - 1090	600	1000
Oxidation limit (°C)	870 - 1090	600	800 - 1000
Melting point $T_m$ (°C)	1480	1668	1460
Poisson's Ratio ( $\nu$ ) RT	0.31	0.34	0.23
Fracture toughness ( $K_{Ic}$ ) (MPa m <sup>1/2</sup> ) RT	77 - 84	44 - 66	11 - 39
Fracture toughness ( $K_{Ic}$ ) (MPa m <sup>1/2</sup> ) 650 - 700°C	75 - 65	-	25
Hardness HV	-	360 - 450	970

Moreover, the most limiting feature, is their low ductility at low to intermediate temperatures (< 3% at room temperature) which makes processing and machining difficult, complicated and subsequently expensive. Even at elevated temperature, formability is restricted. The strong bonds that prevent slip dislocations also prevent ambient temperature ductility. In order to improve their formability, they have been subjected to a great deal of alloying, heat treatments and microstructural control [5, 12].

The binary near- $\gamma$ -TiAl alloys consist of two solid phases, the main phase,  $\gamma$ -TiAl (between 80-98% volume fraction) which is an ordered face-centred tetragonal (fct) L1<sub>0</sub> structure (see Figure 1.3c) and the minor phase,  $\alpha_2$ -Ti<sub>3</sub>Al which is an ordered hexagonal DO<sub>19</sub> structure (see Figure 1.3b).

Deformation of  $\gamma$ -TiAl ( $L1_0$ ) takes place through glide of ordinary dislocations of the type  $1/2\langle 110 \rangle$ <sup>†</sup> and superdislocation glide of the type  $\langle 011 \rangle$ ,  $1/2\langle 112 \rangle$  and only at very high temperatures  $\langle 100 \rangle$ . Preferential glide occurs on the close packed  $\{111\}$  planes (see Figure 1.4) [23, 24].

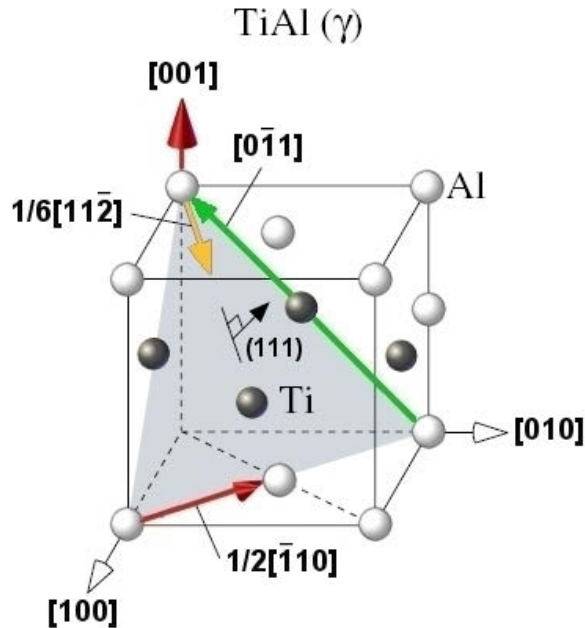


**Figure 1.4:** Preferential directions of glide on the close packed  $(111)$  plane in the  $L1_0$  crystal structure. The possible Burgers vectors of ordinary dislocations of the type  $1/2\langle 110 \rangle$  and  $\langle 001 \rangle$  and the superdislocations of the type  $\langle 011 \rangle$  and partial dislocations  $1/6\langle 112 \rangle$  [11, 23, 24].

Ordinary dislocations, also referred to as ‘easy slip’ which prevail in the  $1/2\langle 110 \rangle$  direction and do not destroy the ordered  $L1_0$  structure of the  $\gamma$ -TiAl phase (see Figures 1.4, 1.5a and 1.5b). Superdislocations occur in pairs which slip in the direction  $\langle 011 \rangle$ , the first dislocation  $1/2\langle 011 \rangle$  destroys the ordered structure, however, the second  $1/2\langle 011 \rangle$  re-establishes it (see Figures 1.5a and 1.5b) [11, 25]. An anti-phase domain boundary (APB) is present between these dislocations creating high energy regions of the lattice [26]. These dislocations can further split into partial dislocations bringing about complicated stacking faults. Further partial dislocations in the  $1/2\langle 112 \rangle$  direction have been described as ‘complex split’ superdislocations (see Figure 1.5a and 1.5b).

<sup>†</sup> The vectors  $[011]$  and  $[101]$  in the ordered  $L1_0$  structure are equivalent, but not equivalent to  $[110]$ , hence the parenthesis  $\langle 011 \rangle$  is used to notate all distinct permutations of only  $\pm h$  and  $\pm k$  but not  $l$  [23].

## 1. Introduction

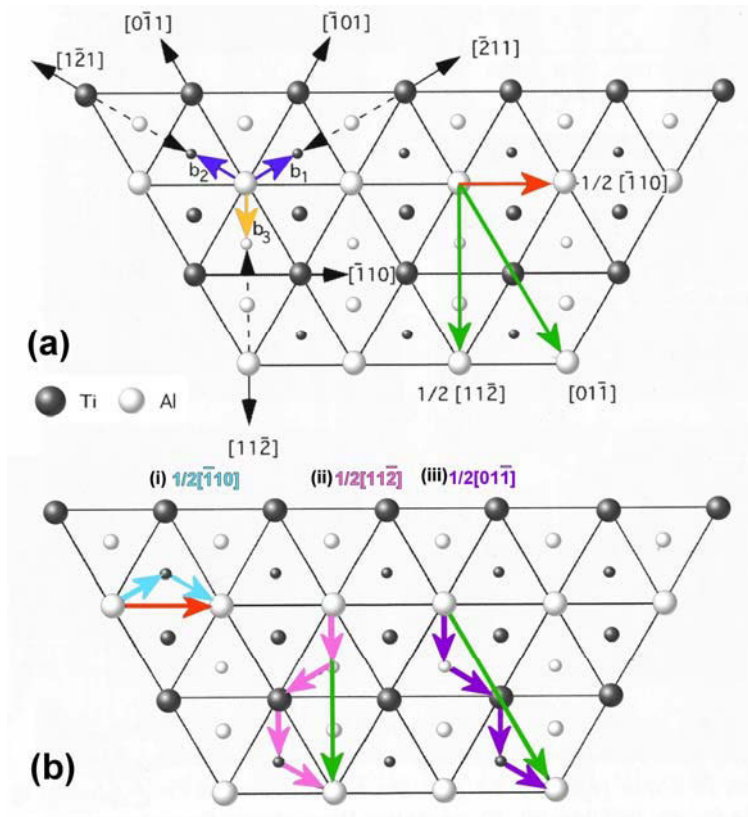


**Figure 1.5:** Schematic illustration of potential slip and twinning systems in the L1<sub>0</sub> structure (a) the three layer atom stacking sequence on the (111)  $\gamma$ -plane. Ordinary dislocations  $1/2[\bar{1}10]$  (red arrow) and superdislocations  $[01\bar{1}]$  and  $1/2[11\bar{2}]$  (green arrows). The Burgers vectors of the pseudo-twinning (partial dislocations)  $b_1 = 1/6[\bar{2}11]$ ,  $b_2 = 1/6[1\bar{2}1]$  (blue arrows) and for true twinning  $b_3 = 1/6[11\bar{2}]$  (yellow arrow) which is perpendicular to Burgers vector  $b = 1/2[\bar{1}10]$  for ordinary slip. (b) Core configurations of completely dissociated dislocations with Burgers vectors (i)  $1/2[\bar{1}10]$  (pale blue arrows) (ii)  $1/2[11\bar{2}]$  (pink arrows) and (iii)  $1/2[01\bar{1}]$  (purple arrows) [11, 23].

An important feature in the plastic deformation of  $\gamma$ -TiAl at low temperatures arises from mechanical twinning of the type  $1/6\langle 11\bar{2} \rangle \{111\}$  which significantly contribute to the total deformation. Mechanical twinning exist in two forms, true and pseudo-twinning, these form along Burgers vectors associated with partial dislocations. In particular:  $b_1 = 1/6[\bar{2}11]$ ,  $b_2 = 1/6[1\bar{2}1]$  and  $b_3 = 1/6[11\bar{2}]$  in Figure 1.5a. For true twinning, the glide of the Shockley partial dislocation is along  $b_3 = 1/6[11\bar{2}]$  on (111), and for pseudo-twinning along  $b_1$  and  $b_2$  (see Figure 1.5a). Shear in the reversed direction along  $-2b_3$  is known as anti-twinning or complementary twinning mode [11, 23, 25, 27].

In two phase ( $\alpha_2 + \gamma$ ) duplex  $\gamma$ -TiAl microstructures,  $\gamma$ -grain deformation takes place by mechanical twinning and ordinary slip dislocations along the  $1/2[110]$  direction. The same

slip dislocations along  $1/2\langle 110 \rangle$  occur in the  $\gamma$ -lamellae grains. The mechanisms of deformation remain the same with increasing temperature at the same time they also become more proliferate [25]. Brittle fracture at low temperature is caused by low dislocation mobility, which hinders the formation of the plastic zone at the crack tip. Without this damage mechanism, there is no stress relaxation just a stress concentration which in turn brings about rapid failure [4].

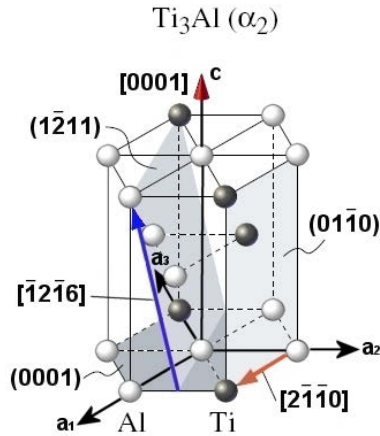


**Figure 1.6:** Preferential directions of glide (shaded) in the  $D0_{19}$  crystal structure. The slip dislocations  $2/3\langle 11\bar{2}0 \rangle$  on the basal  $\langle 11\bar{2}0 \rangle$   $\{0001\}$ , prismatic  $\langle 11\bar{2}0 \rangle$   $\{11\bar{0}0\}$  and pyramidal  $\langle \bar{1}\bar{1}26 \rangle$   $\{11\bar{2}1\}$  slip planes [24, 28]

Deformation in the  $\alpha_2$  phase in the  $D0_{19}$  structure occurs by slip dislocations  $2/3\langle 11\bar{2}0 \rangle$  on the basal  $\langle 11\bar{2}0 \rangle$   $\{0001\}$ , prismatic  $\langle 11\bar{2}0 \rangle$   $\{11\bar{0}0\}$  and pyramidal  $\langle \bar{1}\bar{1}26 \rangle$   $\{11\bar{2}1\}$  slip planes (see Figure 1.6) [24, 28]. A small amount of tensile ductility is seen in basal slip and very large tensile elongations observed in prism slip. There is no stress relief due to twinning mechanisms as seen in the  $\gamma$ -phase, therefore strain incompatibilities and stress concentrations accumulate at grain boundaries, which can cause cleavage fracture [4]. Above  $700^\circ\text{C}$  pyramidal slip is the primary cause of deformation. The small scale and lack of slip systems in the  $\alpha_2$  phase, especially when the  $c$ -axis is parallel to the tensile load, is thought to be the main reason for the low ductility of the two-phase TiAl [11, 23, 24].

**Table 1.3:** Microstructures of  $\gamma$ -TiAl and the effects on mechanical properties [28-31].

Microstructure		Mechanical influence	
		(+)	(-)
<b>Globular-<math>\gamma</math></b> (Figure 1.7a)	Relatively small $\alpha_2$ -Ti <sub>3</sub> Al grains which lie between mostly equiaxed $\gamma$ -TiAl grains.	Higher ductility at HT	Poor ductility at RT
<b>Duplex</b> (Figure 1.7b)	Interspersed lamellar grains (alternating lathes of $\alpha_2$ and $\gamma$ ) and equiaxed $\gamma$ -TiAl grains, roughly equal in size.	High tensile strength and ductility	Poor fracture toughness and low creep strength
<b>Near lamellar</b> (Figure 1.7c)	Large volume fraction of lamellar grains intermixed with some smaller grains of $\gamma$ -TiAl.	Better fracture toughness and creep properties	Low ductility
<b>Fully lamellar</b> (Figure 1.7d)	Consists entirely of very large lamellar grains (in the order of 100 $\mu\text{m}$ , sometimes mm in size)	Good fracture toughness and creep properties.	Poor tensile ductility

## 1. Introduction

Thermal history and processing techniques play a large role on the outcome of the microstructure.  $\gamma$ -TiAl phase is near equiatomic in composition i.e., between 49-55 at% Al and near- $\gamma$ -TiAl refers to alloys that have between 45-55 at% Al. Above 1100°C, from the  $\alpha_2$  and  $\gamma$ -phases ( $\alpha_2 + \gamma$ ) the microstructure undergoes changes which are classified according to the dominant phase present, i.e. globular- $\gamma$ , duplex, near lamellar and fully lamellar (see Table 1.3). As these phases each have their own effects on the mechanical properties they can be generated, via processing technology and heat treatments, to suit the needs of the end product (see Figure 1.7) [13, 23].

The globular- $\gamma$  microstructure refers to the phase formed after a heat treatment of above 1125°C, i.e. above the eutectoid temperature ( $T_e$ ). It consists of a small amount of  $\alpha_2$  phase at the grain boundaries of the mostly equiaxed (grains that have axes approximately equal in length)  $\gamma$ -TiAl grains. Coarse annealing twins are sometimes formed during grain growth in the  $\gamma$ -TiAl grains (Figure 1.7a) [25, 32].

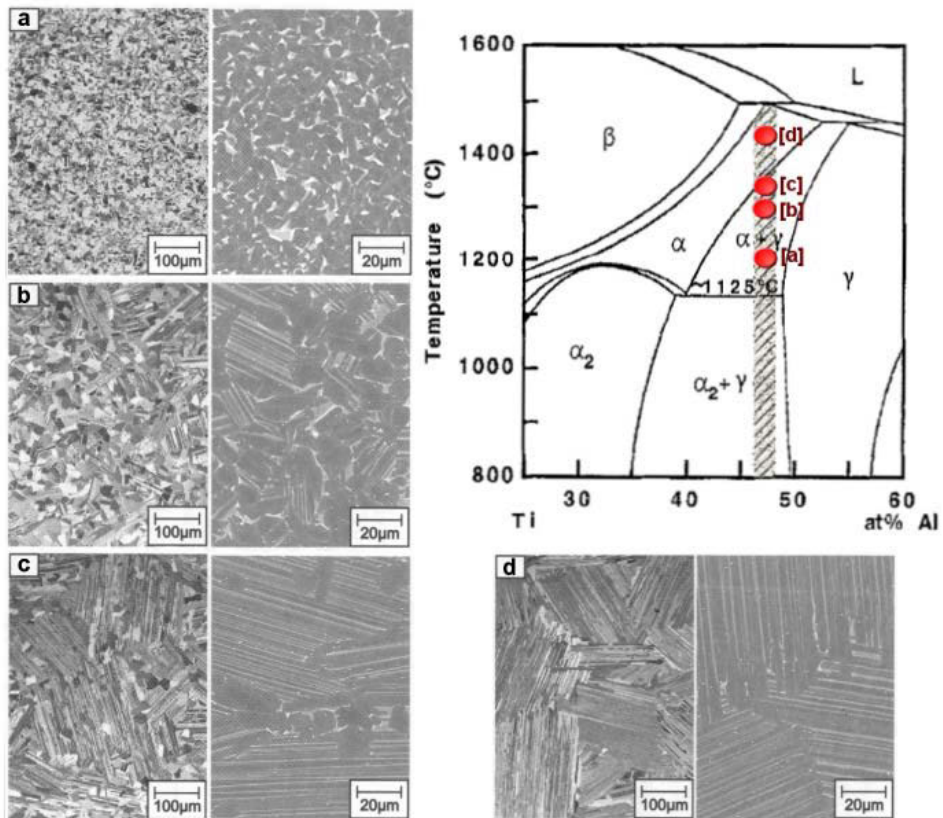


**Figure 1.7:** The different types of microstructure encountered in heat treated  $\gamma$ -TiAl, a) globular- $\gamma$ , b) duplex, c) near lamellar, d) fully lamellar ( $\gamma$ -grains are contrasted darker to the lighter  $\alpha_2$ -grains) and their approximate location on the central section of the assessed TiAl binary phase diagram. The shaded vertical line represents the composition of  $\gamma$ -TiAl alloys that have the most technical significance [23, 25, 27, 32].

The duplex microstructure is interspersed lamellar and  $\gamma$ -TiAl grains, roughly equal in size. This phase is formed after a heat treatment at  $\sim 1300^\circ\text{C}$  (dependant on composition), in the middle of ( $\alpha + \gamma$ ) region. The lamellar grains consist of fine  $\alpha_2$ -Ti<sub>3</sub>Al and  $\gamma$ -TiAl lamellae, with thicknesses of several tens of nanometres. The proportion of lamellar grains increases with increasing temperature in the ( $\alpha + \gamma$ ) region (Figure 1.7b).

Just below the  $\alpha$  transus temperature, a microstructure is formed which is known as near lamellar (see Figure 1.7c). This consists mainly of a large volume fraction of fine grained lamellar microstructure intermixed with some finer grains of  $\gamma$ -TiAl.

Heating above the  $\alpha$  transus temperature, in this single  $\alpha$ -phase region, gives rise to a fully lamellar microstructure, (see Figure 1.7d) entirely consisting of very large, 100-500 $\mu\text{m}$  lamellar colonies. The absence of  $\gamma$ -grains allows the unhindered growth of the lamellar microstructure. However, the  $\alpha_2$  lamellae are not as thick as those seen in the duplex or near-lamellar microstructures. The grain boundaries between the grains are not smooth but serrated and give good creep behaviour [13, 25, 30].

The range of  $\gamma$ -TiAl alloys has developed considerably, with the first generation in 1975, to the current 3rd generation (1997 to the present day). Generally, the 3rd generation alloys contain more additional trace elements, but, at the same time the Al concentration has been gradually reduced to 44 at%. Table 1.4 shows this thirty year development [33-35].

**Table 1.4:** TiAl alloy development [Atomic %] [33-35]

Content in at%	Generation	Structure	Year
Ti-48Al-1V-0.1-(0.1-0.3)C Ti-49Al-1.5Mn	1	Single phase	1975-81 1982-85
Ti-(47-48)Al-2(Cr,Mn)-2Nb Ti-(45-47)Al -2Nb-2Mn+0.8Vol-%TiB <sub>2</sub> Ti-47Al-2W-0.5Si Ti-46.5Al-3Nb -2Cr -0.2W – (0.2C-0.2Si) Ti-47Al-1.6Fe-1.4V-2.4B	2	Lamellar – grain refined	1986 1986-95 1993-98
Ti-47Al-5(Cr, Nb, Ta) Ti-(45-47)Al-(1-2)Cr-(1-5)Nb-(0-2)(W, Ta, Hf, Mo, Zr)- (0-0.2)B-(0.03-0.3)C-(0.03-0.2)Si-(0.1-0.25)O <sub>x</sub>	3	Duplex	1997- 2004

The additions of trace elements have been shown to affect the mechanical properties in the following ways:

- Al/Nb - Increasing strength levels
- C, Si, N - Improving creep resistance and high temperature Performance
- Nb, Ta, Mo, W - Improving oxidation resistance
- B - Grain refinement
- Cr, V, Mn, Si - Improved ductility but reduced oxidation resistance

The more recent TiAl alloys that have been developed, tend to have a higher content of Nb up to 10 at%. This has been found to strengthen the  $\gamma$ -phase in single phase alloys, it was also found to embrittle it [36]. Nb and C addition is found to reduce minimum creep rate and retard creep acceleration in the tertiary creep stage of TiAl alloy [37]. B addition encourages grain refinement and improves ambient temperature mechanical properties [38, 39]. This is particularly noticeable with lamellar colonies which become more randomly distributed and reduced in size by grain refinement. However, there is a minimum B level for grain

## 1. Introduction

refinement (~0.5 at%) and this is additionally dependent on the alloy composition [40]. There is also a critical level at which B has no effect on grain refinement [38]. The negative effects of some of these additional trace elements have been the gradual loss of ductility, decreased damage tolerance and subsequent increased processing difficulties [12, 34, 35].

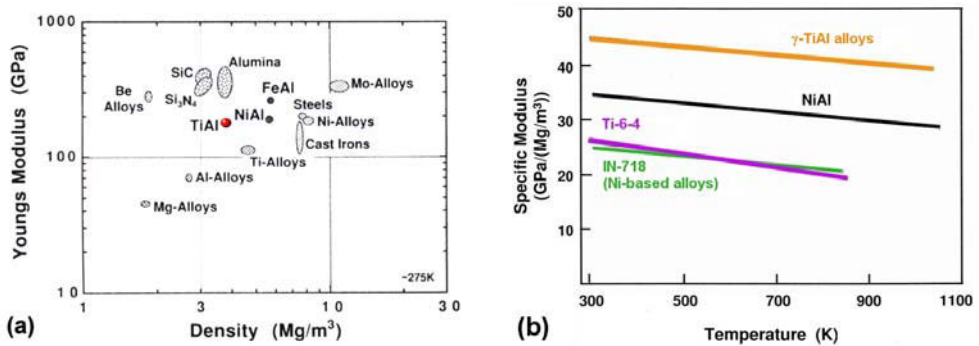


**Figure 1.8:** Comparison of (a) room temperature Young's modulus versus density and (b) specific modulus versus temperature, for various structural metals and intermetallics.[6]

$\gamma$ -TiAl alloys were considered as an ideal material for rotating components, mainly because of their low density (see Figure 1.8a), which simply reduces the centrifugal loading and the overall disc stresses. The stress caused by centrifugal loading on a Ni-based turbine blade root with a blade length 100mm and radius of 0.5m is ~180MPa [1], the same blade made of  $\gamma$ -TiAl would exert a stress of ~80MPa on the blade root. At higher temperatures  $\gamma$ -TiAl alloys have a specific modulus (stiffness) which is 50-70% greater than for Ti alloys and exceeds Ni-based polycrystalline alloys at all temperatures (see Figure 1.8b) [6]. Their relative low density also reduces vibration problems, especially when the size of shafts, frames and bearings are concerned [41]. However, these alloys have some negative properties which restricted their application within the gas turbine industry. These are essentially, their low ductility at low to intermediate temperatures; high fatigue crack growth rates which leads to poor damage tolerance and low fracture toughness [15]. These factors alone make fabrication and machining difficult and expensive which has tended to hold back their general application. Lasalmonie [42] considered that the introduction of TiAl into aero engines would only be considered if the technical needs of weight saving could be afforded and that their use limited to components which were not subjected to strong thermal gradients, this in turn, would consequently limit their size and application. Recina and Karlsson [43] highlighted the need to control the replication of the microstructure, due to the effects microstructure has on mechanical properties. This involves accurate heat treatments and processing procedures. They additionally considered chemical composition as an important aspect of the mechanical properties. These issues would subsequently affect the end material cost, and eventual speed of implementation. Once, however, these problems are overcome, the general applications will undoubtedly be numerous. There have been some successful commercial applications of TiAl and these are described in the next section.

### 1.1.1. Applications

The most important issue for a new engineering material is not just its advantages over its potential predecessor, but its commercial viability. If the material is just not cost effective to use then its adoption by industry becomes less probable, otherwise its properties have to



be so beneficial that production costs play less of a role, an example of this is motor sport such as Formula 1 racing. The transition of a developing material to a commercial application demands a cost reduction via higher volume production. However, the growing awareness to environmental damage, noise pollution and fuel economy has, in some cases, compelled manufactures to adopt a more expensive material in order to meet the increasing stringent environmental regulations. These challenges are being addressed by the European and Japanese automobile industries by down sizing their combustion engines, but at the same time, enhancing the engine performance by increasing combustion gas temperatures and engine rpm [44, 45].

One of the first major commercial applications of TiAl was as automobile exhaust valves (see Figure 1.9) [45]. These were first commercially adopted by the automobile manufacturer Mitsubishi in its Lancer-6 engine [46].  $\gamma$ -TiAl was chosen because of its low density, its corrosion resistance and high temperature creep strength [45]. With its introduction it has brought along other major benefits such as, higher fuel economy, reduced noise and vibration problems and lower emissions [44, 47].

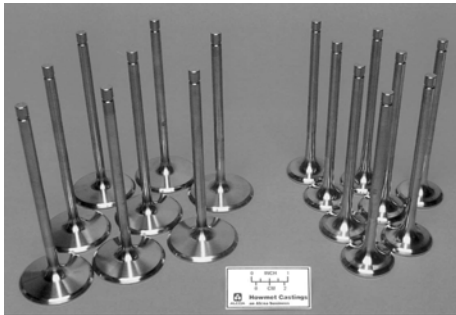


**Figure 1.9:** Cast  $\gamma$ -TiAl automobile exhaust valves (Howmet Castings)[3]

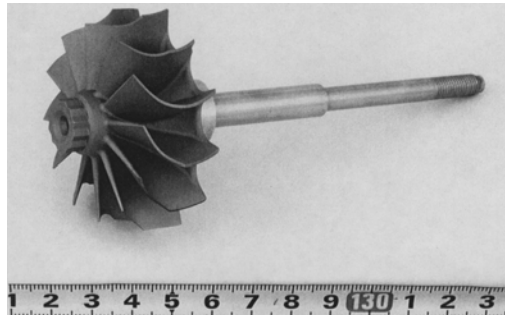


**Figure 1.10:** Commercial  $\gamma$ -TiAl turbocharger turbine wheel for a passenger vehicle (Mitsubishi Heavy Industries, Ltd.)[46]

Another successful commercial application has been that of the turbocharger turbine wheels (see Figure 1.10) developed and tested by Mitsubishi Heavy Industries, Ltd., Nagasaki, Japan. Since 1999 it has been incorporated in the Lancer Evolution series automobile made by Mitsubishi Motors Corporation [48, 49]. Turbocharger turbine wheels are a type of supercharger that is powered by the engine exhaust gas to force intake air into the engine to enhance power and a cleaner ignition. These components are highly loaded, in thermal strain (750°C in diesel engines and 950°C in gasoline engines) and mechanical strain, with high and low cycle fatigue. They are also subjected to creep, oxidation and erosion. Previously turbocharger turbine wheels were made from Ni-based alloys, but these have shown to have too much inertia (turbolag – insufficient transient engine power response), to produce high emissions, to have excessive noise, undue vibration and low lifetimes [44].

However, from its initial discovery, it was envisaged that TiAl would best be suited for aerospace applications, mainly due to its excellent creep strength, toughness, oxidation resistance, burn resistance and general long-term stability, particularly at high temperature.  $\gamma$ -TiAl intermetallics are also favourable for improving thrust-to-weight ratios, this is primarily because of their low density (at least a 40% reduction over conventional components [50]). In addition, this higher efficiency - reduced fuel consumption, reduced fuel costs and subsequent lower exhaust emissions - makes them economically and environmentally

## 1. Introduction

attractive [51]. Key areas for the introduction of this material into aeronautical gas turbine engines are as low pressure turbine (LPT) blades and high pressure compressor (HPC) blades, where the component is subjected to moderate to high temperatures and centrifugal loading (see Figure 1.11) [3, 15]. The General Electric GEnx (General Electric Next-generation) which is an advanced turbofan under development by GE-Aviation for the Boeing 787 and 747-8, will contain TiAl stage 6 and 7 LPT blades [52-54].

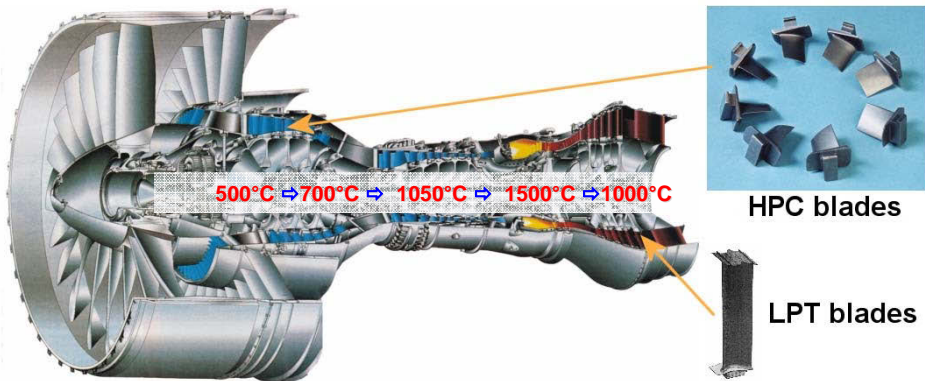


**Figure 1.11:** Schematic illustration of an aero gas turbine engine showing the gas temperature path through the engine with the proposed TiAl blade locations and blade types. The introduction of this material into the aero gas turbine engine would reduce the component weight by 40% (image source: MTU Aero Engines GmbH) [55, 56].

TiAl components will also be incorporated in the new LEAP-X (Leading-Edge Aviation Propulsion) GE36 turbofan engine developed by CFM, a joint venture company owned by Snecma (SAFRAN Group) of France and General Electric Company (GE) of the USA. With 16% higher fuel efficiency, the first LEAP-X demonstrator engine is scheduled to run in 2012 and could be certified by 2016 (see Figure 1.12) [57].



**Figure 1.12:** The CFM LEAP-X GE36 unducted turbofan (open rotor). (image source: CFM) [58].

## 1.2. Fatigue of metals

A metal subjected to fluctuating or repetitive stress (dynamic loading) will fail at a load lower than required for it to fail on a single load application, in fact, lower than the tensile strength or even below the proof stress point. Since the 1830's this has been termed as 'fatigue failure', because the failure usually ensues after the material has been subjected to repeated mechanical loading (mechanical fatigue) over a period of time. This period up to failure, is known as fatigue life ( $N_f$ ). Fatigue failure often happens without warning and with very little plastic deformation at the fracture. The process occurs by the initiation and propagation of cracks with the fracture surface usually perpendicular to the applied stress. Macroscopically, the progress of the fracture is indicated by a series of rings or "beach marks" which progress inwards from the point of fracture initiation [19, 59-61].

Fatigue failure can occur in different forms. Progressive deformation of a metal at a constant load ( $T > 0.5 T_m$ ) is referred to as creep. If significant plastic deformation occurs during cyclic loading, as a result of high stress concentrations or stress amplitudes, then the metal is subjected to low cycle fatigue (LCF). Thermal fatigue refers to fluctuation in thermal stress induced at elevated temperatures which can exclude the presence of any external mechanical stresses. Combining thermal fatigue with cyclic mechanical loading is known as thermo-mechanical fatigue (TMF). Cyclic mechanical loading in the presence of corrosive environments it is known as corrosion fatigue. Sliding contact and rolling contact fatigue are caused by the repeated application of sliding loads or rolling contact loads. Fretting fatigue is caused by frictional sliding between surfaces. Another characteristic of fatigue is that failure occurs due to a point of stress concentration such as a notch, corner, inclusion or due to impact damage. Today fatigue failure accounts for 90% of all in service metallic failures [19, 59-61].

In summary fatigue is caused by three basic factors:

1. a sufficiently high value of maximum tensile stress
2. fluctuation or adequately large variations in the applied stress
3. a sufficient number of cycles of the applied stress

Additional variables that alter the conditions of fatigue are, overloading, residual stresses, stress concentrations, combined stresses, temperature, environment and the metallurgical structure [59].

The types of fluctuating stresses (axial, flexural and torsional) which cause fatigue can be in the form of *completely reversed*, in which the stress is equally cycled under tension and compression (see Figure 1.13a), *repeated* in which the maximum and minimum stresses are not equal (see Figure 1.13b and 1.13c) or *irregular* where stresses can be complicated such as those experienced by an aircraft wing subjected to gusts of wind (see Figure 1.13d).

The stress amplitude alternates about the mean stress  $\sigma_m$ , which is defined as:

$$\sigma_m = \frac{\sigma_{max} + \sigma_{min}}{2} \quad \text{Eq. 1.1}$$

and the alternating or variable stress amplitude  $\sigma_a$ , is one half of the stress range,  $\Delta\sigma$ :

## 1. Introduction

$$\sigma_a = \frac{\Delta\sigma}{2} = \frac{\sigma_{max} - \sigma_{min}}{2} \quad . \quad \text{Eq. 1.2}$$

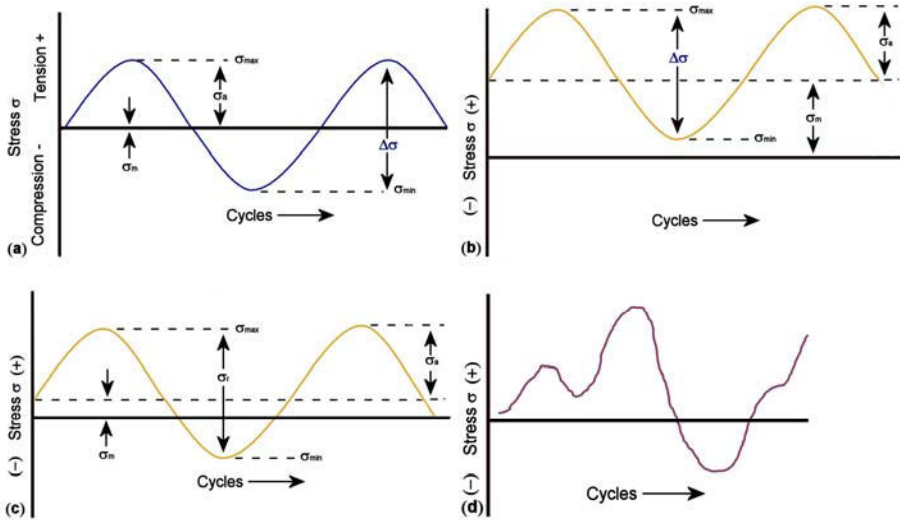


**Figure 1.13:** Schematic representation of the fatigue stress cycles for a) a fully reversed stress cycle where  $\sigma_{max}$  and  $\sigma_{min}$  are symmetrical to the zero stress level,  $\sigma_m = 0$ , b) a repeated stress cycle where  $\sigma_{max}$  and  $\sigma_{min}$  are asymmetrical to the zero stress level, here shown just in tension also possible in compression or c)  $\sigma_{max}$  and  $\sigma_{min}$  of the opposite sign or both and d) a random or irregular stress [19, 59]

In 1910, Basquin related the stress amplitude with the numbers of cycles to failure as a linear expression:

$$\frac{\Delta\sigma}{2} = \sigma_a = \sigma'_f (2N_f)^b, \quad \text{Eq. 1.3}$$

where  $\sigma'_f$  is the fatigue strength coefficient,  $2N_f$  is the number of load reversals to failure (one cycle is two reversals), and  $b$  is the fatigue strength exponent or Basquin exponent (varies between -0.05 and -0.12 for most metals).

The stress range,  $\Delta\sigma$ , is the difference between the maximum and minimum stress in a cycle:

$$\Delta\sigma = \sigma_{max} - \sigma_{min} \quad . \quad \text{Eq. 1.4}$$

The strain range,  $\Delta\varepsilon$ , is the difference between the maximum and minimum strain in a cycle:

$$\Delta\varepsilon = \varepsilon_{max} - \varepsilon_{min} \quad . \quad \text{Eq. 1.5}$$

The stress ratio  $R$ , is the ratio between minimum and maximum stress amplitudes:

$$\text{Stress load ratio: } R = \frac{\sigma_{min}}{\sigma_{max}} \quad . \quad \text{Eq. 1.6}$$

$$\text{Amplitude ratio: } A = \frac{\sigma_a}{\sigma_m} = \frac{1-R}{1+R}. \quad \text{Eq. 1.7}$$

For example for a fully reversed cycle, when  $\sigma_m = 0$ , the stress ratio is  $R = -1$  [19, 59, 60].

The influence of mean stress  $\sigma_m$ , is important when considering fatigue in engineering components as they are typically not equally loaded, i.e., the stress is usually in fluctuation. Variation of the mean stress will therefore affect the fatigue life, an increase in mean stress will decrease fatigue life.

Fatigue data are commonly represented by means of the *S-N curve* also known as *Wöhler curves* named after August Wöhler's investigations in Berlin during the 1860's. These are a plot of stress amplitude  $S$ , versus the number of cycles  $N$ , (logarithmic scale) to failure. Stress amplitude  $\sigma_a$ , values are normally used however  $\sigma_{\max}$  or  $\sigma_{\min}$  can also be used. The *S-N* relationship is determined for a specified value of  $\sigma_m$ ,  $A$ , or  $R$ . For most materials the determination of the fatigue properties has been made in completely reversed bending, where mean stress is zero, however, where the mean stress is not zero (there is no relaxation of stresses), then it has considerably more engineering importance. In summary, the *S-N curve* illustrates that the higher the magnitude of the applied stress the smaller will be the number of cycles the material is capable of sustaining before failure.

Two types of *S-N* behaviour are observed, one in which there is a clear limit of cycles until failure and another in which there is no obvious fatigue limit (see Figure 1.14a and b). Fatigue behaviour can be further subdivided into three regions, low cycle fatigue (LCF), high-cycle fatigue (HCF) and the fatigue limit also known as the endurance limit.

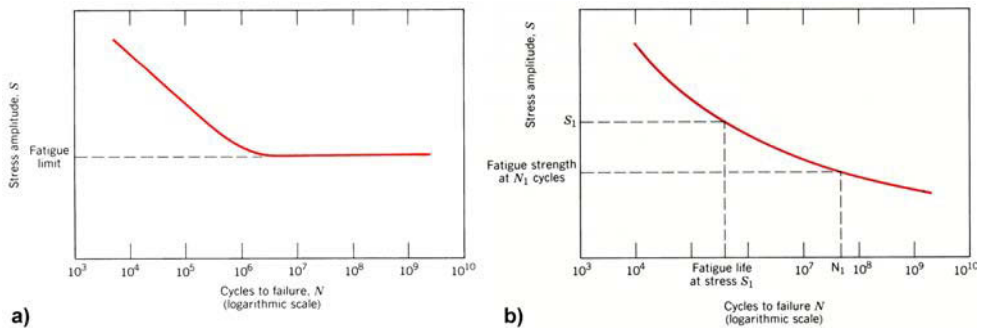


**Figure 1.14:** Stress amplitude  $\sigma_a$ , ( $S$ ) versus number of cycles to fatigue failure ( $N$ ) for a) a material with a fatigue limit and b) a material that does not show a fatigue limit [19, 59].

LCF can be defined as high stresses over a small number of loading cycles to failure. Typically, this is less than  $10^3$  cycles ( $N$ ) but not more than  $10^5$  cycles. The relatively high loading produces both elastic and plastic strain during each cycle, consequently the fatigue life is short. Mechanical testing is usually conducted at constant strain amplitude.

HCF, on the other hand, is at lower stress levels, where the material is under totally elastic strain. Therefore, the number of cycles which cause failure is very high and is usually greater than  $10^5$  cycles. The level at which fracture will occur at a specified number of cycles ( $N_f$ ) is referred to as the fatigue strength (see Figure 1.14b). Examples of metals which fall into this category are non-ferrous alloys such as Al, Cu and Mg, failure ultimately transpires regardless of the stress magnitude.

## 1. Introduction

The fatigue limit is effectively the limiting stress level at which the largest value of fluctuating stress, that will not cause failure over an infinite number of cycles, will occur. For some iron based and titanium based alloys the *S-N curve* becomes flatter, running parallel to the x-axis, with increasing cycles indicating a limited stress level below which fatigue failure will not take place (see Figure 1.14a) [19]. Fatigue life ( $N_f$ ) is defined as the number of cycles to cause failure at a specified stress level ( $S_f$ ) and can be extracted directly from the *S-N curve* (see Figure 1.14b).

The information gained from cyclic stress is mainly relevant to elastic unconstrained deformation. However, engineering components generally undergo localised plastic flow at stress concentrations and have some form of structural constraint. It is therefore more appropriate to consider strain-life relationships, as the strain relation in a material provides a simpler description. Coffin and Manson both proposed a characterization of fatigue life based on plastic strain amplitude (the *Manson-Coffin relation* published independently by L. F. Coffin in 1954 and S. S. Manson in 1954). They observed that when the logarithm of plastic strain amplitude  $\Delta\epsilon_p/2$ , was plotted against the logarithm number of cycles to failure  $2N_f$ , the result was a linear relationship (see Figure 1.15) [60].

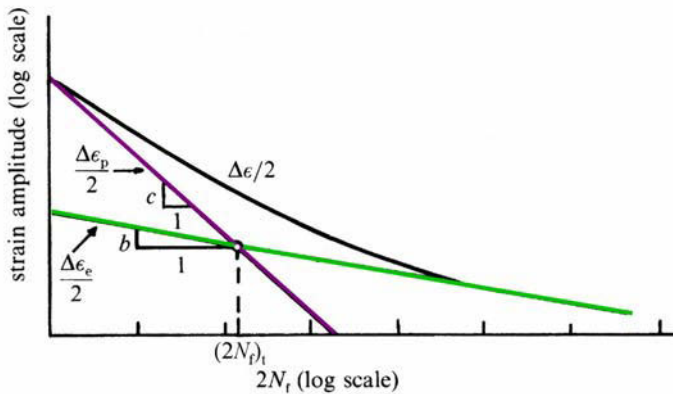


**Figure 1.15:** Total strain amplitude  $\Delta\epsilon/2$ , versus number of cycles to fatigue failure ( $2N_f$ ). The elastic and plastic strains show linear relationships [60].

$$\frac{\Delta\epsilon_p}{2} = \epsilon'_f (2N_f)^c, \quad \text{Eq. 1.8}$$

where:  $\Delta\epsilon_p/2$  is the plastic strain amplitude,  
 $\epsilon'_f$  is an empirical constant known as the fatigue ductility coefficient, this is approximately equal to the true fracture ductility in monotonic tension;  
 $2N_f$  is the number of reversals to failure;  
 $c$  is an empirical constant known as the fatigue ductility exponent, commonly ranging from -0.5 to -0.7 for metals.

The *Manson-Coffin relationship* (Eq.1.8) provides an expression for the total fatigue life as it contains the total strain amplitude  $\Delta\epsilon/2$  consisting of the sum of both elastic  $\Delta\epsilon_e/2$  and plastic strain amplitudes  $\Delta\epsilon_p/2$ , (see Figure 1.15)

$$\frac{\Delta\varepsilon}{2} = \frac{\Delta\varepsilon_e}{2} + \frac{\Delta\varepsilon_p}{2}. \quad \text{Eq. 1.9}$$

Using the Basquin (Eq. 1.3) and noting that,

$$\frac{\Delta\varepsilon_e}{2} = \frac{\Delta\sigma}{2E} = \frac{\sigma_a}{E}, \quad \text{Eq. 1.10}$$

where  $E$  is the Young's modulus, it follows that,

$$\frac{\Delta\varepsilon_e}{2} = \frac{\sigma'_f}{E} (2N_f)^b. \quad \text{Eq. 1.11}$$

Combining Eq. 1.8, Eq. 1.9 and Eq. 1.11 we have an expression for strain-life:

$$\frac{\Delta\varepsilon}{2} = \frac{\sigma'_f}{E} (2N_f)^b + \varepsilon'_f (2N_f)^c. \quad \text{Eq. 1.12}$$

There is a point however, when the elastic and plastic strains are equal. This is known as the transition life  $(2N_f)_t$ , and is defined from Eq. 1.8 and Eq. 1.11,

$$(2N_f)_t = \left( \frac{\varepsilon'_f E}{\sigma'_f} \right)^{1/(b-c)}, \quad \text{Eq. 1.13}$$

where  $(2N_f)_t$  are the number of reversals to failure at the transition life (see Figure 1.15).

Mean stress has also to be considered in the characterisation of fatigue life. The assumption is made that tensile mean stress  $\sigma_m$  reduces fatigue strength  $\sigma'_f$ . When the mean stress is not zero:

$$\sigma_a = (\sigma'_f - \sigma_m) (2N_f)^b. \quad \text{Eq. 1.14}$$

The strain life relationship can be re-formulated as:

$$\frac{\Delta\varepsilon}{2} = \frac{\sigma'_f - \sigma_m}{E} (2N_f)^b + \varepsilon'_f (2N_f)^c. \quad \text{Eq. 1.15}$$

The stress-strain hysteresis loop under constant strain cycling is illustrated in Figure 1.16. Initial tensile loading is from  $O$  to  $A$ : the point of maximum stress and strain ( $\sigma_{max} / \varepsilon_{max}$ ) (dashed line in Figure 1.16). On unloading, or compression, from  $A$ , the stress-strain path stops at  $B$ , the point of minimum stress and strain ( $\sigma_{min} / \varepsilon_{min}$ ). On tensile re-loading from point  $B$  to  $A$ , a hysteresis loop develops. The hysteresis loop is described by its width, the total strain range  $\Delta\varepsilon$ , the elastic and the plastic components:

$$\Delta\varepsilon = \Delta\varepsilon_p + \frac{\Delta\sigma}{E}, \quad \text{Eq. 1.16}$$

# 1. Introduction

and by its height, the total stress range  $\Delta\sigma$  (Eq. 1.4). The width of the hysteresis loop depends on the level of cyclic strain. Because plastic deformation is not completely reversible, changes in the stress-strain response may take place, which are known as cyclic softening or cyclic hardening. Sometimes both responses can occur, however, these are dependant on testing conditions and/or the condition of the material [60, 62].

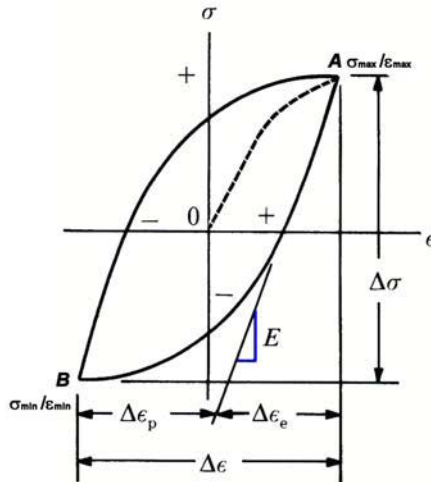


**Figure 1.16:** A stable hysteresis loop for constant strain cycling.  $\Delta\epsilon_e$  denotes elastic strain range,  $\Delta\epsilon_p$  denotes plastic strain range,  $\Delta\epsilon$  denotes total strain range and  $\Delta\sigma$  denotes total stress range. Maximum stress-strain is reached at point A and minimum stress-strain is reached at point B [59, 60].

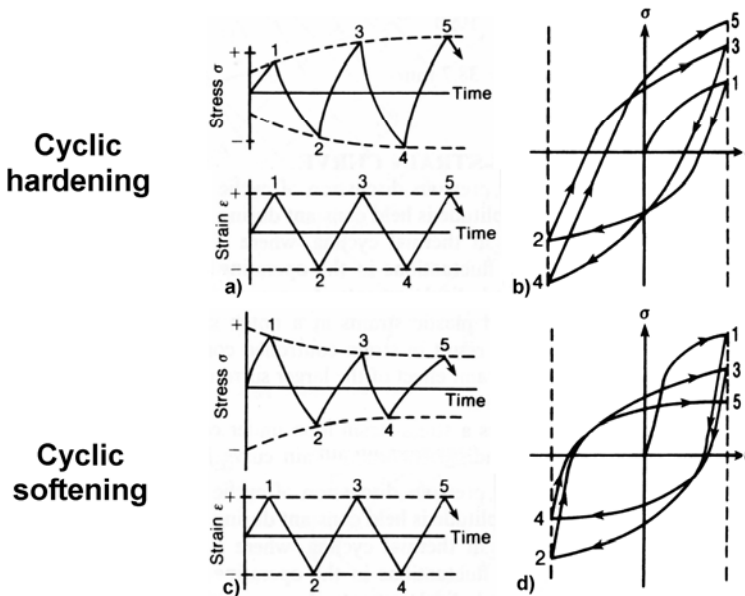


**Figure 1.17:** Cyclic strain cycles for, cyclic hardening - a) the stress response under strain control and b) corresponding strain controlled hysteresis loops, and cyclic softening - c) the stress response under strain control and d) corresponding strain controlled hysteresis loops. [60]



Under strain control, cyclic hardening occurs when there is a progressive increase in the stress range with increasing cycles (see Figure 1.17a and 1.17b) leading to early fracture. During cyclic softening (see Figure 1.17c and 1.17d) there is a progressive decrease in the stress range with increasing cycles. In general, the hysteresis loops tend to stabilise (follow the same stress-strain path) after the initial 'shakedown' period (approximately 100 cycles), when the material is said to have arrived at equilibrium [59].

### 1.2.1. Uniaxial and multiaxial fatigue tests

The importance of the damaging effects on metallic components caused by cyclic loading, especially at higher temperatures and in particular damage after an endurance of less than  $10^5$  cycles (Low Cycle Fatigue - LCF), has been recognised for many years. One type of mechanical test performed the most is that of the uniaxial LCF test. The specimen is subjected to relatively large cyclic stresses in tension and compression so that macroscopic plastic strain occurs in each cycle. This type of testing does not only concern the determination of lifetimes but also information regarding the cyclic deformation behaviour, such as cyclic softening or hardening. Comparing the results with monotonic stress-strain data indicates whether the yield strength and the strain hardening exponent have altered due to the cyclic plastic straining. If the LCF tests are conducted at elevated temperature, other time dependant factors are introduced such as creep and oxidation. The results can be further influenced by the introduction of a dwell period (hold period), the cyclic frequency or strain rate [63].

Many engineering components are subjected to more than just uniaxial cyclic loading, additional stress states can include torsion, tension-torsional and/or pressure. Different modes of imposed loads may occur as either static (steady torque, bending moment, mean pressure) or they may fluctuate in and out of phase. The incorporation of these complex loading conditions into LCF testing is known as multiaxial testing. The overall fatigue life under multiaxial conditions is driven by the complex phase relations between the different modes of loading. This is a form of test not commonly performed, mainly due to the high expenses involved. This type of test is complicated and time consuming, it requires specially designed servo-hydraulic testing machines, furnaces, intricate specimen design and other equipment in order to perform them [64, 65].

Multiaxial testing consists of two testing methods, one in which specimens of variable geometry are tested under a single load system, such as cantilever bending, anticlastic bending, bulge tests, and the other in which specimens of fixed geometry are tested under two or more loads, tension-torsion, tension-torsion-pressure, uniaxial plus hydrostatic pressure and cruciform loading. In all cases, multiaxial stresses are obtained [66].

Figure 1.18 shows the strain loading paths of mechanical strain  $\varepsilon_m$  versus shear strain  $\gamma/\sqrt{3}$ , for a) pure axial, b) pure torsion, c) proportional and d) non-proportional loadings. If the axial and shear strains vary in constant proportion to one another and the phase angle between them is zero, i.e., when the relationship between  $\gamma/\sqrt{3}$  to  $\varepsilon_m$  is constant, then the strains are said to be proportional. This is represented schematically in Figure 1.18c.

## 1. Introduction

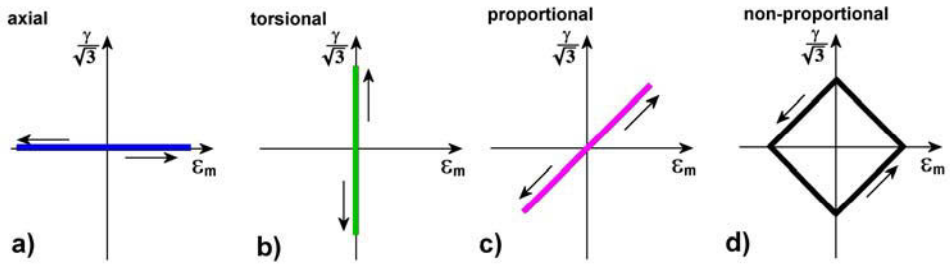


**Figure 1.18:** Schematic representation of the strain paths for a) normal (pure uniaxial strain) b) pure torsional c) proportional d) non-proportional axial-torsional 90 degree out-of-phase known as the ‘diamond-path’.  $\epsilon_m$  denotes mechanical strain and  $\gamma/\sqrt{3}$  the shear strain.

When changing the phase angle so that the variation between axial and shear strain  $(\gamma/\sqrt{3})/\epsilon_m \neq \text{constant}$ , the loadings are non-proportional. If  $\varphi_{T-\epsilon} = 90$  then this type of straining is commonly referred to as the ‘diamond-path’ due to the appearance of the schematic shape it forms (see Figure 1.18d). To obtain the same strain range in non-proportional loading as with proportional loading, the applied normal and shear strains must be increased, as maximum strains are smaller for non-proportional loading than for proportional loading. When maximum strains are compared, between non-proportional and proportional loading, generally, non proportional loading is more damaging than proportional loading [60].

### 1.2.2. Isothermal and non-isothermal fatigue

So far, only fatigue due to various loading conditions has been considered, however as mentioned earlier, temperature plays a decisive role in fatigue life. Isothermal fatigue refers to the fatigue testing which takes place at a constant temperature, whereas non-isothermal fatigue is, of course, variation in temperature. Isothermal fatigue is useful for studying the effects that a single temperature has on mechanical properties of a material over a period of time and can be conducted in air or vacuum. The actual temperature measurement and maintenance of its constancy is of importance here. The limits of temperature accuracy are defined in the applied testing standard.

Thermo-mechanical fatigue (TMF) refers to a form of non-isothermal fatigue in which a material is simultaneously subjected to varied temperatures and independently controlled loading [67]. As the mechanical properties of a material are temperature dependant, the variation in temperature associated with TMF, inevitably leads to different damage mechanisms taking place. Service components such as the leading edge of a turbine blade in gas turbine engines, are typically subjected to TMF loadings, during turbine start-up and shut-down. Simulation of these service conditions can be achieved by variation in the relationship between mechanical and thermal strains.

The total strain  $\epsilon_{tot}$  is the sum of the elastic,  $\epsilon_{el}$ , plastic,  $\epsilon_{pl}$  and thermal strains,  $\epsilon_{th}$ :

$$\epsilon_{tot} = \underbrace{\epsilon_{el} + \epsilon_{pl}}_{mech} + \epsilon_{th} \cdot \quad \text{Eq. 1.17}$$

There are two forms of standard TMF tests, the in-phase (IP) and the out-of-phase (OP) test. If the maximum value of completely reversed tensile strain coincides with the maximum temperature value: the test is defined as ‘in-phase’. If the maximum value of

completely reversed tensile strain coincides with the minimum temperature value, the test is defined as 180° 'out-of-phase' (see Figure 1.19) [68].

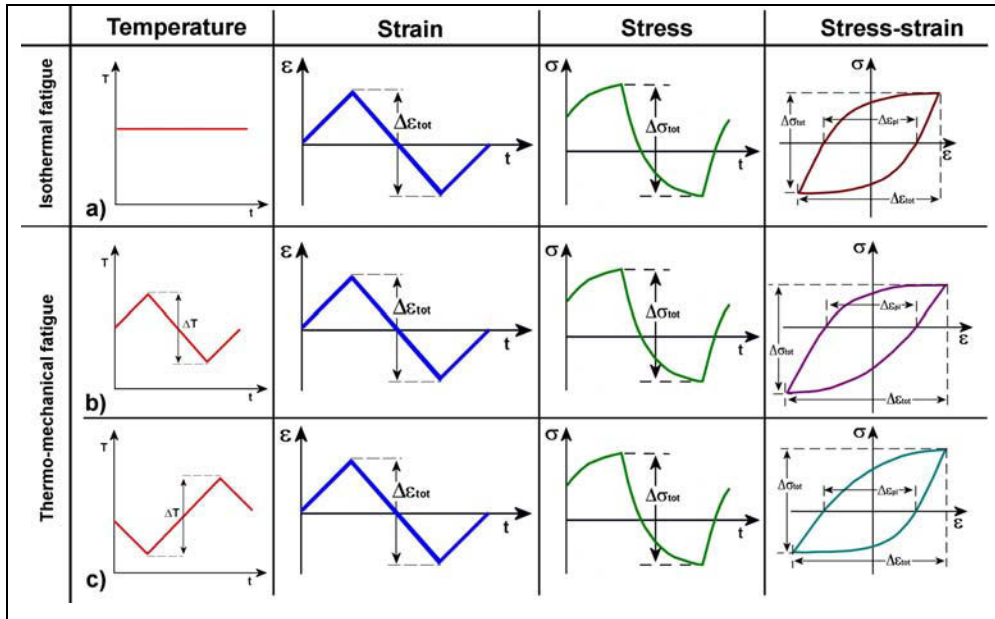


**Figure 1.19:** Schematic representation of the temperature vs. time, strain vs. time, stress vs. time and stress-strain loading in a) isothermal, b) In-phase and c) out-of-phase fatigue tests at  $R = -1$  [69].

### 1.2.3. Fatigue of TiAl

A component or specimen that is subjected to fatigue loading, is one of the most important, if not critical, aspects of materials engineering, the significance with regard to safety cannot be overstated. Fatigue damage is caused by defects, which initiates a microcrack that then propagates as a macrocrack eventually causing catastrophic failure. The rate and conditions at which fatigue damage occurs are strongly influenced by microstructural, mechanical and environmental factors [60]. This section summarises previously investigated fatigue behaviour of TiAl under various fatigue conditions.

The lifetime of a fatigued component or specimen made of any metal is established via crack nucleation, microcrack propagation and macrocrack growth [60]. TiAl has only a limited number of facile slip systems, four mechanical twinning systems and four ordinary dislocation slip systems with two common directions [70]. The various forms of microstructures that are formed in  $\gamma$ -TiAl have shown to have their own influence on fracture modes and subsequent fatigue lifetime.

In duplex microstructures, crystal orientations, grain boundary misorientations, and the directions of principal tensile stress describe the crack nucleation and microcrack propagation. According to Bieler et. al. [70], fracture is caused when a highly stressed twinning system that is nearly aligned with the maximum tensile stress direction intersects with grain boundaries. The grain boundaries prevent the highly localised strain, caused by mechanical twinning, from propagating. Intergranular fracture occurs along the weaker grain boundaries, these then link up by cleavage as intergranular macrocracks cannot propagate

## 1. Introduction

through the stronger grain boundaries [70]. Skrotzki [71] identified mechanical twinning as an important deformation mechanism for improving the ductility in the ordered  $L1_0$  structure of the  $\gamma$ -phase of near- $\gamma$ -TiAl. Twinning is observed to occur at low strains in lamellar and  $\gamma$ -grains of the duplex microstructure. Twinning can provide additional slip systems which reduces the strain incompatibilities caused by  $1/2 \langle 110 \rangle$  dislocations. The effects of twinning are, however, influenced by the volume fraction of twins in the microstructure [71, 72]. Fine grained duplex microstructures show better short-term strength and ductility due to grain boundary sliding but are detrimental to creep resistance [4, 43]. Reduction in the Al content increases the volume fraction of  $\alpha_2$ -phase. This, in effect, reduces the Young's modulus, increases the yield strength and lowers the cyclic plastic deformation behaviour, generating a longer fatigue life [73].

In fully lamellar microstructures, the microstructural texture, i.e., orientation, and alignment of the lamellar colonies, can influence the overall fracture toughness [24, 74]. Crack initiation appears to be associated with lamellar colonies and the orientation of the lath normal when oriented approximately parallel to the loading axis [31, 75]. Their good crack growth resistance has been attributed to the lamellar boundaries which act as natural barriers to crack propagation, inducing deviations in the crack path and subsequently enhancing fracture toughness. With increasing temperature, failure changes from predominantly translamellar to a mixture of both interlamellar/translamellar failures to intergranular failure. The desired microstructural texture can be induced via an extrusion process [24, 75-77]. At ambient temperatures, lamellar microstructures show better lifetime properties than duplex microstructures [78].

Fatigue behaviour in TiAl is highly temperature dependent. This is related to the brittle–ductile transition temperature (BDTT) [79, 80]. Fatigue crack propagation behaviour of  $\gamma$ -TiAl alloys shows that for all the different TiAl alloys investigated, the highest fatigue resistance was at 800°C, around the BDTT. Generally, at temperatures below BDTT, the material shows cyclic hardening, while above the BDTT cyclic stability is observed [81]. At ambient temperature the lamellar microstructures show superior fatigue crack growth (FCG) resistance and  $\gamma$  microstructures the least FCG resistance [31, 78, 82]. FCG resistance of TiAl alloys is greatly reduced in air compared to a vacuum environment. The atmospheric environment strongly enhances crack propagation in the different microstructures, but decreases as the temperature is increased above the BDTT [31].

According to Hénaff et. al. [31], the prevailing mechanism for crack closure in TiAl alloys is roughness induced closure. This phenomenon is caused by small plastic zone dimensions at the crack tip, which are usually smaller than an average grain dimension, by small crack tip opening displacement, or by coarse grain microstructures, which hinder slip. Roughness-induced closure effects are less pronounced in powder metallurgy alloys (fine microstructure- smooth crack path) than in cast alloys. Oxidation does not encourage closure in air at elevated temperature [31, 60].

The cyclic stress-strain (CSS) behaviour of TiAl is strongly affected by the total strain amplitude,  $\Delta\varepsilon/2$ . CSS behaviour testing conducted by Hénaff et. al. [31], on a cast Ti–48Al–2Cr–2Nb alloy at 750°C exhibits a stability of the stress amplitude during the whole fatigue life, regardless of the total strain amplitude ( $\pm 0.8\%$ ,  $\pm 0.6\%$  and  $\pm 0.4\%$ ), which is in contrast with ambient temperature behaviour where pronounced cyclic strain hardening was observed at high strain amplitudes. The high strain amplitude cyclic strain hardening at room temperature is related to deformation twinning. At lower strain amplitudes cyclic hardening was less prevalent and deformations were described as vein-like structures. At the lowest strain amplitude deformation mainly constituted of  $1/2 \langle \bar{1}10 \rangle$  ordinary dislocations and with very little cyclic hardening taking place [31]. The same high temperature behaviour

was seen in a Ti–46Al–2Nb–2Cr alloy with a fully lamellar microstructure under similar straining conditions, at 650°C and at 800°C. It was observed that this microstructure consisted of a formation of long and pointed dislocations signifying that cross slip and climb may be active at this temperature [31, 71, 83].

HCF fatigue behaviour of TiAl-based alloys has been previously investigated on a binary Ti–36.5Al (wt%) alloy with a lamellar microstructure by Hénaff et. al. [31]. They observed that regardless of temperature, the *S–N curves* were extremely flat, meaning that the fatigue resistance is not significantly degraded when the temperature is raised up to 800°C. A slight variation in the applied stress amplitude, led to significant differences in the number of cycles to failure. These trends were also confirmed on different microstructures namely the Ti–46Al–2Cr–3Nb–0.2W alloy with coarse lamellar, fine lamellar, and duplex microstructures [31].

LCF behaviour has been investigated with a number of different TiAl alloy compositions and it has been established that LCF behaviour is influenced by alloy composition and microstructure. Hénaff et. al. [31], concluded that the XD45 alloy (Ti–45Al–2Mn–2Nb+0.8% vol. TiB<sub>2</sub>) shows the highest resistance to LCF at 600°C, while fine grained duplex microstructures show the highest LCF resistance in comparison to a coarse grained near-lamellar microstructure. Where lamellae microstructures are dominant, LCF resistance can be slightly improved by refining the lamellae, this can be achieved by increasing the carbon content, or by the presence of interstitial atoms or via processing techniques [43, 79, 84].

Most components, operating at high temperature, fail predominantly by LCF where in addition to creep, fatigue and oxidation and other mechanisms, dwell sensitivity may play an important role. Service loads in a gas turbine engine change with respect to time, for example, under start-up and shut-down conditions, or during cruising when the loads are held at near steady conditions for a period of time. The later behaviour is known as dwell sensitivity fatigue or creep–fatigue behaviour. In order to best represent these service conditions a hold period is incorporated into the mechanical test [85].

Park et.al. [86, 87], observed that during LCF tests at 800°C, additional creep damage was caused by the introduction of a hold period of between 5 and 30 minutes at maximum tensile loading. These tests, when compared with tests without hold periods, showed a shorter fatigue lifetime. Some gas turbine components, such as LPT blades, are restricted to 1% creep within 10,000 hours at 700°C under tensile stresses of 100-150MPa, which corresponds with a very low average strain rate of  $\dot{\epsilon} = 10 \times 10^{-10} \text{ s}^{-1}$  [23, 86, 88-90]. Creep investigations have shown that near-lamellar or fully lamellar microstructures have superior creep strength (apart from primary creep) compared to equiaxed and duplex microstructures. However, higher ductility, higher tensile strength and longer fatigue life are achieved for an alloy with duplex microstructures [23, 91]. Grain size, phase distribution, and lamellar thickness, were found to play an important role in creep properties. In duplex or near-lamellar alloys, deformation was found to start within single  $\gamma$ -phase grains, and subsequently to lead to sub-grain formation and to an increase in the dislocation density [92]. In duplex microstructures, creep is aided by dynamic re-crystallisation [93] and mechanical twinning [94]. Twins are extensively activated under high stress during the primary creep stage [92].

Investigation into isothermal fatigue of near- $\gamma$ -TiAl (Ti-47Al-2Nb-2Mn at% with 0.8 wt% TiB<sub>2</sub>) has been conducted by Christ et al [81]. They found that the cyclic deformation behaviour of near  $\gamma$ -TiAl was strongly dependant on temperature. Above BDTT the material was observed to be cyclically stable, whereas below BDTT they observed cyclic hardening. Fatigue lifetime was also found to be affected by the environment, in vacuum, the number

## 1. Introduction

of cycles to failure decreased with increasing temperature, while in air, fatigue life increased [31, 81].

There have been investigations conducted on the effects of non-isothermal fatigue (TMF) on  $\gamma$ -TiAl, purely under uniaxial loading [69, 80, 95-97]. Roth and Biermann [96, 97] investigated the TNB-V5 alloy (Ti-45Al-5Nb-0.2C-0.2B at%) with a near- $\gamma$  microstructure. They conducted uniaxial IP, OP, clockwise direction (CD) and counter clockwise direction (CCD) strain-controlled TMF tests at temperatures between 400 and 800°C under two mechanical strain amplitudes (0.575% and 0.65%). They observed that the shortest lifetimes were in OP loading and the longest in IP, with both CD and CCD loadings lying in-between OP and IP loadings. In all tests the deciding fatigue life factor was the magnitude of the strain amplitude and the value of maximum tensile stress. They observed twinning and dislocation movement as the cause of plastic deformation. However, there were qualitative differences between the OP and IP microstructures [96, 97]. Christ [95] and Schallow [98, 99] investigated  $\gamma$ -TiAl alloys (Ti-47Al-5.1Nb-0.25C-0.4B at% and Ti-46.5at%-4at% (Cr, Nb, Ta, B)) under OP and IP TMF loading, similar to Roth and Biermann, they also observed the shorter lifetimes in the OP tests which were attributed to an oxide scale formed at high temperature becoming brittle at lower temperatures. As this part of the OP cyclic loading is in tension, cracking of the oxide scale could easily promote oxidation induced crack initiation and consequential reduced fatigue life [95]. Cui et. al., made similar conclusions to Christ in their investigation of a powder metallurgical (PM)  $\gamma$ -TiAl alloy (Ti-47Al-5.1Nb-0.25C-0.4B at%). In addition they added that this oxide layer cracking in OP loading, caused creep damage arising from grain boundary sliding, hence the shorter life times [80].

The environmental effects that air, water vapour or other gases have on TiAl have been thoroughly investigated. After thermal exposure at temperatures between 500°C and 700°C in both air and vacuum, tensile ductility and elongation at ambient temperature is reduced and fatigue resistance diminished. Water vapour reduces lifetime at low strain rates, giving rise to a strain rate-dependent softening effect [56, 100-104].

The influence which surface defects have on the fatigue strength, caused by surface preparation, machining, turning, shot peening, etc., has been investigated by Hénaff et. al. [31]. They observed that in the absence of sharp notches, fatigue resistance of TiAl alloys should not be a concern [31]. The effect of impact damage on TiAl has also been investigated [105-108]. The effects on fatigue strength of post ballistic impact damage on two TiAl alloys (Ti-48Al-2Nb-2Cr and Ti-47Al-2W-0.5Si) were examined by Draper et. al. [109]. They concluded fatigue strength decreases with increasing impact energy [109].

In spite of the previous investigations on TiAl summarized above, a vital area of research that has not been examined is that of complex high temperature multiaxial TMF. Surprising though it seems, considering the forthcoming introduction of TiAl in gas turbine engines where multiaxial non-isothermal fatigue is an environmental fact, this sphere of research has not been fully investigated. The affect this mechanical loading has on fatigue lifetimes, what type of loading is the most damaging, the effects on the microstructure and how TiAl compares to other high temperature materials tested under similar multi-axial TMF, are the questions that need to be addressed for a better understanding of this material.

### 1.3. Objectives

In 2002, the president and C.E.O of MTU Aero Engines, Dr. Klaus Steffens, presented the first titanium aluminide test blade to Bavaria's Minister of Economics Otto Wiesheu. He

commented: '*This weight reduction is a quantum leap in the engine industry. I doubt there will be any alternative technology to it in the foreseeable future*' [110].

Despite the imminent introduction of TiAl alloys into aero gas turbines [52, 53] and turbofan engines [57], until this study, no previous research on multiaxial TMF is known to have been conducted on TiAl, such as that already seen on Ni-based alloys and stainless steels [65, 111-115]. The conditions in the aero gas turbine will remain identical for TiAl alloys as they currently are for the Ni-based components. The low pressure turbine blades and high pressure compressor blades are subjected to moderate to high temperatures and centrifugal loading which can be described as tri-axial TMF [3, 15, 116]. The geometry of the blades is complex. They are loaded multiaxially, cyclically - under non-proportional stress states - and subjected to thermal strain giving rise to thermal gradients and plastic deformation. Generally, the plastic behaviour of a metal is due to its deformation and temperature history and can be readily observed in cyclically loaded tests by the width of the hysteresis loop. Repeated strain-temperature cyclic loading can harden, soften or leave a material unchanged, depending on its initial state. In low cycle TMF, the sequence of loading and variation in the temperature (strain-temperature phasing) can influence the fatigue lifetime. Ziebs et al. [112, 117] reported that the lifetime of the Ni-based alloy, IN 738, is related to the length of the strain-temperature path. The shortest lifetimes were observed in tests that followed a sinusoidal non-proportional loading path, which is coupled with the highest amount of plastic work (per cycle).

From investigations of Cu and austenitic steels it is known that non-proportional loading induces greater hardening than under proportional loading [118]. However, Al alloys have the same hardening behaviour under proportional and under non-proportional loading. There are indications that the additional cyclical hardening under non-proportional loading is connected with the glide character of the dislocations [119]. Metals with a high stacking fault energy, in which cross slip can easily occur, do not show any additional cyclical hardening. Whereas, those metals with a low stacking fault energy tend to favour planar glide and these show significant additional hardening [119]. Additional hardening is defined as the difference between the maximum equivalent stress obtained at the steady state (after the twentieth cycle) and the stress given by a cyclic curve for the maximum equivalent plastic strain [120]. TiAl also has low stacking fault energy and it is therefore interesting, from the metallurgical point of view, whether additional hardening also takes place in this material.

From previous investigations it is clear that the TMF behaviour of the near- $\gamma$ -TiAl has not been fully examined. In particular, TMF under multiaxial loading has been virtually ignored, even though this material is to be used in components which are subjected to severe service induced stresses at high temperatures [69, 97, 121, 122]. This study will investigate the mechanical behaviour of a near- $\gamma$ -TiAl under non-isothermal multiaxial stress and the effects these parameters have on fatigue lifetimes. As reference data, uniaxial OP and IP and pure torsional TMF tests, conducted under equivalent strain amplitudes, will be used to compare fatigue lifetimes with data from the multiaxial loading. Hold period experiments will be included to investigate creep effects on fatigue lifetime. Qualitative and quantitative examinations on the microstructure will accompany the experimental work to characterize, not only the grain size effects, but also deformation processes such as mechanical twinning and the dislocation structures.

From the mechanical testing data, it shall be possible to formulate a lifetime model, where all lifetime results can be described by a narrow scatter band, using a single loading parameter. A loading parameter based on the plastic work per cycle, being independent of material planes, will be considered as a measure of total accumulated damage [123]. This

## 1. Introduction

will be applied to the complex multiaxial loading paths using a time incremental lifetime rule, which will be further enriched to account for the complete TMF loading.

To emphasise the importance of TiAl as a future replacement to Ni-based superalloys, the mechanical test results will additionally be compared with previously investigated Nimonic 90 and IN 738, to ascertain their similarities in TMF behaviour [114, 115, 117, 124]



## 2. Experimental method

### 2.1. Material

For the purpose of this study the material investigated, is a third generation, near  $\gamma$ -TiAl, with a nominal composition of Ti45Al-5Nb-0.2B-0.2C at% (see Table 2.1). This alloy is referred to as TNB-V5.

**Table 2.1:** Nominal composition of the TNB-V5 alloy

Content in percent (%)					
	Titanium (Ti)	Aluminium (Al)	Niobium (Nb)	Boron (B)	Carbon (C)
Atom %	49.6	45	5	0.2	0.2
Weight %	58.5	30	11.4	0.05	0.05

The material was supplied by GfE Metalle und Materialien GmbH of Nuremberg. It was produced by vacuum arc re-melting (double VAR) followed by an extrusion process, at a ratio of approximately 15:1, with die temperatures of over 1200°C. For extrusion, the TiAl alloy is encased in stainless steel cans. These stainless steel cans help to keep the whole billet at a constant temperature during extrusion and avoid the cooling down of the outer regions of the ingots. There is a diffusion barrier between the TiAl alloy and the steel, to avoid Ti-Fe-reactions and to support thermal isolation. The diffusion barrier is either a foil of  $Al_2O_3$ , molybdenum or stainless steel. The processing is schematically shown in Figure 2.1a and the end product in Figure 2.1b [32, 125, 126].

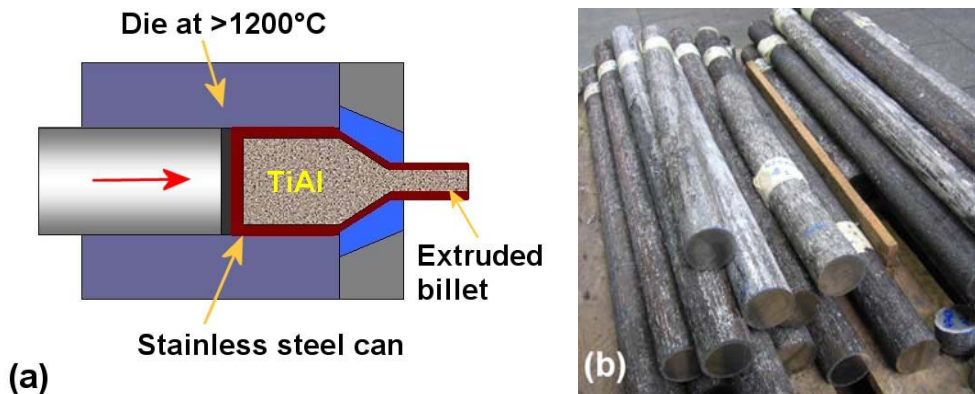


**Figure 2.1:** a) Schematic drawing of the hot extrusion process b) the product – sectioned billets after extrusion (image GfE Metalle und Materialien GmbH).

### 2.2. Specimen preparation

Twenty five specimens were machined from the two supplied canned billets, 610mm and 730mm in length respectively, both approximately 54mm in diameter. The billets were first sectioned into nine 135mm smaller billets and from these smaller billets the test pieces in the form of tubes were then electrically eroded using the electrical discharge machining (EDM) and wire cut electrical discharge machining (WEDM) processes. The post EDM test piece, labelled 'Y' in Figure 2.2, requires further conventional machining in order to attain the correct test specimen geometry.

## 2. Experimental method

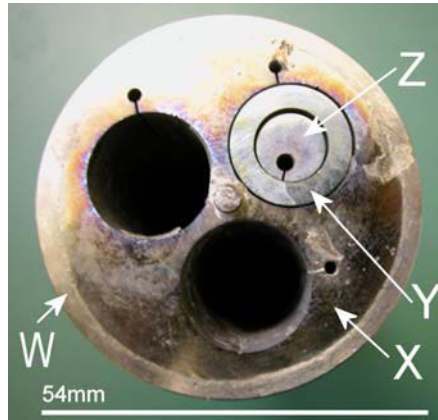


**Figure 2.2:** The billet after EDM and WEDM processes. The stainless steel can (W) containing the billet (X), the wire eroded test piece (Y) and the wire eroded test piece core (Z).

For TMF testing, the hollow cylindrical specimen geometry with an hour glass form was used. This tubular form of geometry for multiaxial tests, has been envisaged and developed over many decades [127, 128]. The advantage of this type of geometry is that it minimises the radial temperature gradient especially at high heating and cooling rates compared to solid test pieces [68]. As the test is performed under strain control the thermal expansion has significant influence upon the control of the test. A disadvantage of this geometry is that it has a much greater surface area due to its tubular form, than a solid test piece has. Because cracks normally initiate at surfaces, the larger surface area will therefore tend to shorten the TMF lifetime [68, 128, 129]. The TMF test specimen geometry is illustrated in Figure 2.3.

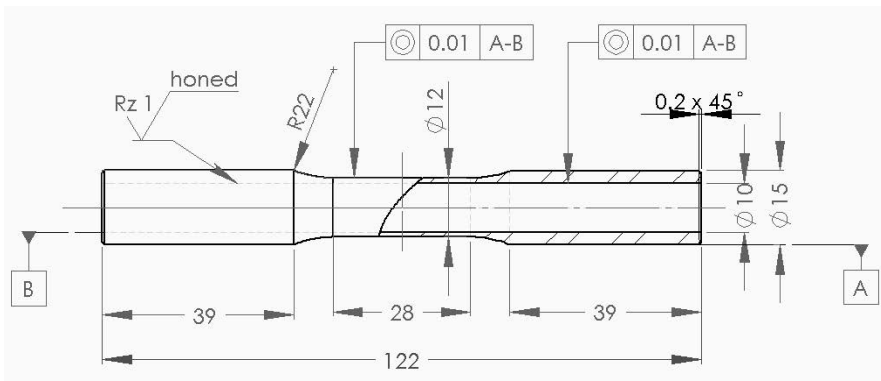


**Figure 2.3:** TMF test specimen geometry. Units are in millimetres. Scale approximately 1:2.

The exterior gauge section was mechanically polished in three stages:

- Initial polishing with 30 $\mu$ m grain diamond paste lubricated with paraffin oil, for 4 hours.
- Intermediate polishing with 15 $\mu$ m grain diamond paste lubricated with paraffin oil, for 4 hours.
- Final polishing with 6 $\mu$ m grain diamond suspension lubricated with alcohol, for 4 hours.

After each polishing stage the specimen was cleaned in an ultrasound bath. The final surface finish had roughness values of  $R_a = 0.02 \mu\text{m}$ . The inner bore plays an important role and requires an extremely smooth surface finish to prevent unwanted premature failure during the testing. Therefore, post-EDM specimens were additionally honed internally to a high precision surface roughness value of  $R_a = 0.08 \mu\text{m}$ . The post polished specimens were ultimately inspected with fluorescent dye penetrants (Helling - *Met-L-check*) for the presence of surface defects or cracks, however, none were discovered. The specimens were allocated an identifying serial number which incorporates the internal BAM project code (see Figure 2.4). These identification codes and numbers were applied to both ends of the specimen so that if catastrophic failure occurs the complete specimen can be identified and fracture surfaces compared.

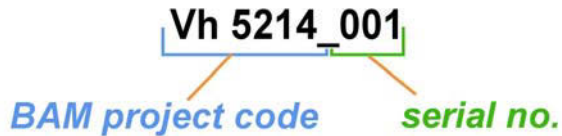


**Figure 2.4:** The specimen identification code and serial number used in this study.

In order to be tested in a servo-hydraulic testing machine, the specimens need to be gripped using water cooled hydraulic clamps. The brittle nature of this material requires an additional tight fitting steel plug which is inserted into each end of the specimen to act as a compression member, allowing sufficient grip to be applied in the hydraulic clamps. The compression members are 30mm in length which are sufficiently small enough not to protrude into the gauge section Figure 2.5).

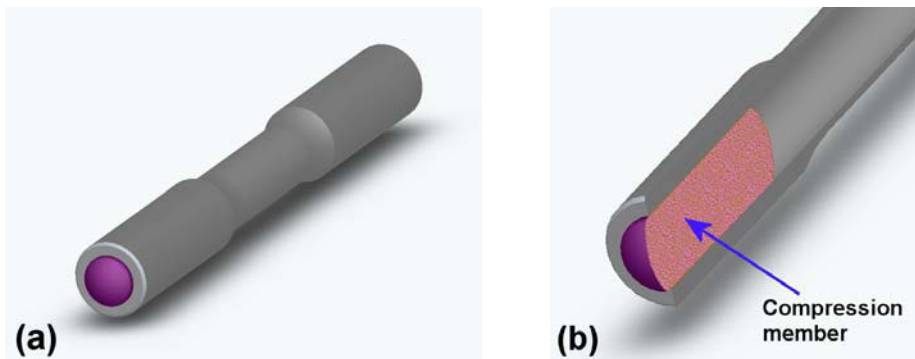


**Figure 2.5:** The specimen prepared for TMF testing fitted with a 30mm steel compression member. a) schematic external view and b) sectioned view.

### 2.3. Evaluation of elastic and shear moduli

Pre-test data are required for accurate control of the machine testing parameters especially for the determination of stress and strain. One such physical property is the elastic modulus [68, 130]. Using the sonic resonance method, dynamic Young's modulus,  $E$ , and shear modulus,  $G$ , were obtained from the as-received material using a Elastotron 2000. In this technique the specimen is suspended between two embedded graphite heating elements of a furnace within a vacuum chamber. The equipment can be used up to temperatures of 1900°C. A sinusoidal signal from the transmitter vibrates the specimen with constant amplitude to bending vibrations using a piezoelectric sensor (transmitter). A second

## 2. Experimental method

piezoelectric sensor (receiver) detects the corresponding oscillations. The resonant peaks are detected and the elastic moduli determined by specially developed software. These experimentally measured resonance frequencies are then compared with the predictions from the theory for certain values of the Young's and the shear moduli. There is a very small relative uncertainty in measurement of 1 to 2% [131]. The measurements were carried out between 26°C and 1000°C to include intermediate temperatures outside of the test temperature range of 400°C to 800°C. This ensures correct operation of the stress, strain and temperature measurement systems [68, 132].

### 2.4. Mechanical testing

Tensile tests and multiaxial thermo-mechanical tests were conducted on a MTS 100kN tension-torsion closed-loop servo-hydraulic testing machine under computer control (Figure 2.6a). The load cell has an axial rating of 100kN and torsional rating of 1100Nm. The water cooled hydraulic grips are of the type MTS 646. Strain measurement was performed using a MTS 632-68F-08 axial-torsion strain extensometer with a 25mm gauge length. Data acquisition was obtained via MTS FlexTest™ controller software. The testing system contains an induction heating unit with a temperature monitoring device (Figure 2.6b). Cooling is achieved by free air convection and heat conduction to the water-cooled grips. The specimens can be subjected to controlled axial, torsional and axial-torsional loading under a defined temperature-time history.

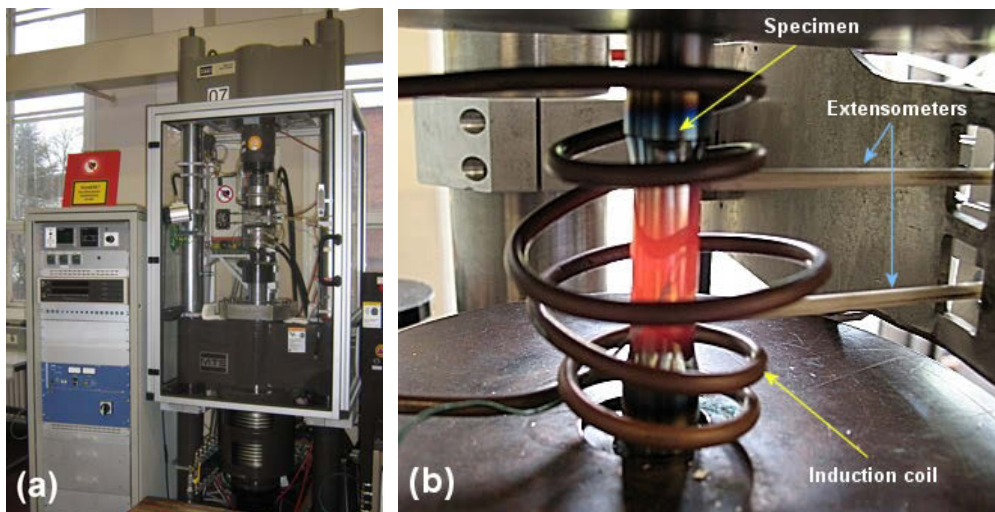


**Figure 2.6:** The testing equipment situated at BAM (Division V.2) a) The MTS 100kN tension-torsion closed-loop servo-hydraulic testing machine and b) the high frequency induction heating unit shown here during a test at 800°C. The axial-torsional extensometers can be seen in the right of the picture.

Before testing a thermal strain trajectory is acquired via a pre-cycling 'zero stress test' procedure. This is particularly important when tests are to be performed in total strain control mode under non-isothermal conditions as it verifies the accuracy of the thermal strain compensation. Thermal strain is calculated in real time from the measured temperature  $T$  and added to the mechanical strain  $\varepsilon_m$ , to obtain the total strain  $\varepsilon_{tot}$  as a command input for the strain control [68].

$$\varepsilon_{tot} = \varepsilon_{th}(T) + \varepsilon_m(t). \quad \text{Eq. 2.1}$$

The equivalent strain  $\varepsilon_{eq}$  is calculated using the Mises relation [111, 128, 133]:

$$\varepsilon_{eq} = \sqrt{\varepsilon^2 + \frac{\gamma^2}{3}}, \quad \text{Eq. 2.2}$$

where  $\varepsilon$  is the axial strain and  $\gamma$  is the shear strain.

The macroscopic stress, via Hooke's law, corresponds to the macroscopic elastic strain. In order to correlate and compare lifetime behaviour, between the uniaxial, torsional and axial-torsional tests, the Mises equivalent stress  $\sigma_{eq}$  is used, which is defined as:

$$\sigma_{eq} = \sqrt{\sigma^2 + 3\tau^2} \quad \text{Eq. 2.3}$$

where  $\sigma$  is the axial stress and  $\tau$  is the shear stress, and it therefore follows that for uniaxial loading  $\sigma_{eq} = |\sigma|$ .

The equivalent stress amplitude is defined as:

$$\sigma_{eq,a} := \max_{cycle} \sigma_{eq}. \quad \text{Eq. 2.4}$$

The TMF test matrix consisted of:

- uniaxial in-phase (IP),
- uniaxial out-of-phase (OP),
- torsional in-phase (Tors IP),
- non-proportional axial-torsional out-of-phase tests (also known as the 'diamond' path)
- non-prop.axial-tors.

Tests were conducted under total strain control with  $R = -1$ . The mechanical strain ( $\varepsilon_m$ ) was calculated by subtracting the thermal strain ( $\varepsilon_{th}$ ) from the total measured strain ( $\varepsilon_t$ ):

$$\varepsilon_m = \varepsilon_{tot} - \varepsilon_{th}. \quad \text{Eq. 2.5}$$

Hold period tests (180 seconds at 800°C) were also included in this study to observe if this causes any additional damage via creep mechanisms.

In the torsional tests the phase-shift of temperature is 180° with respect to shear strain which is equivalent to thermo-mechanical IP loading. At pure torsional loading, the mean tensile stress  $\bar{\sigma}_m$ , (also known as hydrostatic stress which affects cavity growth [134]) is zero and is defined as:

$$\bar{\sigma}_m := \frac{1}{3}(\sigma_1 + \sigma_2 + \sigma_3), \quad \text{Eq. 2.6}$$

## 2. Experimental method

where  $\sigma_1 + \sigma_2 + \sigma_3$  are the principal stresses.

Figure 2.7 shows schematically mechanical strain and temperature vs. time. In IP tests, temperature and mechanical strain,  $\epsilon_m$ , proceed parallel, while in OP tests, there is a phase shift  $\varphi_{T-\epsilon}$ . In Figure 2.7 the phase shift is  $180^\circ$ , however, other phase shift values are also possible.

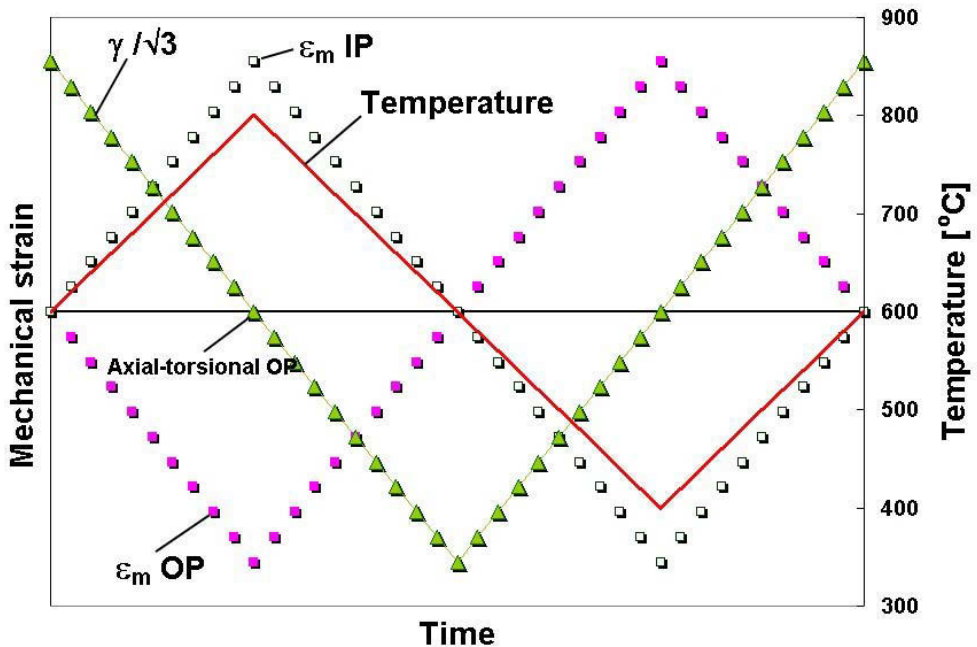


**Figure 2.7:** Schematic representation of the axial mechanical strain  $\epsilon_m$  and temperature vs. time for OP and IP tests, and torsional shear strain  $\gamma/\sqrt{3}$  vs. time for the performed non-proportional axial-torsional tests

The specimens were heated with a high frequency induction heater. The heating/cooling rate was 5 K/s and axial temperature deviations within the gauge length were below  $\pm 15^\circ\text{C}$ . All tests were performed in air. Temperature was measured with a thermocouple (type K) spot welded to the centre of the specimen gauge section. The temperature range  $T_{\min} = 400^\circ\text{C}$  to  $T_{\max} = 800^\circ\text{C}$  remained the same for all tests.

Table 2.2 summarizes the tests with respect to testing parameters such as axial, torsional and equivalent mechanical strain amplitudes and strain rates as well as phase shifts between strain and temperature. The Mises equivalent mechanical strain was used as a formal test control parameter (Eq. 2.2).

The shear stress  $\tau$ , like the shear strain  $\gamma$ , is always greatest at the outer diameter of a specimen. Most strain-controlled axial-torsional fatigue tests are conducted under elasto-plastic loading conditions. In bulk specimens the shear stress and strain are not constant in cross section.

**Table 2.2:** Test matrix showing the test temperature rate  $\dot{T}$ , the mechanical strain amplitude,  $\varepsilon_m$ , the mechanical strain rate,  $\dot{\varepsilon}_m$ , the shear strain,  $\gamma$ , the shear strain rate,  $\dot{\gamma}$ , the equivalent mechanical strain amplitude,  $\varepsilon_{eq}$ , the equivalent mechanical strain rate,  $\dot{\varepsilon}_{eq}$ , the phase shift between axial mechanical strain and temperature,  $\varphi_{T-\varepsilon}$ , shear strain and temperature,  $\varphi_{T-\gamma}$ , and axial mechanical strain and shear strain,  $\varphi_{\varepsilon-\gamma}$ . The test temperature range is  $T_{min} = 400^\circ\text{C}$ ,  $T_{max} = 800^\circ\text{C}$ . All tests were performed under strain control  $R = -1$ .

Test Type	$\dot{T}$ [K <sup>-1</sup> ]	$t_{\text{hold at 800}^\circ\text{C}}$ [s]	$\pm\varepsilon_m$ [%]	$\dot{\varepsilon}_m$ [s <sup>-1</sup> ]	$\gamma$ [%]	$\dot{\gamma}$ [s <sup>-1</sup> ]	$\varepsilon_{eq}$ [%]	$\dot{\varepsilon}_{eq}$ [s <sup>-1</sup> ]	$\varphi_{T-\varepsilon}$ [°]	$\varphi_{T-\gamma}$ [°]	$\varphi_{\varepsilon-\gamma}$ [°]
Uniaxial	5	-	0.15	$3.75 \times 10^{-5}$	-	-	0.15	$3.75 \times 10^{-5}$	180	-	-
(OP)	5	180	0.15	$3.75 \times 10^{-5}$	-	-	0.15	$3.75 \times 10^{-5}$	180	-	-
"	5	-	0.17	$4.25 \times 10^{-5}$	-	-	0.17	$4.25 \times 10^{-5}$	180	-	-
"	5	-	0.20	$5.00 \times 10^{-5}$	-	-	0.20	$5.00 \times 10^{-5}$	180	-	-
"	5	-	0.30	$7.50 \times 10^{-5}$	-	-	0.30	$7.50 \times 10^{-5}$	180	-	-
Uniaxial	5	-	0.30	$7.50 \times 10^{-5}$	-	-	0.30	$7.50 \times 10^{-5}$	0	-	-
(IP)	5	-	0.50	$1.25 \times 10^{-4}$	-	-	0.50	$1.25 \times 10^{-4}$	0	-	-
"	5	-	0.55	$1.38 \times 10^{-4}$	-	-	0.55	$1.38 \times 10^{-4}$	0	-	-
"	5	180	0.55	$1.38 \times 10^{-4}$	-	-	0.55	$1.38 \times 10^{-4}$	0	-	-
"	5	-	0.70	$1.75 \times 10^{-4}$	-	-	0.70	$1.75 \times 10^{-4}$	0	-	-
Torsional	5	-	-	-	0.26	$6.50 \times 10^{-5}$	0.15	$3.75 \times 10^{-5}$	-	0	-
(IP)	5	-	-	-	0.29	$7.25 \times 10^{-5}$	0.17	$4.25 \times 10^{-5}$	-	0	-
"	5	-	-	-	0.33	$8.25 \times 10^{-5}$	0.19	$5.00 \times 10^{-5}$	-	0	-
"	5	180	-	-	0.33	$8.25 \times 10^{-5}$	0.19	$5.00 \times 10^{-5}$	-	0	-
"	5	-	-	-	0.35	$8.50 \times 10^{-5}$	0.20	$5.00 \times 10^{-5}$	-	0	-
Prop. axial-tors. (OP)	5	-	0.106	$2.65 \times 10^{-5}$	0.18	$4.50 \times 10^{-5}$	0.15	$3.75 \times 10^{-5}$	180	180	0
Non-prop. axial-tors. (OP)	5	-	0.17	$4.25 \times 10^{-5}$	0.29	$7.25 \times 10^{-5}$	0.17	$4.25 \times 10^{-5}$	180	90	-90
"	5	180	0.15	$2.65 \times 10^{-5}$	0.26	$6.49 \times 10^{-5}$	0.15	$3.75 \times 10^{-5}$	180	90	-90

Shear strain,  $\gamma$ , results from the application of a torsional moment to a cylindrical specimen. Similar to axial strain the shearing displacement is measured by the relative tangential displacement on the specimen:

$$\gamma = \frac{\Delta L_s}{L_0} \quad \text{Eq. 2.7}$$

where  $\Delta L_s$  is the shearing displacement (measured directly by extensometer) which is perpendicular to the gauge length  $L_0$ .

In these tests shear strain was calculated over the mean diameter of the specimens.

$$\gamma = \frac{2\pi\alpha(d_o + d_i)}{(360 L_0 4)} \times 100 \quad \text{Eq. 2.8}$$

where  $\alpha$  is the torsional angle,  $d_o$  and  $d_i$  are the outer and inner diameters of the tubular test specimen, respectively.

## 2. Experimental method

In tubular specimens shear stress also vary nonlinearly, but, a uniformly distributed shear stress is assumed. The relationship between shear stress applied at the mean diameter of the gauge section and the torsional moment,  $M$ , is:

$$\tau = \frac{16M}{\pi(d_o^2 - d_i^2)(d_o + d_i)}, \quad \text{Eq. 2.9}$$

where,  $\tau$  is the shear stress (see Figure 2.8) [128].

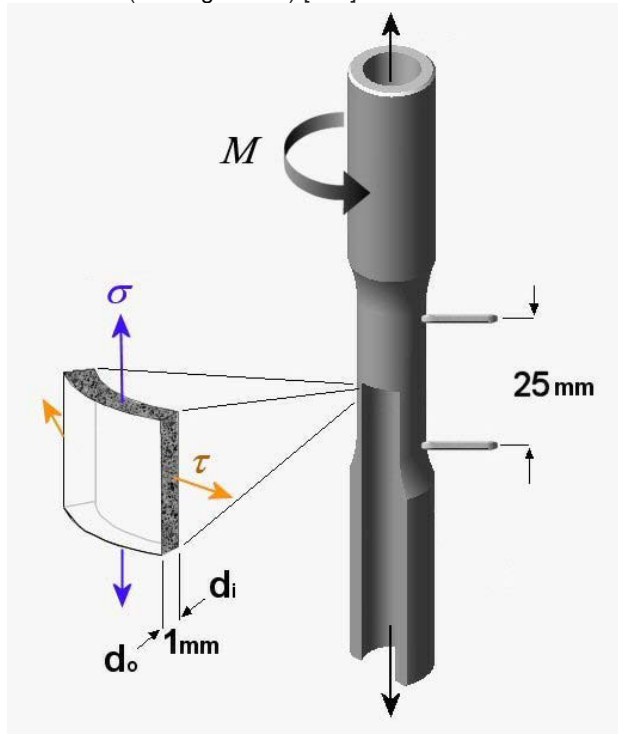


**Figure 2.8:** Schematic illustration of a thin-walled (1mm) tubular TMF specimen under axial-torsional loading. The shear stress  $\tau$ , is calculated at the mean diameter of the gauge section. Strain measurement is achieved via the axial-torsion extensometer which has a 25mm measuring distance within the gauge section.

### 2.5. Microscopy

The microscopic characterisation of this material was undertaken with stereo-optical microscopy and scanning electron microscopy. All images obtained via these investigations were in digital form.

For fractographic investigations, a Leica M420 stereo optical microscope was used. Images were obtained via the Leica DFC290 colour digital camera with a resolution of 3 megapixels. The integrated software Leica Application Suite (LAS) enables a series of images to be dynamically built up and processed into one single image that has a greater depth of field than any single image may have. This is particularly important when imaging rough undulating surfaces, where the whole area can be seen in sharp focus.



Scanning electron microscopy (SEM) has been used to characterize the as-received and thermo-mechanically loaded states. Imaging with secondary electrons (SE) and backscattered electrons (BSE) are commonly used for grain contrast imaging [135]. Most images were obtained using the BSE mode without any surface etching. This is a particularly useful for identifying multi-phased structures such as heavy elements which appear brighter than lower density elements. For all investigations the scanning electron microscope LEO Gemini 1530 VP with field-emission gun was used (FEG-SEM, Zeiss, Germany).

Chemical compositions were determined using energy dispersive x-ray spectroscopy (EDS) operating at 10-20 kV. The system used was a INCA 2000 (Oxford Instruments) with a "Premium"-Si (Li) detector and a Pentafet window (called ATW2). An electron probe micro analyzer (EPMA) of type JEOL *JXA 8900 RL* was also applied to identify the material's chemical composition, especially in relation to specific particles that were bright contrasted by BSE. This apparatus employs wave length dispersive x-ray micro-analysis (WDX) to provide the chemical mass composition. Quantitative point analyses of individual particles were performed at 15 kV, 50 nA.

For the BSE investigations, material samples were water cooled mechanically ground using 600 to 1200 grade SiC paper, ultimately they were cleaned in a ultrasound bath. Electro-polishing was performed on a Struers Lectropol 5 in an electrolyte solution of methanol (60 vol%), 1-butanol (34 vol%) and perchloric acid (6 vol%) at 20°C with a 27 volt current for approximately 30 seconds. For EDS and EPMA the samples were ground using 80 to 4000 grade SiC paper. This was followed by polishing with Dia-Pro-Mol, 0.01µm diamond paste on a Steuers MD Chem. polishing cloth and subsequent polishing for five minutes with colloidal silica. All samples were ultimately cleaned with H<sub>2</sub>O.

The samples that were chosen for surface damage characterisation using the SEM were initially nickel plated and embedded in an electro-conductive epoxy. The nickel plate, in this case is the hardest substance, remains proud after polishing. The Ni protects the sample edges against the effects of rounding during the polishing, preserving any surface cracks and oxidation scale that may be present.

The volume fraction ( $V_f$ ) of  $\alpha_2$ ,  $\gamma$  and lamellar grains was established via two methods, the point fraction counting method and the linear intercept method, both according to Underwood [136]. Point fraction counting is the ratio of the number of points that fall in a phase of interest to the total number of test points. In this method a virtual orthogonal grid is placed over the BSE micrograph (plane of polishing), where the grid intersects with a grain boundary a point is marked on the grid. The volume fraction of a phase equals the fraction of points in an array that lies on that phase. The linear intercept method determines the  $V_f$  from linear ratios. Here a series of lines are laid on a BSE micrograph, the number of intersections across lines of given length is counted, and divided by the line length. The volume fraction of a phase equals the fraction of the total line length that lies on that phase. Twenty BSE longitudinal and transverse micrographs (each being 278µm<sup>2</sup>) taken randomly over the microstructure of the as-received material, were analysed using these methods and an approximate percentage  $V_f$  value of each grain type was established.

Transmission electron microscopy (TEM) specimens were prepared by jet polishing using the same electrolyte mentioned above ( $T = -15\text{ }^\circ\text{C}$ ,  $U = 20\text{ V}$ ). A Philips CM20 microscope was used for TEM investigations operating at 200 kV.

### 3. Results

In the following chapter, the experimental and microstructural results will be presented. The first section 3.1, describes the as-received microstructure, its general characteristics and the volume fraction of the various phases present. The material composition is described in section 3.2 which also includes the results from processes used to identify specific microstructural inclusions. The mechanical behavioural investigations begin at section 3.3 with the presentation and evaluation of the pre-test investigations of the dynamic Young's and shear moduli, by the use of the sonic resonance technique. The main body of this chapter, section 3.4, concerns the results from thermo-mechanical fatigue testing. Section 3.4 is further sub-divided into the test type beginning with the TMF tests of uniaxial OP, IP and torsion, before concluding with the more complex proportional-axial-torsional and non-proportional-axial-torsional tests. An additional test with a hold period (with the exception of the proportional-axial-torsional test) was performed to establish any creep fatigue effects. All of these hold period tests are presented in the results and observed differences are highlighted. The fractographic characterisation follows this, with an analysis of the deformed microstructure and description of damage mechanisms that have been identified.

#### 3.1. The as-received material

The microstructure of the as-received extruded Ti45Al-5Nb-0.2B-0.2C at% (nominal composition) alloy is shown in Figure 3.1. The region examined corresponds to the middle of the diameter of the extruded bar.

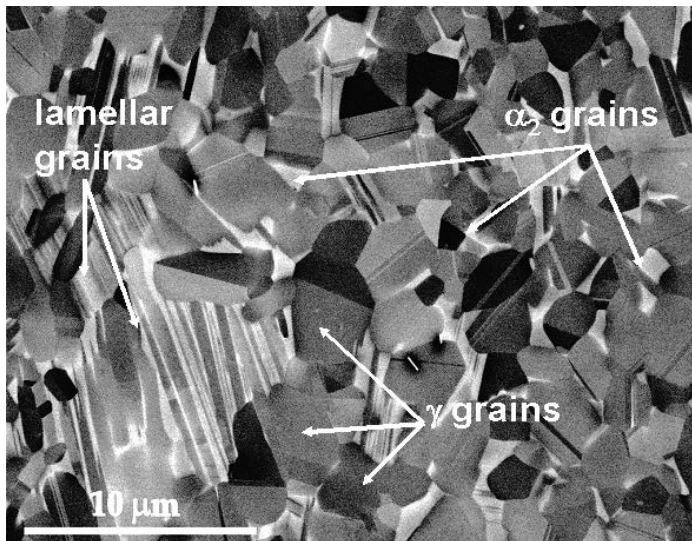


**Figure 3.1:** The microstructure of the as-received material. SEM micrograph in transverse section showing the fine duplex microstructure, extrusion direction and specimen axis are perpendicular to the image plane (BSE).

The duplex microstructure consists of mainly globular  $\gamma$ -grains (approximately 2 - 3  $\mu\text{m}$ ) with a small volume fraction of lamellar colonies (approximately 24%) and some  $\alpha_2$  at  $\gamma$ -grain boundaries. The  $\gamma$ -grain distribution is comparatively random perpendicular to the extrusion direction. Lamellae interfaces are roughly parallel to the extrusion direction. Grains are roughly the same size in both longitudinal and transverse sections (see Figure 3.2).

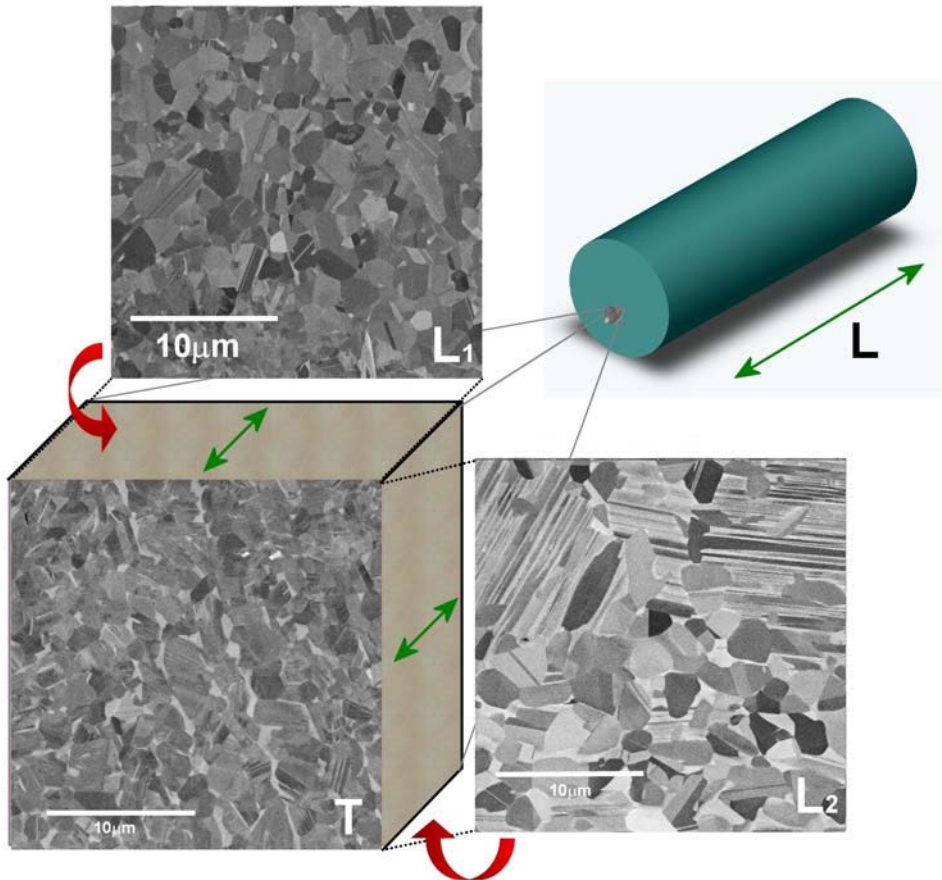


**Figure 3.2:** Grain structure of the as-received (AR) material illustrated in cubic form. Double-headed arrows indicate extrusion direction ( $L$ ).  $T$ : indicates transverse section where the extrusion direction is perpendicular to the image,  $L_1$  and  $L_2$ : indicates longitudinal sections where the extrusion direction is parallel to the images. (BSE)

The volume fraction ( $V_f$ ) of  $\alpha_2$ ,  $\gamma$  and lamellar grains was established using the point fraction and the linear intercept methods [136].

**Table 3.1:** The volume fraction ( $V_f$ ) and average grain size of  $\alpha_2$ ,  $\gamma$  and lamellar grains established from the as-received material.

Grain type	Transverse section		Longitudinal section		$V_f$ [%]	Average grain size [ $\mu\text{m}$ ]
	$V_f$ [%]	Average grain size [ $\mu\text{m}$ ]	$V_f$ [%]	Average grain size [ $\mu\text{m}$ ]		
$\alpha_2$	6	0.8	6	0.9	6	0.9
$\gamma$	74	2.3	65	2.8	70	2.5
Lamellar	20	5.7	29	5.9	24	5.8

Results in Table 3.1 show that the major phase is clearly  $\gamma$  at around 70%, and  $\alpha_2$  as the minor phase at 6%, the remaining 24% consist of lamellar colonies.

### 3. Results

#### 3.2. Material composition

EDS was employed to establish the chemical composition of the as-received microstructure. The results are presented in Table 3.2.

**Table 3.2:** Measured composition using EDS.

Content in percent (%)			
	Titanium (Ti)	Aluminium (Al)	Niobium (Nb)
Atomic %	50.8	43.9	5.3
Weight %	59.2	28.8	12.0

Under closer SEM examination numerous bright particles - indicating higher density elements/compounds - are also visible. In the longitudinal section these brighter particles are elongated and orientated parallel to the extrusion direction. In the transverse section they are more rounded and show no specific orientation. These bright particles were investigated in more detail using EDS and with an electron probe micro analyzer (EPMA) to establish their chemical composition. In every case the bulk material is included in the scans to highlight any obvious changes in composition.

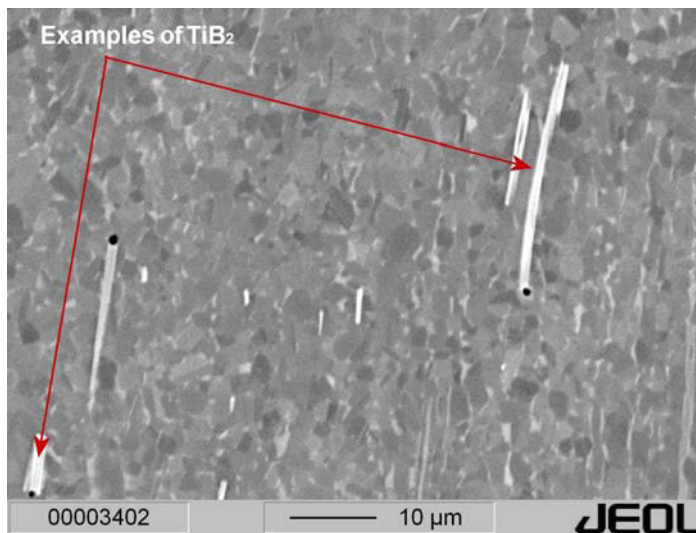


**Figure 3.3:** BSE image of the as-received material showing the bright contrasted rod-shaped particles positively identified as  $TiB_2$  using the EMPA.

EMPA point analysis was undertaken on two separate samples at the brightly contrasted rod-shaped particles, such as those imaged in Figure 3.3, one in transverse and the other in longitudinal section. More chemical elements were included in the analysis, but as seen in Table 3.3 they are in very minor quantities.

Measurement uncertainty lies between 0.1-1% depending on the quantity of the element in the trace. Table 3.3 shows in both cases the B concentration is around 50at% and Ti around 33at%. Al and Nb were also detected but in smaller quantities. This indicates the presence of  $TiB_2$  [137].

**Table 3.3:** EMPA point analysis of particles in sample 1 and sample 2 (transverse and longitudinal).

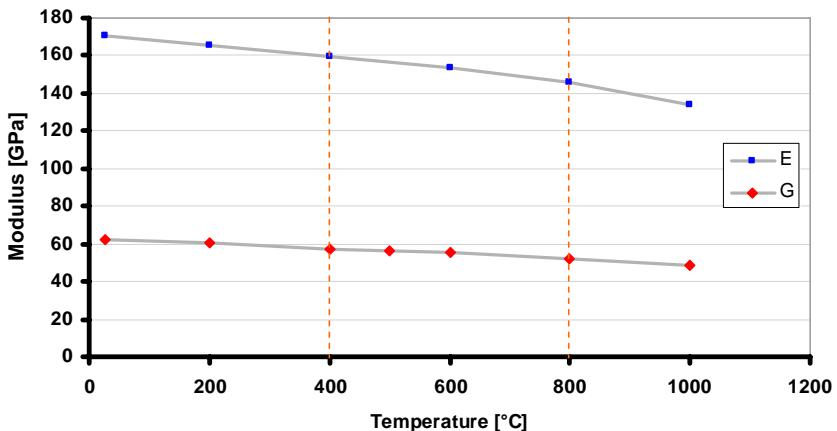
Sample	B		Ti		Al		Nb		V		O	
	at%	wt%	at%	wt%	at%	wt%	at%	wt%	at%	wt%	at%	wt%
1	52.5	19.8	32.0	53.6	8.2	7.7	5.5	17.8	0.06	0.1	1.8	1.0
2	47.6	17.2	34.3	54.9	9.8	8.8	5.6	17.5	0.06	0.1	2.6	1.4

### 3.3. Elastic and shear moduli

The temperature dependence of Young's modulus  $E$ , and shear modulus (rigidity)  $G$  are important parameters to obtain before any mechanical testing can begin. The dynamic moduli of  $E$  and  $G$  were obtained from the as-received material using a *Elastotron 2000*. The results are shown in Table 3.4 and graphically in Figure 3.4.

**Table 3.4:** Results of the determination of the dynamic elastic modulus  $E$  and shear modulus  $G$  measured between 26°C and 1000°C, using the sonic resonance technique. The shaded region covers the TMF test temperature range of 400°C - 800°C.

Temperature [°C]	Average $E$ modulus [GPa]	$E$ modulus reduction from RT [%]	Average $G$ modulus [GPa]	$G$ modulus reduction from RT [%]
26	170.9	0.0	62.54	0.0
200	165.4	3.2	60.33	3.5
400	159.5	6.7	57.23	8.5
600	153.2	10.4	55.50	11.3
800	145.8	14.7	52.41	16.2
1000	133.8	21.7	49.04	21.6

**Figure 3.4:** The dynamic elastic modulus  $E$  and shear modulus  $G$  measured between 26°C and 1000°C using the sonic resonance technique. The TMF test temperature range of 400°C - 800°C is indicated by the dashed lines.

From these results the temperature effects on both  $E$  and  $G$  moduli is clearly shown. Over the testing temperature range of 400-800°C there is a reduction for  $E$  and for  $G$  (see Table 3.4).

### 3. Results

#### 3.4. Thermo-mechanical fatigue behaviour

The test matrix, explained in section 2.4 (Table 2.2), incorporates a range of uniaxial OP, IP and torsional IP tests together with complex multiaxial tests. The TMF results are presented in accordance to the validated code of practice for strain controlled thermo-mechanical fatigue testing [68]. The term mechanical strain  $\epsilon_m$  is the total strain  $\epsilon_{tot}$  after subtraction of the thermal strain  $\epsilon_{therm}$  (see Eq. 2.5). The equivalent strain amplitude  $\epsilon_{eq}$  is calculated from the Mises relation (see Eq. 2.2).

##### 3.4.1. Uniaxial TMF tests

###### *Out-of-phase (OP)*

The uniaxial TMF tests in OP mode were performed over a range of equivalent strain amplitudes  $\epsilon_{eq}$ , from 0.15 to 0.3%. One additional test was performed with a 180 seconds hold period. The characteristics of a typical uniaxial OP TMF test are shown in Figure 3.5.

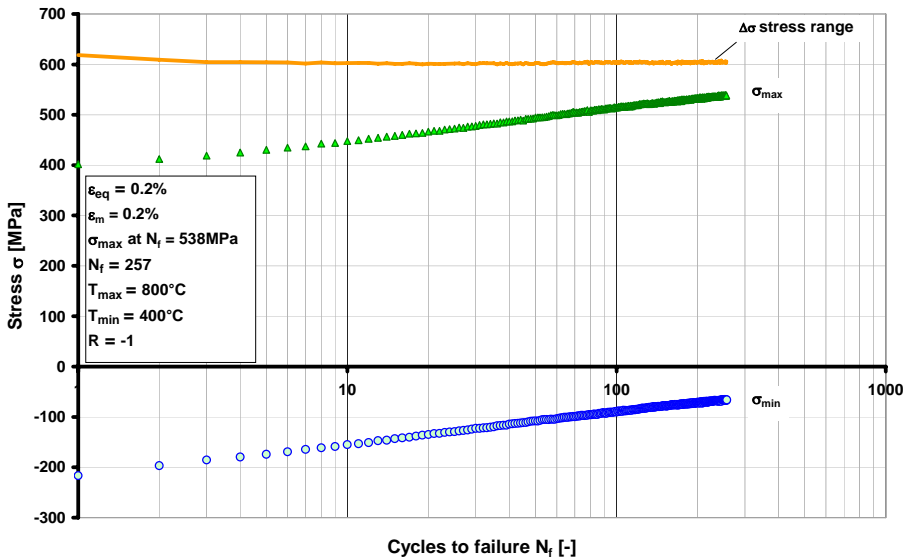


**Figure 3.5:** A typical uniaxial OP TMF test showing stress  $\sigma_{max}$ ,  $\sigma_{min}$ , stress range  $\Delta\sigma$ , vs. cycles to failure  $N_f$ .

Generally, for all OP tests, the stress  $\sigma_{max}$ , and  $\sigma_{min}$  ascend with each loading cycle which results in a constant stress range  $\Delta\sigma$ . Plastic deformation is mostly restricted to the first cycle, while the following cycles show only slight plastic deformation. Nevertheless, the hysteresis curves subsequently ascend parallel from cycle to cycle (see Figure 3.6 and Figure 3.7).

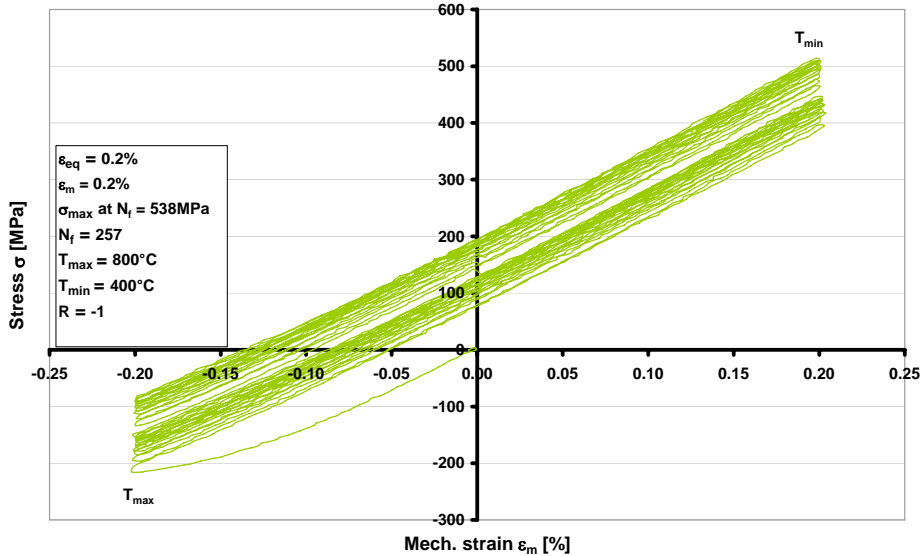


**Figure 3.6:** Stress vs. mechanical strain for a typical uniaxial OP TMF test. Each loading path almost follows the unloading path, however, with each loading cycle the stress-strain hysteresis curves shift positively in stress. The stress range remains constant throughout the test.

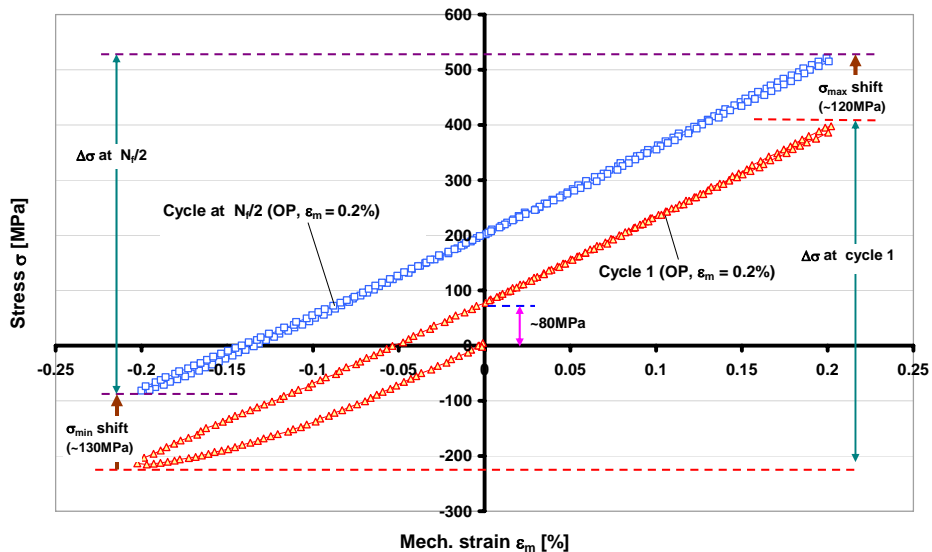


**Figure 3.7:** The initial loading cycle (triangles) and mid-life  $N_f/2$ , (squares) hysteresis curves for the uniaxial OP TMF test shown in Figure 3.6. Clearly seen from this diagram is how (for  $N_f \geq 2$ ) the unloading paths closely follow the loading path, forming extremely narrow hysteresis loops. Over the test, the hysteresis loops shift positively in stress. ( $\epsilon_m = \epsilon_{eq} = 0.2\%$ ).

### 3. Results

In Figure 3.7 at zero strain the stress after the first half cycle increases by approximately 80MPa. In other tests, the values of stress in the first loading path at zero strain are between 60MPa ( $\epsilon_{\text{eq}} = 0.17\%$ ) and 135MPa ( $\epsilon_{\text{eq}} = 0.3\%$ ).

The effect of a hold period on the fatigue lifetime was established using a uniaxial OP test conducted at  $\epsilon_m = 0.15\%$ . The test was identical to one already performed at  $\epsilon_m = 0.15\%$  with one exception, the additional hold period parameter is incorporated at  $T_{\text{max}} = 800^\circ\text{C}$ , where the load is held in compression for 180 seconds.

In Figure 3.8 the stresses  $\sigma_{\text{max}}$ , and  $\sigma_{\text{min}}$ , ascend with each loading cycle. As previously observed with non-hold period tests, after the first cycle, the stress range  $\Delta\sigma$  remains constant throughout.

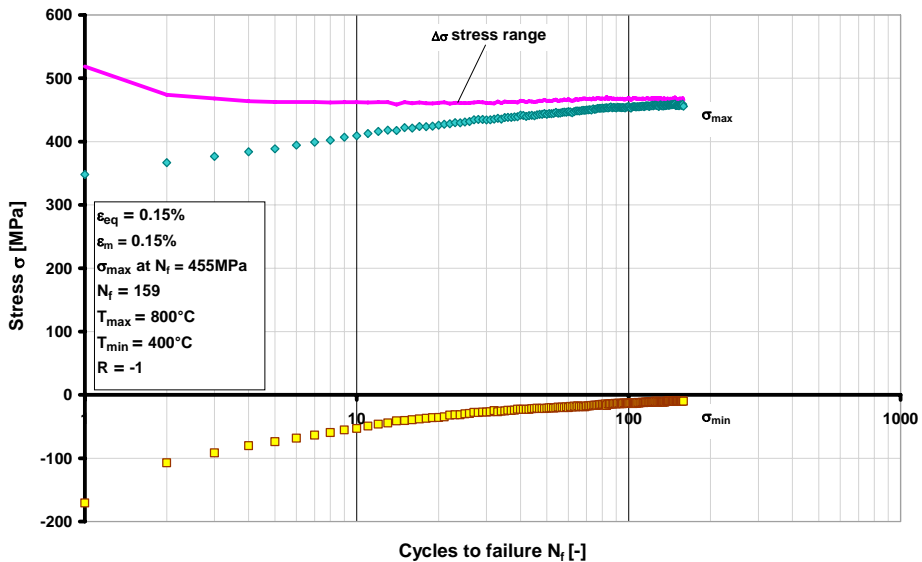


**Figure 3.8:** Uniaxial OP TMF test with a 180 seconds hold period showing stress  $\sigma_{\text{max}}$ ,  $\sigma_{\text{min}}$ , stress range  $\Delta\sigma$ , vs. cycles to failure  $N_f$ .

As with the non-hold period tests the hysteresis loading paths shift positively in stress. This can be seen in Figure 3.9 and with greater clarity in Figure 3.10.

As with previous uniaxial OP tests, the first cycle contains the largest hysteresis loop of the test (see Figure 3.10). At zero strain the unloading path of the first half cycle increases by approximately 110MPa, this is 50MPa more than the test at the same equivalent strain amplitude without a hold period. The first half cycle is also different in another way: during the hold period ( $t_{\text{hold}}$  cycle 1) at  $T_{\text{max}}$  the compressive stress reduces by approximately 65MPa from -170MPa to -105MPa. By mid-life the compressive stress only reduces by about 5MPa over the hold period ( $t_{\text{hold}} N_f/2$ ).

Comparing  $\sigma_{\text{max}}$  and  $\sigma_{\text{min}}$  data from both  $\epsilon_m = 0.15\%$  tests, the hold period test has higher tensile stress and lower compressive stress by approximately 80MPa compared to the test without a hold period (see Figure 3.11). The effect of the hold period on the fatigue lifetime is extremely detrimental. Previously, the OP test at  $\epsilon_m = 0.15\%$  shows a fatigue lifetime of 1076 cycles before failure, in the hold period test the lifetime is 86% shorter, at only 159



cycles before failure (a factor of nearly 7 lower). The stress ranges for both tests are almost identical.

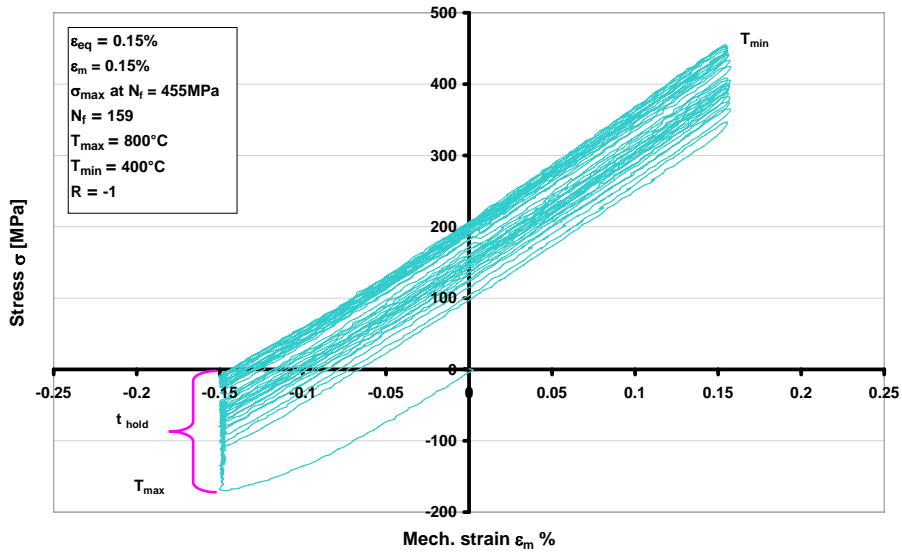


**Figure 3.9:** Stress vs. mechanical strain for the uniaxial OP TMF test with 180 seconds hold period ( $t_{hold}$ ) at  $T_{max}$ . As with non-hold period tests the stress-strain cycle curves do not completely overlap one another after each loading cycle, instead they shift positively in stress.

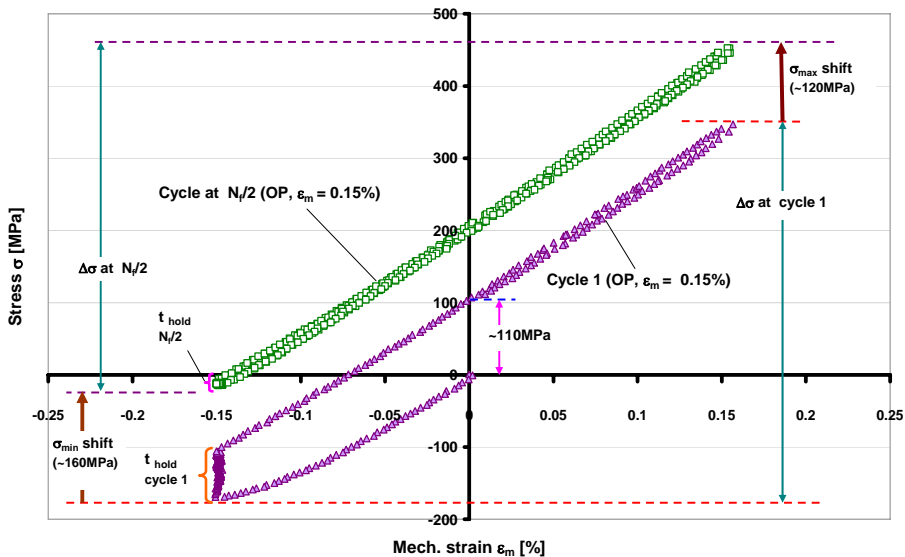


**Figure 3.10:** The initial cycle (triangles) and mid-life (squares) hysteresis loading curves for the uniaxial OP TMF test with 180 seconds hold period. ( $\epsilon_m = \epsilon_{eq} = 0.15\%$ ).

### 3. Results

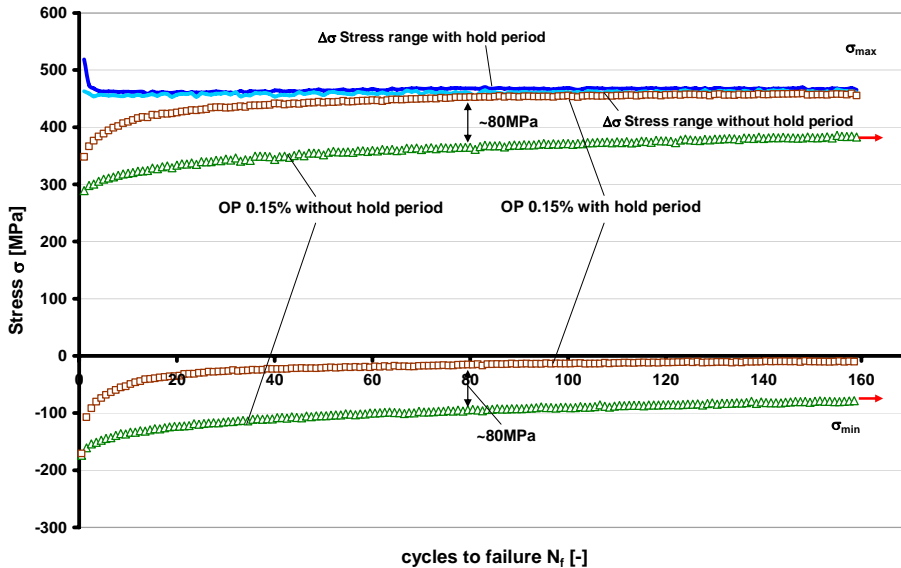


**Figure 3.11:** Diagram of  $\sigma_{max}$  and  $\sigma_{min}$  vs.  $N_f$ . Comparison of two uniaxial OP TMF tests, both at  $\epsilon_m = 0.15\%$ . One test with a 180 seconds hold period (squares) and the other without a hold period (triangles). The hold period test has a higher tensile stress by approximately 80MPa per cycle at mid-life and a decreased compressive stress by approximately 80MPa per cycle mid-life than the test without a hold period. The arrows indicate that this test continues beyond this point ( $\epsilon_m = \epsilon_{eq} = 0.15\%$ ).

In summary, for uniaxial OP tests, the peak tensile loading  $\sigma_{max}$ , takes place at  $T_{min}$ . The OP loading also shows a high sensitivity to strain amplitude, a very slight increase consequently shortened fatigue lifetime. The first loading-unloading cycle has the largest hysteresis loop. The fatigue lifetimes range from 8 at  $\epsilon_m = 0.3\%$  to 1076 at  $\epsilon_m = 0.15\%$ . The constant stress ranges indicate that neither cyclic hardening nor softening is taking place.

#### ***In-phase (IP)***

The uniaxial TMF tests in IP mode were performed over a range of mechanical strain amplitudes  $\epsilon_m$ , from 0.3% to 0.7%. For all performed IP tests, the stresses  $\sigma_{max}$  and  $\sigma_{min}$  descend with each loading cycle, the exact opposite to OP loading. A decrease is also observed in the stress range  $\Delta\sigma$ , which indicates that some cyclic softening is taking place (see Figure 3.12).

At  $\epsilon_m = 0.3\%$ , the hysteresis loops are similar to those of the OP uniaxial tests in terms of each loading path follows the unloading path very closely for  $N > 1$ . At the higher strain amplitudes (0.5 – 0.7%) the IP uniaxial cyclic stress-strain loading-unloading paths form large hysteresis loops, which, over the test, descend in stress. The example shown in Figure 3.13 demonstrates this well. However, in this example, the hysteresis loops appear to have become stabilised (follow the same stress-strain path) after the initial ‘shakedown’ period appearing at the end of approximately 100 cycles, when the hysteresis loops superimpose over one another.

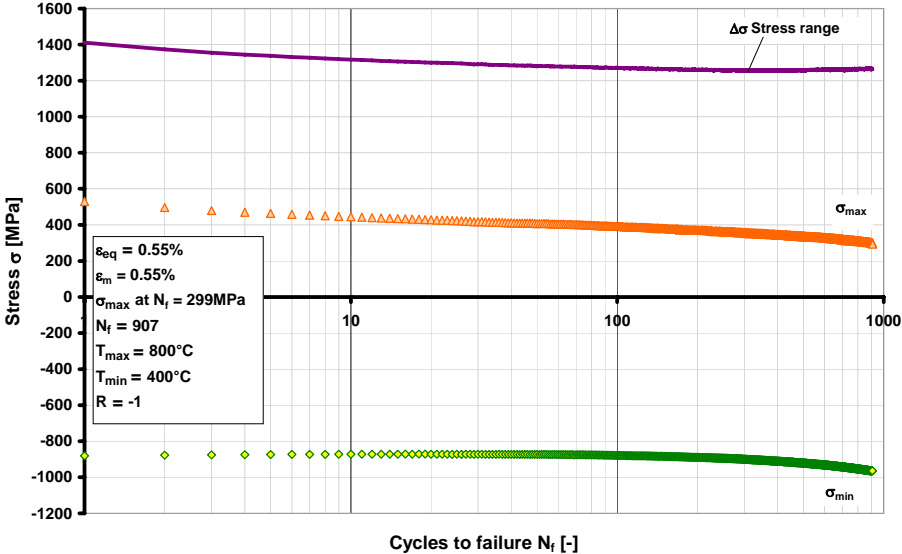


Figure 3.12: A uniaxial IP TMF test showing stress  $\sigma_{max}$ ,  $\sigma_{min}$ , stress range  $\Delta\sigma$ , vs. cycles to failure  $N_f$ . In this test the stress range  $\Delta\sigma$ , steadily decreases until approximately the 300th cycle before slightly increasing.

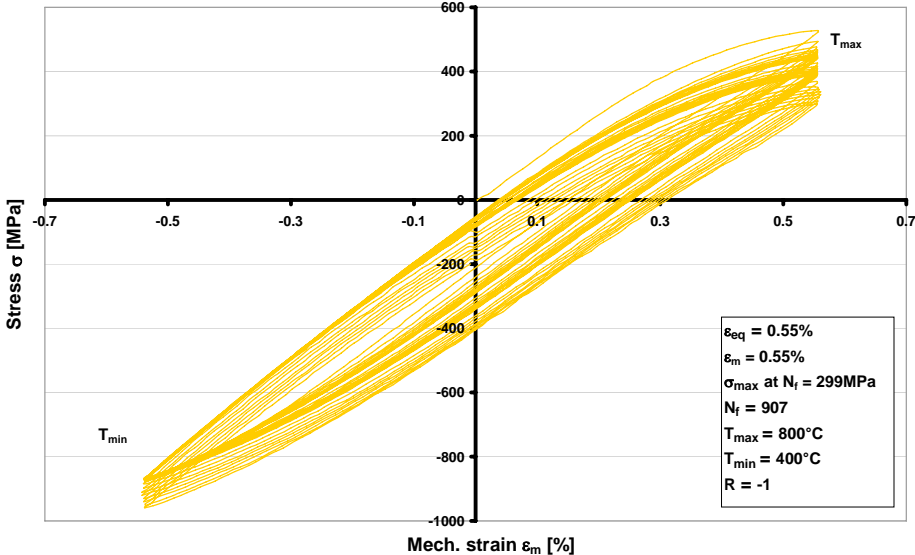
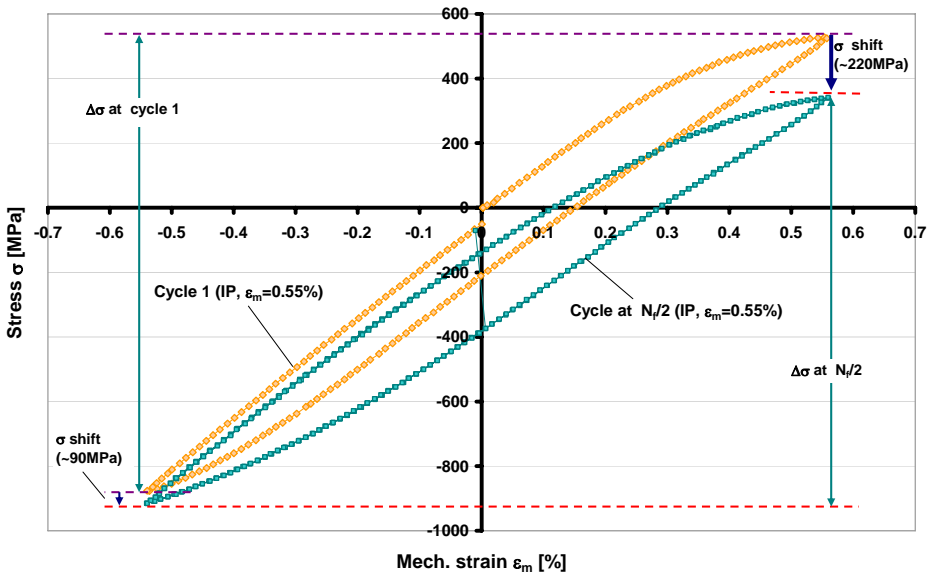


Figure 3.13: Stress vs. mechanical strain for a typical uniaxial IP TMF test. The stress-strain cycle curves do not closely follow the loading/unloading paths, instead they form wide hysteresis loops. In this example cyclic stabilization occurs after approximately the 100th cycle, when the hysteresis loops superimpose over one another. The max tensile stress decreases over the test causing negative stress shift.

### 3. Results

The stress-strain hysteresis ‘wider’ looped paths are seen more clearly in Figure 3.14 where the first cycle and the mid-life cycle ( $N_f/2$ ) of the example shown in Figure 3.13 are illustrated.



**Figure 3.14:** The initial loading cycle (triangles) and mid-life (squares) hysteresis curves for the uniaxial IP TMF test shown in Figure 3.13. At mid-life there is a smaller stress shift over the compressive loading ( $\sim 90\text{MPa}$ ) than seen over the tensile loading ( $\sim 220\text{MPa}$ ) ( $\varepsilon_m = \varepsilon_{eq} = 0.55\%$ ).

The first cycle always contains the least symmetrical hysteresis loop of the test. In the test shown in Figure 3.14 at the end of the first cycle, when the strain returns to zero, the loading path is shifted negatively by approximately 50MPa. In other tests, the values of stress in the first loading path at zero strain are between  $-182\text{MPa}$  ( $\varepsilon_{eq} = 0.5\%$ ) and  $100\text{MPa}$  ( $\varepsilon_{eq} = 0.7\%$ ). Throughout the test, the tensile stress decreases to a much greater extent than the compressive stress, this is reflected by the dip in the stress range seen in Figure 3.12.

The uniaxial IP loading brings about very high compressive stresses and very low tensile stresses compared to the OP tests. This is because the peak tensile loading occurs at maximum temperature  $T_{max} = 800^\circ\text{C}$ . The uniaxial IP TMF lifetimes range from  $>3656$  cycles at  $\varepsilon_{eq} = 0.3\%$  (interrupted) to 572 at  $\varepsilon_{eq} = 0.7\%$  (highest amplitude). In summary, for the uniaxial IP tests, increasing the strain amplitude, increases the tensile stress, this in turn reduces the fatigue lifetime.

Hold period effects on fatigue lifetimes were also established with a single IP uniaxial test conducted at  $0.55\%$  mechanical strain amplitude  $\varepsilon_m$ . At  $\sigma_{max}$ , a hold period (180 seconds at  $T_{max} = 800^\circ\text{C}$ ) was applied to this test. A matched test previously performed at  $\varepsilon_m = 0.55\%$  was used for direct comparison.

From the uniaxial IP test example in Figure 3.15, it can be seen that the peak tensile stress  $\sigma_{max}$ , decreases with each loading cycle, however, the peak compressive stress  $\sigma_{min}$ , is fairly constant. The stress range  $\Delta\sigma$ , similar to  $\sigma_{max}$ , decreases constantly throughout the test indicating some cyclic softening.

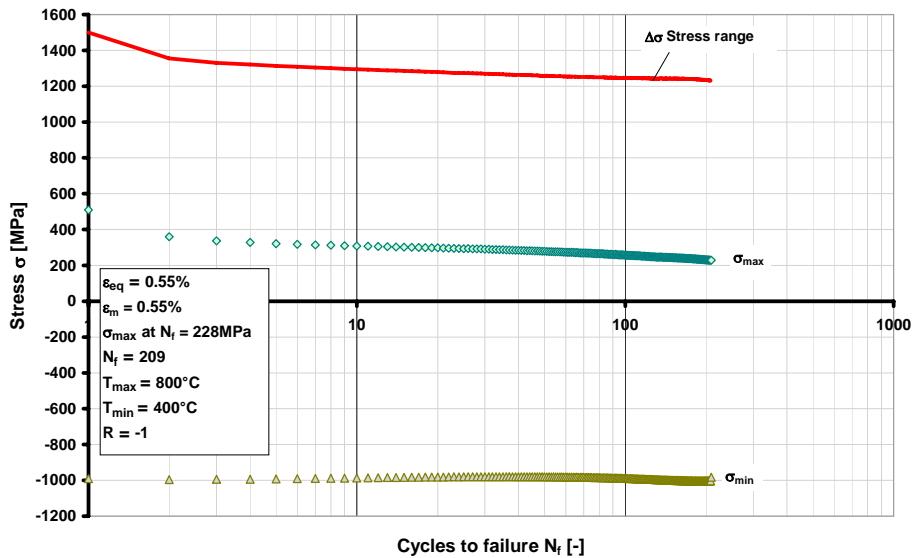


**Figure 3.15:** A uniaxial IP TMF test with 180 seconds hold period showing stress  $\sigma_{max}$ ,  $\sigma_{min}$ , stress range  $\Delta\sigma$ , vs. cycles to failure  $N_f$ . The stress range clearly decreases over the test.

The stress-strain hysteresis curves for the uniaxial IP test at  $\epsilon_{eq} = 0.55\%$  with 180 seconds hold period is illustrated in Figure 3.16.

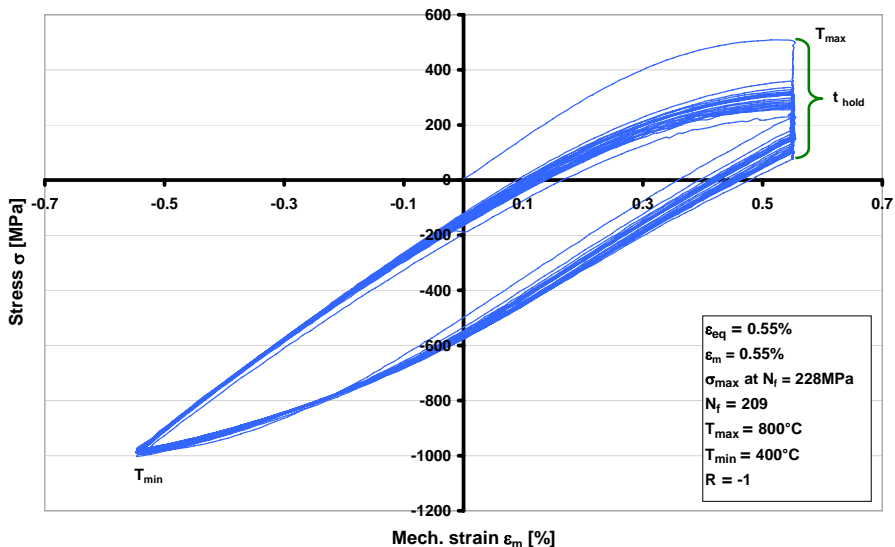


**Figure 3.16:** Stress vs. mechanical strain for the uniaxial IP TMF test with 180 seconds hold period ( $t_{hold}$ ) at peak tensile stress  $\sigma_{max}$ . At  $T_{max}$  the hysteresis curves shift negatively in stress, whereas at  $T_{min}$  the curves return to the same stress level with each unloading cycle.

### 3. Results

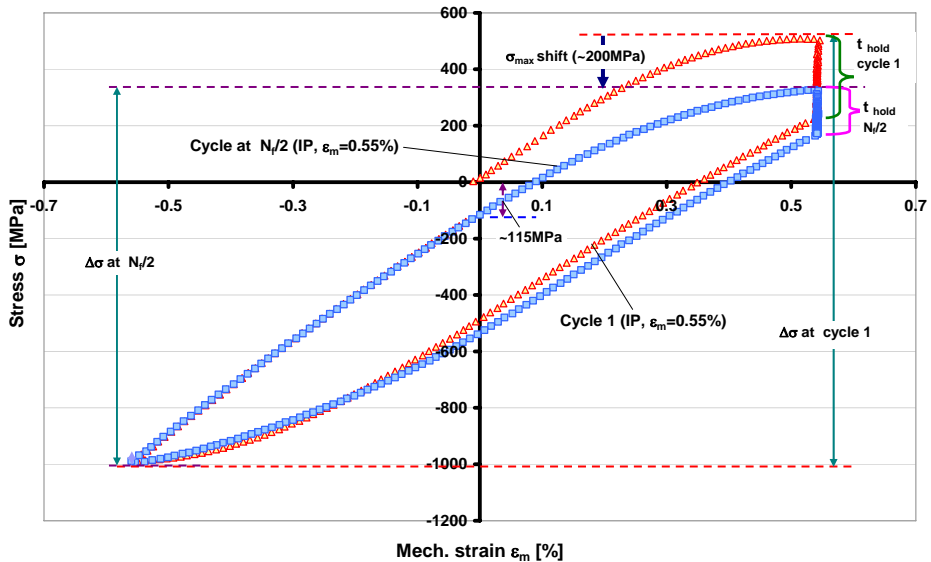


**Figure 3.17:** The initial cycle (triangles) and mid-life (squares) hysteresis stress-strain curves for the uniaxial IP TMF test with 180 seconds hold period. The reduced tensile stress with each cycle causes a negative stress shift in the hysteresis stress-strain curves. This is not apparent in the compressive region of the stress-strain curves where there appears to be little or no stress shift ( $\epsilon_m = \epsilon_{eq} = 0.55\%$ ).

The first cycle contained the largest hysteresis loop of the test. At the end of the first cycle, when the strain returns to zero, the loading path has shifted negatively by approximately 115MPa (see Figure 3.17). During the 180 seconds hold period in the first loading cycle, the stress decreases by approximately 270MPa ( $t_{\text{hold cycle 1}}$ ). By mid-life over the hold period ( $t_{\text{hold } N_f/2}$ ) the stress decreases by about 130MPa. This stress shift has reduced the maximum tensile stress  $\sigma_{\text{max}}$  by  $\sim 200\text{MPa}$  at  $N_f/2$ . However, there is no apparent difference in stress in the compressive region of the hysteresis curves of  $N=1$  and  $N_f/2$ , they remain constant throughout the test. This is in contrast to the test without a hold period where a shift was observed during the compressive phase at  $\sigma_{\text{min}}$  (see Figure 3.12).

As seen in the uniaxial OP tests, the effects of the 180 seconds hold period on the fatigue lifetime reduces it considerably. The IP test at  $\epsilon_m = 0.55\%$  had a fatigue lifetime of 907 cycles before failure, in the hold period test the lifetime was 77% shorter, at only 209 cycles before failure which amounts to factor of over 4 lower. Although the tensile stress  $\sigma_{\text{max}}$  is reduced the compressive stress remains fairly constant. This still affects the stress range by decreasing it.

Comparing  $\sigma_{\text{max}}$  and  $\sigma_{\text{min}}$  data from both  $\epsilon_{eq} = 0.55\%$  tests, the hold period test has lower tensile stress by approximately 130MPa per cycle and lower compressive stress by approximately 110MPa per cycle. Again the stress ranges for both tests are almost identical, both decreasing per cycle, but here the hold period stress range is slightly lower (opposite to uniaxial OP) than the stress range without a hold period (see Figure 3.18).

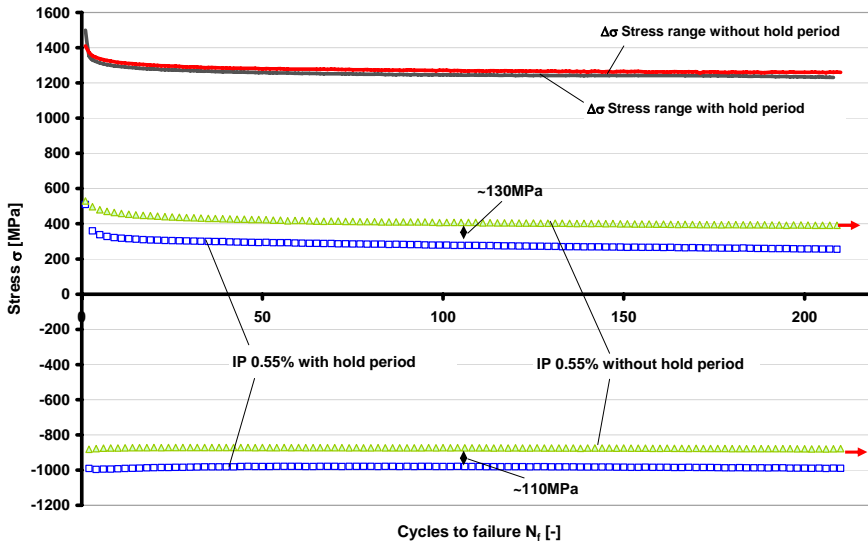


**Figure 3.18:** Diagram of  $\sigma_{max}$  and  $\sigma_{min}$  vs.  $N_f$ . Comparison of two uniaxial IP TMF tests, both at  $\epsilon_m$  0.55%. One test with a 180 seconds hold period (squares) and the other without a hold period (triangles). The hold period reduces the tensile stress by approximately 130MPa and increases the compressive stress by approximately 110MPa in every loading cycle. The fatigue life is reduced by 77% over the non-hold period test. ( $\epsilon_m = \epsilon_{eq} = 0.55\%$ ).

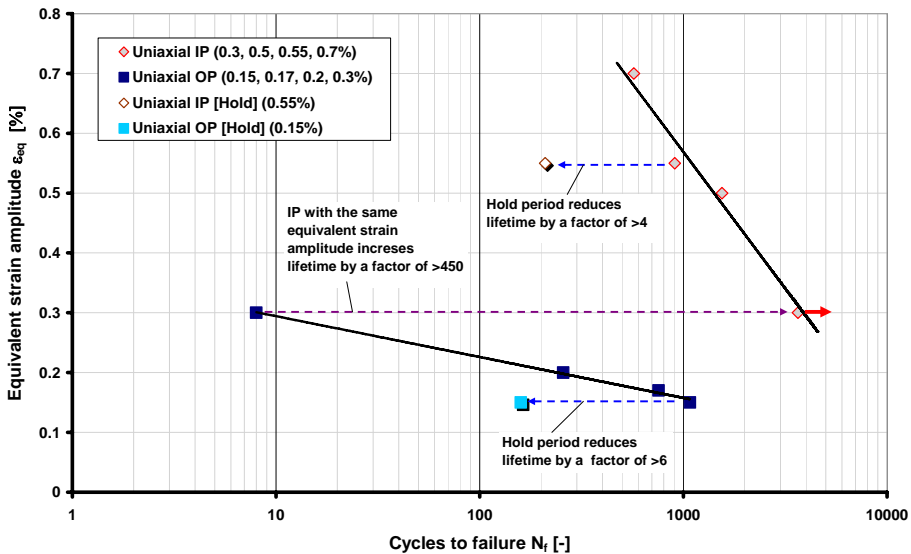


**Figure 3.19:** Uniaxial OP and IP TMF tests depicting equivalent strain amplitude  $\epsilon_{eq}$  vs. cycles to failure  $N_f$ . The greater the strain amplitude the shorter the fatigue lifetimes. OP loadings are more sensitive to strain amplitude than IP loadings. Clearly seen the phase effect on IP and OP with the same strain amplitude of  $\epsilon_{eq}=0.3\%$  (dashed arrow). This IP test has a longer lifetime than the OP test by a factor of >450. Hold period tests reduce lifetimes by a factor of >4 for IP loadings and a factor of >6 for OP loadings with the same  $\epsilon_{eq}$ . There is a linear relationship between lifetime and strain amplitude. The arrow indicates an interrupted test.

### 3. Results

Directly comparing uniaxial OP and IP tests against the effects of strain amplitude proves that OP loadings are more sensitive to strain amplitude than IP loadings. A direct comparison can be made where OP and IP tests are performed at the same strain amplitude  $\varepsilon_{eq} = 0.3\%$ . The lifetime difference here is more than a factor of 450 longer for IP than for OP (see Figure 3.19). The tests also reveal a linear relationship between lifetime and strain amplitude.

The hold period effectively transposes the  $\sigma_{max}$  and  $\sigma_{min}$  positively for OP or negatively for IP. In the OP loadings the hold period increases  $\sigma_{max}$  and reduces  $\sigma_{min}$  reducing fatigue lifetime by a factor of more than 6 compared to a non-hold period test at the same equivalent strain amplitude. For the IP loadings the hold period lowers the compressive stress and raises the tensile stress.

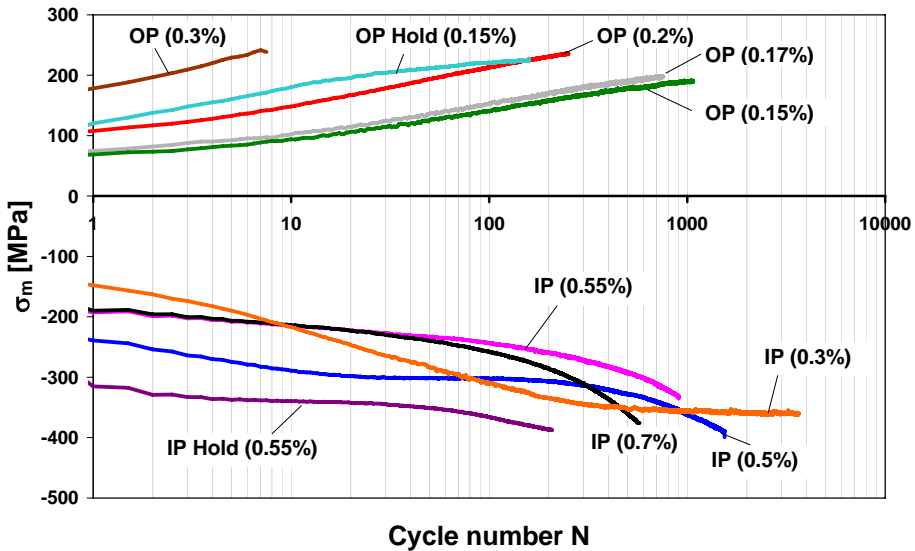


**Figure 3.20:** Cyclic mean stress,  $\sigma_m$ , vs. number of cycles,  $N$ , for OP and IP TMF tests with and without hold periods. Tensile mean stresses develop during OP loading while they are compressive in IP tests. Hold periods amplify mean stresses.

Comparing the mean stress,  $\sigma_m$ , data for uniaxial IP and OP tests (see Figure 3.20), uniaxial OP loading generates a positive mean stress which increases until fracture because of mounting  $\sigma_{max}$  and declining  $\sigma_{min}$ . The opposite is the case for uniaxial IP loading, where compressive stresses are higher and tensile stresses are lower, resulting in an overall negative mean stress. Hold period tests have higher compressive mean stresses than those tests with the same strain amplitude without a hold period.

#### 3.4.2. Torsional TMF tests

The torsional TMF tests in IP mode (temperature-strain phase angle  $\varphi_{T-\gamma} = 0^\circ$ ) were performed over a range of equivalent strain amplitudes  $\varepsilon_{eq}$  from 0.15 to 0.2%. The typical characteristics of a torsional IP TMF test are shown in Figure 3.21.



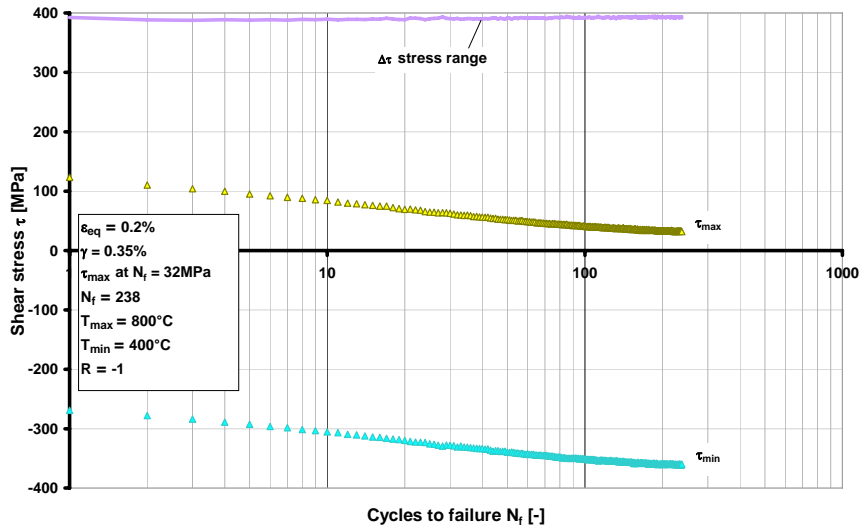


**Figure 3.21:** A torsional IP TMF test showing shear stress  $\tau_{max}$ ,  $\tau_{min}$ , shear stress range  $\Delta\tau$ , vs. cycles to failure  $N_f$ .

From the torsional IP test example in Figure 3.21, it can be seen that the shear stresses  $\tau_{max}^{\ddagger}$ , and  $\tau_{min}$ , descend with each loading cycle. The shear stress range  $\Delta\tau$ , remains constant throughout.

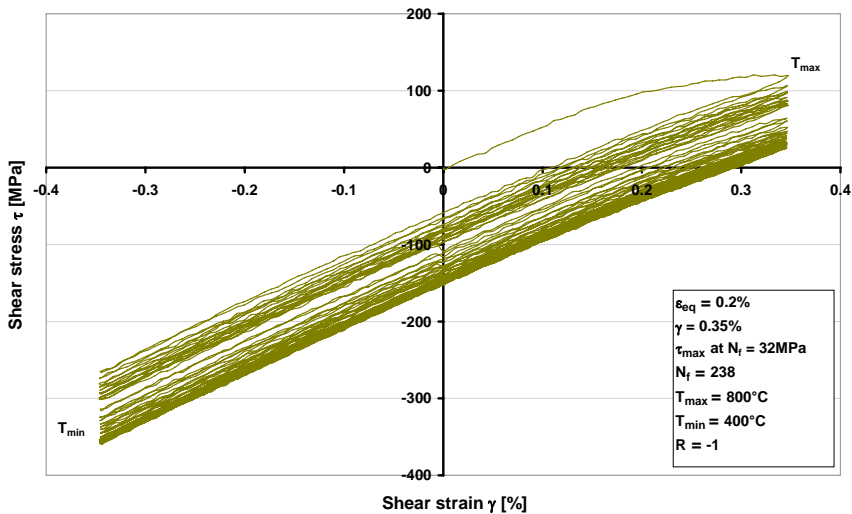


**Figure 3.22:** Shear stress vs. shear strain for a typical torsional IP TMF test. As with the uniaxial OP tests the stress-strain cycle curves initially do not overlap one another instead they shift negatively in shear stress and only towards the end of the test they become more overlapped.

<sup>‡</sup> The sign  $\tau$  has no meaning it is based purely on an arbitrary definition.

### 3. Results

The shear loading path follows the unloading path very closely and the shear stress range,  $\Delta\tau$ , is constant which indicates no cyclic softening or hardening has occurred. Similar to the OP uniaxial hysteresis curves the torsional hysteresis curves do overlap one another after each loading cycle. The hysteresis curves descend parallel. This shift is seen more clearly in Figure 3.23 where the first cycle and the mid-life cycle ( $N_f/2$ ) of Figure 3.22 are illustrated.

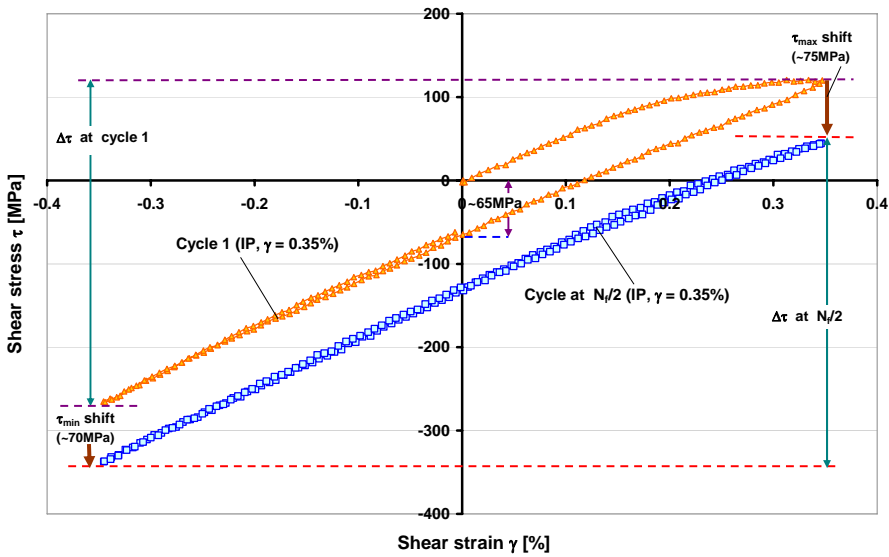


**Figure 3.23:** The initial loading cycle (triangles) and mid-life (squares) hysteresis curves for a typical torsional IP TMF test. The stress range  $\Delta\tau$ , remains constant throughout the test although the actual loading paths shift negatively in stress ( $\gamma = 0.35\%$ ,  $\epsilon_{eq} = 0.20\%$ ).

The first cycle always contains the largest hysteresis loop of the test. This behaviour was observed in every test (see the example in Figure 3.23). At the end of the first cycle in this test, when the strain returns to zero, the loading path has shifted negatively by approximately 65MPa. In other tests, the values of stress in the first loading path at zero strain are between -40MPa ( $\epsilon_{eq} = 0.17\%$ ) and -35MPa ( $\epsilon_{eq} = 0.19\%$ ). At  $N_f/2$ , this shift with each cycle lowers shear stress at  $\tau_{min}$  and  $\tau_{max}$  by 70MPa and 75MPa respectively.

The torsional IP TMF lifetimes range from 4896 cycles at  $\epsilon_{eq} = 0.17\%$  (lowest) to 238 at  $\epsilon_{eq} = 0.2\%$  (highest), a lifetime increase by a factor of >20 for an equivalent strain amplitude reduction of 0.03%.

Hold period effects on fatigue lifetimes have also been established with a single torsional test conducted at  $\epsilon_{eq} = 0.19\%$  strain amplitude. As with other tests, a matched test previously performed at  $\epsilon_{eq} = 0.19\%$  is drawn on for comparison. A hold period of 180 seconds is incorporated at  $T_{max} = 800^\circ\text{C}$  (see Figure 3.24).

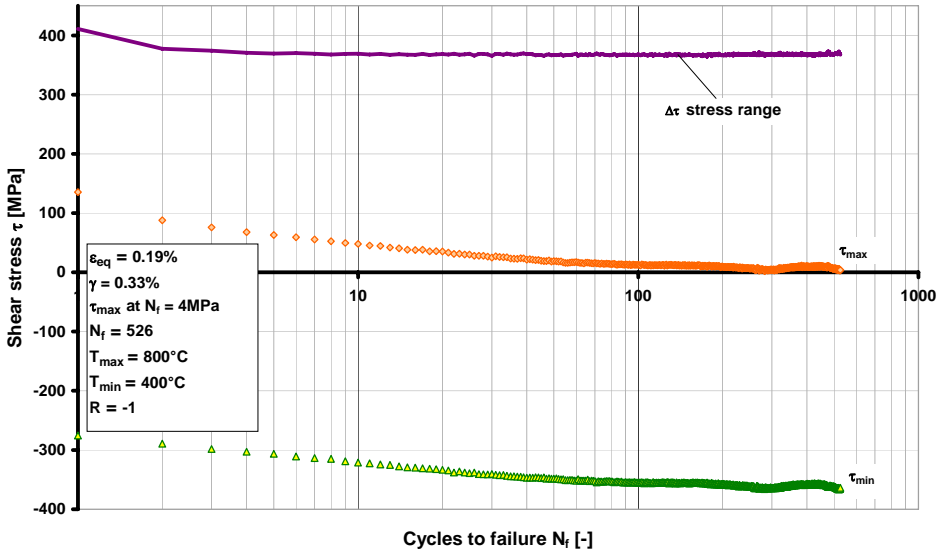


**Figure 3.24:** A torsional IP TMF test with 180 seconds hold period, showing shear stress  $\tau_{max}$ ,  $\tau_{min}$ , shear stress range  $\Delta\tau$ , vs. cycles to failure  $N_f$ . The stress range  $\Delta\tau$ , remains constant throughout the test.

As seen in the torsional IP tests without hold periods, the shear stresses  $\tau_{max}$ , and  $\tau_{min}$  descend with each loading cycle, and the negative shear stress  $\tau_{min}$ , increases with each loading cycle. The shear stress range  $\Delta\tau$ , remains constant throughout.

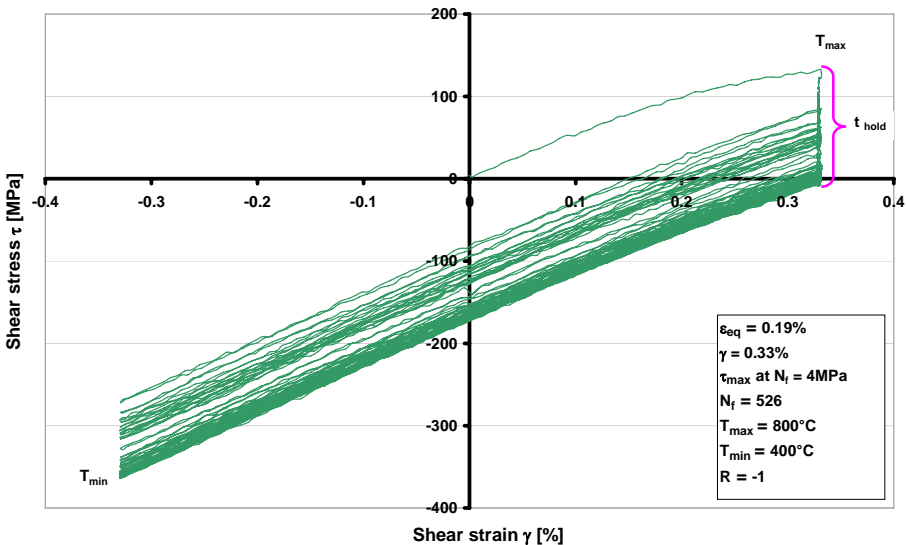


**Figure 3.25:** Shear stress vs. shear strain for the torsional IP TMF test with 180 seconds hold period. The shear stress-strain loading curves initially shift negatively however, before  $N_f/2$  this stress shifting diminishes.

### 3. Results

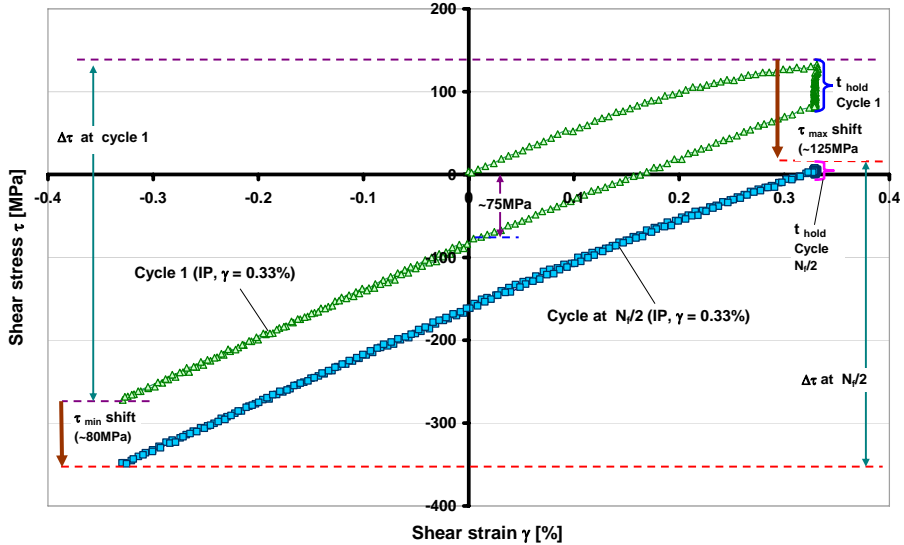


**Figure 3.26:** The initial loading cycle (triangles) and mid-life (squares) hysteresis curves for the torsional IP TMF test illustrated above in Figure 3.25 ( $\gamma = 0.33\%$ ,  $\varepsilon_{eq} = 0.19\%$ ).

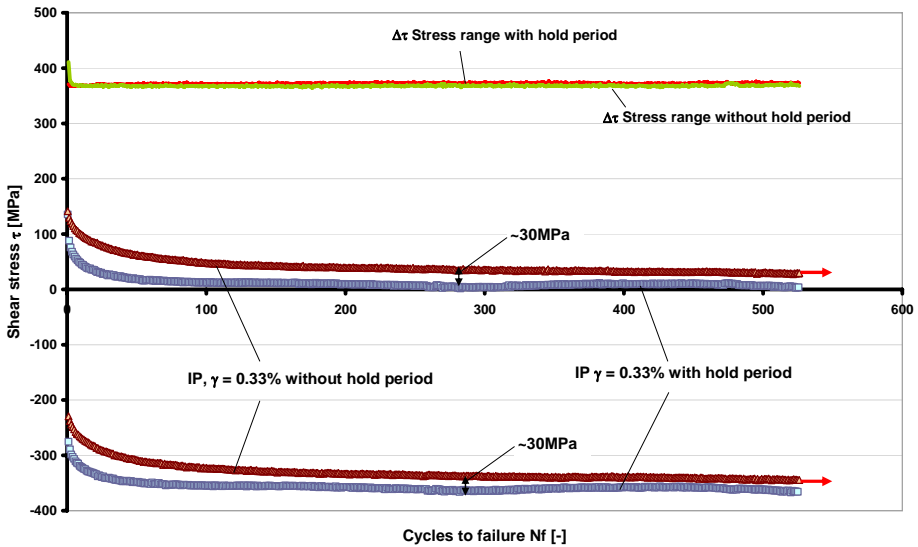


**Figure 3.27:** Diagram of shear stress  $\tau$ , vs.  $N_f$ . This diagram compares two torsional IP TMF tests, both at  $\gamma = 0.33\%$ , one test with a 180 seconds hold period (squares) and the other without a hold period (triangles). The hold period decreases the shear stress by approximately 30MPa in every loading cycle. The fatigue life is reduced by 45% over the non-hold period test. The arrows indicate the test continues beyond this point ( $\gamma = 0.33\%$ ,  $\varepsilon_{eq} = 0.19\%$ ).

The first cycle contained the largest hysteresis loop of the test. At the end of the first cycle, when the strain returns to zero, the loading path has shifted negatively by approximately

75MPa (see Figure 3.26). The difference between  $\tau_{\max}$  at cycle 1 and  $\tau_{\max}$  at  $N_f/2$  is approximately 125MPa ( $\tau_{\max}$  shift). In the negative region of the hysteresis curves, the difference between  $\tau_{\min}$  at cycle 1 and  $\tau_{\min}$  at  $N_f/2$  is approximately 80MPa ( $\tau_{\min}$  shift). In the first half loading cycle during the hold period at  $T_{\max}$ , the shear stress decreases by approximately 50MPa ( $t_{\text{hold}}$  cycle 1), by mid-life it is almost none existent at only about 2MPa over the hold period ( $t_{\text{hold}}$   $N_f/2$ ).

Comparing  $\tau_{\max}$  and  $\tau_{\min}$  data from both  $\epsilon_{\text{eq}}$  0.19% tests, the hold period test has descending shear stress by 30MPa than the test without a hold period. The shear stress ranges for both tests are almost identical (see Figure 3.27).

Similarly, but not as severely as the uniaxial tests, the effects of the 180 seconds hold period also reduces fatigue lifetime by almost one half. The torsional tests also show strain amplitude sensitivity, increasing the strain amplitude by 0.03% decreases fatigue lifetime by a factor of >20. The lifetime reduction is not as severe as it is with the uniaxial hold period tests (see Figure 3.28).

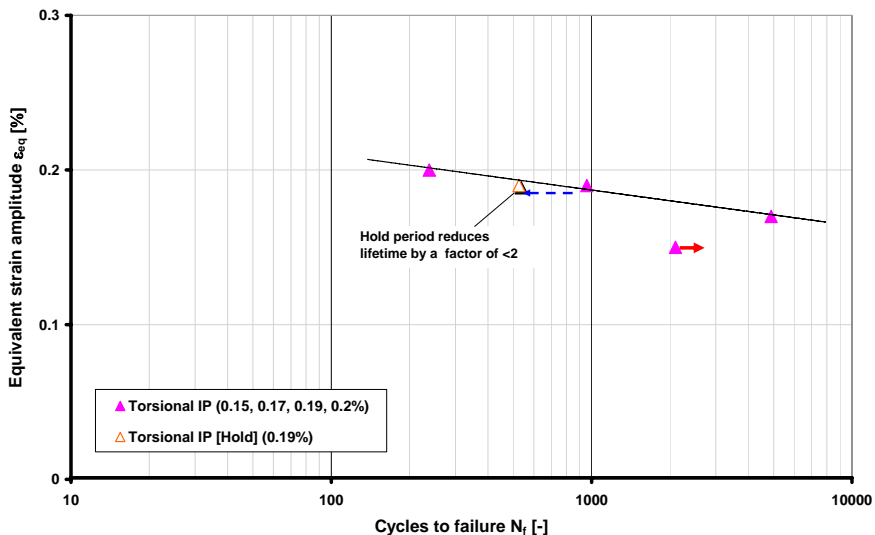


**Figure 3.28:** Torsional IP TMF tests showing the equivalent strain amplitude  $\epsilon_{\text{eq}}$ , vs. cycles to failure  $N_f$ . The greater the strain amplitude the shorter the fatigue lifetimes. Hold period tests reduce lifetimes by a factor of nearly two. The torsional IP TMF lifetimes decrease by a factor of >20 with the increase of the equivalent strain amplitude by 0.03%. The arrow indicates an interrupted test.

### 3.4.3. Axial-torsional TMF tests

The axial-torsional TMF tests are sub-divided into proportional-axial-torsional OP (temperature-strain phase angles  $\varphi_{T-\epsilon} = 180^\circ$ ,  $\varphi_{T-\gamma} = 180^\circ$ ,  $\varphi_{\epsilon-\gamma} = 0^\circ$ ) and non-proportional-axial-torsional OP (temperature-strain phase angles  $\varphi_{T-\epsilon} = 180^\circ$ ,  $\varphi_{T-\gamma} = 90^\circ$ ,  $\varphi_{\epsilon-\gamma} = -90^\circ$ ) modes. The tests are complex and are therefore broken down into their constituent parts of axial loading results followed by the torsional results. The combined equivalent stress results are presented at the end.

### 3. Results

#### Proportional-axial-torsional OP

The axial loading constituent of the proportional-axial-torsional OP TMF test is shown in Figure 3.29. Similar to the uniaxial OP tests, the tensile and compressive stresses ascend with each cycle. The stress range  $\Delta\sigma$ , remains relatively constant throughout the test.

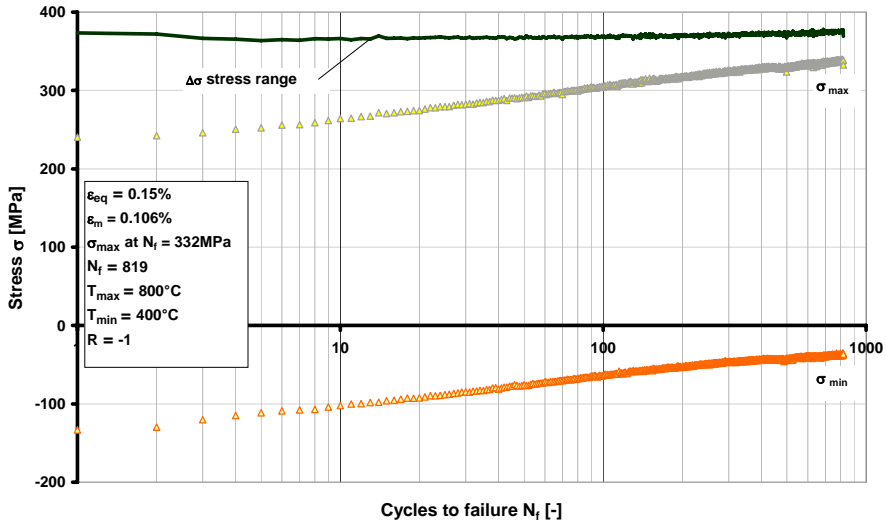


**Figure 3.29:** The proportional-axial-torsional OP TMF test showing axial stress  $\sigma_{max}$ ,  $\sigma_{min}$ , stress range  $\Delta\sigma$ , vs. cycles to failure  $N_f$ .

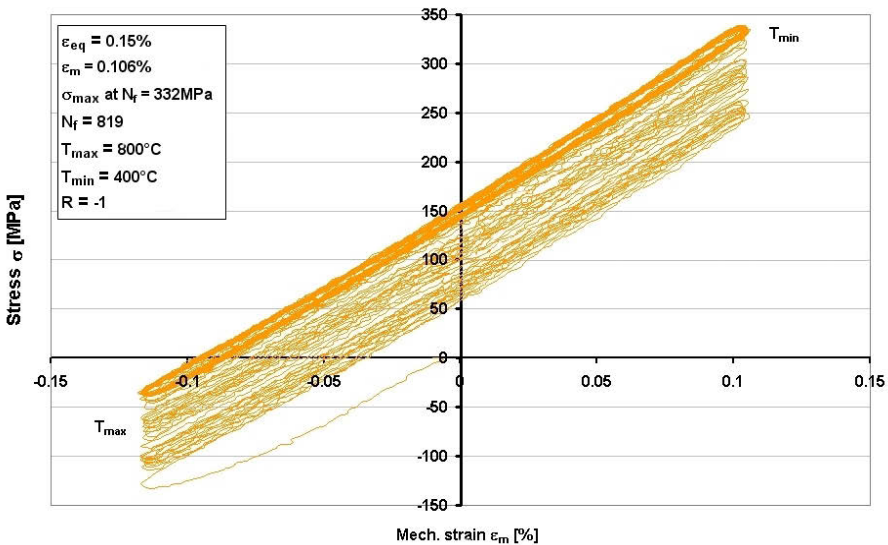


**Figure 3.30:** Axial stress vs. mechanical strain for the proportional-axial-torsional test. The stress-strain cycle curves initially shift positively in stress however before  $N_f/2$ , the stress shifting diminishes.

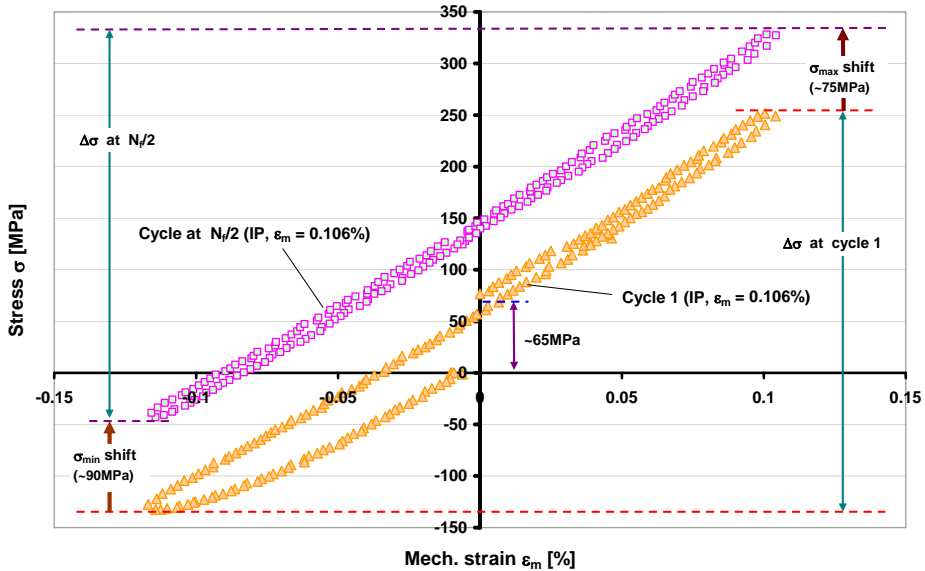


Figure 3.31: The initial loading cycle (triangles) and mid-life (squares) hysteresis curves for the proportional-axial-torsional test from Figure 3.30 ( $\epsilon_m = 0.106\%$  and  $\epsilon_{eq} = 0.15\%$ ).

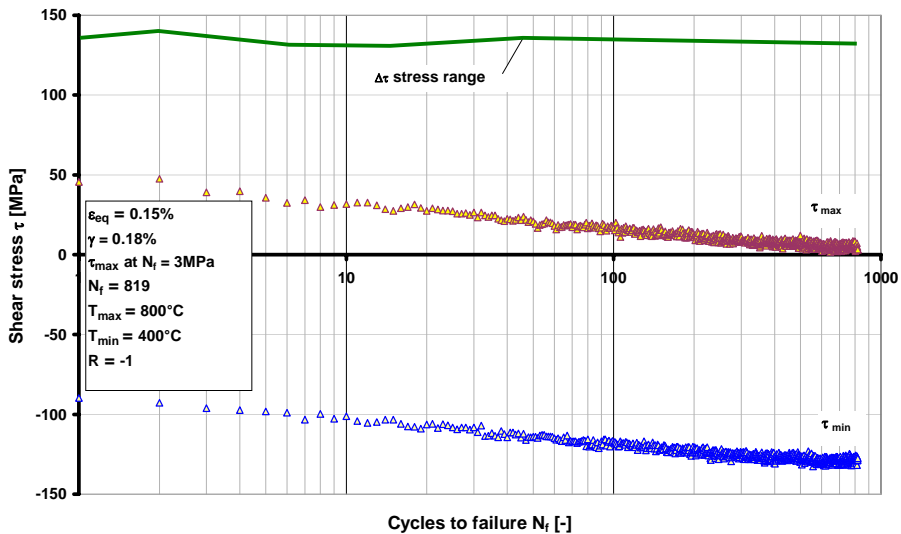


Figure 3.32: The proportional-axial-torsional test showing shear stress  $\tau_{max}$ ,  $\tau_{min}$ , shear stress range  $\Delta\tau$ , vs. cycles to failure  $N_f$ .

The axial stress-strain loading paths differ slightly from both uniaxial OP and IP, in that cyclic unloading paths form wider hysteresis loops than in uniaxial OP. However, the loops are much narrower than uniaxial IP tests (with  $\epsilon_m \geq 0.3\%$ ). Similarly the hysteresis loops also shift positively in stress as seen in uniaxial OP loadings. The first cycle contains the

### 3. Results

largest hysteresis loop of the test and this occurs during the initial loading in the first half cycle. At the end of the first cycle, when the strain returns to zero, the unloading path has shifted positively by approximately 65MPa (see Figure 3.31). At  $N_f/2$ , this positive shift increases tensile stress by 75MPa and reduces the compressive stress by 90MPa respectively.

The torsional loading in the proportional-axial-torsional TMF test results are shown in Figure 3.32. There are some similarities to the pure torsional TMF IP tests such as the shear stresses  $\tau_{\max}$ , and  $\tau_{\min}$  descend with each cycle. The shear stress range  $\Delta\tau$ , remains fairly constant despite some small fluctuation, there is no obvious cyclic softening or hardening taking place.

Comparable to the pure torsional test, the hysteresis curves do not overlap one another after each loading cycle, the loading cycles shift in negative shear stress (see Figure 3.33). However, this shift diminishes with the test progression and the loading unloading paths become overlaid on one another. Figure 3.34 shows the first cycle and the mid-life cycle ( $N_f/2$ ) of this test.

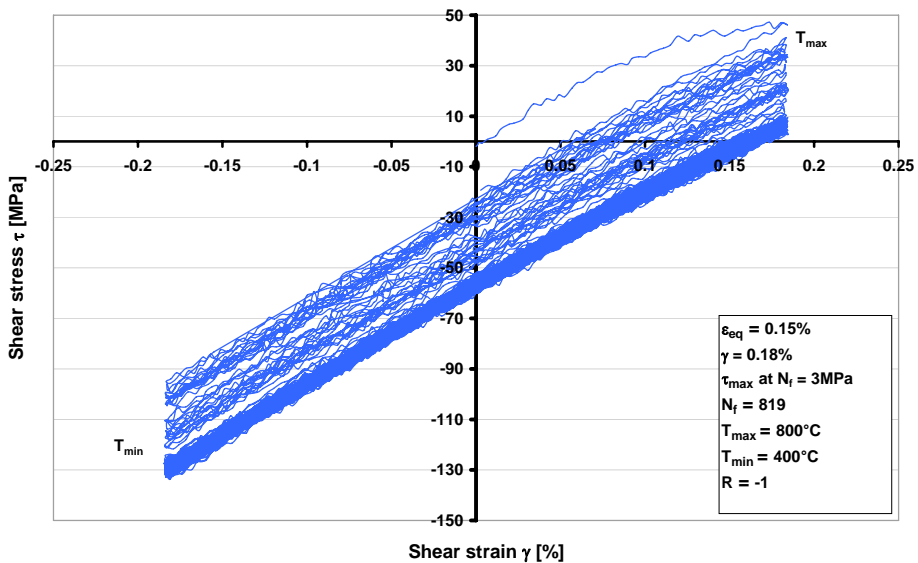


**Figure 3.33:** Shear stress vs. shear strain for proportional-axial-torsional test. As with the pure torsional tests the stress-strain cycle hysteresis curves do not overlap one another instead they shift negatively in stress. This shift diminishes with the test progression and the loading unloading paths become overlaid with one another.

The first half cycle again contains the largest hysteresis loop of the test and this was only during the initial loading in the first half cycle. At the end of the first cycle, when the strain returns to zero, the loading path shifts negatively by approximately 20MPa (see Figure 3.34). At  $N_f/2$ , the negative shift with each cycle has increased shear stress at  $\tau_{\min}$  by 30MPa and reduces  $\tau_{\max}$  and 35MPa.



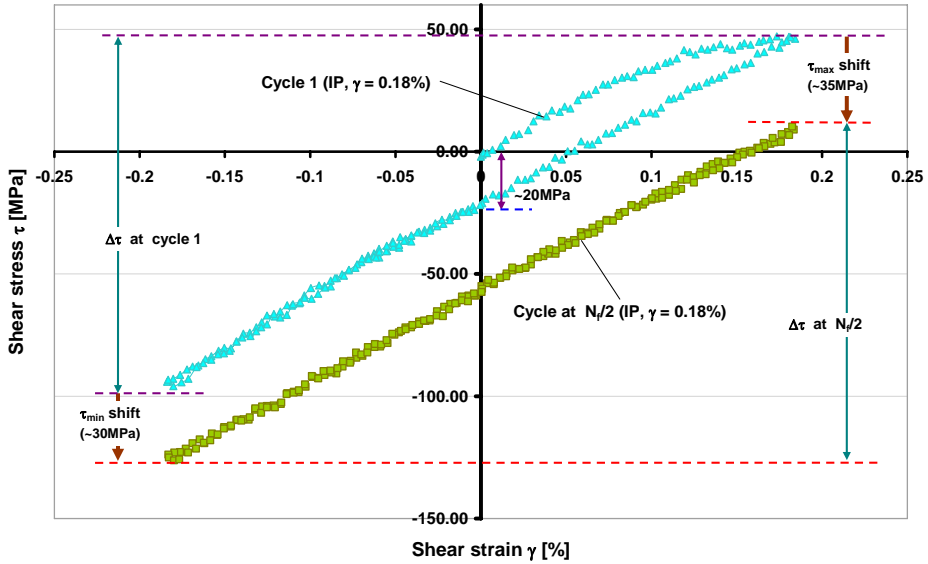


**Figure 3.34:** The initial loading cycle (triangles) and mid-life (squares) hysteresis curves for a proportional-axial-torsional test. ( $\gamma = 0.18\%$ ,  $\varepsilon_{\text{eq}} = 0.15\%$ ).

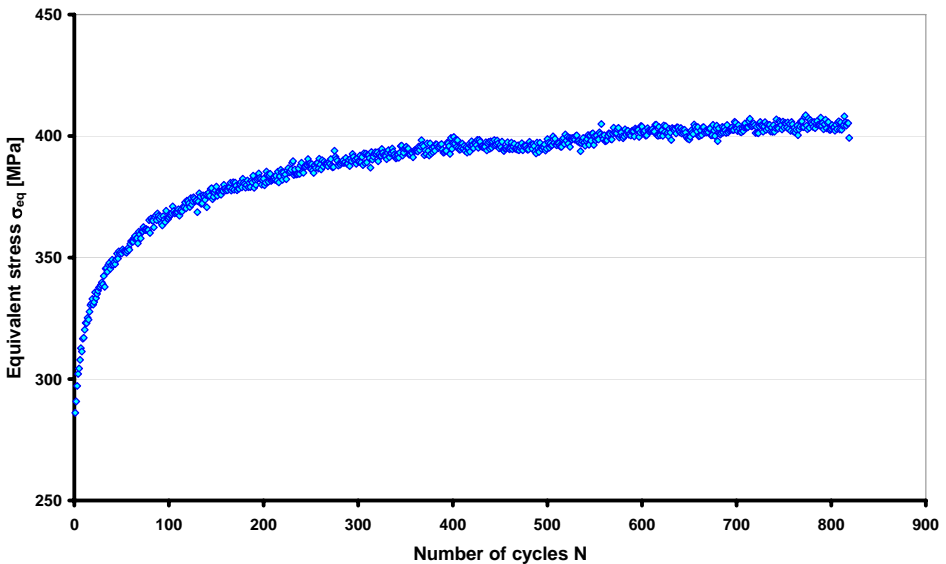


**Figure 3.35:** Maximum equivalent stress  $\sigma_{\text{eq max}}$  calculated at  $T_{\min}$  vs.  $N$  of the proportional-axial-torsional OP TMF ( $\varepsilon_{\text{eq}} = 0.15\%$ ).

By calculating the Mises equivalent stress  $\sigma_{\text{eq}}$  (Eq 2.3), it is possible to combine axial and torsional data. The maximum equivalent stress is always found at  $T_{\min}$  and the development of  $\sigma_{\text{eq max}}$  with number of cycles to failure is shown in see Figure 3.35. At  $T_{\min}$  the axial

### 3. Results

stress is at maximum and the magnitude of the shear stress component is also at maximum. At mid-life this proportional-axial-torsional test has a  $\sigma_{eq \max}$  of 395MPa, comparing this with the  $\sigma_{eq \max}$  value of a torsional test performed at the same equivalent strain amplitude, the proportional-axial-torsional OP test is lower by approximately 80MPa and 15MPa lower than a uniaxial OP test. However, the lifetime of this proportional-axial-torsional test is less than half that of the torsional test and three quarters that of a uniaxial test.

#### ***Non-proportional-axial-torsional OP***

The axial stress-strain results of the non-proportional-axial-torsional OP TMF test are shown in Figure 3.36.

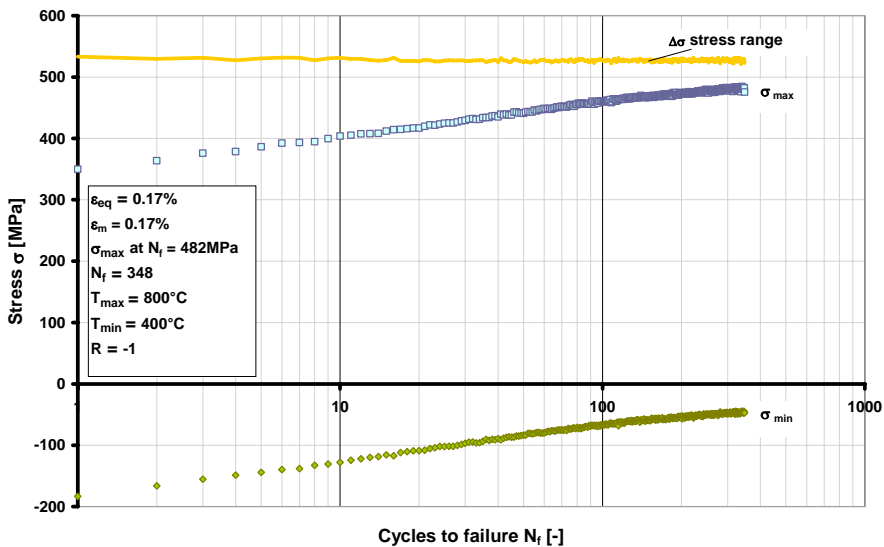


**Figure 3.36:** The non-proportional-axial-torsional OP TMF test showing axial stress  $\sigma_{max}$ ,  $\sigma_{min}$ , stress range  $\Delta\sigma$ , vs. cycles to failure  $N_f$ .

This test also reveals some similarities with the uniaxial OP and proportional-axial-torsional tests already described, in that the peak tensile stress  $\sigma_{max}$ , increases with each cycle, and the peak compressive stress  $\sigma_{min}$ , decreases with each cycle. The stress range  $\Delta\sigma$ , remains constant throughout the test (see Figure 3.36).

The axial stress-strain loading paths are similar to the proportional-axial-torsional test in that the hysteresis loops are very narrow, the loading-unloading paths follow almost exactly the same course are similar to those seen in the uniaxial OP tests (see Figure 3.38). As previously observed the first cycle contains the largest hysteresis loop of the test. At zero strain the unloading path of the first cycle increases by approximately 120MPa in stress.

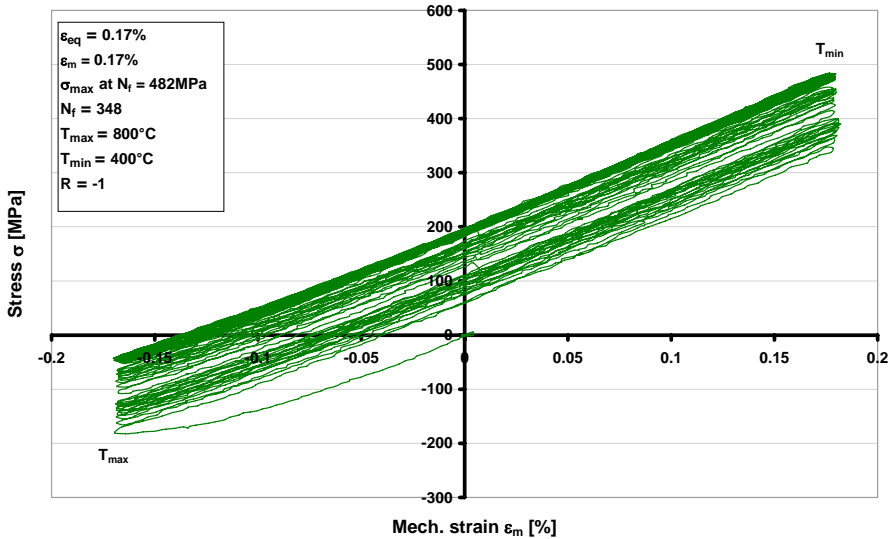


**Figure 3.37:** Complete axial stress-strain hysteresis curves for the non-proportional-axial-torsional test. Peak tensile loading is at  $T_{min} = 400^{\circ}C$ . The stress-strain cycle curves initially shift positively however before  $N_f/2$  the shift in the stress diminishes.

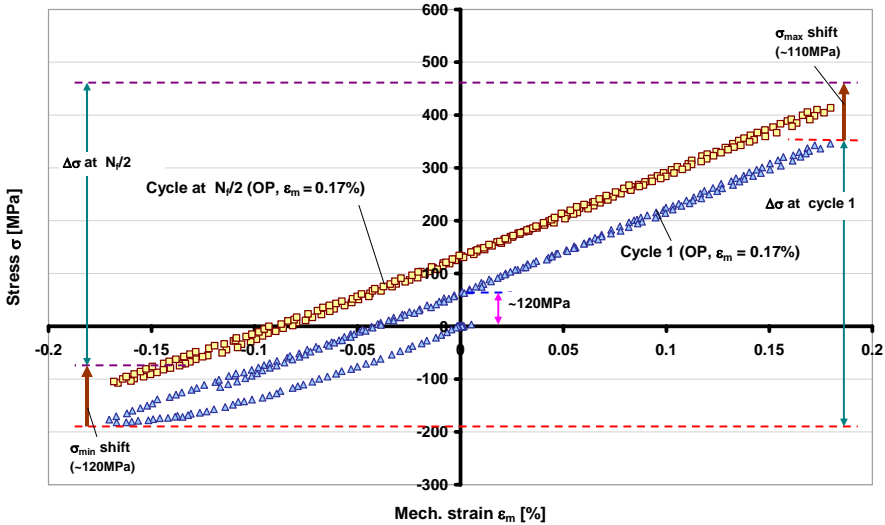


**Figure 3.38:** The initial loading cycle (triangles) and mid-life (squares) hysteresis curves for the axial stress-strain part of the non-proportional-axial-torsional test from Figure 3.37 ( $\epsilon_m = \epsilon_{eq} = 0.17\%$ ).

The torsional loading of the non-proportional-axial-torsional test results are shown in Figure 3.39.

### 3. Results

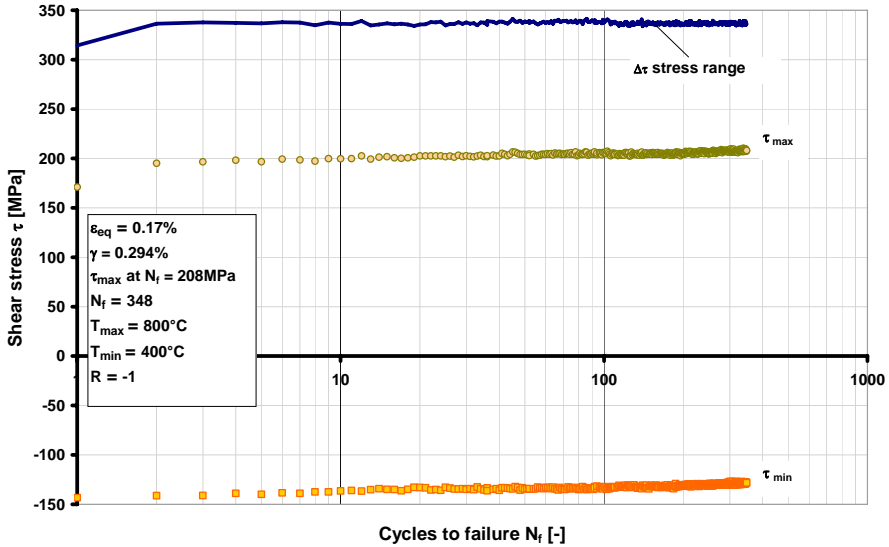


**Figure 3.39:** The non-proportional-axial-torsional OP TMF test showing shear stress  $\tau_{max}$ ,  $\tau_{min}$ , shear stress range,  $\Delta\tau$ , vs. cycles to failure  $N_f$  ( $\gamma = 0.294\%$ ,  $\epsilon_{eq} = 0.17\%$ ).

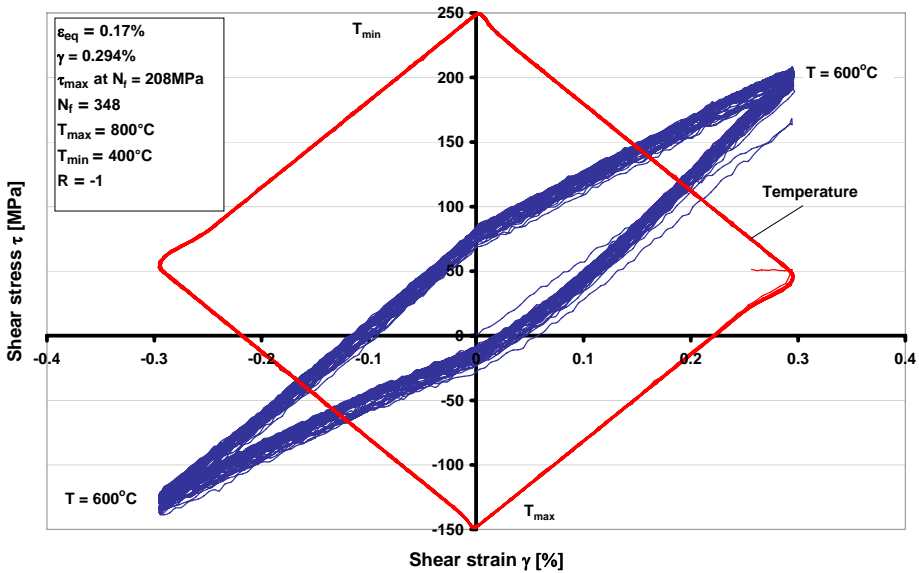


**Figure 3.40:** Shear stress vs. shear strain for non-proportional-axial-torsional test. The wide centres of the hysteresis loops, at zero strain, are caused by the raise or decrease in temperature. Clearly seen here are the stress-strain paths overlapping one another and a small amount of positive shift in stress. The temperature path is  $90^\circ$  off-set to the shear loading hence the diamond temperature path.

A marked difference with previous tests that include shear loading is that in this test the positive shear stress,  $\tau_{max}$ , increases very slightly with each cycle. This is because peak shear loading occurs during the mid temperature cycle, i.e.,  $600^\circ\text{C}$ , this being less

damaging than if peak tensile loading is at  $T_{\min}$ , but more damaging than if at  $T_{\max}$ . The shear stresses  $\tau_{\max}$  and  $\tau_{\min}$ , are slightly ascended over each loading cycle. No cyclic softening or hardening has occurred, as the shear stress range  $\Delta\tau$  is constant.

The temperature being  $90^\circ$  off-set to the shear strain means that at zero shear strain the temperature is either at  $T_{\max}$  or  $T_{\min}$ . The subsequent stress reaction to the change in temperature causes a slight deviation in the corresponding loading-unloading path. When the loading changes from positive to negative or vice versa, the stress-strain hysteresis path abruptly changes direction, this gives the hysteresis loops the appearance of a flattened rhombus (see Figure 3.40). However, the main consideration is the loading-unloading path which remains remarkably consistent, in fact they are almost superimposed over one another and stress shift is minimal, just slightly positive (as opposed to the previous torsional test all having lower shifts). Neither cyclic softening, hardening nor additional hardening has occurred as both axial and shear stress ranges are constant over the complete test.

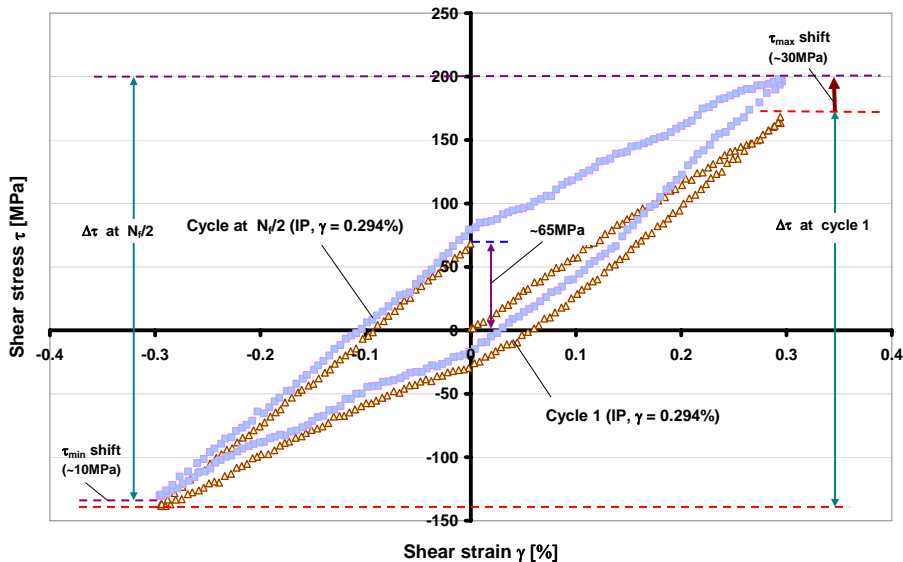


**Figure 3.41:** The initial loading cycle (triangles) and mid-life (squares) hysteresis curves for the non-proportional-axial-torsional test. The small differences in stress-strain paths from cycle 1 to the cycle at  $N_f/2$  are very obvious as they are almost superimposed over one another. There is a small amount of positive stress shift most of which occurs at cycle 1 ( $\gamma = 0.294\%$ ,  $\epsilon_{eq} = 0.17\%$ ).

Figure 3.41 shows the first cycle and the mid-life cycle ( $N_f/2$ ). The first half cycle contained the smallest hysteresis loop of the test because the initial temperature of the first loading was at  $T_{\max}$ , i.e. the least plastic deformation. On returning to zero strain at the end of the first cycle of the loading path, the stress has increased by approximately 65MPa. Overall shift in the shear stress in this test is almost negligible, most occurs in the first loading cycle.

### 3. Results

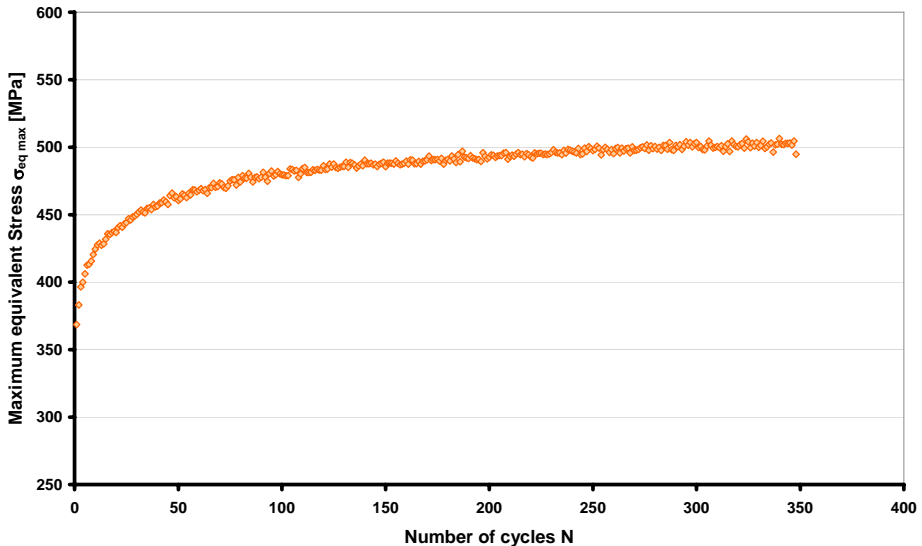


**Figure 3.42:** Maximum equivalent stress  $\sigma_{eq\ max}$  calculated at  $T_{min}$  vs.  $N$  from the non-proportional-axial OP TMF ( $\epsilon_{eq} = 0.17\%$ ).

The maximum Mises equivalent stress  $\sigma_{eq\ max}$ , is employed to represent the combined axial-torsional loading (see Figure 3.42). The  $\sigma_{eq\ max}$ , is always found at  $T_{min}$ , similar to the proportional OP loading. At  $T_{min}$  the axial stress is at maximum. Although  $\tau$  is max at  $600^{\circ}\text{C}$ , the magnitude of the shear stress at  $T_{min}$  is high enough to result in the maximum equivalent stress at this point. As with the proportional-axial-torsional test the  $\sigma_{eq\ max}$ , is also seen to increase with  $N$  due to the mounting axial stress constituent.

A hold period test was also implemented with a non-proportional-axial-torsional test, however the test was conducted under a lower strain amplitude ( $\epsilon_{eq} = 0.15\%$ ) than that for the non-hold period test. The axial stress-strain results of the non-proportional-axial-torsional axial OP TMF test are shown in Figure 3.43.

Similar to the non-proportional-axial-torsional tests already described above the peak tensile stress  $\sigma_{max}$ , increases with each cycle, and the peak compressive stress,  $\sigma_{min}$ , decreases with each cycle. The stress range,  $\Delta\sigma$ , is reasonably constant throughout the test. The hysteresis loops shift positively in stress as seen previously in uniaxial OP loadings (see Figure 3.44).

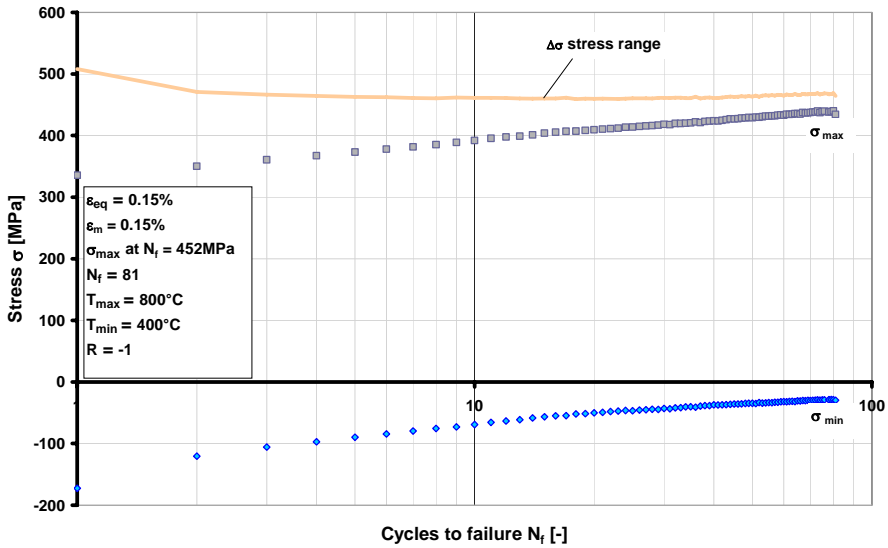


**Figure 3.43:** The non-proportional-axial-torsional OP TMF test with hold period showing axial stress  $\sigma_{max}$ ,  $\sigma_{min}$ , stress range  $\Delta\sigma$ , vs. cycles to failure  $N_f$ , hold period.

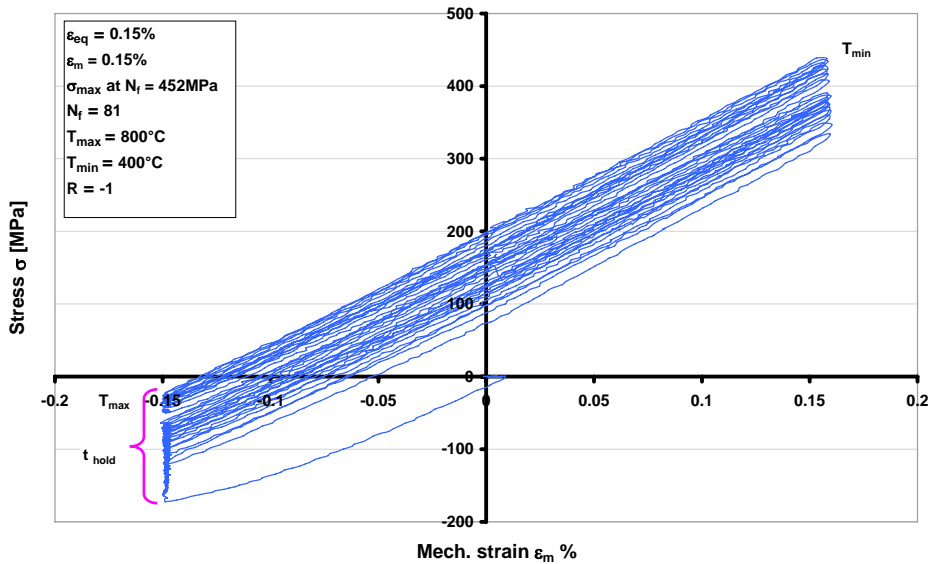


**Figure 3.44:** Complete axial stress-strain hysteresis curves vs. temperature for the non-proportional-axial-torsional test with 180 seconds hold period. The stress-strain hysteresis curves shift positively in stress.





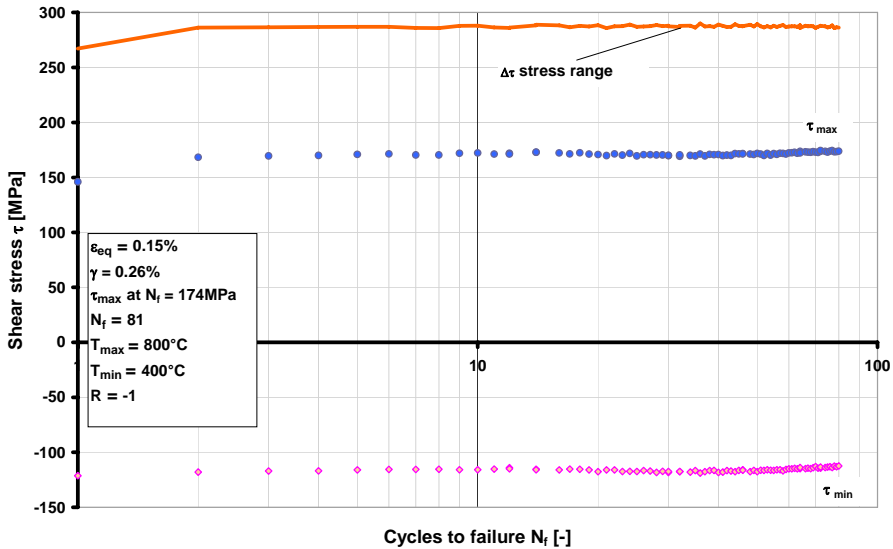


**Figure 3.46:** The proportional-axial-torsional OP TMF test with 180 seconds hold period showing shear stress  $\tau_{max}$ ,  $\tau_{min}$ , shear stress range  $\Delta\tau$ , vs. cycles to failure  $N_f$ .

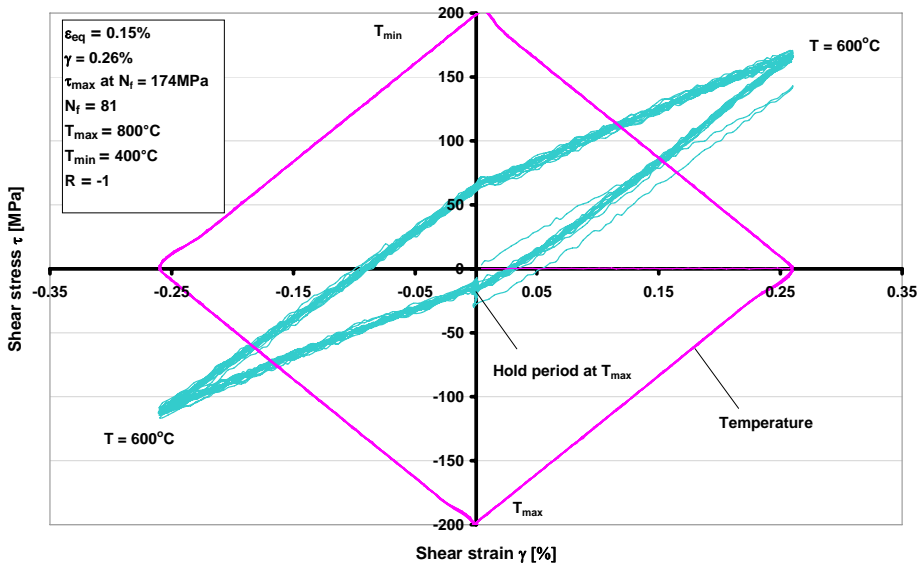


**Figure 3.47:** Shear stress vs. shear strain hysteresis curves for non-proportional-axial-torsional test with 180 seconds hold period. The hold period (indicated on the diagram) takes place at  $T_{max}$  mid point of the shear unloading.

Figure 3.49 shows the first cycle and the mid-life cycle ( $N_f/2$ ). Similar to the non-hold period test above, the first half cycle contains the smallest hysteresis loop of the test because the initial temperature of the first loading was at  $T_{max}$ . This singular loading curve stands out very clearly in Figure 3.47. On returning to zero strain at the end of the first cycle, the stress

### 3. Results

has increased by approximately 60MPa. Overall shift in the shear stress in this test is almost negligible, most occurs in the first loading cycle (positive by approximately 20MPa). The effect of the hold period is hardly noticeable here. Occurring at  $T_{max}$  the stress increases by approximately 10MPa in the first cycle, at  $N_f/2$  it increases by about 5MPa over the hold period (similar to the axial part at mid-life).

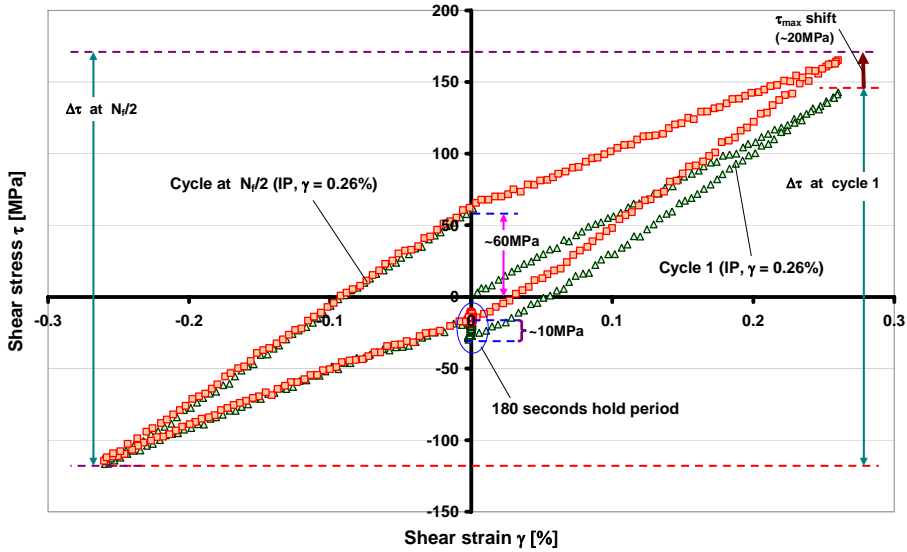


**Figure 3.48:** The initial loading cycle (triangles) and mid-life (squares) hysteresis curves for the non-proportional-axial-torsional test shown in Figure 3.47. There appears to be minimal shift in stress in this test ( $\gamma = 0.26\%$ ,  $\epsilon_{eq} = 0.15\%$ ).

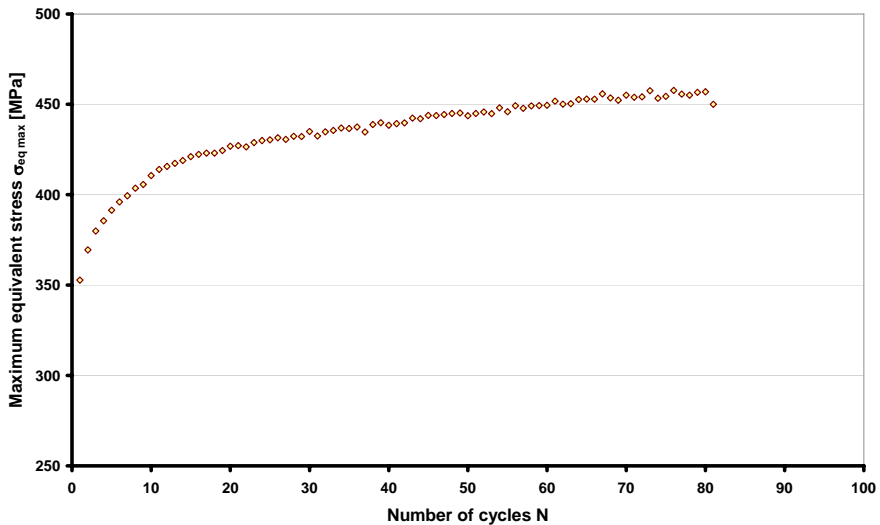


**Figure 3.49:** Maximum equivalent stress  $\sigma_{eq\ max}$  calculated at  $T_{min}$  vs.  $N$  of the non-proportional-axial-torsional OP TMF with hold period ( $\epsilon_{eq} = 0.15$ ).

Figure 3.49 shows the maximum equivalent stress  $\sigma_{eq, max}$ , of the combined axial-torsional damage. The calculation was performed as with the non-proportional axial torsional test without hold period. At  $N_f/2$   $\sigma_{eq, max}$  is 438MPa, this is 50MPa (at  $N_f/2$ ) less than the non-proportional-axial test without a hold period performed at slightly lower equivalent strain amplitude. The lifetime of this test is a factor of >4 less than that of the test without a hold period.

### 3.4.4. Summary of thermo-mechanical fatigue behaviour

Table 3.5 summarises the complete test results with respect to testing parameters such as the test type, the equivalent strain amplitude,  $\epsilon_{eq}$ , the equivalent maximum stress  $\sigma_{eq, max}$  at  $N_f/2$ , the maximum axial stress/shear stress  $\sigma_{max}/\tau_{max}$  at  $N_f/2$ , the minimum axial stress/shear stress  $\sigma_{min}/\tau_{min}$  at  $N_f/2$ , the maximum axial stress/shear stress  $\sigma_{max}/\tau_{max}$  at  $N_f$  (at failure), the minimum axial stress/shear stress  $\sigma_{min}/\tau_{min}$  at  $N_f$  (at failure), the mean stress  $\sigma_m$  at  $N_f/2$ , Cycles at mid-life  $N_f/2$ , Cycles at failure  $N_f$ , and temperature at failure. The hold period tests are additionally highlighted.

**Table 3.5:** Complete test results matrix showing the equivalent strain amplitude,  $\epsilon_{eq}$ , the equivalent maximum stress  $\sigma_{eq, max}$  at  $N_f/2$ , the maximum axial stress/shear stress  $\sigma_{max}/\tau_{max}$  at  $N_f/2$ , the minimum axial stress/shear stress  $\sigma_{min}/\tau_{min}$  at  $N_f/2$ , the maximum axial stress/shear stress  $\sigma_{max}/\tau_{max}$  at  $N_f$ , the minimum axial stress/shear stress  $\sigma_{min}/\tau_{min}$  at  $N_f$ , the mean stress  $\sigma_m$  at  $N_f/2$ , Cycles to failure  $N_f$ , and temperature at failure. The test temperature range is  $T_{min} = 400^\circ\text{C}$ ,  $T_{max} = 800^\circ\text{C}$ . Hold period tests are highlighted.

Test Type	$\epsilon_{eq}$ [%]	$\sigma_{eq, max}$ at $N_f/2$ [MPa]	$\sigma_{max}/\tau_{max}$ at $N_f/2$ [MPa]	$\sigma_{min}/\tau_{min}$ at $N_f/2$ [MPa]	$\sigma_{max}/\tau_{max}$ at $N_f$ [MPa]	$\sigma_{min}/\tau_{min}$ at $N_f$ [MPa]	$\sigma_m$ at $N_f/2$ [MPa]	Total $N_f$	Fail Temp [°C]
Uniaxial (OP)	0.15	412	412	-55	428	-46	179	1076	408
"	0.17	440	440	-71	456	-60	185	756	406
"	0.20	522	522	-82	538	-66	220	257	599
"	0.30	671	671	-242	695	-212	215	8	402
(Hold period)	0.15	453	453	-15	456	-10	219	159	411
Uniaxial (IP)	0.30	795	74	-795	74	-795	-361	3656	-
"	0.50	946	256	-946	208	-986	-345	1546	779
"	0.55	916	342	-916	299	-964	-287	907	789
"	0.70	990	376	-990	358	-1017	-307	572	704
(Hold period)	0.55	966	239	-966	208	-610	-364	209	597
Torsional (IP)	0.15	479	21	-274	21	-274	288	2098	-
"	0.17	511	24	-297	19	-300	255	4896	747
"	0.19	592	30	-342	26	-331	291	958	421
"	0.20	612	39	-353	32	-360	294	238	403
(Hold period)	0.19	631	4	-364	4	-364	338	526	410
Prop. axial-tors. (OP)	0.15	395	330 /11	-44 /-136	333 /3	-36 /-138	142	819	407
Non-prop. axial-tors. (OP)	0.17	491	470 /206	-58 /-130	482 /208	-47 /-128	207	348	407
(Hold period)	0.15	438	424 /171	-37 /-118	434 /175	-30 /-113	193	81	403

The fatigue lifetimes are strongly dependant on the strain amplitude and temperature-strain phase. Generally, within each test type, the higher the strain amplitude the corresponding lifetime is shorter. Figure 3.50 depicts the Mises equivalent strain amplitude vs.  $N_f$ , here the

### 3. Results

effects of higher strain amplitude can be seen in regard to lifetime and how uniaxial IP tests despite higher  $\epsilon_{eq}$  live longer than all other tests.

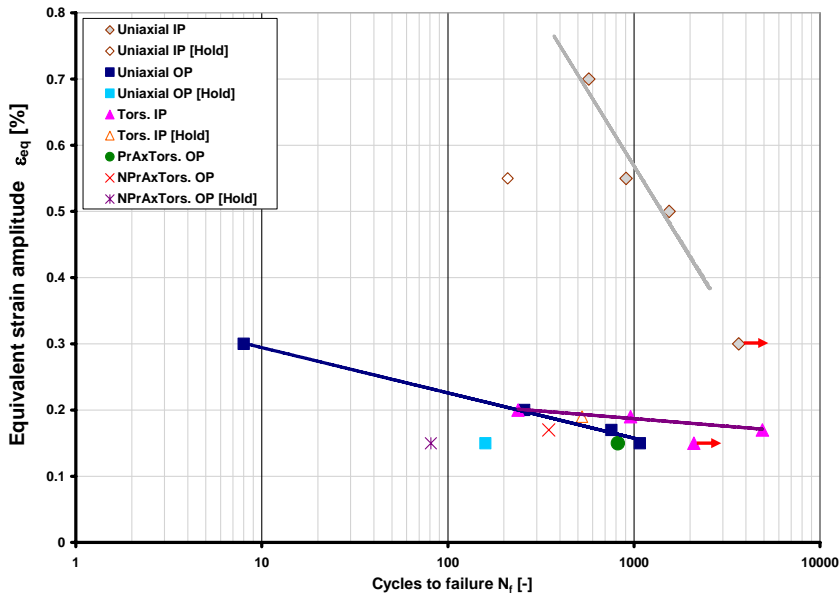


**Figure 3.50:** Equivalent strain amplitude vs. Number of cycles to failure,  $N_f$ .

In Figure 3.51 the data are plotted as Mises equivalent stress amplitude,  $\sigma_{eq, a}$ , within a stabilised cycle (i.e. the cycle at  $N_f/2$  for tests with regular  $N_f$  or the last complete cycle for interrupted tests) vs. number of cycles to failure  $N_f$ . This data representation allows the observed difference in lifetime between uniaxial and multiaxial tests to be explained. Figure 3.51 illustrates that the non-proportional axial-torsional OP test at the same equivalent strain amplitude as the uniaxial OP test (0.17%), has a lower lifetime due to the higher equivalent stress amplitude (491MPa as compared to 440MPa). It also becomes clear that at the same lifetimes uniaxial IP tests have higher equivalent strain amplitude and equivalent stress amplitude than the torsional tests. The mean stress is zero under torsional loading.

Under TMF IP loading the fatigue lifetimes are longer than under TMF OP loading, because under IP loading the maximum tensile stresses are lower and compressive stresses are higher within a cycle. The temperature-strain phase effects are seen as critical criteria for lifetime duration [138]. When comparing the temperature at which the specimen failed with its fatigue lifetime, it is observed that for any test, which includes axial loading, failure always occurs under tension. For uniaxial OP and axial-torsional tests this is below the BDTT, for uniaxial IP tests this is above the BDTT. The torsional specimens fractured either above or below BDTT because of the symmetry of torsional loading.

From the different types of test performed in this study there are several outstanding characteristics that affect the fatigue lifetime of this material:

- The strain amplitude has a strong influence on the fatigue lifetime, a minor increase reduces lifetime considerably.

- The sensitivity to the test type also has a strong influence on the fatigue lifetime. Uniaxial OP tests have a shorter life time than the uniaxial IP tests
- Torsional IP loading, has a longer lifetime than the uniaxial OP loading at the same Mises equivalent stress amplitude, as the mean stress is zero.
- The non-proportional-axial OP test has a shorter lifetime than the uniaxial OP test with the same Mises equivalent mechanical strain amplitude.
- Hold periods reduce lifetimes in all types of test.

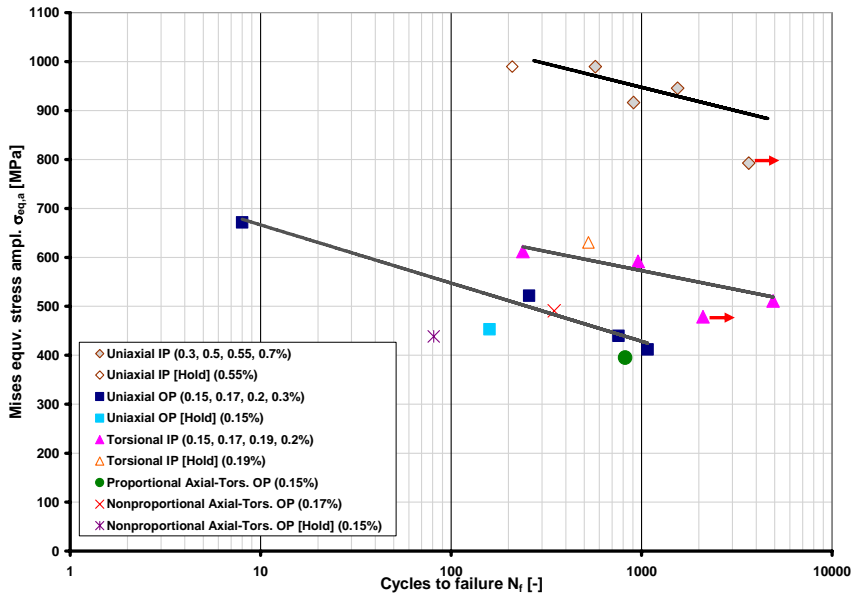


**Figure 3.51:** Mises equivalent stress amplitude within a stabilised cycle vs. number of cycles to failure.  $N_f$ . The Mises equivalent mechanical strain amplitude is given in parentheses for each test of the corresponding type. IP = thermal-mechanical in-phase. OP = axially thermal-mechanical 180° out-of-phase. Lifetimes of interrupted tests are indicated by arrows.

### 3.5. Fractography

Examination of the fracture surface is implemented to gain important information about the nature of fracture mechanisms. The images presented here are those which demonstrate notable features. The fractographic results are divided into the different test types. Hold period specimens are covered separately within the test category type. The terminology used in the text to describe the appearances of the fracture surfaces are those used according to the *ASM Handbook Vol. 12, Fractography* [139].

**Uniaxial OP specimens:** The uniaxial OP specimens all fractured perpendicular to the external stress, resulting in a 90° separation of the specimen into two complete halves. A typical fracture surface of the uniaxial OP TMF specimen is illustrated in Figure 3.52.

Fatigue, being a cyclic and time-dependent process, can be separated into various stages with each stage exhibiting different features. After a certain number of cycles, a crack will begin to initiate at the region of the greatest stress concentration, this is termed as stage I fatigue. The crack will grow in length and direction perpendicular to the applied stress with

### 3. Results

continued cycling. This crack propagation is known as stage II fatigue. Finally, stage III fatigue is the unstable fast fracture caused by overload [139].

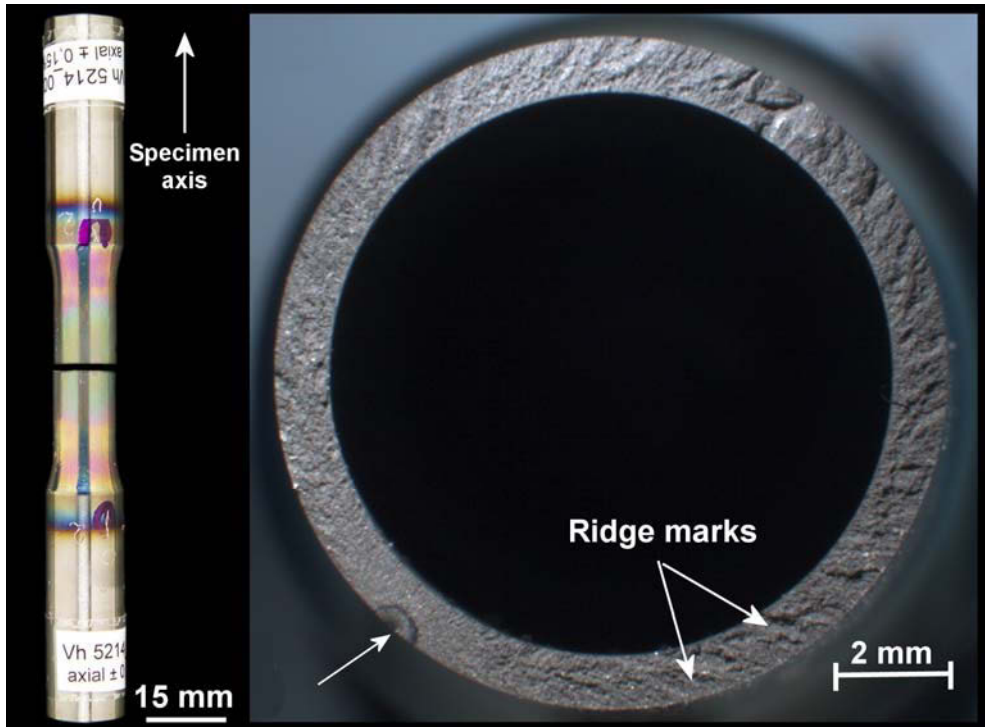


**Figure 3.52:** Light microscopic (LM) view of the uniaxial OP TMF specimen ( $\epsilon_{eq} = 0.15\%$ ). This is typical of the uniaxial OP specimens which all fractured perpendicular to the external stress, resulting in a  $90^\circ$  separation of the specimen. The fracture surface of one half of the specimen is shown on the right. The fracture initiation site can be identified by small pits in the material surface (indicated by the arrow) and the microcrack propagation area identified by the semi-circular oxidised zone on the fracture plane. Also visible are the ridge marks of final fracture.

Macroscopically, the crack initiation sites are clearly visible on the specimen's outer surface by small pits which coincide with the attachment location of the thermocouple to the specimen. On the fracture plane the crack initiation sites are visible by an abraded area which is always adjacent to the pits on the outer surface. In the majority of cases the region of crack propagation can be identified by a small semi-circular (fan-shaped) discoloured (oxidised) zone on the plane of fracture situated on the outer surface of the specimen (see Figure 3.53). Around this oxidised zone, approximately 1mm either side, the surface is fairly flat before the topography takes the form of ridge marks. These ridge marks are initially rough, becoming smoother further from the crack propagation zone.

The fan-shaped oxidised area is caused by stable crack growth exposing the material to hot air as it advances progressively into the material. This oxidised area varies in size between specimens. The smallest observed penetrates from the outer specimen wall by approximately  $200\mu\text{m}$ , the largest by approximately  $400\mu\text{m}$ . These crack propagation areas tend to be larger with specimens that were tested at the lowest strain amplitude.

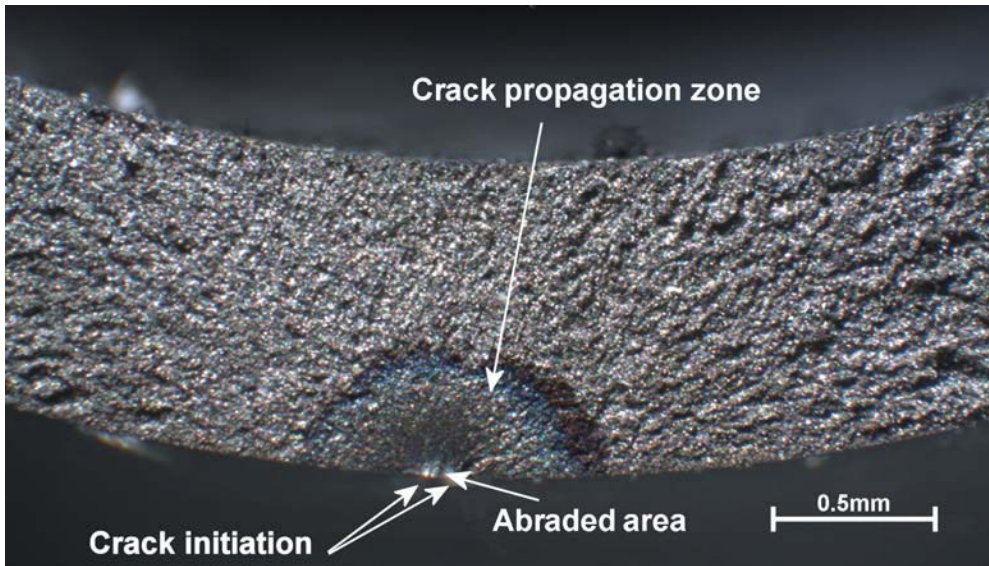


**Figure 3.53:** Macrograph of the crack initiation site. On the outer surface pits caused by the thermocouple attachment are indicated by the arrows. The fan-shaped oxidised crack propagation zone in this example penetrates approximately  $400\mu\text{m}$  into the specimen from the crack initiation site on the outer surface. Ridge marks can also be seen radiating out away from the crack propagation zone ( $\epsilon_{\text{eq}} = 0.15\%$ ) (LM).

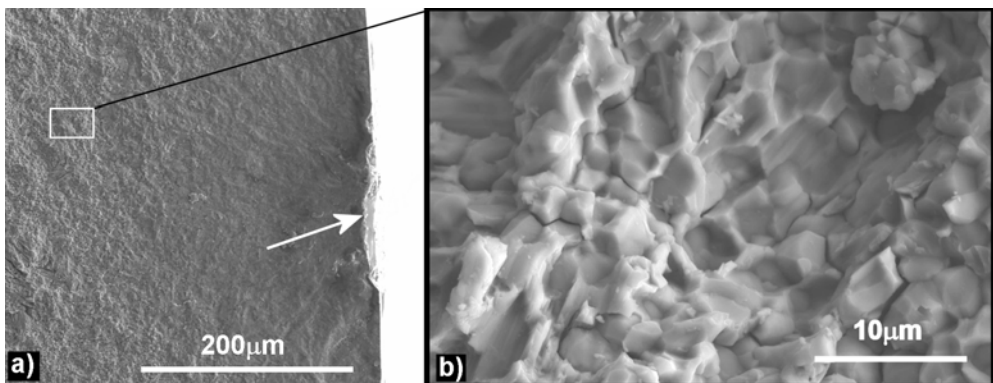


**Figure 3.54:** Micrographs of the crack initiation site. a) The damaged surface caused by the thermocouple can be seen at the right centre of the image (indicated by the arrow). b) The area indicted by the square in (a) within in the unstable crack growth region under higher magnification clearly shows the intergranular decohesion and secondary cracks along grain boundaries ( $\epsilon_{\text{eq}} = 0.15\%$ ) (SE). Images courtesy of Janine Pfetzing, Ruhr-University Bochum.

The uniaxial OP microstructures were subjected to further fractographic investigation using the SEM (see Figure 3.54). Most obvious are the voids left by decohesion of whole grains (globular  $\gamma$ -grains) an indication of intergranular fracture. Intergranular fracture, also referred to as decohesive rupture or grain-boundary separation, is caused when the boundary surrounding the grain fractures, separating the grain from its neighbour. This is a phenomenon associated with high temperatures and brittle solids. The high temperature

### 3. Results

increases the thermal stress by the thermal contraction mismatch of adjacent grains causing the boundaries to crack [139], [60]. The intergranular fracture is such a strong feature in the uniaxial OP microstructures that the grain shapes are clearly defined by their former impressions. Secondary cracks are also visible along grain boundaries (see Figure 3.54).

The fracture surfaces were further investigated in longitudinal section to investigate the presence of any sub-surface secondary cracks or outer and inner surface cracks. Figure 3.55a, b and c, shows the fracture surface of a uniaxial OP specimen.

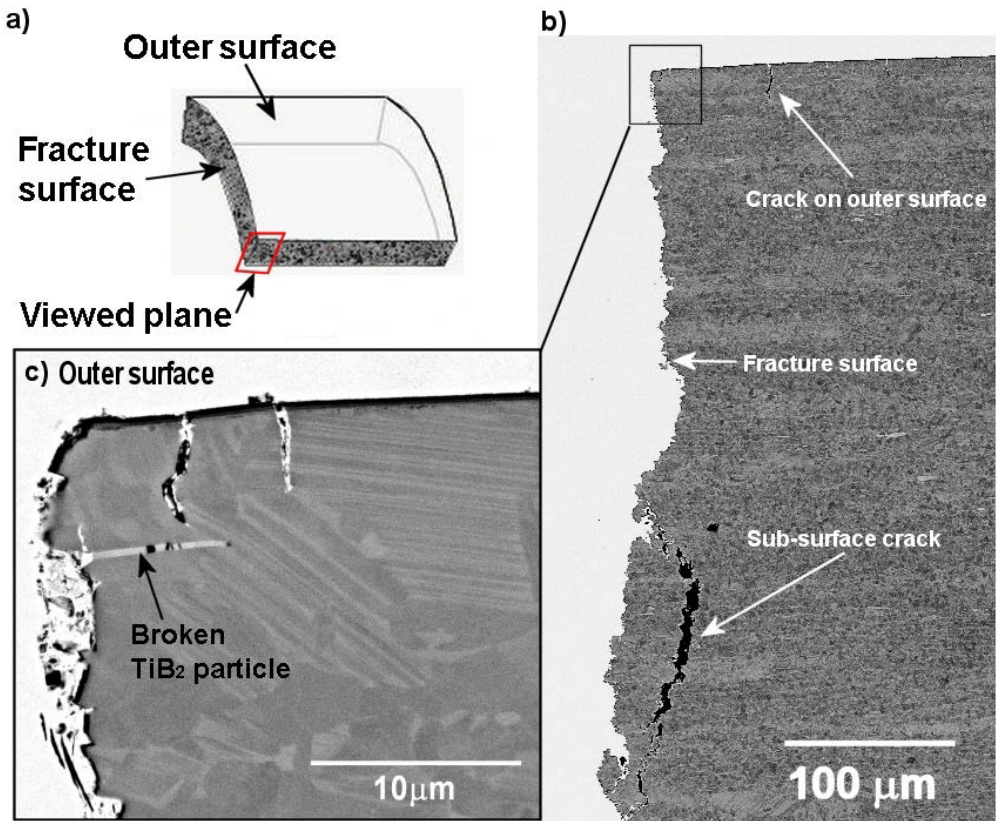


**Figure 3.55:** Longitudinal section of a fractured uniaxial OP TMF specimen ( $\epsilon_{eq} = 0.15\%$ ). a) Schematic diagram showing the approximate location of the image in (b) with respect to the specimen orientation. b) The fracture surface is uneven and has some sub-fracture-surface secondary cracks and outer surface cracks close to the fracture surface. c) A higher magnified view of the left top corner of (b) showing the outer surface cracks some 5-10 $\mu\text{m}$  in length. The crack on the right appears to be translamellar (BSE).

Observed here is a large sub-surface secondary crack, approximately 120 $\mu\text{m}$  in length and 5 $\mu\text{m}$  wide, at the centre of the fracture (Figure 3.55b). There are also smaller cracks (approx. 20 $\mu\text{m}$ ) penetrating from the outer surface close to the fracture surface. The inner wall surface is, however, void of cracks. The image in Figure 3.55c is a higher magnification of the smaller cracks which are approximately 5 - 10 microns in length on the outer wall surface close to the final fracture front. The cracks seen here have grown along  $\gamma$ -grain boundaries and some are seen to propagate transverse across lamellar colonies.



Macroscopically, the uniaxial OP TMF specimen with hold period ( $\epsilon_{eq} = 0.15\%$ ) has a similar flat fracture surface to the other uniaxial OP specimens without a hold period. It also fractured in the gauge section perpendicular to the external stress, resulting in a  $90^\circ$  separation of the specimen halves. As previously observed the crack initiation sites are clearly visible on both the outer surface. The fan-shaped crack propagation zone is smaller than seen on the non-hold period specimens as it only penetrates the specimen wall by about  $200\mu\text{m}$ . The ridge marks can also be identified becoming deeper farther away from the crack propagation zone.

The microstructure is similar to the non-hold period tests revealing intergranular fracture by the many voids left by decohesion of grains. Some cleavage fracture has been identified by the feather markings.

In longitudinal section, this specimen has greater damage to the fracture surface than with the test without a hold period. It shows large extensive sub-surface cracks approximately  $100\mu\text{m}$  below the fracture surface. The crack shown in Figure 3.56a is approximately  $500\mu\text{m}$  long. From the outer surface long cracks penetrate deep into the bulk material. A crack path shown in Figure 3.56b, illustrates how the crack path has progressed around the globular  $\gamma$ -grains via the grain boundaries. The inner surface wall was also void of cracks.

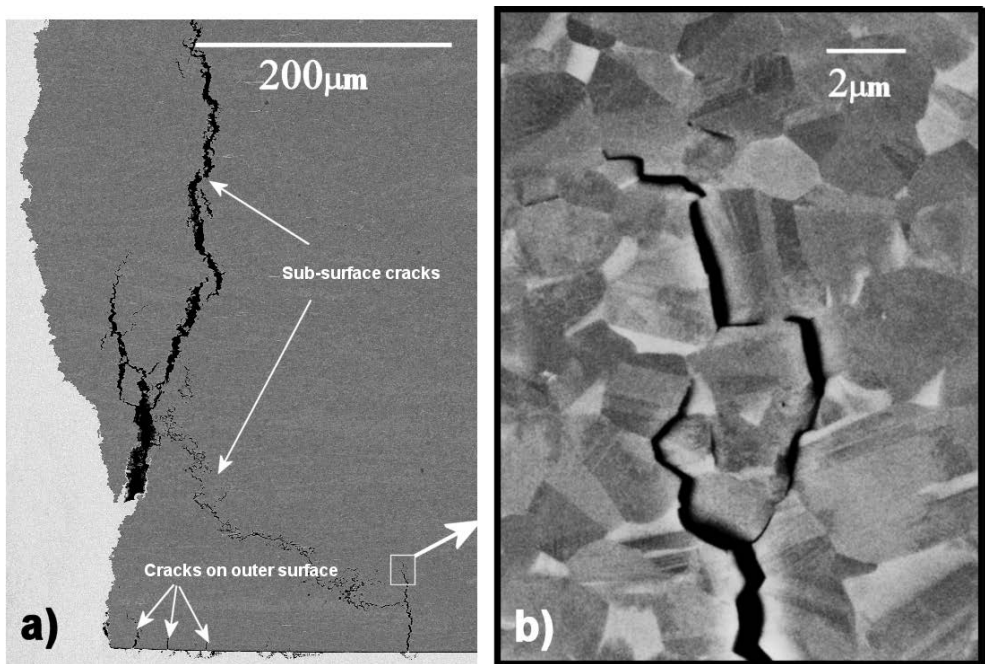


**Figure 3.56:** Longitudinal section of a fractured uniaxial OP specimen with a hold period ( $\epsilon_{eq} = 0.15\%$ ). a) shows the fracture surface has greater sub-surface damage than with the uniaxial test without a hold period. The crack indicated in this image is approximately  $500\mu\text{m}$  long. b) An enlarged crack path indicated by the square in (a) which has progressed via  $\gamma$ -grain boundaries (BSE).

**Uniaxial IP specimens:** As with the uniaxial OP specimens, the uniaxial IP TMF specimens also fractured perpendicular to the external stress, also resulting in a  $90^\circ$  separation of the specimen into two halves. Macroscopically, the fracture initiation sites were again evident by pits on the outer surfaces and abraded and pitted areas on the fracture plane. The fan-

### 3. Results

shaped crack propagation zone on the fracture planes are also very evident as in some specimens they penetrate the specimen wall completely. Generally, around the crack propagation zone the surfaces are flat for approximately 1-2mm and then ridge marks begin to form or, some strong v-shaped chevron markings are identified (the apexes of the chevrons point back to the crack origin [139]).

The crack initiation sites of the uniaxial IP specimens, in the main, coincide where the thermocouple was spot welded to the specimen surface. When present, the oxidised crack propagation zone completely penetrates the specimen wall (1mm).

One specimen was observed to have two fracture initiation sites, 3-4mm apart; both on the plane of fracture (see Figure 3.57). One site was identified as the point at which the thermocouple was spot welded to the specimen surface the other also appears to be caused by some form of surface damage.

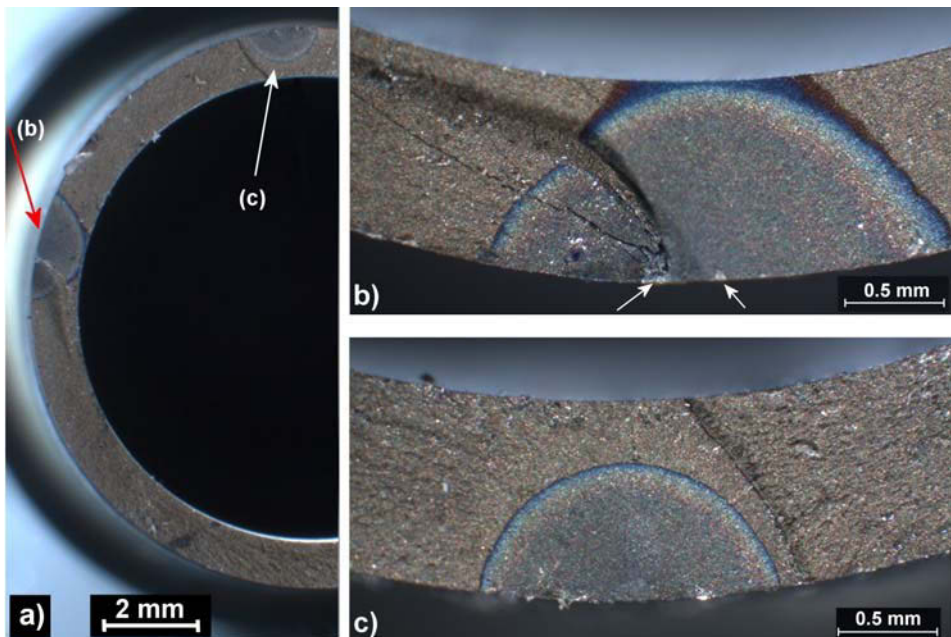


**Figure 3.57** a) A uniaxial IP specimen ( $\epsilon_{eq} = 0.5\%$ ) with two crack initiation sites, the arrows indicate the two oxidised zones. b) The marks left by the thermocouple are indicated by the arrows. Oxidation is extensive, completely penetrating the specimen wall. c) The second site is smaller but the oxidised zone is still large penetrating the wall by approximately  $700\mu\text{m}$  (LM).

The microstructures at both oxidised zones, shown in Figure 3.57, are examined in more detail (see Figure 3.58). A magnified view of the point where the thermocouple was attached reveals the microstructure to have deep crack running into the bulk material, at  $90^\circ$  to the outer surface. At the second site shown in Figure 3.58b a fine crack also runs perpendicular to the outer specimen wall.

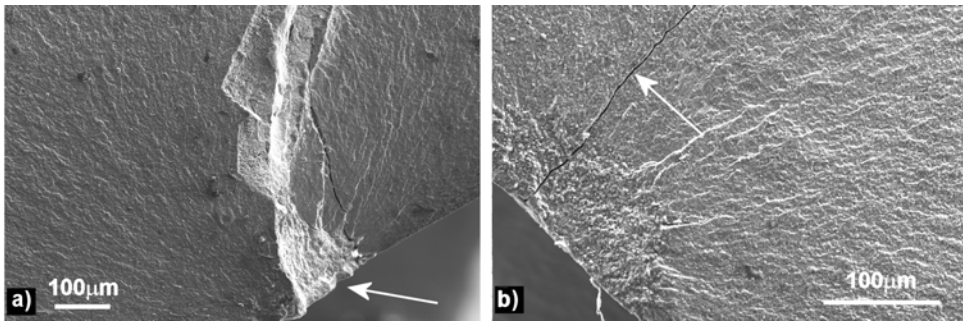


**Figure 3.58** a) Fractographs of the two oxidised zones shown in Figure 3.57. a) A magnified view of the area where the thermocouple was attached (indicated by the arrow). A deep crack can be seen initiating perpendicular from the outer surface running into the bulk material. b) A micrograph of the second site shown in Figure 3.57c also here at this site, a fine crack runs perpendicular to the outer specimen wall (indicated by the arrow). (SE). Images courtesy of Dennis Peter, Ruhr-University Bochum.

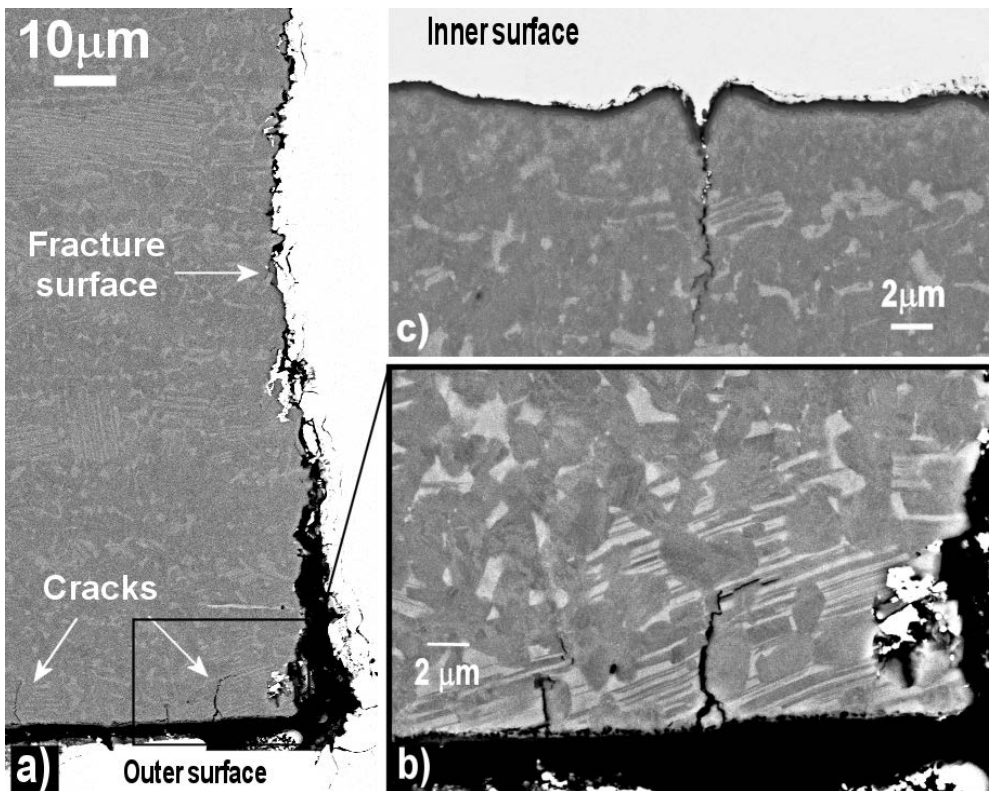


**Figure 3.59:** Longitudinal section of a fractured uniaxial IP specimen ( $c_{eq} = 0.7\%$ ). a) Numerous small cracks can be seen along the outside edge of the specimen, close to the fracture surface. b) A higher magnification of the  $\sim 5\text{-}15\mu\text{m}$  cracks on the outer surface near the fracture surface (indicated by the square in a). Intergranular fracture can be clearly seen in this image. c) A small  $\sim 5\text{-}10\mu\text{m}$  long fissure on the inner surface (BSE).

### 3. Results

Investigation of the fracture surface in longitudinal section is shown in Figure 3.59a and b. Observed here are numerous small cracks along the outside edge of the specimen, close to the fracture surface. From the outer surface the cracks penetrate approximately 5-15 $\mu\text{m}$  into the bulk. Figure 3.59b shows a magnification of the cracks along the outer surface which clearly shows intergranular fracture. The inner surface although uneven did not have cracks near the fracture surface, there were however, some very small (~5-10 $\mu\text{m}$ ) cracks observed some 200 $\mu\text{m}$  away from the fracture surface (see Figure 3.59c). Sub-surface secondary cracks were smaller than seen in the OP specimens being 20-30 $\mu\text{m}$  long and only 10 $\mu\text{m}$  below the fracture surface. They were also very few in number.

**Torsional specimens:** The torsional IP specimens all failed in a catastrophic manner, in every case the gauge section was completely fragmented. There are not always obvious signs of a crack initiation sites as with the uniaxial pieces. The direction of fracture is also difficult to establish. However, judging by the overall shape of the specimen fragments it appears to be at approximately 45° to the specimen axis. Closer investigation of the fracture surfaces reveal, where ridge marks are present they are stronger and have greater topography than seen in the uniaxial specimens. The fracture surfaces also tend to have a gradient none are level and most are jagged and stepped.

Fractographic investigations using the SEM revealed a slightly more varied microstructure to that seen in the uniaxial specimens. The main differences to the uniaxial microstructures are the large cleavage fractures of the lamellar grains and the abundance of cleavage steps and facets.

The torsional test with hold period also suffered from fragmentation of the gauge section on reaching its fatigue limit, in this instance there were less fragmented pieces than those without hold period. Fracture is orientated approximately 45° to the specimen axis. The location of the crack initiation site was clearly identified on the outer surface and is marked with an arrow in Figure 3.60.

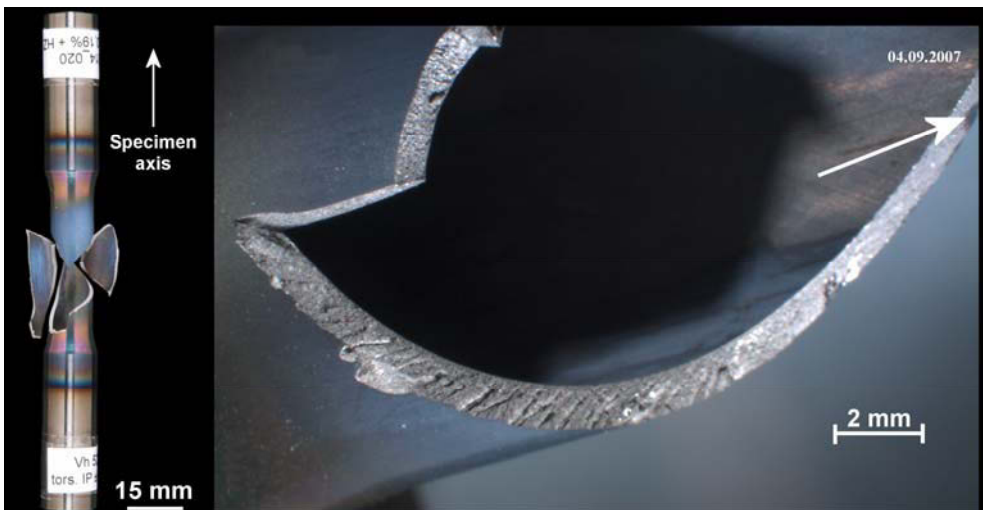


**Figure 3.60:** The torsional specimen with hold period ( $\epsilon_{\text{eq}} = 0.19\%$ ). This specimen failed (fragmented) at mid-point of the gauge section at approximately 45° to the specimen axis. The deep ridge marks seen along the fracture surface and the crack initiation site (indicated by the arrow) (LM).

As seen with the uniaxial specimens the crack initiation site is on the outer surface and apparent by the pits caused by the thermocouple attachment. This specimen also has a semi-circular oxidised crack propagation zone which projects ~500 $\mu\text{m}$  (half way) through the specimen wall (see Figure 3.61). The surrounding surface to the crack propagation zone is ridge marked with the occasional deep facet (see Figure 3.62). Further from the crack initiation site and propagation zone the ridge marks become large and deep.

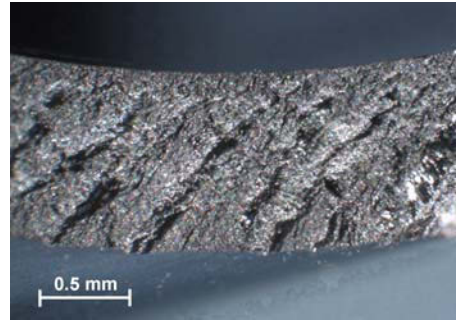
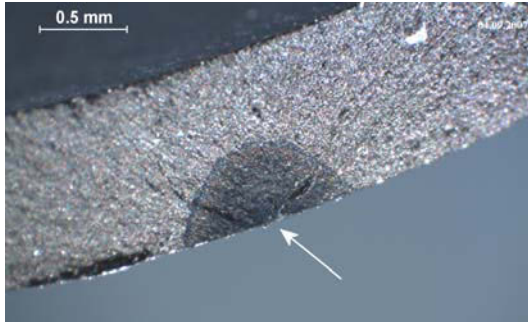


**Figure 3.61:** The crack initiation site (indicated by the arrow) and the semi-circular oxidised crack propagation zone projecting half way through the specimen wall. (LM).

**Figure 3.62:** Large ridge marks found on the fracture surface further from the crack propagation zone. (LM).

The ridge marks are very strong macroscopically and under high magnification in the SEM it can be seen to be comprised of mainly cleavage fracture of lamellar colonies and intergranular fracture of the globular  $\gamma$ -grains (see Figure 3.63).

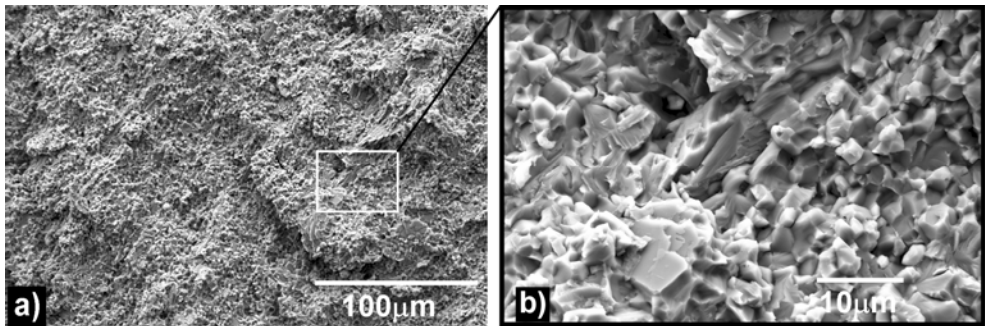


**Figure 3.63.** Fractographs of a) the ridge marked region showing b) The mixture of cleavage and intergranular fracture. (SE). Images courtesy of Dennis Peter, Ruhr-University Bochum.

### 3. Results

**Proportional-axial-torsional OP specimen:** The proportional-axial-torsional OP test separated at the gauge section without fragmentation (see Figure 3.64). The fracture is at approximately 30° to the specimen axis, however, it has a spiral path ending parallel to the specimen axis. Although the specimen fractured, the crack had penetrated much further around the specimen.

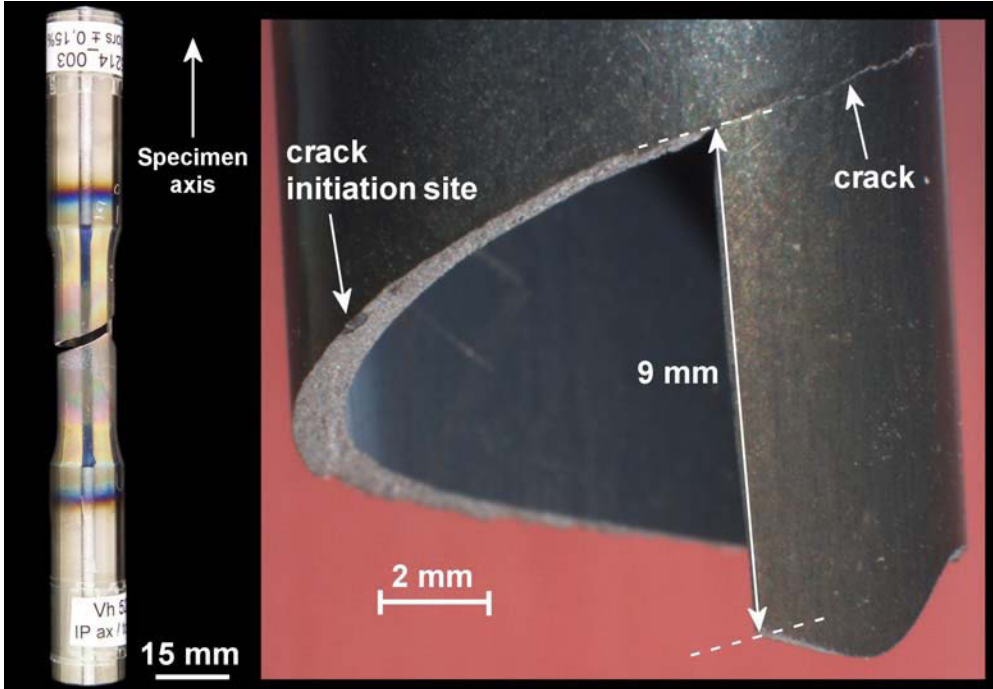


**Figure 3.64:** This proportional-axial-torsional OP specimen ( $\epsilon_{eq} = 0.15\%$ ) failed at mid-point of the gauge section at approximately 30° to the specimen axis. The spiral fracture path ending with a perpendicular fracture approximately 9mm long. The outer wall of the specimen is cracked beyond the final fracture (LM).

The crack initiation site is as previously observed identifiable by the small pits left in the surface by the attachment of the thermocouple. Also clearly visible by its semi-circular shape is the crack propagation zone which penetrates from the outer surface one third into the specimen wall (~300 $\mu$ m). Surrounding the propagation zone the surface becomes more ridge marked, these ridges are largest and deepest opposite the crack initiation site (see Figure 3.65).

Fractographs of the ridge marked fracture surface show large areas of grain decohesion. The microstructure shows intergranular fracture and some cleavage fracture in the lamellar grains (see Figure 3.66).

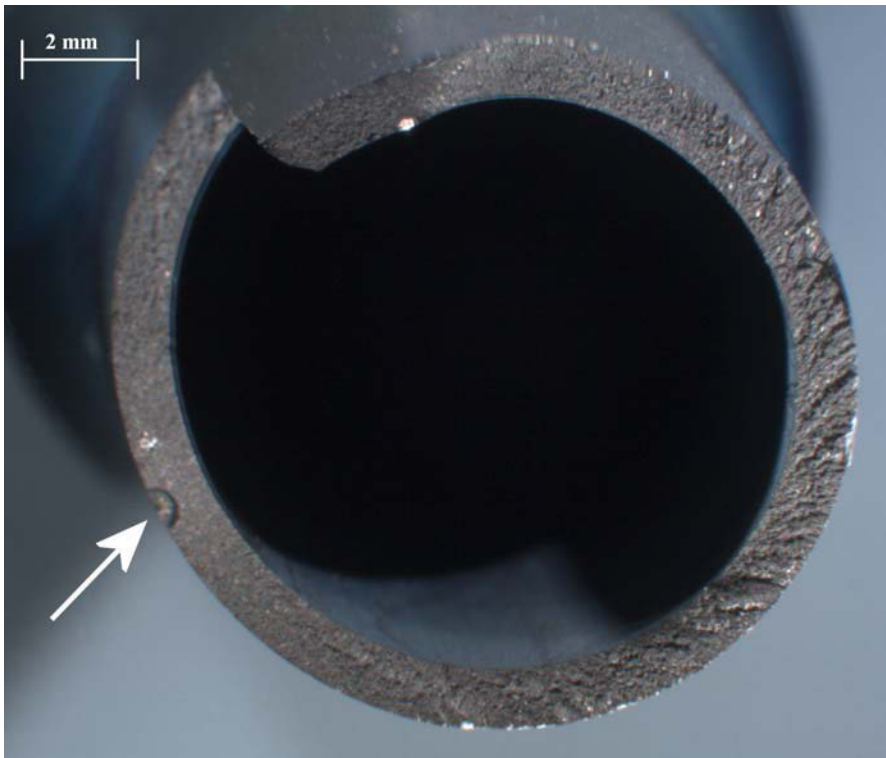


**Figure 3.65:** The crack initiation site (indicated by the arrow) is located, adjacent to the semi-circular oxidised crack propagation zone which penetrates one third into the specimen wall. The largest ridge markings found on the fracture surface opposite the crack initiation site (LM).

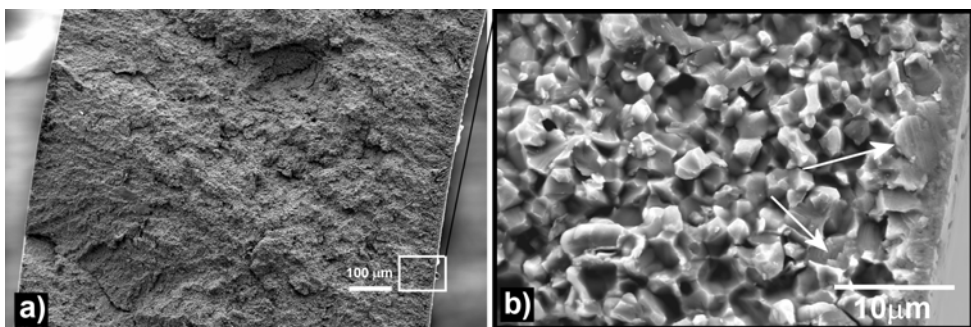


**Figure 3.66.** Fractograph of the proportional-axial-torsional OP TMF specimen. a) The ridge marked fracture surface showing the large areas of grain decohesion. b) An enlargement of the microstructure shows predominantly intergranular fracture with some cleavage fracture of the lamellar grains (indicated by the arrows) (SE). Images courtesy of Janine Pfetzing, Ruhr-University Bochum.

**Non-proportional-axial-torsional OP specimens:** The non-proportional-axial-torsional specimen separated into two pieces at the gauge section. The fracture is at approximately  $90^\circ$  to the specimen axis (see Figure 3.67). The fracture surface of this specimen is relatively flat.

### 3. Results

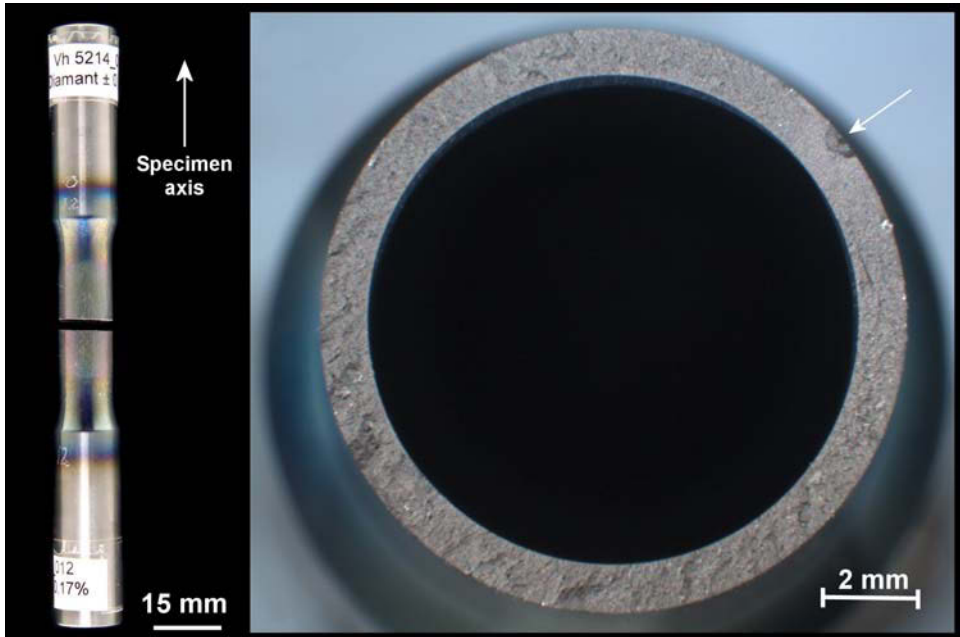


**Figure 3.67:** This non-proportional-axial-torsional OP specimen ( $\epsilon_{eq} = 0.17\%$ ) failed at approximately mid-point of the gauge section perpendicular to the specimen axis. On the fracture plane the crack initiation site is identified by the semi-circular oxidised zone (indicated by the arrow) (LM).

The fracture initiation site was again easily identified by the small pits on the outer specimen surface caused by the attachment of the thermocouple. The semi-circular oxidised crack propagation zone was also present and penetrates approximately  $300\mu\text{m}$  into the specimen wall (see Figure 3.68).

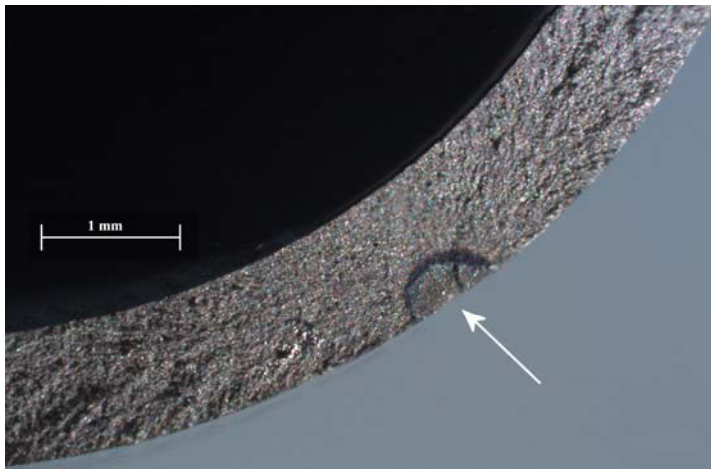


**Figure 3.68:** Location of the crack initiation site (indicated by the arrow), was as previously readily identified by the small pits on the outer surface as was the semi-circular oxidised crack propagation zone here penetrating one third into the specimen wall. The deep ridge markings found on the fracture surface are close to the crack initiation site (LM).



Around the crack propagation zone the structure is clearly intergranular. Further from the crack propagation zone the ridge marks have an undulating topography with many facets.

In the ridge marked area the facets are rough and with higher magnification some are seen penetrating deep into the microstructure. The fracture surface consists of intergranular fracture. Examination of the fractured surface in longitudinal section discovered relatively large sub-surface cracks varying from between 50 and 200  $\mu\text{m}$  in length and 5-10  $\mu\text{m}$  wide, 50  $\mu\text{m}$  below the fractured edge of the specimen. Along the outer wall close to the fracture front small ~10-15  $\mu\text{m}$  cracks penetrate into the bulk material. The crack path can be clearly identified as intergranular. There were no cracks observed on the inner wall surface.

The non-proportional-axial-torsional OP tested specimen with hold period separated into two pieces just within the gauge section. The fracture is at approximately 90° to the specimen axis (see Figure 3.69). The fracture surface of this specimen is also relatively flat. As seen previously at the crack propagation zone the fracture surface is relatively smooth, however, the topography changes to chevron markings and beyond these, there are large ridge markings. Unusually for this specimen, the crack initiation site lies on the inner wall. This was not observed with any other specimen (see Figure 3.69).

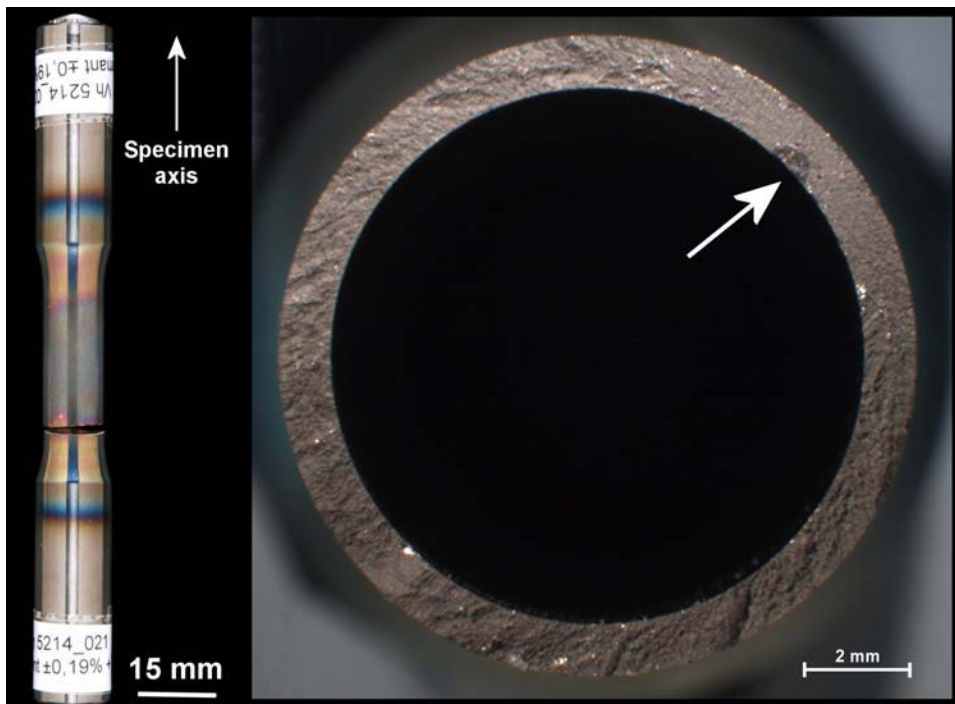


**Figure 3.69:** This non-proportional-axial-torsional OP specimen with hold period ( $\epsilon_{\text{eq}} = 0.15\%$ ) failed close to the end of the gauge section. The fracture plane shows the crack propagation zone situated at the inner wall. The crack initiation site lies adjacent to the centre of the semi-circular area on the inner wall (indicated by the arrow). (LM).

The semi-circular oxidised crack propagation zone is also found originating from the inner wall of this specimen. The oxidised zone penetrates ~400  $\mu\text{m}$  into the specimen wall (see Figure 3.70).

### 3. Results

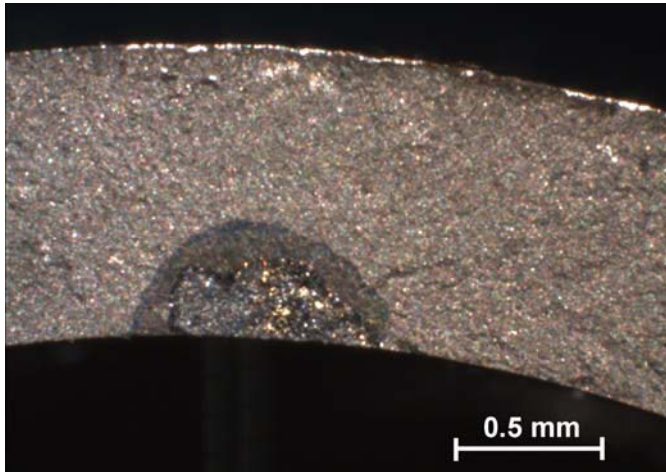


**Figure 3.70:** The crack initiation site identified by the semi-circular oxidised zone here penetrating almost half way into the specimen wall (LM).

SEM fractographs show predominantly intergranular fracture with some cleavage fracture sites. Cleavage fracture of the lamellar grains has undoubtedly given rise to a cleavage step on the fracture plane. Although the microstructure mainly consists of intergranular fracture there is also transgranular fracture among the  $\gamma$ -grains. Among the ridge marked areas the microstructure consists of numerous cleavage facets. Here mixed mode fracture of intergranular and transgranular fracture is observed.

The fractured surface in longitudinal section revealed the inner wall to contain longer wider cracks penetrating from the surface close to the fracture front. These are approximately 25-40  $\mu\text{m}$  in length and  $\sim 5 \mu\text{m}$  wide. On the outer wall there are also cracks penetrating from the surface however, these are not as long or as wide as those observed on the inner wall (approximately 15-25  $\mu\text{m}$  in length and 2-3  $\mu\text{m}$  wide) They can be clearly identified as intergranular (see Figure 3.71a and b). The smaller cracks on both the outer and inner surfaces were only observed near the fracture surface. There were no sub-surface cracks seen at the fracture front.

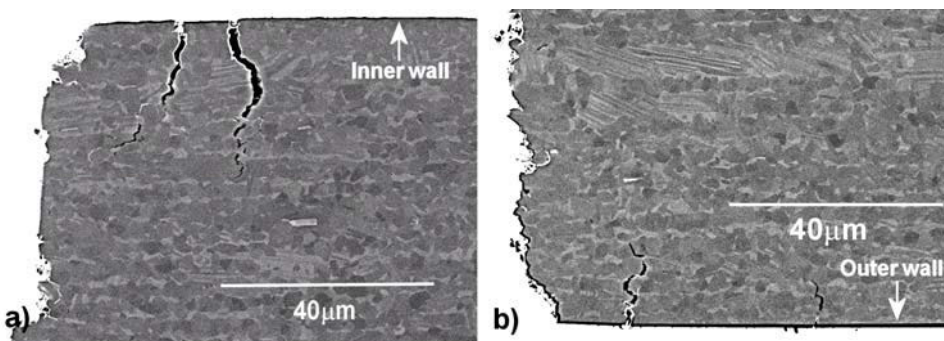


**Figure 3.71:** Longitudinal section of a fractured non-proportional-axial-torsional specimen with hold period revealing a) small cracks ( $\sim 25\text{-}40 \mu\text{m}$  in length) along the inner wall of the specimen, close to the fracture front. b) On the outer wall the cracks are slightly smaller than those on the inner wall ( $\sim 15\text{-}25 \mu\text{m}$  in length). In both areas the fracture is intergranular (BSE).

Summarising the fractography investigations, fracture of the uniaxial tests (OP and IP) and the non-proportional-axial-torsional specimens all occurred perpendicular to the external stress resulting in 90° fracture and parting the specimen into two pieces. For the torsional tests, crack propagation occurred at approximately 45° to specimen axis and the gauge section fragmented into a number of pieces. The proportional-axial-torsional specimen fractured at approximately 30° to specimen axis without fragmentation. The crack initiation sites were, in the majority of case, identified by the pits on the outer surface of the specimen where the thermocouple was spot welded to the surface of the material and in only one case two crack initiation sites identified. The crack initiation, in all but one example, began on the outer surface.

Macroscopically, the oxidised crack propagation zones are very obvious, as are the ridge marks and in some cases strong chevron markings. Microscopically the surfaces were rougher with deeper facets in the multi-axial tested specimens than those seen in the uniaxial specimens.

In all types of tests intergranular fracture is predominant, mainly in areas of globular  $\gamma$ -grains while cleavage failure is mostly observed in the lamellar colonies. There is some additional transgranular fracture of the  $\gamma$ -grains in the non-proportional-axial-torsional OP specimen with hold period.

The fracture surfaces in longitudinal section reveal sub-surface secondary cracks in all of the specimens examined. In all examined specimens the outer surface walls all revealed the presence of cracks. Inner wall surface cracking was only observed with uniaxial IP and the non-proportional-axial-torsional specimen with a hold period.

## 4. Discussion

In section 4.1 the test results are discussed and compared to the behaviour of the material so far described in the literature. This section ends with observations accumulated from the fractography investigations. The near- $\gamma$ -TiAl alloy investigated in this study is considered with previously investigated Ni-based IN 738 and Nimonic 90 alloys in section 4.2. The similarities between the materials are compared and evaluated. Behavioural differences are investigated and explained. Section 4.3 describes the lifetime model which has been developed for this material. The reasoning behind the model and build-up of its development are elucidated and discussed. The model developed shows that regardless of test type performed and can describe all lifetime results in a narrow scatter band using just one loading parameter.

### 4.1. Evaluation of the mechanical tests

#### 4.1.1. Lifetime behaviour of TiAl

From the results various factors can be attributed to affect the fatigue lifetime behaviour of TiAl. The fatigue lifetimes are clearly very sensitive to the strain amplitude and the temperature-strain phase. In order to address the effects of temperature-strain phase on this material it is practical to begin with the uniaxial tests.

The lifetimes under axial thermal-mechanical IP loading at the same maximum stress magnitude,  $\max |\sigma|$ , or at the same mechanical strain amplitude, are longer than under thermal-mechanical OP loading. Nitta and Kuwabara [140] proposed that if a metallic material subjected to OP loading fails sooner than under IP loading, embrittlement of the surface/sub surface and subsequent crack initiation and growth are the causes of failure. On the other hand if IP loading fails sooner than under OP loading, then creep is the dominant damage mechanism. If, however, OP and IP loadings have similar lifetimes then neither environment nor creep damage dominates.

To discuss environmental effects on lifetime of TNB-V5 the oxidation behaviour needs to be addressed. The structure of oxide scales of TNB-V5 has not been investigated in this work as this was already well described in the literature. At high temperature TiAl forms a multi-layered oxide structure. On the outer surface it is known to form  $\text{TiO}_2$ , below that  $\text{Al}_2\text{O}_3$ , then a  $\text{TiO}_2 + \text{Al}_2\text{O}_3$  mixture, all on top of an Al depleted zone. This Al depleted zone consists of  $\text{Ti}_3\text{Al}$  which is known to absorb oxygen, making it brittle. Extended exposure to high temperature extends the depth of this zone and thus increasing its susceptibility to weaken [4, 100, 141].

In TMF testing oxidation takes place at high temperature under OP and as well as IP loading. Under OP loading at the subsequent lower temperature and the higher tensile stresses (and the higher mean stress) the oxide zone may crack easily. Microcracks may form in the embrittled zone under mechanical loading providing macrocrack initiation sites. It has been established by Christ [95] that the near surface region exhibits higher hardness and embrittlement after testing in air than when tested in vacuum. For IP loading the tensile stress is applied at  $T_{\max}$  which may cause creep damage but tensile stresses are lower in an IP cycle. Thus the lower lifetimes under OP loading indicate that oxidation is the predominant damage mechanism. It is reasonable to assume that the maximum tension stress is responsible for crack growth failure.

The cyclic stress-strain hysteresis loops for the uniaxial OP loading are slightly bowed between  $\sigma_{\max}$  and  $\sigma_{\min}$  (for an example see Figure 3.7) and not linear as one would expect

for isothermal tests. This is caused by the change in elastic modulus ( $E$ ) from 160GPa at  $T_{\min}$  to 145GPa at  $T_{\max}$  over the loading cycle (see section 3.3). This can be interpreted as asymmetric thermal loading.

The cyclic stress-strain hysteresis curves also have a shift in stress over the test, upwards for OP and downwards for IP. For IP it is more pronounced at  $\sigma_{\max}$  than  $\sigma_{\min}$  for the higher strain amplitudes (0.5 – 0.7%). The reason for the different cyclic developments of the maximum and minimum stresses at IP loading with larger plastic strain is the superposition of the cyclic mean stress shift down to lower values and the stress range softening: these two effects accumulate at  $\sigma_{\max}$  while they neutralise each other at  $\sigma_{\min}$  (see Figure 3.12).

Cyclic softening is also reflected in an increase in the plastic strain amplitude  $\Delta\varepsilon_p/2$ . The plastic mechanical strain has been calculated by subtracting elastic strain from the mechanical strain:

$$\varepsilon_p = \varepsilon_m - \varepsilon_e \quad \text{Eq. 4.1}$$

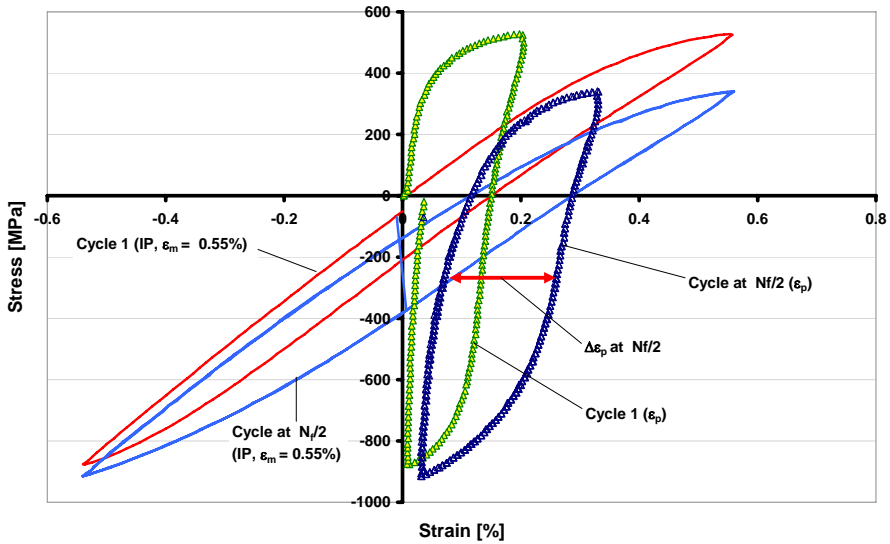
To calculate the elastic strain the temperature dependant Young's modulus  $E$  has been used:

$$\varepsilon_e = \frac{\sigma}{E(T)} \quad \text{Eq. 4.2}$$

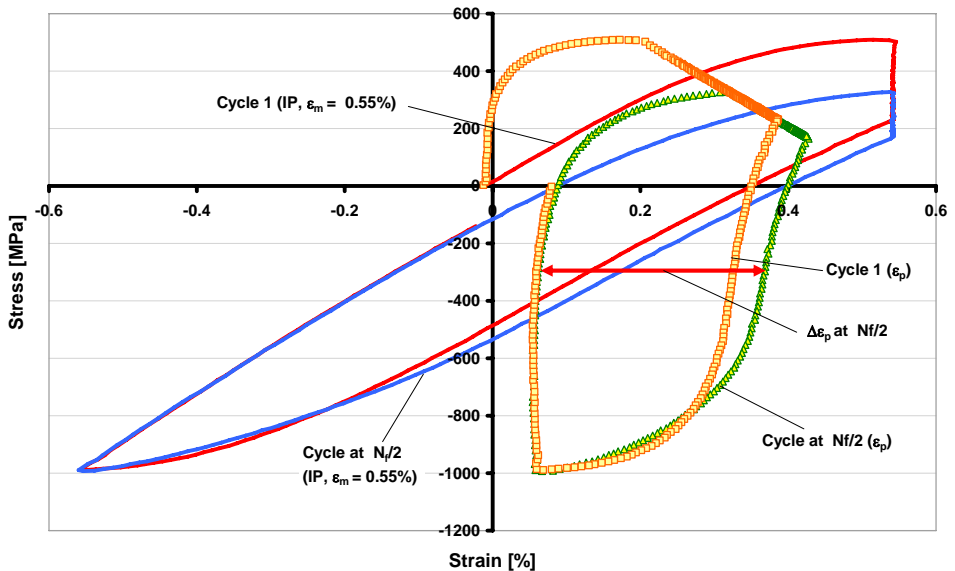
The same was applied for shear strain  $\gamma$  using the temperature dependant shear modulus;  $G$ . Figure 4.1 shows the plastic strain over the first loading cycle and at mid-life loading cycle for the uniaxial IP test at  $\varepsilon_m$  0.55%. The plastic strain hysteresis loops become wider with increasing loading cycles. The plastic strain range  $\Delta\varepsilon_p$ , is calculated at the mean stress of the plastic strain hysteresis loop at mid-life this is indicated on Figure 4.1 by the double headed arrows. Figure 4.2 shows the plastic strain over the first and at mid-life loading cycle for the uniaxial IP test with hold period at  $\varepsilon_m$  0.55%. Clearly seen here are the larger plastic hysteresis loops compared to those seen in Figure 4.1 of the corresponding test without hold period. This increase in plastic strain explains the shorter lifetime of the hold period test because it results in additional damage.

Figure 4.3 shows the equivalent plastic strain amplitudes,  $\varepsilon_{eq\ p} = \Delta\varepsilon_p/2$  vs.  $N_f$  for all tests. The data show that the plastic strain is less than 0.01% for all OP tests (these tests do not show any cyclic softening) and it is higher than 0.01% for all IP uniaxial tests. A higher plastic strain in uniaxial IP than in uniaxial OP was also observed by Schallow and Christ [98, 99]. The torsional tests show similarly low values of plastic strain to the uniaxial OP tests. The plastic strain hysteresis loops are very narrow for uniaxial, axial-torsional OP and torsional loadings therefore the accurate determination of the strain range is very difficult and gives rise to scatter. Note that the plastic strain values are very low. The plastic strain amplitude is higher in the uniaxial IP tests than in the uniaxial OP tests due to the higher mechanical strain amplitudes. The uniaxial tests with a hold period have higher plastic strain than the corresponding tests without hold periods at the same mechanical strain amplitude (see Figure 4.3). The effect of the hold period is less distinct for the torsional and the axial-torsional tests. For the torsional test with hold period the plastic strain amplitude is somewhat smaller. The same is true for the non-proportional axial-torsional test. However, the mechanical strain amplitude was 0.02 percentage points smaller for the test with a hold period. Also consideration has to be given for the very narrow stress-plastic strain hysteresis curves which makes exact determination difficult.

#### 4. Discussion



**Figure 4.1:** The mechanical strain  $\varepsilon_m$  and plastic strain  $\varepsilon_p$  hysteresis loops for the first loading cycle and at mid-life of a typical uniaxial IP test. The plastic strain range  $\Delta\varepsilon_p$ , is calculated from the mean stress of the plastic strain hysteresis loop at mid-life indicated on the diagram by the double arrows. Plastic strain continuously increases over the test ( $\varepsilon_m = \varepsilon_{eq} = 0.55\%$ ).



**Figure 4.2:** The mechanical strain  $\varepsilon_m$  and plastic strain  $\varepsilon_p$  hysteresis loops for the first loading cycle and at mid-life of the uniaxial IP test with hold period. Plastic strain continuously increases over the test ( $\varepsilon_m = \varepsilon_{eq} = 0.55\%$ ).

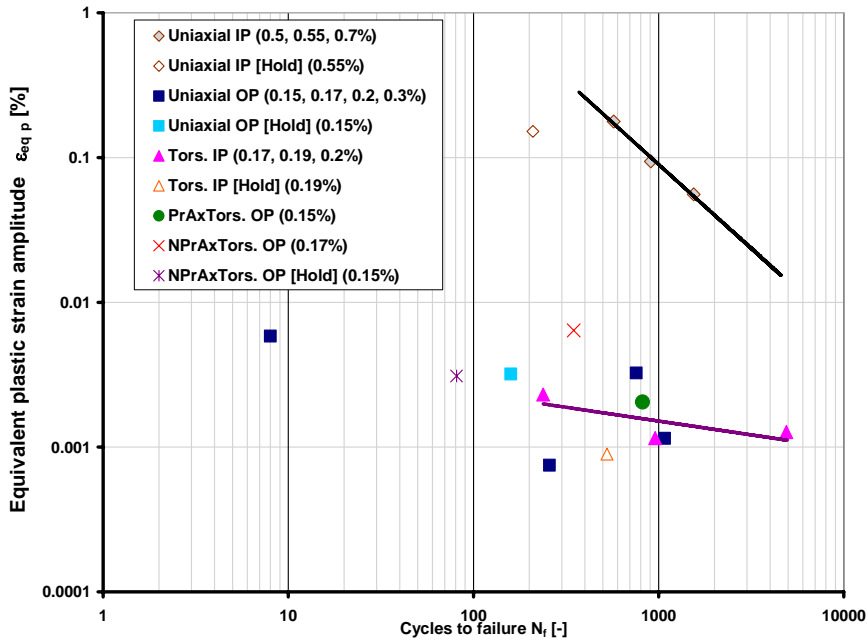


Figure 4.3: The equivalent plastic strain amplitude measured at mid-life  $N_f/2$ , for all performed tests.

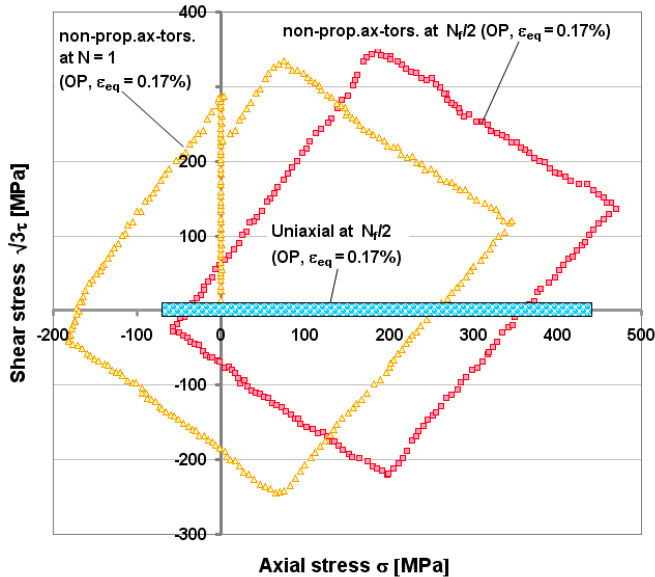


Figure 4.4: The stress response of torsional stress vs. axial stress for the non-proportional axial-torsional test at initial loading cycle (triangles) and mid-life (squares) compared with the axial stress from a uniaxial OP test at mid-life (solid bar on the x-axis) with the same equivalent strain amplitude ( $\epsilon_{eq} = 0.17\%$ ).

#### 4. Discussion

The lifetime of the non-proportional axial-torsional OP test is 50% shorter than that of a uniaxial specimen and only one tenth that of the torsional test with the same equivalent strain amplitudes. Figure 3.51 illustrates that for the non-proportional axial torsional test the equivalent stress at  $N_f/2$  is 490MPa as compared to 440MPa for the uniaxial test. The Figure 4.4 explains the higher maximum equivalent stress, is caused by the torsional stress which is still retained at maximum axial stress even though at the point of maximum axial mechanical strain the shear strain is zero (see Figure 1.18). Figure 4.4 shows the stress response of torsional shear stress vs. axial stress for this test compared with the axial stress of the uniaxial OP test with the same equivalent strain amplitude. This is related to the higher equivalent stress and plastic strain.

The stress diamond in Figure 4.4 is fractionally “rotated”, with respect to the mechanical strain. This is due to the torsional and axial stress-strain hysteresis caused by the slight plastic deformation as seen in Figure 3.38 by the shift in  $\sigma_{max}$ . With pure uniaxial loading, there is of course the total absence of torsional stress, represented by the shaded block parallel to the x-axis in Figure 4.4.

This combination of axial-torsional loading subjects the material to continuous stress over the whole temperature cycle. Maximum axial stress  $\sigma_{max}$  is at  $T_{min}$  (OP) which may cause oxide layer cracking. The short lifetime of this test is due to the greater damage than compared to the other types of test at the same equivalent strain amplitude.

The additional damage and consequential reduction of fatigue lifetime caused by the introduction of a hold period of 180 seconds at  $T_{max} = 800^\circ\text{C}$  for the uniaxial, torsional and non-proportional-axial-torsional TMF tests was also investigated. From the various tests uniaxial OP was most severely affected, compared to a test at the same strain amplitude without a hold period. The higher maximum tensile stress at lower temperature for OP with hold period may well accelerate crack growth as compared to tests without hold periods explaining the additional damage. For the IP loadings the hold period increases compressive stress  $\sigma_{min}$ , reducing  $\sigma_{max}$ . This, in theory, should increase the fatigue lifetime, which, however, is not the case. Therefore, there must be additional damage mechanisms taking place. Plastic strain is greater in hold period tests than with non-hold period tests the mechanical strain remains constant, the stress relaxes and the plastic strain increases during hold time (Figure. 4.3).

The fatigue lifetime reduction phenomenon caused by a hold period has also been observed in the literature. With a fully lamellar Ti-46.6Al-1.4Mn-2Mo alloy, Park et al. [87, 142] observed that with tensile hold periods (5, 10 and 30 minutes) during isothermal LCF tests at  $800^\circ\text{C}$  and at 0.35% mechanical strain, the fatigue lifetime was compared to continuous fatigue tests radically reduced. This became more pronounced with longer hold periods. The shorter lifetimes were attributed to additional creep damage during the tensile hold period inducing  $\alpha_2$  to  $\gamma$ -phase transformation at grain boundaries which, they claim, encourages intergranular fracture. This conclusion was drawn from the existence of entirely  $\gamma$ -phase near intergranular cracks, since under creep fatigue conditions only intergranular cracks are observed. The newly formed  $\gamma$ -grains are weaker and therefore become more susceptible to plastic deformation and eventually cause intergranular fracture [87, 142]. In the present study no  $\alpha_2$  to  $\gamma$ -phase transformation was observed, however, intergranular fracture was observed as was the reduced fatigue lifetimes caused by the hold period even though the hold period was considerably shorter than those performed by Park et al.

Time dependent creep fatigue crack propagation and evidence of grain boundary cracking was observed with a fully lamellar alloy Ti-34wt% Al at  $800^\circ\text{C}$  with a 900 seconds hold period by Tsutsumi et al. [74]. They determined a faster crack propagation rate at high



temperature than at ambient temperature. From this they concluded that their material exhibited better fatigue crack growth resistance at room temperature than at high temperatures, hence the shorter lifetimes caused by the high temperature hold period. Microstructural examination revealed cracks propagated perpendicularly to the stress axis transversing the lamellae boundaries [74]. In this present study no creep fatigue was identified however, crack propagation was also perpendicular to the stress axis.

The mechanical test observations can be summarised as follows:

- Fatigue lifetimes are strongly influenced by the strain amplitude, a small increase in amplitude reduces the lifetime considerably.
- Uniaxial OP tests have a shorter lifetime than the uniaxial IP tests, as OP has a higher maximum tensile stress which can easily break an oxide zone ahead of a crack tip formed during the preceding high temperature loading phase.
- Uniaxial IP tests at the same equivalent mechanical strain and the same equivalent stress amplitude result in even higher lifetimes than pure torsional TMF tests, as under IP loading the maximum principal stress and with it the maximum mean tensile stress is low.
- Torsional OP loading, loading, has a longer lifetime than the uniaxial OP loading at the same Mises equivalent stress amplitude as the mean tensile stress is zero at torsional loading.
- The non-proportional axial-torsional 90° out-of-phase OP test has a shorter lifetime than the uniaxial OP test with the same Mises equivalent mechanical strain amplitude, due to the diamond path having a higher equivalent stress amplitude.
- There is no additional hardening due to the non-proportional axial-torsional loading in this investigated high temperature material.
- Hold periods at maximum temperatures reduce the lifetime for all test types. However, the additional damage is more pronounced in uniaxial OP tests than in uniaxial IP or torsional tests. Hold times in OP tests result in higher maximum tensile stresses than without hold periods which, in combination with further oxidation damage, accelerates crack growth. Hold times in IP tests cause higher plastic strains which induce additional damage.

#### 4.1.2. Fractography and microstructure observations

The crack initiation sites were, in the majority of cases, identified by the pits on the outer surface of the specimen where the thermocouple was spot welded to the surface of the material and in only one case two crack initiation sites were identified. Effectively, the spot weld acts as a small surface defect which in turn acts as a stress raiser, further initiating a crack and eventual crack growth and failure this however does not cause any scatter in the results. The fracture surfaces in the longitudinal section reveal sub-surface secondary cracks and numerous cracks in the outer wall in all specimens examined, perpendicular to the loading direction. The cracks grow mainly intergranular along  $\gamma$ -grain and phase boundaries.

The fine grained duplex microstructure has a large volume fraction of  $\gamma$ -grains and hence multiple quantities of grain boundaries. Grain boundary strength is reduced by high temperatures leading to intergranular fracture. Rapid crack propagation and partially oxidised fracture surfaces in both OP and IP loadings were also observed by Christ [95] in a duplex Ti-47Al-5.1Nb-0.25C-0.4B (at%) alloy which he also attributed to grain boundary weakening.

#### 4. Discussion

Cleavage failure is mostly observed in the lamellar colonies, with the exception of non-proportional-axial-torsional OP specimen with hold period where there appears to be some additional transgranular fracture of the  $\gamma$ -grains. Christ [95] specifically identified transgranular crack growth in the crack propagation zone with IP loading and intergranular crack growth with OP loading. Such a clear separation of fracture types was not observed in this study.

Fatigue at elevated temperature is often accompanied by intergranular fracture [143]. Many materials show a transition from transgranular fracture at ambient temperature to intergranular fracture at high temperature when subjected to fatigue. This transition is affected by many test variables such as frequency, strain rate, wave form, hold periods and environment [143]. At least three different damage mechanisms are known which cause intergranular fracture: oxidation, creep cavitation and modification in slip character [143]. The important role of oxidation in high strength Ni-based alloys is well known, however, the mechanisms on oxygen penetration on grain boundaries are still open to question. It seems that the grain boundaries become embrittled and lose their mobility. Lower strength highly ductile materials such as austenitic stainless steels show creep damage, especially if hold periods are introduced, i.e., grain boundary cracks are observed in the bulk of the specimen. From the creep literature, it is well established that grain boundary sliding is important for the initiation of grain boundary cavities [143]. Grain boundary sliding was also observed in austenitic stainless steel during TMF (IP and OP) and under isothermal fatigue conditions [144]. The slip characteristics have been shown to be important. For IN 738 it was reported that intergranular fracture is favoured by the inhomogeneity of plastic deformation. The mechanisms however, are not fully understood. It might be associated by pronounced planarity of slip or by large stresses related to the intersection of slip bands with grain boundaries, initiating cavities without requiring macroscopic creep strain [143]. It is reasonable to assume that in this investigated alloy, embrittlement of grain boundaries by oxidation causes the observed intergranular fracture. This was also suggested by Riedel [145] who reported that brittle fracture of intermetallics has been ascribed to environmental interaction with oxygen. Also there are indications that grain boundary sliding might provide a contribution, as Peter et al. [146] found evidence for such a mechanism during creep deformation of TNB-V5.

As part of the Deutsche Forschungsgemeinschaft (German Research Foundation) research project that funded this research the microstructural investigations were performed at the Ruhr-University at Bochum and selected observations are included here to complete this study.

The fraction of twinned  $\gamma$ -grains was measured from SEM micrographs. In TiAl twinning is an important deformation mechanism [72, 147, 148]. Having taken the scatter into consideration, the number of twinned grains observed in the fractured specimens is only slightly higher than that seen in the as-received state (AR) (see Figure 4.5). The AR state already contains a high fraction of twinned  $\gamma$ -grains which are more a result of the extrusion process, therefore there seems to be no reason to assume the testing has had any effect on the fraction of twins. There is also no observed twinning in the lamellar grains this is seen by the lamellar space distance measurements which are virtually unchanged from the as-received state. These results suggest that deformation twinning is not a dominant deformation mechanism. The microstructural characterisation involved the use of a TEM to measure the interface distance in the lamellar grains (not shown), and the dislocation density. There seems to be a small decrease of the interface distances in the deformed states however, the scatter is relatively large and variations may also lie well within the scatter band.

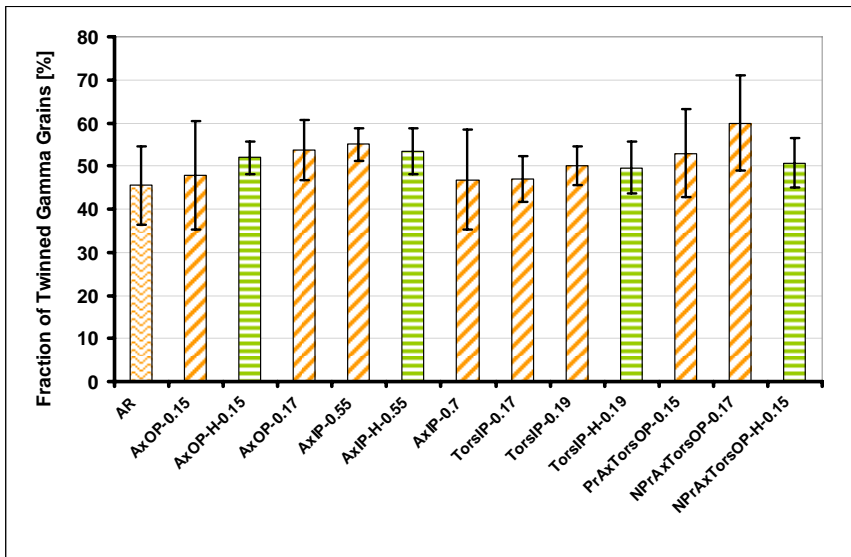


**Figure 4.5:** Fraction of twinned  $\gamma$ -grains in the as-received state (AR) and after TMF loading. Taking into account the scatter of the measurement, the deformed states have only a slighter higher fraction of twinned grains as the as-received material. AxOP-0.15: uniaxial OP at  $\varepsilon_{eq} = 0.15$  %; AxOP-H-0.15: uniaxial OP with hold period at  $\varepsilon_{eq} = 0.15$  %; AxOP-0.17: uniaxial OP at  $\varepsilon_{eq} = 0.17$  %; TorsIP-0.17: torsional IP at  $\varepsilon_{eq} = 0.17$  %; TorsIP-0.19: torsional IP at  $\varepsilon_{eq} = 0.19$  %; TorsIP-H-0.19: torsional IP with hold period at  $\varepsilon_{eq} = 0.19$  %; AxIP-0.2: uniaxial IP at  $\varepsilon_{eq} = 0.2$  %; AxIP-0.5: uniaxial IP at  $\varepsilon_{eq} = 0.5$  %; AxIP-0.7: uniaxial IP at  $\varepsilon_{eq} = 0.7$  %; PrAxTorsOP-0.15: proportional-axial-torsional OP at  $\varepsilon_{eq} = 0.15$  %; NPrAxTorsOP-0.17: non-proportional-axial-torsional OP at  $\varepsilon_{eq} = 0.17$  %; NPrAxTorsOP-H-0.15: non-proportional-axial-torsional OP with hold period at  $\varepsilon_{eq} = 0.15$  %. Results, by courtesy of Dennis Peter, Ruhr-University Bochum.

The first results from the still on-going study of the dislocation structures (characterised in TEM) indicate that the dislocation density is low within most globular  $\gamma$ -grains. In fact only a few grains exhibit dislocations even after TMF loading. Most of the globular  $\gamma$ -grains which contain relatively distinct dislocation substructures are located next to lamellar colonies. In lamellar grains dislocations were found within  $\gamma$ -laths and on lamellar interfaces. Dislocation densities were quantified for  $\gamma$ -grains which contained dislocations (this might result in an overestimation of the actual dislocation density). The density of ordinary dislocations is similar in both the deformed and un-deformed material.

The density of superdislocations is somewhat higher in the deformed state. Bearing in mind that although the quantitative data are based entirely on the measurement of grains which in fact show any dislocations. Figure 4.6 shows a TEM image of superdislocations observed after TMF loading of a proportional-axial-torsional OP at  $\varepsilon_{eq} = 0.15$ %. The generation of superdislocations are a characteristic feature of the slip geometry of the  $L1_0$  structure occurring in pairs and affecting the ordered structure [23]. It has been suggested by Huang and Hall [149] that twinning and superdislocation nucleation are competing mechanisms in TiAl-based alloys each being favoured in different composition ranges. The nucleation of twins is thought to be caused by the transformation in the core structure of a superdislocation. Higher densities of superdislocations may therefore be explained by the fact that twinning has reached saturation (due mainly to the extrusion process) and superdislocations are the only alternative form of deformation.

#### 4. Discussion

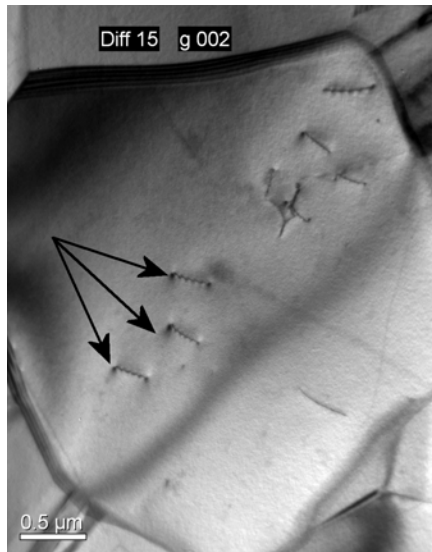


**Figure 4.6:** Superdislocations indicated by the arrows observed in the proportional-axial-torsional OP ( $\epsilon_{\text{eq}} = 0.15\%$ ) after TMF loading. TEM Image, by courtesy of Janine Pfetzing, Ruhr-University Bochum.

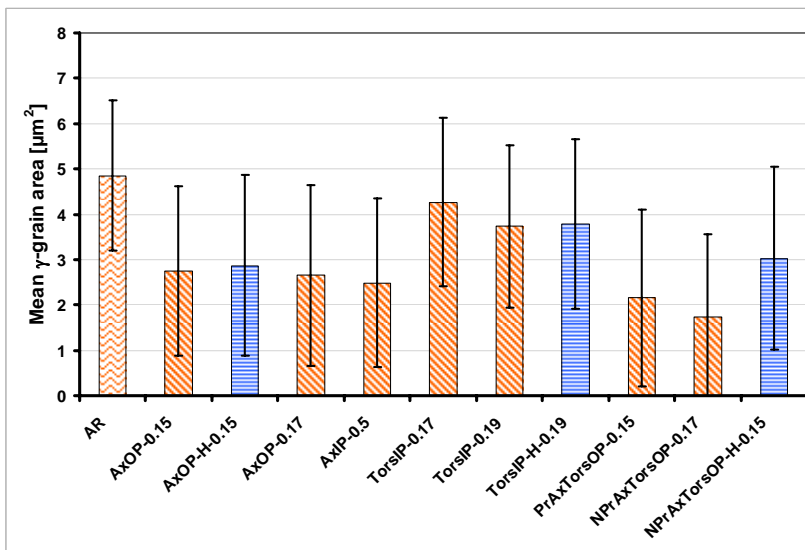


**Figure 4.7:** Mean  $\gamma$ -grain area for the as-received state and after TMF loading. For explanation of specimen designation see Figure 4.5. Results, by courtesy of Dennis Peter, Ruhr-University Bochum.

Mean  $\gamma$ -grain areas were quantified by analysing SEM micrographs [126]. The results show that in the as-received state, the mean  $\gamma$ -grain area is approximately  $5\mu\text{m}^2$  (see Figure 4.7). The  $\gamma$ -grain areas appear to be slightly smaller after TMF loading to that of the as-received state there is however a large margin of uncertainty in the results. The grain areas of the torsional tests are not as reduced as seen in the other tests. When taking into consideration the error bars the grains lie within the overall scatter.

Change in grain size and subsequent grain area reduction in  $\gamma$ -TiAl has been linked to dynamic re-crystallisation accompanied by the formation of dislocation free grains at high temperatures [28, 93, 98, 99, 150-157]. The re-crystallisation of the microstructure is dependent on deformation temperature, stress and the strain rate. The degree of dynamic re-crystallisation increases with increasing strain. At temperatures around half the melting point of the alloy,  $0.5 T_m$ , new, relatively dislocation free grains nucleate and grow at the expense of the old plastically deformed grains. Dislocation density and hence strain energy is reduced and the material's ductility returns. The grain size is dependent on applied force, finer grains will nucleate with increasing load [158]. This mechanism is found to be active during creep deformation [93]. However, Schallow and Christ [98, 99] observed dynamic re-crystallisation under uniaxial IP TMF loadings which they assigned to cyclic softening. This they justified was due to decomposition of the  $\alpha_2$  phase to  $\gamma$ -phase which results from increased dislocation density formed during the compression part of the loading cycle. Kim et al. [150] observed that grain boundary sliding at high temperature was considered to have been enhanced by dynamic re-crystallisation in a duplex  $\gamma$ -TiAl Ti46.2Al1.0 Cr 2.0Nb 0.18W 0.05B 0.12C alloy under tensile loading. Cao et al. suggest that the same occurs at high strain torsion in a two-phase lamellar and globular TiAl-based alloy (Ti-45Al-4(Cr, Nb, Ta, B)) [159]. Appel and Wagner [23] observed re-crystallisation in front of immobilised twinned grains. Liss et al remarked that thermal recovery and re-crystallisation did not occur under 710°C [160].

In this present study on TiAl, some slight cyclic softening behaviour is only observed in the uniaxial IP tests. This however, is also not convincing evidence that dynamic re-crystallisation has occurred, as the tests conducted at higher strain amplitudes show no major difference in grain areas to those tests at lower strain amplitudes and certainly the torsion tests have little indication for this process as no cyclic softening is observed. The change in  $\gamma$ -grain areas is not conclusive enough and requires closer investigation.

TMF deformation neither proceeds by deformation twinning nor by dislocation activity which raises the question what exactly the deformation mechanism could be? Attention has to be drawn to the amount of deformation induced by TMF loading being rather low compared to creep. Consequently, dislocation activity and deformation twinning should be less pronounced than during creep. It might well be that grain boundary sliding plays a role as observed by Peter et al [146], but the amount of its contribution is unknown at this present time.

#### **4.2. A comparison of TiAl with the Ni-based IN 738 and Nimonic 90 alloys**

With the imminent introduction of TiAl to replace some current high temperature Ni-based alloy components in aero gas turbine engines, it is extremely important to make some comparisons with them and TiAl. A turbine blade in gas turbine engine experiences variation in cyclic thermal stresses over its surfaces. The outside of a cooled blade can be subjected to tension-compression of (180°) OP loading, whereas an un-cooled blade can experience torsion (90°) OP counter clock-wise loading. The inner surfaces of a cooled blade can experience torsion (0°) IP loading and an un-cooled blade can experience non-proportional tension-torsion (90°) OP clock-wise loading [161]. Multi-axial and uniaxial TMF investigations have previously been conducted on Ni-based superalloys IN 738 and Nimonic 90 [112, 117, 124, 162]. Data from that research were re-examined and compared to the TiAl data from this study.

#### 4. Discussion

The alloy IN 738 [133, 162] is widely used for turbine components (blades, high temperature parts, etc.) [124, 163, 164]. Nimonic 90 [124] is currently used in discs and blades in gas turbines. It is also a candidate material for advanced steam turbines [165, 166] where it is expected to replace steel as it can cope better with the higher operating temperatures desired. Table 4.1 gives the nominal compositions of both alloys.

**Table 4.1:** Nominal compositions of the two compared Ni-based superalloys [124, 133, 162]

Content in weight percent													
	C	Cr	Co	Al	Si	Mn	Ni	Nb	Fe	Zn	Mo	Ta	W
IN 739	0.11	16	8.7	3.4	0.1	0.3	63.85	0.8	0.3	0.04	1.8	1.9	2.7
	C	Cr	Co	Al	Si	Mn	Ni	Ti	B	Zr			
Nimonic 90	0.07	19.5	16.5	1.5	0.3	0.3	59	2.5	0.003	0.0006			

The results of uniaxial OP and IP TMF tests of the two Ni-base alloys are presented together with the results on TNB-V5 in Figure 4.8 which shows the equivalent strain amplitude vs. number of cycles to failure (this means 10% load drop for Nimonic 90 material and the number of the last completed cycle for IN 738 and TiAl).

The TMF tests performed in this study on TiAl are not entirely identical with those previously performed with the two Ni-based alloys. The temperature ranges are not identical, for instance, IN 738 was tested over two different temperature ranges (450-950°C and 600-850°C at most exceeding the maximum temperature of this study by 150°C), with lower heating rates from 2.08Ks<sup>-1</sup> to 4.17Ks<sup>-1</sup>. Nimonic 90 was also tested over a larger temperature range (450°C), between 400°C and 850°C exceeding the temperature range of this study by 50°C. However, the temperature rate was identical (5Ks<sup>-1</sup>) but the strain amplitudes were generally higher.

The most noticeable observation is that the Nimonic 90 fatigue lifetimes are longer when loaded in OP than in IP, which is a completely opposite response compared to TiAl and IN 738. Whereas, the difference in lifetime between Nimonic 90 IP and OP is much smaller, than for TiAl, for example Nimonic 90 at an equivalent strain amplitude of 0.5%, under OP loading, has a longer lifetime by a factor of 3 more than for IP loading. Whereas, for TiAl there was difference in OP/IP loading by a factor of >450 at the same equivalent strain amplitude of 0.3%.

At  $\epsilon_{eq} = 0.5\%$  TiAl (IP) has a longer lifetime than Nimonic 90 (IP) by a factor of >8 and a factor of >2 more than Nimonic 90 (OP). In general, the TiAl IP loadings have the best resistance to TMF compared to either Nimonic 90 or IN 738. This is completely the opposite for OP loadings of TiAl where they have the lowest fatigue lifetimes, even at very low equivalent strain amplitudes. There is, unfortunately, no direct comparison of TiAl OP to Nimonic 90 OP or indeed IN 738 with the same  $\epsilon_{eq}$ , with which to refer, however the chart in Figure 4.8 clarifies the differences.

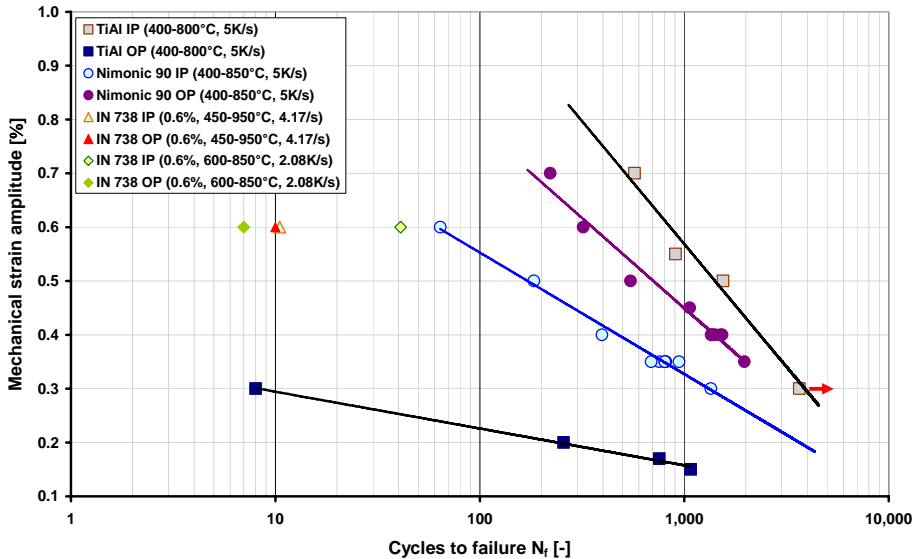


**Figure 4.8:** Uniaxial OP and IP TMF tests of TiAl, IN 738 and Nimonic 90 depicting mechanical strain amplitude vs. cycles to failure  $N_f$ . The material types are identified in the legend with the temperature range and heating rate. The data presented here are extracted from the investigations of [112, 117, 124, 162].

Comparing the TiAl data to the IN 738 results there are similarities between them. The OP loadings tend to have shorter lifetimes than IP loadings. The shortest lifetimes are those with the greatest maximum temperature, i.e. 450-950°C. From the data the following observations can be made. IN 738 OP at  $\epsilon_{eq} = 0.6\%$  has the same lifetime as TiAl OP at  $\epsilon_{eq} = 0.3\%$ , but the heating rate for IN 738 ( $2.08\text{Ks}^{-1}$ ) is less than half that of TiAl and as lower heating rates are usually less detrimental quite probably with a higher heating rate, lifetime would be even shorter. TiAl IP at 0.55% has a longer lifetime by a factor of 154 more than IN 738 IP at  $\epsilon_{eq} = 0.6\%$ . Even allowing for the 0.05% point difference in amplitudes, this is a considerable distinction. Another interesting comparison is between IN 738 IP at  $\epsilon_{eq} = 0.6\%$  and Nimonic 90 at  $\epsilon_{eq} = 0.6\%$  Nimonic 90 has a longer lifetime by a factor of >6 more (see Table 4.2).

**Table 4.2:** Comparison between IP loading for IN 738, Nimonic 90 and TiAl showing the equivalent stress  $\sigma_{eq}$  at  $N_f/2$ , equivalent strain amplitudes  $\epsilon_{eq}$ , fatigue lifetimes  $N_f$ , heating rate  $\dot{T}$ , maximum and minimum temperatures,  $T_{max}$  -  $T_{min}$ , and temperature range  $\Delta T$

Test (IP)	$\sigma_{eq}/N_f/2$ [MPa]	$\epsilon_{eq}$ [%]	$N_f$	$\dot{T}$ [K <sup>-1</sup> ]	$T_{max} - T_{min}$ [°C]	$\Delta T$ [°C]
IN 738	860	0.6	10	4.17	450-950	500
Nimonic 90	795	0.6	64*	5	400-850	450
TiAl	989	0.55	1546	5	400-800	400

\*10% load drop for Nimonic 90.

The IN 738 and Nimonic 90 uniaxial equivalent stress test data for both, IP and OP, fall between the results of TiAl. The heating rates  $\dot{T}$  for IN 738 are those tests which were performed within the temperature range 550-750°C. Although the other tests have higher  $\dot{T}$ , they were performed at least 50°C higher temperature than TiAl. It is therefore not

## 4. Discussion

unreasonable to expect similar lifetimes to TiAl if the temperature range  $\Delta T$ , maximum temperature  $T_{\max}$  and  $\dot{T}$  were the same as TiAl. Despite the opposite effects of IP/OP loading and the higher temperature range, Nimonic 90 has longer lifetimes than IN 738 and still falls within the TiAl data. The equivalent stress at mid-life is generally lower than IN 738.

Observations from the three material types presented show that TiAl and IN 738 are sensitive to OP loading and Nimonic 90 to IP loading, clearly indicating that the damage mechanisms develop differently with these different materials. The material type, the environment and/or loading conditions determine the contribution each has made on the collective damage mechanisms.

From this it can be concluded that under laboratory conditions, the  $\gamma$ -TiAl alloy studied here and the IN 738 previously investigated, are susceptible to environmental effects of high temperature oxidation.  $\gamma$ -TiAl shows similar behaviour to IN 738 with respect to TMF OP and IP loading in that OP is more damaging than IP loading. However the difference between OP and IP is smaller with IN 738. Nimonic 90 on the other hand is more susceptible to creep damage, indeed Marchionni et al [124] identified grain boundary damage was greater after IP loading with intergranular crack propagation. Their OP loaded specimens showed mixed mode fracture and transgranular crack propagation. If a hold period is included at  $T_{\max}$  then the extra factor of exposure time will further enhance the creep damage mechanisms. However TNB-V5 lifetimes are longer in IP mode than Nimonic 90 in OP mode. In conclusion, TNB-V5 is a superior material for IP TMF conditions than these Ni-based superalloys.

### 4.3. Lifetime modelling

#### 4.3.1. Description of the Lifetime Model

Structures loaded cyclically usually fail due to fatigue. The fatigue lifetime refers to the initiation of a macro-crack. For a fatigue test which has a combination of stresses i.e. uniaxial and torsional, the von Mises criterion provides a first representation of the data. Additionally for brittle materials the maximum principal stress theory provides the best criterion for fatigue failure [59, 134, 167]. A TMF lifetime rule is an approach for the lifetime consumption per cycle:

$$\frac{1}{N_f} = \left( \frac{\Delta W}{A} \right)^n, \quad \text{Eq. 4.3}$$

where  $A$  and  $n$  are material parameters and describe the stress-dependence of the lifetime behaviour.

A loading parameter ( $\Delta W$ ) based on the plastic work per cycle, being independent of material planes, has been considered as a measure of damage that can be also applied to complex types of loading [123]. The following form of the loading function is adopted here ([123]):

$$\Delta W = \int_{\text{cycle}} \langle \chi(\sigma) \rangle \left( \frac{\dot{p}}{\dot{p}_0} \right)^q \dot{p}_0 dt \quad \text{Eq. 4.4}$$



where  $\chi(\boldsymbol{\sigma})$  is a general scalar-valued function of the stress tensor<sup>IV</sup>. The McCauley brackets  $\langle x \rangle$  give the positive values of  $x$ :

$$\langle x \rangle := \begin{cases} x, & \text{if } x > 0, \\ 0, & \text{otherwise} \end{cases} \quad \text{Eq. 4.5}$$

$\dot{\rho}$  is the von Mises equivalent inelastic strain-rate:

$$\dot{\rho} := \sqrt{\frac{2}{3}} \|\dot{\epsilon}_{in}\| \quad \text{Eq. 4.6}$$

$\dot{\rho}_0$  in Eq. 4.4 is just a normalisation constant. The notion ‘inelastic strain’ includes all types of non-elastic deformation. Inelastic strain is the energy dissipated in a loading cycle (the area of the hysteresis loop) [168]. The deformation due to all kinds of dislocation movement is addressed here.

The influence of time on the lifetime is caused by oxidation and creep effects: this is described by the non-linear dependence on  $\dot{\rho}$  in the loading function (Eq. 4.4). The effect of time is characterised in a material specific way, i.e. by a material parameter ( $q$ ). The time-influence can be significant at strain hold periods although the inelastic strain-rate decreases quickly during the stress relaxation therefore:  $1 \geq q \geq 0$ , the lower  $q$  the stronger the effect of hold periods on the lifetime.

Under axial-torsional loading the Mises equivalent inelastic strain-rate is given as:

$$\dot{\rho} = \sqrt{\dot{\epsilon}_{in}^2 + \frac{\dot{\gamma}_{in}^2}{3}} \quad \text{Eq. 4.7}$$

The stress function  $\chi(\boldsymbol{\sigma})$  is for isotropic materials, in general, a non-linear combination of three isotropic stress invariants [169]:

$$\chi(\boldsymbol{\sigma}) \equiv \chi(\sigma_{eq}, \bar{\sigma}_m, \sigma_{P,max}) \quad \text{Eq. 4.8}$$

where  $\sigma_{eq}$  is the von Mises stress (also known as octahedral shear stress, relating to shear effects [134, 169]) which is defined as:

$$\sigma_{eq} := \sqrt{\frac{3}{2}} \|\boldsymbol{\sigma}'\|, \quad \boldsymbol{\sigma}' := \boldsymbol{\sigma} - \bar{\sigma}_m \mathbf{1} \quad \text{Eq. 4.9}$$

where  $\|\boldsymbol{\sigma}'\| := \sqrt{\sigma'_{11}{}^2 + \sigma'_{12}{}^2 + \sigma'_{33}{}^2 + 2(\sigma'_{12}{}^2 + \sigma'_{13}{}^2 + \sigma'_{23}{}^2)}$  is the Euclidean norm of a matrix<sup>V</sup>  
 $\bar{\sigma}_m$  is the mean tensile stress (Eq. 2.6) and  $\mathbf{1}$  the unit matrix.

<sup>IV</sup> Tensors are in boldface script.

<sup>V</sup> Square root of the squares of the components.

#### 4. Discussion

$\sigma_{P,max}$  is the maximum principal stress (causes the opening and growth of micro-cracks [134]) and is defined as:

$$\sigma_{P,max} := \max_{i=1..3} \sigma_i, \quad \text{Eq. 4.10}$$

Under axial-torsional loading the mentioned stresses are given by (e.g. [170]):

The Mises equivalent stress,  $\sigma_{eq}$  (Eq. 2.3)

$$\bar{\sigma}_m = \frac{\sigma}{3} \quad \text{Eq. 4.11}$$

$$\sigma_{1,2} = \frac{\sigma}{2} \pm \sqrt{\left(\frac{\sigma}{2}\right)^2 + \tau^2}, \quad \sigma_3 = 0 \quad \Rightarrow \quad \sigma_{P,max} = \frac{\sigma}{2} + \sqrt{\left(\frac{\sigma}{2}\right)^2 + \tau^2} \quad \text{Eq. 4.12}$$

Under uniaxial compression the maximum principal stress is equal to zero, because the lateral stress (load per unit area in a lateral direction) is zero.

From the test data, it will be possible to differentiate between the effect that the mean tensile stress  $\bar{\sigma}_m$  and the maximum principal stress  $\sigma_{P,max}$  has on the lifetime by considering the torsion and the uniaxial, thermo-mechanical IP loading at the same maximum von Mises stress within a stabilised cycle. Under pure torsion, the mean tensile stress is identically zero, however, the maximum principal stress is not vanishing. During uniaxial thermo-mechanical IP loading, the maximum principal stress as well as the positive mean tensile stress is extremely small in a stabilised cycle. Hence, the latter loading type could produce the longest lifetime. The investigated mechanical testing revealed that, indeed, this is the case for  $\gamma$ -TiAl, Figure 3.51.

With a hollow specimen the axial stress  $\sigma$  and the torsional shear stress  $\tau$  are calculated directly [128] and then the elastic deformation  $\varepsilon_e$  is given via Hooke's law of thermo elasticity  $\sigma(\varepsilon_e, T)$ , so that the inelastic deformation  $\varepsilon_{in}$  can be determined:

$$\boldsymbol{\varepsilon}_{in} = \boldsymbol{\varepsilon}_m - \varepsilon_e(\boldsymbol{\sigma}, T), \quad \boldsymbol{\varepsilon}_m := \boldsymbol{\varepsilon}_{tot} - \varepsilon_{th}(T) \quad \text{Eq. 4.13}$$

$$\dot{\varepsilon}_{in} = \dot{\varepsilon}_m - \left( \frac{\sigma}{E(T)} \right) \cdot \quad \text{Eq. 4.14}$$

$$\dot{\gamma}_{in} = \dot{\gamma}_m - \left( \frac{\tau}{G(T)} \right) \cdot \quad \text{Eq. 4.15}$$

#### 4.3.2. Modelling approaches

Since the loading parameter is based on the plastic work per cycle at mid-life all lifetimes are initially represented, as a basis, against the following inelastic work parameter:

$$\Delta W = \int_{\text{cycle}} \sigma_{eq} \dot{p} dt \quad \text{Eq. 4.16}$$

The result, Figure 4.9, essentially represents the same as the pure Mises stress amplitude (Figure 3.51), except for the non-proportional axial-torsional (“Diamond”-type) loading the inelastic work parameter increased relative to the other points. This is due to the absence of elastic unloading phases at non-proportional loading. Inelastic work is done there during practically the whole cycle.

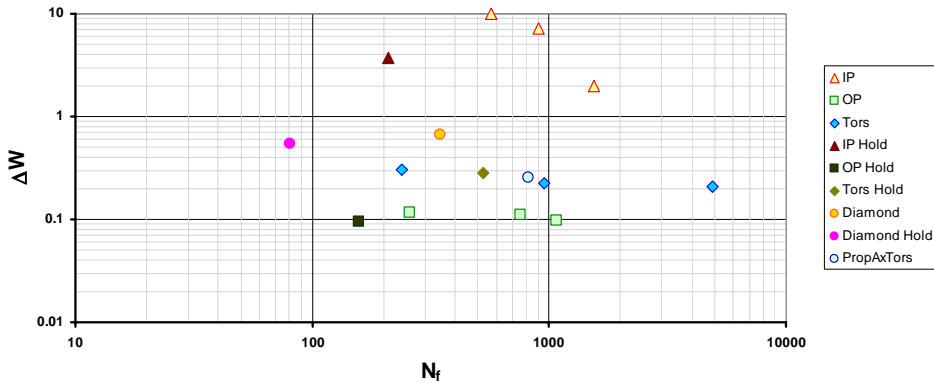


**Figure 4.9:** Experimental number of cycles-to-failure,  $N_f$ , vs. the plastic work parameter  $\Delta W$  according to Eq.4.16.

### 4.3.3. The maximum principal stress model

The maximum principal stress, which is low at IP loading and high at OP loading, is considered as the most important stress part. Because the investigated tests show that the uniaxial, thermo-mechanical IP loading produces the longest lifetimes and the uniaxial OP loading the shortest lifetimes at the same von Mises stress amplitude, The time dependence material parameter  $q$  is, at the outset, set in both models to a reasonable value,  $q = 0.3$ . The normalisation constant  $\dot{p}_0$  is chosen to  $\dot{p}_0 = 10^{-5} \text{ s}^{-1}$ . The following approach is investigated first:

$$\chi(\sigma_{P, \max}) = \sigma_{P, \max} \quad \text{Eq. 4.17}$$

In Figure 4.10 the results of this approach are given without any material parameter in the stress function  $\chi$ .

#### 4. Discussion

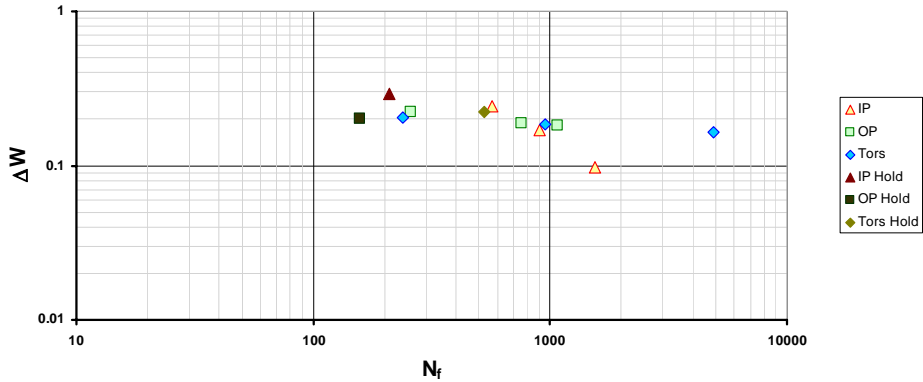


**Figure 4.10:** Experimental number of cycles-to-failure,  $N_f$ , vs. the loading parameter  $\Delta W$  according to Eq. 4.4 with Eq. 4.17,  $q = 0.3$

The effect of the loading parameter  $\Delta W$  is now very low at uniaxial IP loading, caused by the low maximum principal stress. The maximum principal stress under torsional loading, acting within the loading parameter, is relatively high especially at the highest lifetime, when compared with uniaxial IP loading.

#### 4.3.4. The maximum principal stress sensitivity model

Due to the above mentioned observation a sensitivity parameter is introduced at this point.

$$\chi(\sigma_{P,max}, \sigma_{eq}) = \beta \sigma_{P,max} + (1 - \beta) \sigma_{eq} \quad \text{Eq. 4.18}$$

The results of this approach with one material parameter  $\beta$  in the stress function  $\chi$ , are given in Figure 4.11. The values of the loading parameter  $\Delta W$  are increased for the uniaxial IP loading due to the presence of the Mises stress in Eq. 4.18 which takes into account a small amount of damage under compression. But the longest lifetime achieved in a purely cyclic torsional test should be described by the lowest value of the loading parameter  $\Delta W$ . Therefore the influence of the mean tensile stress which is identically zero under pure torsion, is considered next.

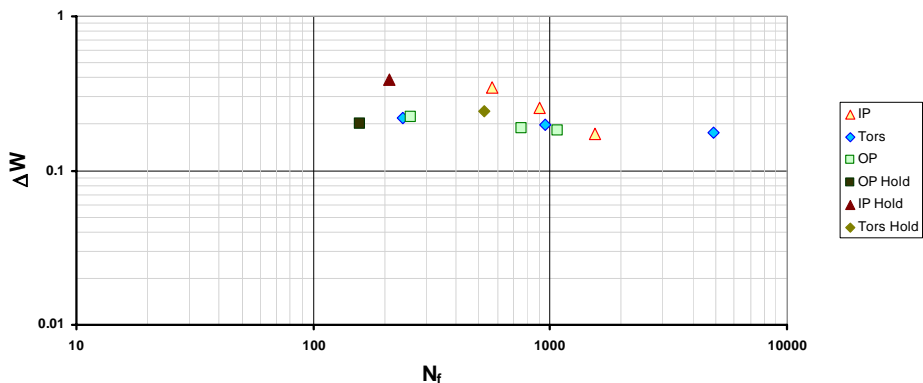


**Figure 4.11:** Experimental number of cycles-to-failure,  $N_f$ , vs. the loading parameter  $\Delta W$  according to Eq.4.4 with Eq. 4.18,  $\beta = 0.9$ ,  $q = 0.3$

#### 4.4. A generalised lifetime model

In order to maintain a small amount of damage under compressive loading McCauley brackets are introduced on the mean tensile stress, so that any negative mean tensile stress values are reverted to equal zero and the work of the Mises stress under compression is not counterbalanced:

$$\chi(\sigma_{p,max}, \bar{\sigma}_m, \sigma_{eq}) = \beta_1 \langle \sigma_{p,max} \rangle + \beta_2 3 \langle \bar{\sigma}_m \rangle + (1 - \beta_1 - \beta_2) \sigma_{eq} \quad \text{Eq. 4.19}$$

In accordance with the mean tensile stress, McCauley brackets are also set on the maximum principal stress for a general multiaxial loading. Moreover, the stress function (Eq. 4.19) has already positive values and reduces to just the uniaxial stress for uniaxial tension loading. Thus, the quantity (Eq. 4.19) could be called a *generalised equivalent stress*.

From the test results three phenomena are observed:

1. the lifetime relation between uniaxial IP and OP loading,
2. the lifetime relation between axial and torsional loading and
3. the hold period effect.

These three phenomena compare with the three material parameters  $\beta_1$ ,  $\beta_2$  and  $q$ , respectively. Thus, these three parameters can be uniquely determined by the three phenomena. The sum  $\beta_1 + \beta_2$  describe the uniaxial IP/OP lifetime relation and  $\beta_2$  characterises the influence of the mean tensile stress which vanishes at pure torsion. The material parameter  $q$  within the loading function  $\Delta W$  (Eq. 4.3) describes the reduction of the lifetime due to hold periods. The loading function  $\Delta W$  is optimised by these material parameters so that the data scatter is reduced from effectively three separate ranges to a grouped range, see Figure 4.12.

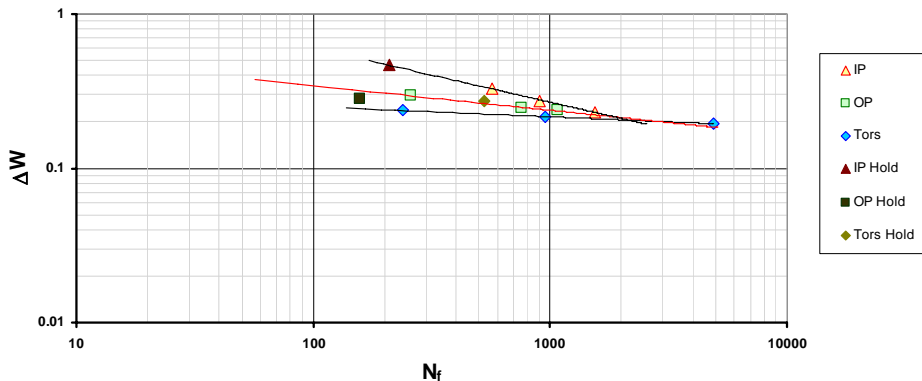


**Figure 4.12:** Experimental number of cycles-to-failure,  $N_f$ , vs. the loading parameter  $\Delta W$  according to Eq.4.4 with Eq. 4.19,  $\beta_1 = 0.54$ ,  $\beta_2 = 0.2$ ,  $q = 0.1$

In order to achieve this reduced scatter the material parameters  $q$ ,  $\beta_1$  and  $\beta_2$  were varied according to the data output, until it was considered that one particular parameter should remain unchanged.

#### 4. Discussion

By the stress function (Eq. 4.19) all lifetime results can be described in a narrow scatter band by the loading parameter  $\Delta W$ , see Figure 4.12. For example, the longest lifetime in torsion and the shorter lifetimes under uniaxial IP loading can be now represented by corresponding values of  $\Delta W$ , i.e. the highest lifetime of all tests achieved in torsion is described by the lowest  $\Delta W$  and all shorter lifetimes, for example at uniaxial IP loading, have higher values than this.

Torsion loading is extremely sensitive to the strain amplitude but despite this sensitivity, the results show the torsional tests lie well within the overall data scatter.

The axial-torsional test with a hold period which is the best representation of the actual loading conditions of a component in service, also lies within the data scatter. Therefore, the combined axial-torsional tests can be said to verify the results (see Figure 4.13).

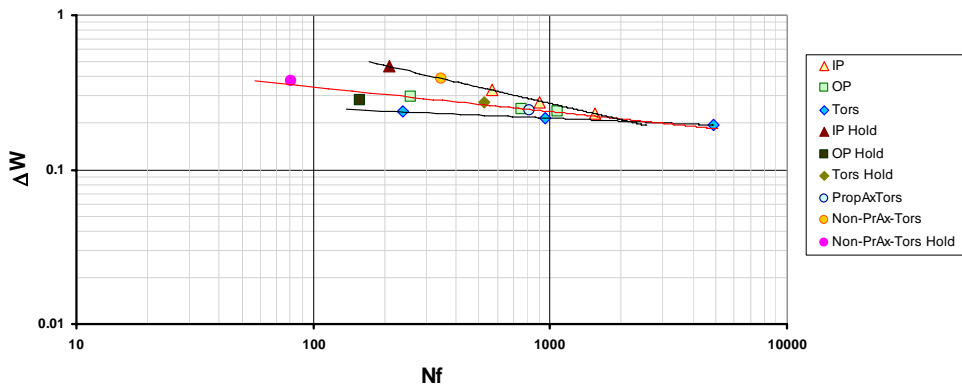


**Figure 4.13:** Experimental number of cycles-to-failure,  $N_f$ , vs. the loading parameter  $\Delta W$  according to Eq.4.4 with Eq. 4.19,  $\beta_1 = 0.54$ ,  $\beta_2 = 0.2$ ,  $q = 0.1$ , including the non-proportional and proportional tests which verify the results.

The material parameters are only valid for the temperature range 400-800°C. Different material elements in a component on the other hand experience different maximum temperatures and different stress levels. Thus, further TMF tests with different maximum temperatures should be performed in the future.

## 5. Summary

The near- $\gamma$ -TiAl alloy TNB-V5 with a duplex microstructure has been mechanically tested under non-isothermal thermo-mechanical fatigue conditions at various strain amplitudes and temperature-strain cycles over a temperature range of 400–800°C. For the first time, TMF tests were successfully conducted under axial-torsional loading on a TiAl alloy. These results have shown that strain amplitude and phase type are important factors in fatigue lifetime for this material: a small increase in strain amplitude reduces the lifetime considerably.

Uniaxial OP tests have shorter lifetimes than the uniaxial IP tests which can be attributed to the positive mean stress, the higher maximum tensile stress which can crack the oxide layer more readily. At high temperature an oxide layer forms which becomes brittle at lower temperatures. The uniaxial IP TMF loading promotes longer lifetimes due to the negative mean stress and the lower maximum tensile stress applied at high temperatures. The tensile loading at high temperature is less damaging. During the cooler, compressive stage, the oxide layer is better able to withstand the compressive loading. The results for uniaxial IP and OP tests are in accordance with previous studies of TMF on  $\gamma$ -TiAl.

Torsional loading has a longer lifetime than the uniaxial OP loading at the same Mises equivalent stress amplitude within a stabilised cycle, as the mean tensile stress is zero. The torsional fatigue lifetimes are very sensitive to strain amplitude, a minor increase in strain amplitude decreases lifetime considerably. Uniaxial IP tests at the same equivalent mechanical strain amplitude result in even higher lifetimes than pure torsional TMF tests, as under IP loading the maximum principal stress as well as the maximum mean stresses are low.

The non-proportional axial-torsional 90 degree OP test resulted in a shorter lifetime than the uniaxial OP test with the same Mises equivalent mechanical strain amplitude, due to the resulting diamond stress path having a higher equivalent stress amplitude. But there is no additional hardening due to the non-proportional axial-torsional loading with this investigated high temperature material.

A hold period at maximum temperatures reduced the lifetime for all tests regardless of the temperature-strain history. There is however, more pronounced additional damage in uniaxial OP tests than in uniaxial IP or torsional tests. Hold periods in OP tests result in higher maximum tensile stress than those tests without a hold period, which in combination with further oxidation damage accelerates crack growth.

The fractographic investigations revealed that fracture was caused by surface damage and, in the majority of cases, the stable crack propagation zones were oxidised. The microstructural investigations did not reveal significant differences between the specimens with or without hold periods. Intergranular fracture was identified for all types of tests, mainly in areas of globular  $\gamma$ -grains while cleavage failure is mostly observed in the lamellar colonies. The non-proportional-axial-torsional OP specimen with hold period has some additional transgranular fracture of the  $\gamma$ -grains. In all of the specimens examined, the fracture surface in longitudinal section reveal sub-surface secondary cracks.

From the microscopic characterisation investigations the overall difference between the as-received state and the TMF state are relatively minor. The fraction of twinned grains is not any different from the as-received state which implies that the extrusion process has caused the twinning and is not due to the TMF loading. The density of ordinary dislocations also appears almost unchanged when the scatter is taken into account Mean grain areas

## 5. Summary

appear slightly smaller after TMF loading than those of the as-received state which could be interpreted to be due to re-crystallisation. However, there is a large margin of uncertainty in the results, which makes interpretation difficult.

Results from uniaxial OP and IP TMF tests of this TNB-V5 were compared to Nimonic 90 and IN 738. For TiAl the least damaging temperature-strain phase is IP TMF and the most damaging OP TMF. IN 738 is similar to TNB-V5. However, the difference between OP and IP is much smaller. Nimonic 90 shows the opposite behaviour and lifetimes are somewhat longer than for TNB-V5 and IN 738 at the same equivalent strain amplitude. The damage mechanisms for TNB-V5 and IN 738 are high temperature oxidation effects whereas the Nimonic 90 is susceptible to creep damage.

A lifetime model formulated for this TNB-V5 alloy, successfully describes all temperature-strain TMF loading conditions over the test temperature range, with the use of a single loading parameter. The loading parameter is based on the plastic work per cycle, and is not only dependant on the mean tensile stress but also on the maximum principal stress. The loading parameter responds to diverse strain-temperature-paths differently. It describes the lifetime relation between uniaxial IP and OP loading, axial and torsional loading and the hold period effect. The model is subsequently verified by the axial-torsional tests with and without a hold period, as they lie within the data scatter.



## 6. References

- [1] Reed, R. C.: *The Superalloys: Fundamentals and applications*. Cambridge University Press, (2006).
- [2] Dimiduk, D. M., Miracle, D. B. and Ward, C. H.: Development of intermetallic materials for aerospace systems. *Mat Sci Technol* **8** (1992), pp. 367-375.
- [3] Loria, E. A.: Quo vadis gamma titanium aluminide. *Intermetallics* **9** (2001), pp. 997-1001.
- [4] Sauthoff, G.: *Intermetallics*. VCH Verlagsgesellschaft mbH, Weinheim (1995).
- [5] Umakoshi, Y.: Deformation of Intermetallic Compounds, in: *Materials Science & Technology: a comprehensive treatment:6/7*, R.W. Cahn, Edition. Wiley-VCH, Weinheim (2005), pp. 251-310.
- [6] Dimiduk, D. M.: Gamma titanium aluminide alloys - an assessment within the competition of aerospace structural materials. *Mat Sci Eng A* **263** (1999), pp. 281-288.
- [7] Ashby, M. F.: *Materials selection in mechanical design*. Butterworth Heinemann, Oxford (1997).
- [8] Peters, M., Hemptenmacher, J., Kumpfert, J. et al.: Titan und Titanlegierungen: Struktur, Gefüge, Eigenschaften, in: *Titan und Titanlegierungen*, M. Peters and C. Leyens, 1st Edition. Wiley-VCH, Weinheim (2002), pp. 1-38.
- [9] Massalski, T. B.: *Binary alloy phase diagrams*, Second Edition. Materials Park, Ohio ASM International (1996) p. 226.
- [10] Polmear, I. J.: *Light Alloys: From traditional alloys to nanocrystals*, Fourth Edition. Butterworth-Heinemann, Amsterdam, Boston (2006).
- [11] Appel, F. and Oehring, M.:  $\gamma$ -Titanaluminid Legierungen: Legierungsentwicklung und Eigenschaften in Titan und Titanlegierungen, in: *Titan und Titanlegierungen*, M. Peters and C. Leyens, Edition. Wiley-VCH, Weinheim (2002), pp. 39-103.
- [12] Polmear, I. J.: *Light Alloys: metallurgy of the light metals*, third Edition. Halsted Press, John Wiley & Sons, Inc., New York, Toronto (1996).
- [13] Skrotzki, B.: *Mechanical Loading of Light Alloys at Elevated Temperature*. Fortschritt-Berichte VDI, Reihe 5, Nr. 629. VDI-Verlag GmbH, Düsseldorf (2001).
- [14] Brookes, S. P., Kühn, H.-J., Skrotzki, B. et al.: Axial-Torsional Thermomechanical Fatigue of a near-Gamma TiAl-Alloy. *Mat Sci Eng A* **submitted**.
- [15] Voice, W. E., Henderson, M., Shelton, E. F. J. et al.: Gamma titanium aluminide, TNB. *Intermetallics* **13** - 9 (2005), pp. 959-964.
- [16] Rudolf, T.: Beitrag zur mechanischen und mikrostrukturellen Analyse der Elementarprozesse des Kriechens einer intermetallischen near- $\gamma$  TiAl-Legierung mit Duplexgefüge. PhD Thesis, Ruhr-Universität Bochum, Fakultät für Maschinenbau (2001).
- [17] Smith, L. S., Threadgill, P. and Gittos, M.: *Welding titanium; a designers and users handbook*, ed. D. Peacock. Titanium Information Group, Cambridge (1999).
- [18] Fukuhara, M. and Sanpei, A.: Elastic moduli and internal frictions of inconel 718 and Ti-6Al-4V as a function of temperature. *J. Mater. Sci. Lett* **12** (1993), pp. 1122-1124.
- [19] Callister, W. D.: *Materials Science and Engineering*, Third Edition. John Wiley & Sons, Inc., New York, Chichester (1994).
- [20] DiMatteo, N. D.: Fatigue and Fracture Resistance of Nonferrous Alloys, in: *ASM Handbook, Volume:19*, S.R. Lampman, Second Edition. ASM International Handbook Committee, Materials Park, Ohio (1997).
- [21] Trexler, M. D. and Jr., T. H. S.: Quantitative Characterization of Features Affecting Crack Path in a Directionally Solidified Superalloy, in: *Superalloys 2008*, Proc. Int. Conf., R.C. Reed, K.A. Green, P. Caron, T.P. Gabb, M.G. Fahrman, E.S. Huron

## 6. References

- and S.A. Woodard (Eds.), TMS (The Minerals, Metals and Materials Society) (2008), pp. 837-845.
- [22] Campbell, J. P., Rao, K. T. V. and Ritchie, R. O.: The effect of microstructure on fracture toughness and fatigue crack growth behavior in  $\gamma$ -titanium aluminide based intermetallics. *Metall Mater Trans A* **30A** (1999), pp. 563-577.
- [23] Appel, F. and Wagner, R.: Microstructure and deformation of two-phase  $\gamma$ -titanium aluminides. *Mat Sci Eng R* **22 - 5** (1998), pp. 187-268.
- [24] Werwer, M., Kabir, R., Cornec, A. *et al.*: Fracture in lamellar TiAl simulated with the cohesive model. *Engineering Fracture Mechanics* **74** (2007), pp. 2615-2638.
- [25] Clemens, H., Schretter, P. and Glatz, W.: Mikrostruktur und Eigenschaften von  $\gamma$ -TiAl-Basislegierungen. *Practische Metallographie* **33** (1996), pp. 17-35.
- [26] Porter, D. A. and Easterling, K. E.: *Phase transformations in metals and alloys*, Second Edition. Chapman & Hall, London (1996).
- [27] Schallow, P.: Isothermes und thermomechanisches Hochtemperaturermüdungsverhalten zweier  $\gamma$ -TiAl-Blechwerkstoffe, in: *Fortschritt-Berichte VDI, Reihe 5, Grund- und Werkstoffe/Kunststoffe, Nr. 707*, Edition. VDI Verlag, (2005).
- [28] Skrotzki, B., Rudolf, T. and Eggeler, G.: Creep behavior and microstructural evolution of a near- $\gamma$ -TiAl alloy with duplex microstructure. *Z Metallkd* **90 - 6** (1999), pp. 393-402.
- [29] Bartolotta, P. A. and Krause, D. L.: Titanium Aluminide Applications in the High Speed Civil Transport, in: *Gamma Titanium Aluminides*, Y.W. Kim, D.M. Dimiduk and M.H. Loretto, Edition. MMMS, (1999), pp. 3-10.
- [30] Roos, A., Chaboche, J.-L., Gélébart, L. *et al.*: Multiscale modelling of titanium aluminides. *Int J Plasticity* **20** (2004), pp. 811-830.
- [31] Hénaff, G. and Gloanec, A.-L.: Fatigue properties of TiAl alloys. *Intermetallics* **13 - 5** (2005), pp. 543-558.
- [32] Kestler, H. and Clemens, H.: Herstellung, Verarbeitung und Anwendungen von  $\gamma$ (TiAl)-Basislegierungen, in: *Titan und Titanlegierungen*, M. Peters and C. Leyens, Edition. Wiley-VCH, Weinheim (2002).
- [33] Kim, Y.-W., Dimiduk, D.M. : Designing Gamma TiAl Alloys: Fundamentals, Strategy and Production, in: *Structural Intermetallics*, R.D. M.V. Nathal, C.M. Liu, P.L. Martin, D.B. Miracle, R. Wagner und M. Yamaguchi, Edition. MMMS, Warrendale, Pennsylvania (1997), pp. 531-543.
- [34] Kim, Y.-W. *Advances in Gamma Alloy Technology*. ASM/TMS Spring Symposium [Presentation] Materials for Extreme Environments GE Global Research Center, Niskayuna, NY (2005); Available from: [http://www.asm-easternny.org/docs/2004\\_symp/2-3\\_Kim.pdf](http://www.asm-easternny.org/docs/2004_symp/2-3_Kim.pdf).
- [35] Aspinwal, D. K., Dewes, R. C. and Mantle, A. L.: The Machining of  $\gamma$ -TiAl Intermetallic Alloys. *CIRP Annals - Manufacturing Technology* **54 - 1** (2005), pp. 99-104.
- [36] Tetsui, T.: Effects of high niobium addition on the mechanical properties and high-temperature deformability of gamma TiAl alloy. *Intermetallics* **10** (2002), pp. 239-245.
- [37] Yamaguchi, M., Zhu, H., Suzuki, M. *et al.*: Importance of microstructural stability in creep resistance of lamellar TiAl alloys. *Materials Science and Engineering: A* **483-484** (2008), pp. 517-520.
- [38] Hu, D.: Effect of composition on grain refinement in TiAl-based alloys. *Intermetallics* **9 - 12** (2001), pp. 1037-1043.
- [39] Chen, C. L., Lu, W., Lin, J. P. *et al.*: Orientation relationship between TiB precipitate and  $\gamma$ -TiAl phase. *Scripta Mater* **56 - 6** (2007), pp. 441-444.
- [40] Cheng, T. T.: The mechanism of grain refinement in TiAl alloys by boron addition -- an alternative hypothesis. *Intermetallics* **8 - 1** (2000), pp. 29-37.

- [41] Honnorat, Y.: Issues and breakthrough in the manufacture of turboengine titanium parts. *Materials Science and Engineering: A* **213** - 1-2 (1996), pp. 115-123.
- [42] Lasalmonie, A.: Intermetallics: Why is it so difficult to introduce them in gas turbine engines? *Intermetallics* **14** - 10-11 (2006), pp. 1123-1129.
- [43] Recina, V. and Karlsson, B.: High temperature low cycle fatigue properties of Ti-48Al-2W-0,5Si gamma titanium aluminide. *Mat Sci Eng A* **262** (1999), pp. 70-81.
- [44] Baur, H., Wortberg, D. B. and Clemens, H.: Titanium Aluminides for Automotive Applications, in: *Gamma Titanium Aluminides 2003*, Proc. Int. Conf., Y.-W. Kim, H. Clemens and A.H. Rosenberger (Eds.), TMS (The Minerals, Metals and Materials Society) (2003), pp. 23-31.
- [45] Sommer, A. W. and Keijzers, G. C.: Gamma TiAl and the Engine Exhaust Valve, in: *Gamma Titanium Aluminides 2003*, Proc. Int. Conf., Y.-W. Kim, H. Clemens and A.H. Rosenberger (Eds.), TMS (The Minerals, Metals and Materials Society) (2003).
- [46] Tetsui, T.: Gamma Ti aluminides for non-aerospace applications. *Curr Opin Solid St M* **4** (1999), pp. 243-248.
- [47] Clemens, H., Lorch, A., Eberhardt, N. *et al.*: Technology, properties and applications of intermetallic  $\gamma$ -TiAl based alloys. *Z Metallkd* **90** (1999), pp. 569-580.
- [48] Tetsui, T., Shindo, K., Kobayashi, S. *et al.*: A newly developed hot worked TiAl alloy for blades and structural components. *Scripta Mater* **47** (2002), pp. 399-403.
- [49] Tetsui, T.: Development of a TiAl turbocharger for passenger vehicles. *Mat Sci Eng A* **329-331** (2002), pp. 582-588.
- [50] Smarsly, W., Baur, H., Glitz, G. *et al.*: Titanium aluminides for automotive and gas turbine applications, in: *Structural Intermetallics 2001*, K.J. Hemker, D.M. Dimiduk, H. Clemens, R. Darolia, H. Inui, J.M. Larsen, V.K. Sikka, M. Thomas and J.D. Whittenberger, Edition. TMS, (2001).
- [51] Esslinger, J. *Titanium in Aero Engines*. MTU Aero Engines GmbH, Munich, Germany (2003); Available from: [http://www.mtu-maintenance.com/en/technologies/engineering\\_news/33386Esslinger.pdf](http://www.mtu-maintenance.com/en/technologies/engineering_news/33386Esslinger.pdf).
- [52] *General Electric performs first run of new GENx engine* Flightglobal (2006); Available from: <http://www.flightglobal.com/articles/2006/03/21/205589/general-electric-performs-first-run-of-new-genx-engine.html>.
- [53] Mecham, M. (2006) *GENx Development Emphasizes Composites, Combustor Technology*. Aviation Week and Space Technology.
- [54] Weimer, M. and Kelly, T.: Gamma TiAl Applications at GE Aviation, in: *Structural Aluminides for Elevated Temperature Applications: Gamma Titanium and Other Metallic Aluminides*, Proc. Int. Conf., Y.-W. Kim, D. Morris, R. Yang and C. Leyens (Eds.), TMS (The Minerals, Metals and Materials Society) (2008), pp. 5.
- [55] Smarsly, W. *Aero Engine Materials*. [Seminar, Faculty of Mechanical Engineering, Cracow University of Technology, Poland] MTU Aero engines GmbH (2006); Available from: [http://www.mtu.de/en/technologies/engineering\\_news/061221\\_smarsly\\_materials.pdf](http://www.mtu.de/en/technologies/engineering_news/061221_smarsly_materials.pdf).
- [56] Pather, R., Mitten, W. A., Holdway, P. *et al.*: The effect of high temperature exposure on the tensile properties of  $\gamma$  TiAl alloys. *Intermetallics* **11** (2003), pp. 1015-1027.
- [57] *CFM Introduces LEAP-X Turbofan Program; Working in Parallel on Open Rotor Engine*. (2008); Available from: <http://www.greencarcongress.com/2008/07/cfm-introduces.html>.
- [58] *CFM reveals next-generation engine plans*. (2008); Available from: <http://forum.projectopensky.com/index.php?s=91cadfb77b945f614460c7130801acca&showtopic=32658&st=0&p=308616&#entry308616>.
- [59] Dieter, G. E.: *Mechanical Metallurgy*, SI Metric Edition. McGraw-Hill book Company (UK) Limited, London (1988).

## 6. References

- [60] Suresh, S.: *Fatigue of Materials*, Second Edition. Cambridge University Press, Cambridge (1998).
- [61] Brostow, W.: *Science of Materials*. John Wiley & Sons Inc., New York, Chichester (1979).
- [62] Christ, H.-J.: *Wechselverformung von Metallen: Zyklisches Spannungs-Dehnungs-Verhalten und Mikrostruktur*, ed. B. Ilshner. Springer-Verlag, Berlin, Heidelberg, New York (1991).
- [63] Thomas, G. B.: Standards for fatigue testing at high temperatures, in: *Measurement of high temperature mechanical properties of materials*, M. Loveday, M.F. Day and B.F. Dyson, Edition. H.M.S.O., National Physical Laboratory, Teddington (1982), pp. 32-41.
- [64] Brown, M. W.: Low cycle fatigue testing under multiaxial stresses at elevated temperature, in: *Measurement of high temperature mechanical properties of materials*, M. Loveday, M.F. Day and B.F. Dyson, Edition. H.M.S.O., National Physical Laboratory, Teddington (1982), pp. 185-203.
- [65] Jordan, E. H., Brown, M. W. and Miller, K. J.: Fatigue under severe nonproportional loading, in: *Multiaxial fatigue*, K.J. Miller and M.W. Brown, Edition. American Society for Testing and Materials, Philadelphia, PA 19103 (1985), pp. 569-585.
- [66] Found, M. S., Fernando, U. S. and Miller, K.: Requirements of a new multiaxial fatigue testing facility, in: *Multiaxial fatigue*, K.J. Miller and M.W. Brown, Edition. American Society for Testing and Materials, Philadelphia, PA 19103 (1985).
- [67] ASTM **E 2368-04**: A.S.f.t.T.o. Materials Standard Practice for Strain Controlled Thermomechanical Fatigue Testing. ASTM International, (2004).
- [68] Hähner, P., Affeld, E., Beck, T. *et al.*, *Validated Code-of-Practice for Strain-Controlled Thermo-Mechanical Fatigue Testing*. (2006), European Commission: Petten, NL.
- [69] Christ, H.-J., Fischer, F. O. R. and Maier, H. J.: High-temperature fatigue behavior of a near- $\gamma$  titanium aluminide alloy under isothermal and thermo-mechanical conditions. *Mat Sci Eng A* **319-321** (2001), pp. 625-630.
- [70] Bieler, T. R., Fallahi, A., Ng, B. C. *et al.*: Fracture initiation/propagation parameters for duplex TiAl grain boundaries based on twinning, slip, crystal orientation, and boundary misorientation. *Intermetallics* **13** (2005), pp. 979-984.
- [71] Skrotzki, B.: Crystallographic aspects of deformation twinning and consequences for plastic deformation processes in  $\gamma$ -TiAl. *Acta Mater* **48** - 4 (2000), pp. 851-862.
- [72] Skrotzki, B., Ünal, M. and Eggeler, G.: On the role of mechanical twinning in creep of a near-gamma TiAl-alloy with duplex microstructure. *Scripta Mater* **39** - 8 (1998), pp. 1023-1029.
- [73] Recina, V. and Nilsson, D.: High temperature low cycle fatigue properties of Ti-45Al-2Nb-2Mn+0,8vol% TiB<sub>2</sub> and Ti-47Al-2Nb-2Mn+0,8vol% TiB<sub>2</sub> in situ gamma titanium aluminide composites, in: *Gamma Titanium Aluminides 1999*, Y.-W. Kim, D.M. Dimiduk and M.H. Loretto, Edition. TMS, (1999), pp. 447-454.
- [74] Tsutsumi, M., Takano, S., Kitamura, T. *et al.*: Fatigue crack propagation in a cast TiAl intermetallic compound at high temperature. *Intermetallics* **4** (1996), pp. 77-83.
- [75] Cao, R., Yao, H. J., Chen, J. H. *et al.*: On the mechanism of crack propagation resistance of fully lamellar TiAl alloy. *Mat Sci Eng A* **420** - 1-2 (2006), pp. 122-134.
- [76] Choi, C., Kim, H. J., Lee, Y.-T. *et al.*: Effects of microstructural parameters on the fatigue crack growth of fully lamellar  $\gamma$ -TiAl alloys. *Mat Sci Eng A* **329-331** (2002), pp. 545-556.
- [77] Kumpfert, J., Kim, Y.-W. and Dimiduk, D. M.: Effect of microstructure on fatigue and tensile properties of the gamma TiAl alloy Ti-46,5Al-3,0Nb-2,1Cr-0,2W. *Mat Sci Eng A* **192/193** (1995), pp. 465-473.

- [78] Shibata, H., Tokaji, K., Ogawa, T. *et al.*: Microstructure dependence of fatigue strength and fatigue crack propagation in titanium aluminide. *Int J Fatigue* **18** - 2 (1996), pp. 119-125.
- [79] Recina, V.: High temperature low cycle fatigue properties of two cast gamma titanium aluminide alloys with refined microstructure. *Mater Sci Tech* **16** (2000), pp. 333-340.
- [80] Cui, W. F., Liu, C. M., Bauer, V. *et al.*: Thermomechanical fatigue behaviours of a third generation  $\gamma$ -TiAl based alloy. *Intermetallics* **15** (2007), pp. 675-678.
- [81] Christ, H.-J., Fischer, F. O. R. and Schallow, P.: Isothermal high-temperature fatigue behavior of a near- $\gamma$  titanium aluminide alloy. *Z Metallkd* **94** - 5 (2003), pp. 532-538.
- [82] Rao, K. T. V., Kim, Y. W., Muhlstein, C. L. *et al.*: Fatigue-crack growth and fracture resistance of  $\alpha_2$ -phase (Gamma + alpha(2)) TiAl alloy in duplex and lamellar microstructures. *Mat Sci Eng A* **193** (1995), pp. 474-482.
- [83] Jouiad, M., Gloanec, A.-L., Grange, M. *et al.*: Cyclic deformation mechanisms in a cast gamma titanium aluminide alloy. *Mat Sci Eng A* **400-401** (2005), pp. 409-412.
- [84] Recina, V. and Karlsson, B.: High temperature low cycle fatigue properties of Ti-48Al-2Cr-2Nb gamma titanium aluminides cast in different dimensions. *Scripta Mater* **43** (2000), pp. 609-615.
- [85] Goswami, T.: Low cycle fatigue-dwell effects and damage mechanisms. *International Journal of Fatigue* **21** - 1 (1999), pp. 55-76.
- [86] Park, Y. S., Ahn, W. S., Nam, S. W. *et al.*: The enhancement of low cycle fatigue life by carbon addition in lamellar TiAl alloy. *Mat Sci Eng A* **336** (2002), pp. 196-201.
- [87] Park, Y. S., Nam, S. W. and Hwang, S. K.: Intergranular cracking under creep-fatigue deformation in lamellar TiAl alloy. *Materials Letters* **53** - 6 (2002), pp. 392-399.
- [88] Bystrzanowski, S., Bartels, A., Clemens, H. *et al.*: Creep behaviour and related high temperature microstructural stability of Ti-46Al-9Nb sheet material. *Intermetallics* **13** - 5 (2005), pp. 515-524.
- [89] Appel, F.: Mechanistic understanding of creep in gamma-base titanium aluminide alloys. *Intermetallics* **9** - 10-11 (2001), pp. 907-914.
- [90] Oehring, M., Appel, F., Ennis, P. J. *et al.*: A TEM study of deformation processes and microstructural changes during long-term tension creep of a two-phase  $\gamma$ -titanium aluminide alloy. *Intermetallics* **7** - 3-4 (1999), pp. 335-345.
- [91] Lapin, J. and Nazmy, M.: Microstructure and creep properties of a cast intermetallic Ti-46Al-2W-0.5Si alloy for gas turbine applications. *Mat Sci Eng A* **380** - 1-2 (2004), pp. 298-307.
- [92] Malaplate, J., Thomas, M., Belaygue, P. *et al.*: Primary creep at 750°C in two cast and PM Ti48Al48Cr2Nb2 alloys. *Acta Mater* **54** - 3 (2006), pp. 601-611.
- [93] Skrotzki, B., Rudolf, T., Dlouhy, A. *et al.*: Microstructural evidence for dynamic recrystallization during creep of a duplex near-gamma TiAl-alloy. *Scripta Mater* **39** - 11 (1998), pp. 1545-1551.
- [94] Rudolf, T., Skrotzki, B. and Eggeler, G.: Microstructural evolution during creep of a duplex near-gamma TiAl-alloy. *Mat Sci Eng A* **319** (2001), pp. 815-819.
- [95] Christ, H.-J.: Effect of environment on thermomechanical fatigue life. *Mat Sci Eng A* **468-470** (2007), pp. 98-108.
- [96] Roth, M. and Biermann, H.: Thermo-mechanical Fatigue Behaviour of a modern  $\gamma$ -TiAl Alloy. *Int J Fatigue* **30** (2008), pp. 352-356.
- [97] Roth, M. and Biermann, H.: Thermo-mechanical fatigue behaviour of the  $\gamma$ -TiAl alloy TNB-V5. *Scripta Mater* **54** - 2 (2006), pp. 137-141.
- [98] Schallow, P. and Christ, H.-J.: Thermomechanical fatigue behaviour of a  $\gamma$ -TiAl sheet material. *Trans Indian Inst Met* **58** - 2-3 (2003), pp. 399-404.

## 6. References

- [99] Schallow, P. and Christ, H.-J.: Thermomechanical fatigue behaviour of a  $\gamma$ -TiAl sheet material, in: *LCF 5*, Edition. DVM, Berlin, Germany (2003), pp. 195-200.
- [100] Lu, W., Chen, C., Xi, Y. *et al.*: The oxidation behavior of Ti-46.5Al-5Nb at 900°C. *Intermetallics* **15** - 8 (2007), pp. 989-998.
- [101] Zeller, A., Dettenwanger, F. and Schütze, M.: Influence of water vapour on the creep and fatigue properties of TiAl. *Intermetallics* **10** (2002), pp. 33-57.
- [102] Zeller, A., Dettenwanger, F. and Schütze, M.: Influence of water vapour on the oxidation behaviour of titanium aluminides. *Intermetallics* **10** (2002), pp. 59-72.
- [103] Hotta, Y., Kaneno, Y., Takasugi, T. *et al.*: High-Temperature Environmental Embrittlement of Thermomechanically Processed TiAl-Based Intermetallic Alloys. *Metall Mater Trans A* **37A** (2006), pp. 361-369.
- [104] Planck, S. K. and Rosenberger, A. H.: The influence of high temperature exposure on the mechanical performance of a  $\gamma$  titanium aluminide alloy. *Mat Sci Eng A* **325** (2002), pp. 270-280.
- [105] Harding, T. S. and Jones, J. W.: The Effect of Impact Damage on the Room-Temperature Fatigue Behavior of  $\gamma$ -TiAl. *Met Mater Trans A* **31A** (2000), pp. 1741-1751.
- [106] Bache, M. R., Bradshaw, C. and Voice, W.: Characterisation of foreign object damage and fatigue strength in titanium based aerofoil alloys. *Mat Sci Eng A* **354** (2003), pp. 199-206.
- [107] Smith, R., Harding, T. S., Jones, J. W. *et al.*: The role of impact damage and fatigue strength reduction in gamma titanium aluminide alloys, in: *Structural Intermetallics 2001*, K.J. Hemker, D.M. Dimiduk, H. Clemens, R. Darolia, H. Inui, J.M. Larsen, V.K. Sikka, M. Thomas and J.D. Whittenberger, Edition. TMS, (2001).
- [108] Lerch, B. A., Draper, S. L. and Pereira, J. M.: Conducting high-cycle fatigue strength step tests on gamma TiAl. *Metall Mater Trans A* **33A** (2002), pp. 3871-3873.
- [109] Draper, S. L., Lerch, B. A., Pereira, J. M. *et al.*: Effect of impact damage on the fatigue response of TiAl Alloy - ABB-2, in: *Structural Intermetallics 2001*, K.J. Hemker, D.M. Dimiduk, H. Clemens, R. Darolia, H. Inui, J.M. Larsen, V.K. Sikka, M. Thomas and J.D. Whittenberger, Edition. (2001).
- [110] *MTU pursues lightweight materials: Neue Triebwerkswerkstoffe von MTU*. FLUG REVUE Ueberstr. 83, 53173 Bonn, Germany (2002); Available from: <http://www.flug-revue.rotor.com/frnews1/FRNews02/FR020915.htm>.
- [111] Ziebs, J., Meersmann, J., Kühn, H.-J. *et al.*, in: *Third Symposium on Thermo-Mechanical Fatigue Behavior of Materials, ASTM STP 1371*, H. Sehitoglu and H.-J. Mair, Edition. American Society for Testing and Materials, West Conshohocken, PA (1999).
- [112] Ziebs, J., Klingelhöffer, H., Meersmann, J. *et al.*, *Gesetzmäßigkeiten für die werkstoffmechanische Beschreibung der einkristallinen Nickelbasislegierung SC 16 unter ein- und mehrachsiger Beanspruchung*. (1998), Wirtschaftsverlag N. W.: Bremerhaven.
- [113] Marchionni, M., Klingelhöffer, H., Kühn, H.-J. *et al.*: Thermo-mechanical Fatigue of the Nickel-Base Superalloy Nimonic 90. *Key Engineering Materials* **345-346** (2007), pp. 347-350.
- [114] Frenz, H., Meersmann, J., Ziebs, J. *et al.*: High-temperature behaviour of IN 738 LC under isothermal and thermo-mechanical cyclic loading. *Materials Science and Engineering A* **230** - 1-2 (1997), pp. 49-57.
- [115] Meersmann, J., Ziebs, J., Klingelhöffer, H. *et al.*: Thermomechanical deformation behaviour of IN 738 LC and SC 16, in: *European Structural Integrity Society: Volume 25*, Edition. Elsevier, (1999), pp. 69-86.

- [116] Dimiduk, D. M.: Gamma titanium aluminide alloys - an assessment within the competition of aerospace structural materials. *Mat Sci Eng A* **263** (1999), pp. 281-288.
- [117] Ziebs, J., Meersmann, J., Kühn, H.-J. *et al.*: Multiaxial Thermo-mechanical Deformation Behavior of IN 738 LC and SC 16, in: *ASTM STP 1371, Thermo-mechanical Fatigue Behavior of Materials*, Edition. ASTM, West Conshohocken, USA (2000), pp. 257-277.
- [118] Tanaka, E., Murakami, S. and Ooka, M.: Effects of strain path shapes on non-proportional cyclic plasticity. *J. Mech. Phys. Solids* **33** - 6 (1985), pp. 559-575.
- [119] Doong, S. H. and Socie, D. F.: Deformation mechanisms of metals under complex non-proportional cyclic loading, in: *Fatigue under biaxial and multiaxial loading*, K. Kussmaul, D. McDiarmid and D. Socie, Edition. Mechanical Engineering Publications, London (1991), pp. 305-320.
- [120] Benallal, A. and Marquis, D.: Constitutive Equations for Nonproportional Cyclic Elasto-Viscoplasticity. *Transactions of the ASME* **109** (1987), pp. 326-336.
- [121] Berteaux, O., Jouiad, M., Thomas, M. *et al.*: Microstructure-low cycle fatigue behaviour relationships in a PM  $\gamma$ -TiAl alloy. *Intermetallics* **14** - 10-11 (2006), pp. 1130-1135.
- [122] Christ, H.-J.: Effect of environment on thermomechanical fatigue life. *Materials Science and Engineering A* - 468-470 (2007), pp. 98-108.
- [123] Sommitsch, C., Sievert, R., Wlanis, T. *et al.*: Modelling of creep-fatigue in containers during aluminium and copper extrusion. *Comp Mater Sci* **39** - 1 (2007), pp. 55-64.
- [124] Marchionni, M., Klingelhöffer, H., Kühn, H.-J. *et al.*: Thermo-mechanical fatigue of the nickel-base superalloy Nimonic 90. *Key Eng Mat* **345-346** (2007), pp. 347-350.
- [125] Dietrich, M., *Titan-Aluminid-Legierungen - eine Werkstoffgruppe mit Zukunft*. (2002), Forschungszentrum Jülich - Projektträger Jülich (PTJ): Jülich. pp. 131.
- [126] Peter, D., Pftzing, J., Wagner, M. F.-X. *et al.*: Quantitative Charakterisierung der Gefüge-Anisotropie einer stranggepressten TiAl-Legierung *Praktische Metallographie* **45** - 5 (2008), pp. 210-224.
- [127] Breakwell, P. R., Boxall, J. R. and Webster, G. A.: Specimen manufacture, in: *Measurement of high temperature mechanical properties of materials*, M. Loveday, M.F. Day and B.F. Dyson, Edition. H.M.S.O., National Physical Laboratory, Teddington (1982), pp. 322-332.
- [128] ASTM **E 2207-08**: Standard Practice for Strain-Controlled Axial-Torsional Fatigue Testing with Thin-Walled tubular Specimens. ASTM International, (2008).
- [129] Ellison, E. G.: Thermal-mechanical strain cycling and testing at higher temperatures, in: *Measurement of high temperature mechanical properties of materials*, M. Loveday, M.F. Day and B.F. Dyson, Edition. H.M.S.O., National Physical Laboratory, Teddington (1982), pp. 204-224.
- [130] Branch, G. D.: The design and operation requirements for high temperature mechanical properties data, in: *Measurement of high temperature mechanical properties of materials*, M. Loveday, M.F. Day and B.F. Dyson, Edition. H.M.S.O., National Physical Laboratory, Teddington (1982), pp. 23-31.
- [131] Beckmann, J., Rehmer, B. and M.Finn: Bestimmung der elastischen Eigenschaften von Festkörpern - Teil 1. *Materialprüfung* **48** (2006), pp. 274-281.
- [132] Lins, W., Kaindl, G., Peterlik, H. *et al.*: A novel resonant beam technique to determine the elastic moduli in dependence on orientation and temperature up to 2000°C. *Rev. Sci. Instrum.* **70** - 7 (1999), pp. 3052-3058.
- [133] Frenz, H., Meersmann, J., Ziebs, J. *et al.*: High-temperature behaviour of IN 738 LC under isothermal and thermo-mechanical cyclic loading. *Mat Sci Eng A* **230** (1997), pp. 49-57.

## 6. References

- [134] Chaboche, J. L.: Continuum damage mechanics: present state and future trends. *Nuclear Engineering and Design* **105** (1987), pp. 19-33.
- [135] Canovic, S., Jonsson, T. and Halvarsson, M.: Grain contrast imaging in FIB and SEM. *Journal of Physics: Conference Series* **126** (2008), pp. 1-4.
- [136] Underwood, E. E.: *Quantitative Stereology*. Addison-Wesley Publishing Company, Reading, MA (1970).
- [137] Christodoulou, J. A. and Flower, H. M.: The Role of Borides in Near- $\gamma$  Titanium Aluminides. *Adv Eng Mater* **10** (2000), pp. 631-638.
- [138] Khantha, M., Vitek, V. and Pope, D. P.: Strain-rate Dependence of the Brittle-to-ductile Transition Temperature in TiAl. *Mat. Res. Soc. Symp.* **646** (2001), pp. N1.11.1-6.
- [139] Bagnoli, D. L., Banerji, K., Boardman, B. *et al.*: Fractography, in: *ASM Handbook, Volume 12*, 9th Edition. ASM International Handbook Committee, Materials Park, Ohio (1992).
- [140] Nitta, A. and Kuwabara, K., in: *High Temperature Creep Fatigue*:3, Edition. Elsevier, London (1988), pp. 203-222.
- [141] Leyens, C.: Oxidationsverhalten und Oxidationsschutz von Titanlegierungen und Titanaluminide, in: *Titan und Titanlegierungen*, M. Peters and C. Leyens, 1st Edition. Wiley-VCH, Weinheim (2002), pp. 197-243.
- [142] Park, Y. S., Nam, S. W., Yang, S. J. *et al.*: Effect of creep deformation on creep-fatigue damage in lamellar TiAl alloy. *Mater Trans* **42** - 7 (2001), pp. 1380-1384.
- [143] Pineau, A.: *Fatigue at High Temperature*, ed. R.P. Skelton. Applied Science Publishers, London (1983) p. 305-364.
- [144] Fujino, M. and Taia, S.: *Effect of Thermal Cycles on Low Cycle Fatigue Lives of Steels and Grain Boundary Sliding Characteristics*. ECM-3, vol. 2. Pergamon, Cambridge (1980).
- [145] Riedel, H.: *Fracture at High Temperature*. Springer-Verlag, Berlin (1987).
- [146] Peter, D., Viswanathan, G. B., Wagner, M. F. X. *et al.*: Grain-boundary sliding in a TiAl alloy with fine-grained duplex microstructure during 750°C creep. *Mat Sci Eng A* **510-511** (2009), pp. 359-363.
- [147] Gloanec, A. L., Henaff, G., Jouiad, M. *et al.*: Cyclic deformation mechanisms in a gamma titanium aluminide alloy at room temperature. *Scripta Mater* **52** - 2 (2005), pp. 107-111.
- [148] Morris, M. A. and Lipe, T.: I. Creep deformation of duplex and lamellar TiAl alloys. *Intermetallics* **5** - 5 (1997), pp. 329-337.
- [149] Huang, S. C. and Hall, E. L.: Plastic Deformation and Fracture of Binary TiAl-Base Alloys. *Metall Trans A* **22 A** (1991), pp. 427-439.
- [150] Kim, J. H., Shin, D. H., Semiatin, S. L. *et al.*: High temperature deformation behavior of a  $\gamma$  TiAl alloy determined using the load-relaxation test. *Mat Sci Eng A* **344** - 1-2 (2003), pp. 146-157.
- [151] Appel, F., Buque, C. J., Eggert, S. *et al.*: Processing of gamma-based TiAl alloys by torsional deformation, in: *Gamma Titanium Aluminides 2003*, H.J. Kim, H. Clemens and A.H. Rosenberger, Edition. TMS, (2003), pp. 319-325.
- [152] Kim, J. H., Ha, T. K., Chang, Y. W. *et al.*: High Temperature Deformation Behavior of a gamma TiAl Alloy - Microstructural Evolution and Mechanisms. *Metall Mater Trans A* **34A** (2003), pp. 2165-2176.
- [153] Zhang, W. J., Lorenz, U. and Appel, F.: Recovery, recrystallization and phase transformations during thermomechanical processing and treatment of TiAl-based alloys. *Acta Mater* **48** - 11 (2000), pp. 2803-2813.
- [154] Lin, J. P., Xu, X. J., Wang, Y. L. *et al.*: High temperature deformation behaviors of a high Nb containing TiAl alloy. *Intermetallics* **15** - 5-6 (2007), pp. 668-674.
- [155] Lu, M. and Hemker, K. J.: Intermediate temperature creep properties of gamma TiAl. *Acta Mater* **45** - 9 (1997), pp. 3573-3585.



- [156] Ishikawa, Y. and Oikawa, H.: Structure Change of TiAl During Creep in the Intermediate Stress Range. *Mater T Jim* **35** - 5 (1994), pp. 336-345.
- [157] Tsuzuku, T. and Sato, H.: Superplastic behaviour and mechanical properties of two phase TiAl alloys. *J Phys IV* **3** (1993), pp. 389-395.
- [158] Edwards, L.: *Manufacturing with Materials*. Materials in action series, ed. L. Edwards and M. Edean. Butterworth-Heinemann Ltd., Oxford (1995).
- [159] Cao, G. H., Klöden, B., Rybacki, E. *et al.*: High strain torsion of a TiAl-based alloy. *Mat Sci Eng A* **483-484** (2008), pp. 512-516.
- [160] Liss, K.-D., Bartels, A., Clemens, H. *et al.*: Recrystallization and phase transitions in a  $\gamma$ -TiAl-based alloy as observed by ex situ and in situ high-energy X-ray diffraction. *Acta Mater* **54** (2006), pp. 3721-3735.
- [161] Ziebs, J., Meersmann, J., Kühn, H.-J. *et al.*: Multiaxial Thermomechanical Deformation Behaviour of IN 738 LC and SC 16, in: *Third Symposium on Thermo-Mechanical Fatigue Behavior of Materials, ASTM STP 1371*, H. Sehitoglu and H.-J. Mair, Edition. American Society for Testing and Materials, West Conshohocken, PA (1999).
- [162] Ziebs, J., Meersmann, J., Kühn, H.-J. *et al.*: Multiaxial Thermomechanical Behaviour of IN 738 Alloy, in: *Multiaxial Fatigue and Design*, ESIS 21 Proc. Int. Conf., A. Pineau, G. Caillestaude and T.C. Lindley (Eds.), Mechanical Engineering Publications, London (1996), pp. 83-96.
- [163] Luigia Muolo, M., Ferrera, E., Morbelli, L. *et al.*: Wetting, spreading and joining in the alumina-zirconia-Inconel 738 system. *Scripta Materialia* **50** - 3 (2004), pp. 325-330.
- [164] Hays, C.: Size and Shape Effects for Gamma Prime in Alloy 738. *J Mater Eng Perform* **17** - 2 (2008), pp. 254-259.
- [165] Lou, D. C., Akselsen, O. M., Solberg, J. K. *et al.*: Silicon-boronising of Nimonic 90 superalloy. *Surface and Coatings Technology* **200** - 11 (2006), pp. 3582-3589.
- [166] Viswanathan, R. and Bakker, W.: Materials for Ultrasupercritical Coal Power Plants - Turbine Materials: Part II. *J Mater Eng Perform* **10** - 1 (2001), pp. 96-101.
- [167] Socie, D.: Critical plane approaches for multiaxial fatigue damage assessment, in: *Advances in Multiaxial Fatigue*, D.L. McDowell and R. Ellis, Edition. American Society for Testing and Materials, Philadelphia, PA (1993), pp. 7-36.
- [168] Troshchenko, V.: High-Cycle Fatigue and Inelasticity of Metals, in: *Multiaxial Fatigue and Design*, ESIS 21 Proc. Int. Conf., A. Pineau, G. Caillestaude and T.C. Lindley (Eds.), Mechanical Engineering Publications, London (1996), pp. 335-348.
- [169] Lemaitre, J. and Chaboche, J.-L.: *Mechanics of Solid Materials*. Cambridge University Press, Cambridge, (1990) p. 416.
- [170] Szabó, I.: *Einführung in die Technische Mechanik*. Springer-Verlag Berlin, (1975) p. 196.

## Appendix 1: Test matrix data

Test Type	$\epsilon_{eq}$ [%]	$\epsilon_m$ [%]	$\gamma$ [%]	$\Delta\epsilon_p$ [%]	$\Delta\gamma_p$ [%]	$N_f$ [-]	Specimen number
Uniaxial (OP)	0.15	0.15	-	0.002	-	1076	002
"	0.17	0.17	-	0.007	-	756	010
"	0.20	0.20	-	0.002	-	257	004
"	0.30	0.30	-	0.002	-	8	001
(Hold period)	0.15	0.15	-	0.006	-	159	019
Uniaxial (IP)	0.30	0.30	-	0.004	-	3656	016
"	0.50	0.50	-	0.111	-	1546	011
"	0.55	0.55	-	0.189	-	907	017
"	0.70	0.70	-	0.355	-	572	015
(Hold period)	0.55	0.55	-	0.304	-	209	013
Torsional (IP)	0.15	-	0.26	-	0.005	2098	006
"	0.17	-	0.29	-	0.004	4896	014
"	0.19	-	0.33	-	0.004	958	018
"	0.20	-	0.35	-	0.008	238	005
(Hold period)	0.19	-	0.33	-	0.003	526	020
Prop. axial-tors. (OP)	0.15	0.106	0.18	0.005	0.009	819	003
Non-prop. axial-tors.(OP)	0.17	0.17	0.294	0.06	0.130	348	012
(Hold period)	0.15	0.15	0.26	0.018	0.109	81	021

## Appendix 2: Table of figures

- Figure 1.1: Specific strength  $\sigma_f / \rho$ , plotted against temperature for structural materials.  $\sigma_f$  is the yield strength for metals and tensile strength for composites. The high specific strength of TiAl alloys compared to conventional Ti alloys, heat treated steels and superalloys at higher temperatures are very attractive [7, 8]. 2
- Figure 1.2: The titanium-aluminium binary equilibrium phase diagram [9]. The compounds  $Ti_3Al$  ( $\alpha_2$ ), and  $TiAl$  ( $\gamma$ ) are highlighted and the compounds  $TiAl_2$  and  $TiAl_3$  are indicated by arrows as they are very narrow phases. 2
- Figure 1.3: Crystal structures of the TiAl compounds (a)  $TiAl_3$  ordered tetragonal  $DO_{22}$  structure (for lattice parameters see Table 1.1), (b)  $\alpha_2$ - $Ti_3Al$  ordered hexagonal  $DO_{19}$  structure and (c)  $\gamma$ -TiAl ordered (alternative layers of Ti and Al) face-centred tetragonal (fct)  $L1_0$  [11, 12]. 3
- Figure 1.4: Preferential directions of glide on the close packed (111) plane in the  $L1_0$  crystal structure. The possible glide Burgers vectors of ordinary dislocations of the type  $1/2\langle 110 \rangle$  and  $\langle 001 \rangle$  and the superdislocations of the type  $\langle 011 \rangle$  and partial dislocations  $1/6\langle 112 \rangle$  [11, 23, 24]. 5
- Figure 1.5: Schematic illustration of potential slip and twinning systems in the  $L1_0$  structure (a) the three layer atom stacking sequence on the (111)  $\gamma$ -plane. Ordinary dislocations  $1/2[\bar{1}10]$  (red arrow) and superdislocations  $[01\bar{1}]$  and  $1/2[11\bar{2}]$  (green arrows). The Burgers vectors of the pseudo-twinning (partial dislocations)  $b_1=1/6[\bar{2}11]$ ,  $b_2=1/6[1\bar{2}1]$  (blue arrows) and for true twinning  $b_3=1/6[11\bar{2}]$  (yellow arrow) which is perpendicular to Burgers vector  $b=1/2[\bar{1}10]$  for ordinary slip. (b) Core configurations of completely dissociated dislocations with Burgers vectors (i)  $1/2[\bar{1}10]$  (pale blue arrows) (ii)  $1/2[11\bar{2}]$  (pink arrows) and (iii)  $1/2[01\bar{1}]$  (purple arrows) [11, 23]. 6
- Figure 1.6: Preferential directions of glide (shaded) in the  $DO_{19}$  crystal structure. The slip dislocations  $2/3\langle 11\bar{2}0 \rangle$  on the basal  $\langle 11\bar{2}0 \rangle$   $\{0001\}$ , prismatic  $\langle 11\bar{2}0 \rangle$   $\{1\bar{1}00\}$  and pyramidal  $\langle \bar{1}\bar{1}26 \rangle$   $\{11\bar{2}1\}$  slip planes [24, 28] 7
- Figure 1.7: The different types of microstructure encountered in heat treated  $\gamma$ -TiAl, a) globular- $\gamma$ , b) duplex, c) near lamellar, d) fully lamellar ( $\gamma$ -grains are contrasted darker to the lighter  $\alpha_2$ -grains) and their approximate location on the central section of the assessed TiAl binary phase diagram. The shaded vertical line represents the composition of  $\gamma$ -TiAl alloys that have the most technical significance [23, 25, 27, 32]. 8
- Figure 1.8: Comparison of (a) room temperature Young's modulus versus density and (b) specific modulus versus temperature, for various structural metals and intermetallics.[6] 10
- Figure 1.9: Cast  $\gamma$ -TiAl automobile exhaust valves (Howmet Castings)[3] 11
- Figure 1.10: Commercial  $\gamma$ -TiAl turbocharger turbine wheel for a passenger vehicle (Mitsubishi Heavy Industries, Ltd.)[46] 11

- Figure 1.11: Schematic illustration of an aero gas turbine engine showing the gas temperature path through the engine with the proposed TiAl blade locations and blade types. The introduction of this material into the aero gas turbine engine would reduce the component weight by 40% (image source: MTU Aero Engines GmbH) [55, 56]. 12
- Figure 1.12: The CFM LEAP-X GE36 unducted turbofan (open rotor). (image source: CFM) [58]. 12
- Figure 1.13: Schematic representation of the fatigue stress cycles for a) a fully reversed stress cycle where  $\sigma_{\max}$  and  $\sigma_{\min}$  are symmetrical to the zero stress level,  $\sigma_m = 0$ , b) a repeated stress cycle where  $\sigma_{\max}$  and  $\sigma_{\min}$  are asymmetrical to the zero stress level, here shown just in tension also possible in compression or c)  $\sigma_{\max}$  and  $\sigma_{\min}$  of the opposite sign or both and d) a random or irregular stress [19, 59] 14
- Figure 1.14: Stress amplitude  $\sigma_a$ , (S) versus number of cycles to fatigue failure (N) for a) a material with a fatigue limit and b) a material that does not show a fatigue limit [19, 59]. 15
- Figure 1.15: Total strain amplitude  $\Delta\epsilon/2$ , versus number of cycles to fatigue failure ( $2N_f$ ). The elastic and plastic strains show linear relationships [60]. 16
- Figure 1.16: A stable hysteresis loop for constant strain cycling.  $\Delta\epsilon_e$  denotes elastic strain range,  $\Delta\epsilon_p$  denotes plastic strain range,  $\Delta\epsilon$  denotes total strain range and  $\Delta\sigma$  denotes total stress range. Maximum stress-strain is reached at point A and minimum stress-strain is reached at point B [59, 60]. 18
- Figure 1.17: Cyclic strain cycles for, cyclic hardening - a) the stress response under strain control and b) corresponding strain controlled hysteresis loops, and cyclic softening - c) the stress response under strain control and d) corresponding strain controlled hysteresis loops. [60] 18
- Figure 1.18: Schematic representation of the strain paths for a) normal (pure uniaxial strain) b) pure torsional c) proportional d) non-proportional axial-torsional 90 degree out-of-phase known as the 'diamond-path'.  $\epsilon_m$  denotes mechanical strain and  $\gamma/\sqrt{3}$  the shear strain. 20
- Figure 1.19: Schematic representation of the temperature vs. time, strain vs. time, stress vs. time and stress-strain loading in a) isothermal, b) In-phase and c) out-of-phase fatigue tests at  $R = -1$  [69]. 21
- Figure 2.1: a) Schematic drawing of the hot extrusion process b) the product – sectioned billets after extrusion (image GfE Metalle und Materialien GmbH). 27
- Figure 2.2: The billet after EDM and WEDM processes. The stainless steel can (W) containing the billet (X), the wire eroded test piece (Y) and the wire eroded test piece core (Z). 28
- Figure 2.3: TMF test specimen geometry. Units are in millimetres. Scale approximately 1:2. 28
- Figure 2.4: The specimen identification code and serial number used in this study. 29
- Figure 2.5: The specimen prepared for TMF testing fitted with a 30mm steel compression member. a) schematic external view and b) sectioned view. 29

- Figure 2.6: The testing equipment situated at BAM (Division V.2) a) The MTS 100kN tension-torsion closed-loop servo-hydraulic testing machine and b) the high frequency induction heating unit shown here during a test at 800°C. The axial-torsional extensometers can be seen in the right of the picture. 30
- Figure 2.7: Schematic representation of the axial mechanical strain  $\epsilon_m$  and temperature vs. time for OP and IP tests, and torsional shear strain  $\gamma/\sqrt{3}$  vs. time for the performed non-proportional axial-torsional tests 32
- Figure 2.8: Schematic illustration of a thin-walled (1mm) tubular TMF specimen under axial-torsional loading. The shear stress  $\tau$ , is calculated at the mean diameter of the gauge section. Strain measurement is achieved via the axial-torsion extensometer which has a 25mm measuring distance within the gauge section. 34
- Figure 3.1: The microstructure of the as-received material. SEM micrograph in transverse section showing the fine duplex microstructure, extrusion direction and specimen axis are perpendicular to the image plane (BSE). 36
- Figure 3.2: Grain structure of the as-received (AR) material illustrated in cubic form. Double-headed arrows indicate extrusion direction (L). T: indicates transverse section where the extrusion direction is perpendicular to the image,  $L_1$  and  $L_2$ : indicates longitudinal sections where the extrusion direction is parallel to the images. (BSE) 37
- Figure 3.3: BSE image of the as-received material showing the bright contrasted rod-shaped particles positively identified as  $TiB_2$  using the EMPA. 38
- Figure 3.4: The dynamic elastic modulus E and shear modulus G measured between 26°C and 1000°C using the sonic resonance technique. The TMF test temperature range of 400°C - 800°C is indicated by the dashed lines. 39
- Figure 3.5: A typical uniaxial OP TMF test showing stress  $\sigma_{max}$ ,  $\sigma_{min}$ , stress range  $\Delta\sigma$ , vs. cycles to failure  $N_f$ . 40
- Figure 3.6: Stress vs. mechanical strain for a typical uniaxial OP TMF test. Each loading path almost follows the unloading path, however, with each loading cycle the stress-strain hysteresis curves shift positively in stress. The stress range remains constant throughout the test. 41
- Figure 3.7: The initial loading cycle (triangles) and mid-life  $N_f/2$ , (squares) hysteresis curves for the uniaxial OP TMF test shown in Figure 3.6. Clearly seen from this diagram is how (for  $N \geq 2$ ) the unloading paths closely follow the loading path, forming extremely narrow hysteresis loops. Over the test, the hysteresis loops shift positively in stress. ( $\epsilon_m = \epsilon_{eq} = 0.2\%$ ). 41
- Figure 3.8: Uniaxial OP TMF test with a 180 seconds hold period showing stress  $\sigma_{max}$ ,  $\sigma_{min}$ , stress range  $\Delta\sigma$ , vs. cycles to failure  $N_f$ . 42
- Figure 3.9: Stress vs. mechanical strain for the uniaxial OP TMF test with 180 seconds hold period ( $t_{hold}$ ) at  $T_{max}$ . As with non-hold period tests the stress-strain cycle curves do not completely overlap one another after each loading cycle, instead they shift positively in stress. 43
- Figure 3.10: The initial cycle (triangles) and mid-life (squares) hysteresis loading curves for the uniaxial OP TMF test with 180 seconds hold period. ( $\epsilon_m = \epsilon_{eq} = 0.15\%$ ). 43

- Figure 3.11: Diagram of  $\sigma_{\max}$  and  $\sigma_{\min}$  vs.  $N_f$ . Comparison of two uniaxial OP TMF tests, both at  $\epsilon_m = 0.15\%$ . One test with a 180 seconds hold period (squares) and the other without a hold period (triangles). The hold period test has a higher tensile stress by approximately 80MPa per cycle at mid-life and a decreased compressive stress by approximately 80MPa per cycle mid-life than the test without a hold period. The arrows indicate that this test continues beyond this point ( $\epsilon_m = \epsilon_{\text{eq}} = 0.15\%$ ). 44
- Figure 3.12: A uniaxial IP TMF test showing stress  $\sigma_{\max}$ ,  $\sigma_{\min}$ , stress range  $\Delta\sigma$ , vs. cycles to failure  $N_f$ . In this test the stress range  $\Delta\sigma$ , steadily decreases until approximately the 300th cycle before slightly increasing. 45
- Figure 3.13: Stress vs. mechanical strain for a typical uniaxial IP TMF test. The stress-strain cycle curves do not closely follow the loading/unloading paths, instead they form wide hysteresis loops. In this example cyclic stabilization occurs after approximately the 100th cycle, when the hysteresis loops superimpose over one another. The max tensile stress decreases over the test causing negative stress shift. 45
- Figure 3.14: The initial loading cycle (triangles) and mid-life (squares) hysteresis curves for the uniaxial IP TMF test shown in Figure 3.13. At mid-life there is a smaller stress shift over the compressive loading (~90MPa) than seen over the tensile loading (~220MPa) ( $\epsilon_m = \epsilon_{\text{eq}} = 0.55\%$ ). 46
- Figure 3.15: A uniaxial IP TMF test with 180 seconds hold period showing stress  $\sigma_{\max}$ ,  $\sigma_{\min}$ , stress range  $\Delta\sigma$ , vs. cycles to failure  $N_f$ . The stress range clearly decreases over the test. 47
- Figure 3.16: Stress vs. mechanical strain for the uniaxial IP TMF test with 180 seconds hold period ( $t_{\text{hold}}$ ) at peak tensile stress  $\sigma_{\max}$ . At  $T_{\max}$  the hysteresis curves shift negatively in stress, whereas at  $T_{\min}$  the curves return to the same stress level with each unloading cycle. 47
- Figure 3.17: The initial cycle (triangles) and mid-life (squares) hysteresis stress-strain curves for the uniaxial IP TMF test with 180 seconds hold period. The reduced tensile stress with each cycle causes a negative stress shift in the hysteresis stress-strain curves. This is not apparent in the compressive region of the stress-strain curves where there appears to be little or no stress shift ( $\epsilon_m = \epsilon_{\text{eq}} = 0.55\%$ ). 48
- Figure 3.18: Diagram of  $\sigma_{\max}$  and  $\sigma_{\min}$  vs.  $N_f$ . Comparison of two uniaxial IP TMF tests, both at  $\epsilon_m = 0.55\%$ . One test with a 180 seconds hold period (squares) and the other without a hold period (triangles). The hold period reduces the tensile stress by approximately 130MPa and increases the compressive stress by approximately 110MPa in every loading cycle. The fatigue life is reduced by 77% over the non-hold period test. ( $\epsilon_m = \epsilon_{\text{eq}} = 0.55\%$ ). 49
- Figure 3.19: Uniaxial OP and IP TMF tests depicting equivalent strain amplitude  $\epsilon_{\text{eq}}$  vs. cycles to failure  $N_f$ . The greater the strain amplitude the shorter the fatigue lifetimes. OP loadings are more sensitive to strain amplitude than IP loadings. Clearly seen the phase effect on IP and OP with the same strain amplitude of  $\epsilon_{\text{eq}}=0.3\%$  (dashed arrow). This IP test has a longer lifetime than the OP test by a factor of >450. Hold period tests reduce lifetimes by a factor of >4 for IP loadings and a factor of >6 for OP loadings with the same  $\epsilon_{\text{eq}}$ . There is a linear relationship between lifetime and strain amplitude. The arrow indicates an interrupted test. 49

- Figure 3.20: Cyclic mean stress.  $\sigma_m$  vs. number of cycles. N. for OP and IP TMF tests with and without hold periods. Tensile mean stresses develop during OP loading while they are compressive in IP tests. Hold periods amplify mean stresses. 50
- Figure 3.21: A torsional IP TMF test showing shear stress  $\tau_{max}$ ,  $\tau_{min}$ , shear stress range  $\Delta\tau$ , vs. cycles to failure  $N_f$ . 51
- Figure 3.22: Shear stress vs. shear strain for a typical torsional IP TMF test. As with the uniaxial OP tests the stress-strain cycle curves initially do not overlap one another instead they shift negatively in shear stress and only towards the end of the test they become more overlapped. 51
- Figure 3.23: The initial loading cycle (triangles) and mid-life (squares) hysteresis curves for a typical torsional IP TMF test. The stress range  $\Delta\tau$ , remains constant throughout the test although the actual loading paths shift negatively in stress ( $\gamma = 0.35\%$ ,  $\varepsilon_{eq} = 0.20\%$ ). 52
- Figure 3.24: A torsional IP TMF test with 180 seconds hold period, showing shear stress  $\tau_{max}$ ,  $\tau_{min}$ , shear stress range  $\Delta\tau$ , vs. cycles to failure  $N_f$ . 53
- Figure 3.25: Shear stress vs. shear strain for the torsional IP TMF test with 180 seconds hold period. The shear stress-strain loading curves initially shift negatively however, before  $N_f/2$  this stress shifting diminishes. 53
- Figure 3.26: The initial loading cycle (triangles) and mid-life (squares) hysteresis curves for the torsional IP TMF test illustrated above in Figure 3.25 ( $\gamma = 0.33\%$ ,  $\varepsilon_{eq} = 0.19\%$ ). 54
- Figure 3.27: Diagram of shear stress  $\tau$ , vs.  $N_f$ . This diagram compares two torsional IP TMF tests, both at  $\gamma = 0.33\%$ , one test with a 180 seconds hold period (squares) and the other without a hold period (triangles). The hold period decreases the shear stress by approximately 30MPa in every loading cycle. The fatigue life is reduced by 45% over the non-hold period test. The arrows indicate the test continues beyond this point ( $\gamma = 0.33\%$ ,  $\varepsilon_{eq} = 0.19\%$ ). 54
- Figure 3.28: Torsional IP TMF tests showing the equivalent strain amplitude  $\varepsilon_{eq}$ , vs. cycles to failure  $N_f$ . The greater the strain amplitude the shorter the fatigue lifetimes. Hold period tests reduce lifetimes by a factor of nearly two. The torsional IP TMF lifetimes decrease by a factor of >20 with the increase of the equivalent strain amplitude by 0.03%. The arrow indicates an interrupted test. 55
- Figure 3.29: The proportional-axial-torsional OP TMF test showing axial stress  $\sigma_{max}$ ,  $\sigma_{min}$ , stress range  $\Delta\sigma$ , vs. cycles to failure  $N_f$ . 56
- Figure 3.30: Axial stress vs. mechanical strain for the proportional-axial-torsional test. The stress-strain cycle curves initially shift positively in stress however before  $N_f/2$ , the stress shifting diminishes. 56
- Figure 3.31: The initial loading cycle (triangles) and mid-life (squares) hysteresis curves for the proportional-axial-torsional test from Figure 3.30 ( $\varepsilon_m = 0.106\%$  and  $\varepsilon_{eq} = 0.15\%$ ). 57
- Figure 3.32: The proportional-axial-torsional test showing shear stress  $\tau_{max}$ ,  $\tau_{min}$ , shear stress range  $\Delta\tau$ , vs. cycles to failure  $N_f$ . 57

- Figure 3.33: Shear stress vs. shear strain for proportional-axial-torsional test. As with the pure torsional tests the stress-strain cycle hysteresis curves do not overlap one another instead they shift negatively in stress. This shift diminishes with the test progression and the loading/unloading paths become overlaid with one another. 58
- Figure 3.34: The initial loading cycle (triangles) and mid-life (squares) hysteresis curves for a proportional-axial-torsional test. ( $\gamma = 0.18\%$ ,  $\epsilon_{eq} = 0.15\%$ ). 59
- Figure 3.35: Maximum equivalent stress  $\sigma_{eq\ max}$  calculated at  $T_{min}$  vs.  $N$  of the proportional-axial-torsional OP TMF ( $\epsilon_{eq} = 0.15\%$ ). 59
- Figure 3.36: The non-proportional-axial-torsional OP TMF test showing axial stress  $\sigma_{max}$ ,  $\sigma_{min}$ , stress range  $\Delta\sigma$ , vs. cycles to failure  $N_f$ . 60
- Figure 3.37: Complete axial stress-strain hysteresis curves for the non-proportional-axial-torsional test. Peak tensile loading is at  $T_{min} = 400^\circ\text{C}$ . The stress-strain cycle curves initially shift positively however before  $N_f/2$  the shift in the stress diminishes. 61
- Figure 3.38: The initial loading cycle (triangles) and mid-life (squares) hysteresis curves for the axial stress-strain part of the non-proportional-axial-torsional test from Figure 3.37 ( $\epsilon_m = \epsilon_{eq} = 0.17\%$ ). 61
- Figure 3.39: The non-proportional-axial-torsional OP TMF test showing shear stress  $\tau_{max}$ ,  $\tau_{min}$ , shear stress range,  $\Delta\tau$ , vs. cycles to failure  $N_f$  ( $\gamma = 0.294\%$ ,  $\epsilon_{eq} = 0.17\%$ ). 62
- Figure 3.40: Shear stress vs. shear strain for non-proportional-axial-torsional test. The wide centres of the hysteresis loops, at zero strain, are caused by the raise or decrease in temperature. Clearly seen here are the stress-strain paths overlapping one another and a small amount of positive shift in stress. The temperature path is  $90^\circ$  off-set to the shear loading hence the diamond temperature path. 62
- Figure 3.41: The initial loading cycle (triangles) and mid-life (squares) hysteresis curves for the non-proportional-axial-torsional test. The small differences in stress-strain paths from cycle 1 to the cycle at  $N_f/2$  are very obvious as they are almost superimposed over one another. There is a small amount of positive stress shift most of which occurs at cycle 1 ( $\gamma = 0.294\%$ ,  $\epsilon_{eq} = 0.17\%$ ). 63
- Figure 3.42: Maximum equivalent stress  $\sigma_{eq\ max}$  calculated at  $T_{min}$  vs.  $N$  from the non-proportional-axial OP TMF ( $\epsilon_{eq} = 0.17\%$ ). 64
- Figure 3.43: The non-proportional-axial-torsional OP TMF test with hold period showing axial stress  $\sigma_{max}$ ,  $\sigma_{min}$ , stress range  $\Delta\sigma$ , vs. cycles to failure  $N_f$ , hold period. 65
- Figure 3.44: Complete axial stress-strain hysteresis curves vs. temperature for the non-proportional-axial-torsional test with 180 seconds hold period. The stress-strain hysteresis curves shift positively in stress. 65
- Figure 3.45: The initial loading cycle (triangles) and mid-life (squares) hysteresis curves for the non-proportional-axial-torsional test from Figure 3.44 ( $\epsilon_m = \epsilon_{eq} = 0.15\%$ ). 66



- Figure 3.46: The proportional-axial-torsional OP TMF test with 180 seconds hold period showing shear stress  $\tau_{\max}$ ,  $\tau_{\min}$ , shear stress range  $\Delta\tau$ , vs. cycles to failure  $N_f$ . 67
- Figure 3.47: Shear stress vs. shear strain hysteresis curves for non-proportional-axial-torsional test with 180 seconds hold period. The hold period (indicated on the diagram) takes place at  $T_{\max}$  mid point of the shear unloading. 67
- Figure 3.48: The initial loading cycle (triangles) and mid-life (squares) hysteresis curves for the non-proportional-axial-torsional test shown in Figure 3.47. There appears to be minimal shift in stress in this test ( $\gamma = 0.26\%$ ,  $\epsilon_{\text{eq}} = 0.15\%$ ). 68
- Figure 3.49: Maximum equivalent stress  $\sigma_{\text{eq max}}$  calculated at  $T_{\min}$  vs.  $N$  of the non-proportional-axial-torsional OP TMF with hold period ( $\epsilon_{\text{eq}} = 0.15$ ). 68
- Figure 3.50: Equivalent strain amplitude vs. Number of cycles to failure.  $N_f$ . 70
- Figure 3.51: Mises equivalent stress amplitude within a stabilised cycle vs. number of cycles to failure.  $N_f$ . The Mises equivalent mechanical strain amplitude is given in parentheses for each test of the corresponding type. IP = thermal-mechanical in-phase. OP = axially thermal-mechanical  $180^\circ$  out-of-phase. Lifetimes of interrupted tests are indicated by arrows. 71
- Figure 3.52: Light microscopic (LM) view of the uniaxial OP TMF specimen ( $\epsilon_{\text{eq}} = 0.15\%$ ). This is typical of the uniaxial OP specimens which all fractured perpendicular to the external stress, resulting in a  $90^\circ$  separation of the specimen. The fracture surface of one half of the specimen is shown on the right. The fracture initiation site can be identified by small pits in the material surface (indicated by the arrow) and the microcrack propagation area identified by the semi-circular oxidised zone on the fracture plane. Also visible are the ridge marks of final fracture. 72
- Figure 3.53: Macrograph of the crack initiation site. On the outer surface pits caused by the thermocouple attachment are indicated by the arrows. The fan-shaped oxidised crack propagation zone in this example penetrates approximately  $400\mu\text{m}$  into the specimen from the crack initiation site on the outer surface. Ridge marks can also be seen radiating out away from the crack propagation zone ( $\epsilon_{\text{eq}} = 0.15\%$ ) (LM). 73
- Figure 3.54: Micrographs of the crack initiation site. a) The damaged surface caused by the thermocouple can be seen at the right centre of the image (indicated by the arrow). b) The area indicated by the square in (a) within in the unstable crack growth region under higher magnification clearly shows the intergranular decohesion and secondary cracks along grain boundaries ( $\epsilon_{\text{eq}} = 0.15\%$ ) (SE). Images courtesy of Janine Pfetzing, Ruhr-University Bochum. 73
- Figure 3.55: Longitudinal section of a fractured uniaxial OP TMF specimen ( $\epsilon_{\text{eq}} = 0.15\%$ ). a) Schematic diagram showing the approximate location of the image in (b) with respect to the specimen orientation. b) The fracture surface is uneven and has some sub-fracture-surface secondary cracks and outer surface cracks close to the fracture surface. c) A higher magnified view of the left top corner of (b) showing the outer surface cracks some  $5\text{-}10\mu\text{m}$  in length. The crack on the right appears to be translamellar (BSE). 74

- Figure 3.56: Longitudinal section of a fractured uniaxial OP specimen with a hold period ( $\epsilon_{eq} = 0.15\%$ ). a) shows the fracture surface has greater sub-surface damage than with the uniaxial test without a hold period. The crack indicated in this image is approximately  $500\mu\text{m}$  long. b) An enlarged crack path indicated by the square in (a) which has progressed via  $\gamma$ -grain boundaries (BSE). 75
- Figure 3.57 a) A uniaxial IP specimen ( $\epsilon_{eq} = 0.5\%$ ) with two crack initiation sites, the arrows indicate the two oxidised zones. b) The marks left by the thermocouple are indicated by the arrows. Oxidation is extensive, completely penetrating the specimen wall. c) The second site is smaller but the oxidised zone is still large penetrating the wall by approximately  $700\mu\text{m}$  (LM). 76
- Figure 3.58 a) Fractographs of the two oxidised zones shown in Figure 3.57. a) A magnified view of the area where the thermocouple was attached (indicated by the arrow). A deep crack can be seen initiating perpendicular from the outer surface running into the bulk material. b) A micrograph of the second site shown in Figure 3.57c also here at this site, a fine crack runs perpendicular to the outer specimen wall (indicated by the arrow). (SE). Images courtesy of Dennis Peter, Ruhr-University Bochum. 77
- Figure 3.59: Longitudinal section of a fractured uniaxial IP specimen ( $\epsilon_{eq} = 0.7\%$ ). a) Numerous small cracks can be seen along the outside edge of the specimen, close to the fracture surface. b) A higher magnification of the  $\sim 5\text{-}15\mu\text{m}$  cracks on the outer surface near the fracture surface (indicated by the square in a). Intergranular fracture can be clearly seen in this image. c) A small  $\sim 5\text{-}10\mu\text{m}$  long fissure on the inner surface (BSE). 77
- Figure 3.60: The torsional specimen with hold period ( $\epsilon_{eq} = 0.19\%$ ). This specimen failed (fragmented) at mid-point of the gauge section at approximately  $45^\circ$  to the specimen axis. The deep ridge marks seen along the fracture surface and the crack initiation site (indicated by the arrow) (LM). 78
- Figure 3.61: The crack initiation site (indicated by the arrow) and the semi-circular oxidised crack propagation zone projecting half way through the specimen wall. (LM). 79
- Figure 3.62: Large ridge marks found on the fracture surface further from the crack propagation zone. (LM). 79
- Figure 3.63. Fractographs of a) the ridge marked region showing b) The mixture of cleavage and intergranular fracture. (SE). Images courtesy of Dennis Peter, Ruhr-University Bochum. 79
- Figure 3.64: This proportional-axial-torsional OP specimen ( $\epsilon_{eq} = 0.15\%$ ) failed at mid-point of the gauge section at approximately  $30^\circ$  to the specimen axis. The spiral fracture path ending with a perpendicular fracture approximately  $9\text{mm}$  long. The outer wall of the specimen is cracked beyond the final fracture (LM). 80
- Figure 3.65: The crack initiation site (indicated by the arrow) is located, adjacent to the semi-circular oxidised crack propagation zone which penetrates one third into the specimen wall. The largest ridge markings found on the fracture surface opposite the crack initiation site (LM). 81
- Figure 3.66. Fractograph of the proportional-axial-torsional OP TMF specimen. a) The ridge marked fracture surface showing the large areas of grain

- decohesion. b) An enlargement of the microstructure shows predominantly intergranular fracture with some cleavage fracture of the lamellar grains (indicated by the arrows) (SE). Images courtesy of Janine Pfetzing, Ruhr-University Bochum. 81
- Figure 3.67: This non-proportional-axial-torsional OP specimen ( $\epsilon_{eq} = 0.17\%$ ) failed at approximately mid-point of the gauge section perpendicular to the specimen axis. On the fracture plane the crack initiation site is identified by the semi-circular oxidised zone (indicated by the arrow) (LM). 82
- Figure 3.68: Location of the crack initiation site (indicated by the arrow), was as previously readily identified by the small pits on the outer surface as was the semi-circular oxidised crack propagation zone here penetrating one third into the specimen wall. The deep ridge markings found on the fracture surface are close to the crack initiation site (LM). 82
- Figure 3.69: This non-proportional-axial-torsional OP specimen with hold period ( $\epsilon_{eq} = 0.15\%$ ) failed close to the end of the gauge section. The fracture plane shows the crack propagation zone situated at the inner wall. The crack initiation site lies adjacent to the centre of the semi-circular area on the inner wall (indicated by the arrow). (LM). 83
- Figure 3.70: The crack initiation site identified by the semi-circular oxidised zone here penetrating almost half way into the specimen wall (LM). 84
- Figure 3.71: Longitudinal section of a fractured non-proportional-axial-torsional specimen with hold period revealing a) small cracks ( $\sim 25\text{-}40\mu\text{m}$  in length) along the inner wall of the specimen, close to the fracture front. b) On the outer wall the cracks are slightly smaller than those on the inner wall ( $\sim 15\text{-}25\mu\text{m}$  in length). In both areas the fracture is intergranular (BSE). 84
- Figure 4.1: The mechanical strain  $\epsilon_m$  and plastic strain  $\epsilon_p$  hysteresis loops for the first loading cycle and at mid-life of a typical uniaxial IP test. The plastic strain range  $\Delta\epsilon_p$ , is calculated from the mean stress of the plastic strain hysteresis loop at mid-life indicated on the diagram by the double arrows. Plastic strain continuously increases over the test ( $\epsilon_m = \epsilon_{eq} = 0.55\%$ ). 88
- Figure 4.2: The mechanical strain  $\epsilon_m$  and plastic strain  $\epsilon_p$  hysteresis loops for the first loading cycle and at mid-life of the uniaxial IP test with hold period. Plastic strain continuously increases over the test ( $\epsilon_m = \epsilon_{eq} = 0.55\%$ ). 88
- Figure 4.3: The equivalent plastic strain amplitude measured at mid-life  $N_f/2$ , for all performed tests. 89
- Figure 4.4: The stress response of torsional stress vs. axial stress for the non-proportional axial-torsional test at initial loading cycle (triangles) and mid-life (squares) compared with the axial stress from a uniaxial OP test at mid-life (solid bar on the x-axis) with the same equivalent strain amplitude ( $\epsilon_{eq} = 0.17\%$ ). 89
- Figure 4.5: Fraction of twinned  $\gamma$ -grains in the as-received state (AR) and after TMF loading. Taking into account the scatter of the measurement, the deformed states have only a slighter higher fraction of twinned grains as the as-received material. AxOP-0.15: uniaxial OP at  $\epsilon_{eq} = 0.15\%$ ; AxOP-H-0.15: uniaxial OP with hold period at  $\epsilon_{eq} = 0.15\%$ ; AxOP-0.17: uniaxial OP at  $\epsilon_{eq} = 0.17\%$ ; TorsIP-0.17: torsional IP at  $\epsilon_{eq} = 0.17\%$ ; TorsIP-0.19: torsional IP at

- $\varepsilon_{eq} = 0.19 \%$ ; TorsIP-H-0.19: torsional IP with hold period at  $\varepsilon_{eq} = 0.19 \%$ ; AxIP-0.2: uniaxial IP at  $\varepsilon_{eq} = 0.2 \%$ ; AxIP-0.5: uniaxial IP at  $\varepsilon_{eq} = 0.5 \%$ ; AxIP-0.7: uniaxial IP at  $\varepsilon_{eq} = 0.7 \%$ ; PrAxTorsOP-0.15: proportional-axial-torsional OP at  $\varepsilon_{eq} = 0.15 \%$ ; NPrAxTorsOP-0.17: non-proportional-axial-torsional OP at  $\varepsilon_{eq} = 0.17 \%$ ; NPrAxTors OP-H-0.15: non-proportional-axial-torsional OP with hold period at  $\varepsilon_{eq} = 0.15 \%$ . Results, by courtesy of Dennis Peter, Ruhr-University Bochum. 93
- Figure 4.6: Superdislocations indicated by the arrows observed in the proportional-axial-torsional OP ( $\varepsilon_{eq} = 0.15\%$ ) after TMF loading. TEM Image, by courtesy of Janine Pfetzing, Ruhr-University Bochum. 94
- Figure 4.7: Mean  $\gamma$ -grain area for the as-received state and after TMF loading. For explanation of specimen designation see Figure 4.5. Results, by courtesy of Dennis Peter, Ruhr-University Bochum. 94
- Figure 4.8: Uniaxial OP and IP TMF tests of TiAl, IN 738 and Nimonic 90 depicting mechanical strain amplitude vs. cycles to failure  $N_f$ . The material types are identified in the legend with the temperature range and heating rate. The data presented here are extracted from the investigations of [112, 117, 124, 162]. 97
- Figure 4.9: Experimental number of cycles-to-failure,  $N_f$ , vs. the plastic work parameter  $\Delta W$  according to Eq.4.16. 101
- Figure 4.10: Experimental number of cycles-to-failure,  $N_f$ , vs. the loading parameter  $\Delta W$  according to Eq. 4.4 with Eq. 4.17,  $q = 0.3$  102
- Figure 4.11: Experimental number of cycles-to-failure,  $N_f$ , vs. the loading parameter  $\Delta W$  according to Eq.4.4 with Eq. 4.18,  $\beta = 0.9$ ,  $q = 0.3$  102
- Figure 4.12: Experimental number of cycles-to-failure,  $N_f$ , vs. the loading parameter  $\Delta W$  according to Eq.4.4 with Eq. 4.19,  $\beta_1 = 0.54$ ,  $\beta_2 = 0.2$ ,  $q = 0.1$  103
- Figure 4.13: Experimental number of cycles-to-failure,  $N_f$ , vs. the loading parameter  $\Delta W$  according to Eq.4.4 with Eq. 4.19,  $\beta_1 = 0.54$ ,  $\beta_2 = 0.2$ ,  $q = 0.1$ , including the non-proportional and proportional tests which verify the results. 104

### Appendix 3: Table of tables

Table 1.1: Physical properties of the TiAl compounds [10]	3
Table 1.2: Properties of Ni based, Ti-based and $\gamma$ -TiAl alloys [4, 5, 12, 13, 15-22]	4
Table 1.3: Microstructures of $\gamma$ -TiAl and the effects on mechanical properties [28-31].	7
Table 1.4: TiAl alloy development [Atomic %] [33-35]	9
Table 2.1: Nominal composition of the TNB-V5 alloy	27
Table 2.2: Test matrix showing the test temperature rate $\dot{T}$ , the mechanical strain amplitude, $\varepsilon_m$ , the mechanical strain rate, $\dot{\varepsilon}_m$ , the shear strain, $\gamma$ , the shear strain rate, $\dot{\gamma}$ , the equivalent mechanical strain amplitude, $\varepsilon_{eq}$ , the equivalent mechanical strain rate, $\dot{\varepsilon}_{eq}$ , the phase shift between axial mechanical strain and temperature, $\varphi_{T-\varepsilon}$ , shear strain and temperature, $\varphi_{T-\gamma}$ , and axial mechanical strain and shear strain, $\varphi_{\varepsilon-\gamma}$ . The test temperature range is $T_{min} = 400^\circ\text{C}$ , $T_{max} = 800^\circ\text{C}$ . All tests were performed under strain control $R=-1$ .	33
Table 3.1: The volume fraction ( $V_f$ ) and average grain size of $\alpha_2$ , $\gamma$ and lamellar grains established from the as-received material.	37
Table 3.2: Measured composition using EDS.	38
Table 3.3: EMPA point analysis of particles in sample 1 and sample 2 (transverse and longitudinal).	39
Table 3.4: Results of the determination of the dynamic elastic modulus E and shear modulus G measured between $26^\circ\text{C}$ and $1000^\circ\text{C}$ , using the sonic resonance technique. The shaded region covers the TMF test temperature range of $400^\circ\text{C} - 800^\circ\text{C}$ .	39
Table 3.5: Complete test results matrix showing the equivalent strain amplitude, $\varepsilon_{eq}$ , the equivalent maximum stress $\sigma_{eq\ max}$ at $N_f/2$ , the maximum axial stress/shear stress $\sigma_{max}/\tau_{max}$ at $N_f/2$ , the minimum axial stress/shear stress $\sigma_{min}/\tau_{min}$ at $N_f/2$ , the maximum axial stress/shear stress $\sigma_{max}/\tau_{max}$ at $N_f$ , the minimum axial stress/shear stress $\sigma_{min}/\tau_{min}$ at $N_f$ , the mean stress $\sigma_m$ at $N_f/2$ , Cycles to failure $N_f$ , and temperature at failure. The test temperature range is $T_{min} = 400^\circ\text{C}$ , $T_{max} = 800^\circ\text{C}$ . Hold period tests are highlighted.	69
Table 4.1: Nominal compositions of the two compared Ni-based superalloys [124, 133, 162]	96
Table 4.2: Comparison between IP loading for IN 738, Nimonic 90 and TiAl showing the equivalent stress $\sigma_{eq}$ at $N_f/2$ , equivalent strain amplitudes $\varepsilon_{eq}$ , fatigue lifetimes $N_f$ , heating rate $\dot{T}$ , maximum and minimum temperatures, $T_{max}$ , - $T_{min}$ , and temperature range $\Delta T$	97

## Author's publications

- [1] Ledworuski, S., Klingelhöffer, H., Brookes, S. P., May, T.: Untersuchungen zum automatisierten Zugversuch für die Weiterentwicklung der Norm EN 10002-1 im Rahmen des Europäischen Forschungsprojektes TENSTAND (Tagungsband Werkstoffprüfung: Konstruktion, Qualitätssicherung und Schadensanalyse) pp73-78, 2004.
- [2] Ledworuski, S., Klingelhöffer, H., Brookes, S. P., May, T.: Computer controlled tensile testing according to EN 10002-1 - Results of a comparison test programme to validate a proposal for an amendment of the standard - Final report of the European project TENSTAND - Work Package 4 (Book, 2005).
- [3] Brookes, S. P., Kühn, H.-J., Skrotzki, B., Klingelhöffer, H., Sievert, R., Pfetzling, J., Eggeler, G.: Axial-Torsional Thermo-mechanical Fatigue of Ti-45 Al-5Nb-0.2B-0.2C (11th World Conference on Titanium (JIMIC5) - Ti-2007, Science and Technology -, June 3-7, 2007, Kyoto, Japan pp679-682. 2007).
- [4] Brookes, S. P., Kühn, H.-J., Skrotzki, B., Klingelhöffer, H., Sievert, R., Pfetzling, J., Peter, D., Eggeler, G.: Axial-torsionale thermo-mechanische Ermüdung einer near-Gamma TiAl-Legierung (Tagungsband Werkstoffprüfung: Konstruktion, Qualitätssicherung und Schadensanalyse) pp249-254. 2007.
- [5] Brookes, S. P., Kühn, H.-J., Skrotzki, B., Klingelhöffer, H., Sievert, R., Pfetzling, J., Peter, D., Eggeler, G.: TMS 2008 Annual Meeting & Exhibition, "Structural Aluminides for Elevated Temperatures - Gamma Titanium and Other Metallic Aluminides", March 9-13, 2008, New Orleans, Louisiana, USA (Proceedings) pp103-109.
- [6] Kühn, H.-J., Kahlcke, O., Brookes, S.: A practicable nominal temperature tolerance for TMF-tests, International Journal of Fatigue, 30, (2008), pp277-285.
- [7] Brookes, S. P., Kühn, H.-J., Skrotzki, B., Klingelhöffer, H., Sievert, R., Pfetzling, J., Peter, D., Eggeler, G.: Multi-Axial Thermo-Mechanical Fatigue of a Near-Gamma TiAl Alloy, Advanced Materials Research, 59 (2009), pp283-287.
- [8] Brookes, S. P., Kühn, H.-J., Skrotzki, B., Klingelhöffer, H., Sievert, R., Pfetzling, J., Peter, D., Eggeler, G.: Axial-Torsional Thermomechanical Fatigue of a near-Gamma TiAl-Alloy, Mat. Sci Eng A **submitted** (2009).

## Author's curriculum vitae

**NAME:** Stephen Peter Brookes  
**DATE OF BIRTH:** 25.09.1962  
**PLACE OF BIRTH:** Hitchin, Hertfordshire, England

### EDUCATIONAL HISTORY:

1969 – 1974 Trotts Hill Junior School, Stevenage, Hertfordshire, England.  
1975 – 1978 Thurso High School, Thurso, Caithness, Scotland.  
1979 – 1981 Thurso Technical College, Thurso, Caithness, Scotland.

### ACADEMIC QUALIFICATIONS:

Sept. 1995 – June 1998 **Bachelor of Engineering (B.Eng.):** "Materials Technology – Materials Science and Engineering", (Second Class Honours), Queen Mary and Westfield College, University of London.  
Sept. 1998 – Nov. 1999 **Master of Science (M.Sc.):** "Materials Research – Nanoindentation", Queen Mary and Westfield College, University of London. (Sponsor: National Physical Laboratory)

### PRACTICAL PLACEMENTS:

June 1997 – July 1997 **Bundesanstalt für Materialforschung und -prüfung, (BAM)**  
Untern den Eichen 87, 12205 Berlin, Germany.  
June 1998 – Aug. 1998 **National Physical Laboratory (NPL)**, Centre for Materials Measurement and Technology, Teddington, Middlesex, England.

### EMPLOYMENT HISTORY:

Feb. 1982 – Jan. 1986 **Royal Mail**, Thurso, Scotland und Chatham, Kent, England.  
*Postal employee*  
Feb. 1986 – Sept. 1991 **Post Office Counters Ltd.**, Rochester, Kent, England  
*Postal Officer and Acting Branch Manager*  
Oct. 1991 – Aug. 1995 **Deutsche Bundespost**, Hamburg.  
*Postal employee*  
Nov. 1999 – Oct. 2002 **Queen Mary, University of London**, Department of Materials, London, England.  
*Experimental Officer for Mechanical Testing*  
June 2003 – Dec. 2008 **Bundesanstalt für Materialforschung und -prüfung, (BAM)**, Berlin.  
*Research Scientist*  
Aug. 2009 **Rolls-Royce Mechanical Test Operations Centre GmbH**, Dahlewitz, Brandenburg.  
*Test Engineer*

## Acknowledgements

This PhD thesis is compiled from my work as research scientist at the Federal Institute for Materials Research and Testing, (BAM) Berlin, the department of Mechanics of Materials V.21, and generously funded by the Deutsche Forschungsgemeinschaft (German Research Foundation – DFG Sk 47/7-1/2).

I would very much like to thank my thesis supervisor, Priv.-Doz. Dr. Birgit Skrotzki, not only for sharing her extensive knowledge of titanium aluminides, but also for her enduring support, enthusiasm, faith and encouragement to me over the years.

I am also very grateful to Prof. Dr. Gunther Eggeler from the Institute for Materials, Ruhr-University Bochum, for his support as second supervisor.

I am indebted to Dipl.-Ing. Hans-Joachim Kühn, for his incredible dedication and knowledge of multi-axial thermo-mechanical fatigue testing – a true TMF wizard. I am also grateful to Dipl.-Ing. Monika Finn for the dynamic modulus measurements. My grateful appreciation I extend to Dr. Rainer Sievert, for his invaluable consultation and advice with the lifetime modelling. For their great generosity in sharing their knowledge on superalloys I wish to thank Prof. Dr. Pedro Dolabella Portella, BAM and Dr. Alexander Epishin, Technical University Berlin.

To all my former colleagues in BAM Division V.21, without their friendly presence in my working environment they would not have given me the same unforgettable everlasting memories - thank you all. Very exceptional thanks to Ole Kahlcke and Dr. Bernd Koch for 'Just Testing' – thanks for the other life guys.

I would like to thank to BAM Division V.1, for their generous assistance with SEM investigations especially; Dr. Gert Noltze, Dr. Dirk Bettge, Romeo Saliwan Neumann, Michaela Buchheim, Dipl.-Ing. Heike Nitschke and Gabriele Oder. Grateful thanks to the BAM workshop Z.5, for their expert specimen preparation.

Equally, my sincere gratitude to Dipl.-Ing. Janine Pfetzling, Dipl.-Ing. Dennis Peter, and Dr. J. Pešička, Ruhr-University Bochum for providing SEM Fractographs and allowing me to present the analysis of their TEM investigations.

Very special and heartfelt thanks to secretaries Anja Archie and Marianne Peyer.

Dr. Wilfried Smarsly, MTU Aero Engines GmbH, Munich and Dr. Andreas Otto of GfE Metalle und Materialien GmbH, Nuremberg for providing the material. Dr. Michael Oehring GKSS-Forschungszentrum Geesthacht GmbH, for some additional material properties.

Without the companionship and love of families and friends over the years, my life would just not have been the same. I want to especially thank; Anne, Uwe and Rhea Franke, Liva, Hartmut, Lena and Anna Müller, Sylvie, Cédric, Julian Kahlcke, Nine, Chris, Hannah, Sophia and Nicholas Loble, Sandra and Don Blackford, Jolanda Porembski, Andrew Browne and my parents for being there for me.

Last, but by no means least, for their ever present love, moral support and enduring encouragement, my wife Astrid and my lovely and very wonderful son Oliver.

Steve Brookes  
Berlin, April 2009.